Effects of Turbulence on Heliostat Wind Loads

Azadeh Jafari

School of Mechanical Engineering
University of Adelaide
South Australia, 5005

A thesis submitted in fulfilment of the requirements
for the degree of Ph.D. in Mechanical Engineering
May 2020

Abstract

Concentrated solar thermal systems are being increasingly deployed for industrial process heating and large-scale electricity production. A major constituent of a concentrating solar plant is the field of heliostat mirrors, which reflect the sunlight onto a receiver. Heliostats are subjected to fluctuating wind loads arising from atmospheric wind. These forces are important for design of heliostats, which must survive maximum wind loads under extreme conditions. Furthermore, dynamic wind loads which lead to vibrations of the mirror panel can affect the tracking accuracy of a heliostat field. Therefore, knowledge of wind loads is necessary for design and development of a heliostat field. The main source of unsteady loads on heliostats is the fluctuating wind velocity, which results from the turbulence within the atmospheric boundary layer. Furthermore, heliostats during their operation create a blockage in the flow and unstable vortex structures in their wake. The interaction between the wakes of several heliostats in a field with each other and with the incoming atmospheric boundary layer flow affects turbulence and consequently wind loads in a heliostat field.

The research presented in this thesis focuses on the development of an in-depth understanding of the effects of turbulence within the atmospheric boundary layer on the wind loads on heliostats. Extensive wind tunnel experiments have been conducted to simulate the atmospheric boundary layer turbulence and establish its effect on unsteady wind loads. Similarities and differences of the turbulence properties with respect to the atmospheric boundary layer are discussed and the requirements for achieving similarity in measurement of wind loads in a wind tunnel are established. A correlation is developed between the intensity and integral length scale of the turbulence and the peak lift and drag forces on a heliostat at stow and vertical positions, which is employed to predict the wind loads on full-scale heliostats in a range of terrains where the turbulence characteristics of the flow vary.

In order to develop an understanding of wind loads in a heliostat field, turbulence in the wake of a heliostat in the atmospheric boundary layer is characterised. Based on the findings, variations of flow and turbulence properties in a heliostat field are discussed. Moreover, through analysis of wind loads on a second tandem heliostat placed in the wake of an upstream one, it is demonstrated that wind loads on the second heliostat are correlated with the turbulence properties in the wake. It is concluded that wind loads on a heliostat within a field can be predicted from the approaching wake flow properties. Estimations for variations of wind loads in different regions of a field are thereby made based on the findings.

After demonstrating the strong relationship between turbulence and wind loads, the effect of perimeter fences around a heliostat field on the turbulence within the atmospheric boundary layer is investigated. It is demonstrated that the intensity and integral length scale of the turbulence reduce downstream of wire mesh fences. It is found that the reduction in turbulence properties behind a wire mesh fence is mainly correlated with the mesh porosity. Based on the variations of turbulence properties behind a wire mesh fence, the feasibility of reducing the wind loads on heliostats with application of the fences is analysed.

The research presented in this thesis provides an improved understanding of the effect of turbulence within the atmospheric boundary layer on the unsteady wind loads on heliostats. The findings of this research can be used to determine the design wind loads based on the turbulence characteristics specific to a given terrain. Recommendations for improvement of heliostat design and reduction of wind loads on heliostats are made based on the results, and potentials for reducing the cost of heliostats through reduction of structural costs related to the wind loads are identified. For instance, it is demonstrated that the peak wind loads on a stowed heliostat can be reduced by 80% by decreasing the height of the heliostat panel at stow. Furthermore, it is shown that there is a potential to reduce the peak drag force on an operating heliostat and the peak lift force on a stowed heliostat by application of wire mesh fences by 48% and 53%, respectively. Moreover, the presented study provides an insight into variations of wind loads within a heliostat field which are necessary to be considered in the design of heliostats. For example, up to 80% increase in the unsteady drag force coefficient on a vertical heliostat and up to 70% increase in the peak hinge moment coefficient on an operating heliostat are predicted for high-density regions of a field. Hence, the findings highlight the need to develop the arrangement of heliostats in a field such that the dynamic wind loads on the in-field heliostats can be reduced. The results of this research provide an opportunity for production of cheaper heliostats by reducing the design wind loads.

Declaration

I certify that this work contains no material which has been accepted for the award of any other degree or diploma in my name, in any university or other tertiary institution and, to the best of my knowledge and belief, contains no material previously published or written by another person, except where due reference has been made in the text. In addition, I certify that no part of this work will, in the future, be used in a submission in my name, for any other degree or diploma in any university or other tertiary institution without the prior approval of the University of Adelaide and where applicable, any partner institution responsible for the joint-award of this degree.

I acknowledge that copyright of published works contained within this thesis resides with the copyright holder(s) of those works.

I also give permission for the digital version of my thesis to be made available on the web, via the University's digital research repository, the Library Search and also through web search engines, unless permission has been granted by the University to restrict access for a period of time.

I acknowledge the support I have received for my research through the provision of an Australian Government Research Training Program Scholarship.

Azadeh Jafari

Acknowledgments

I would like to thank my principal supervisor, A/Prof Maziar Arjomandi, for his unwavering support, relentless encouragement, and invaluable guidance throughout the past three years. I truly appreciate the support of my co-supervisors, Prof Ben Cazzolato and Dr Farzin Ghanadi. I have learnt a lot from you all, and I am very grateful for your insightful supervision without which this thesis would not have been completed. I would also like to thank Dr Matthew Emes for his support, helpful comments, and insightful discussions. I really appreciate the time and effort that you all put into my work.

I would also like to thank the support provided by the technical staff of the Mechanical and Electronic workshops, particularly Phil Schmidt, Thomas Stanef, Scott Letton, Robert Dempster, Stephen Kloeden, and Ian Linke for helping me with the design and manufacturing of my experimental rigs. I would like to thank Marc Simpson for his kind support and help when carrying out my experimental testing at Thebarton wind tunnel.

To my family, thank you for your never-ending support. To my father, my mother, my beloved sisters and brothers-in-law, who have always been my best friends. To my beautiful nieces whose smiles would remind me of the joys of life. To my husband, Navid, who has been by my side throughout this journey. Thank you for your unlimited support and encouragement, and for helping me get through the difficult times. I am very grateful for having you as also a colleague to share and discuss research ideas with and for assisting me in solving the technical and scientific challenges of my work. It would not have been possible to accomplish this without you.

Also, to my friends, thank you for your encouragement and all the good times that we spent together, which were always refreshing throughout the journey of the Ph.D., specifically to Jessica, with whom I have shared the ups-and-downs of my Ph.D..

Finally, I would like to acknowledge the financial support I have received for my research through the provision of an Australian Government Research Training Program Scholarship and the Australian Renewable Energy Agency (ARENA) through Australian Solar Thermal Research Initiative (ASTRI).

Contents

Chapter 1

Introduction

1.1 Background

The application of solar power towers is emerging as a means for concentrating solar thermal energy for industrial process heating and large-scale electricity production due to its high power cycle efficiency (Kolb, 2011; Pfahl *et al.*, 2017). In a power tower system, a field of heliostat mirrors are employed to track the sun and reflect the sunlight onto a receiver installed at the top of a tower. A large number of heliostats are used in such solar plants, which are arranged in either a central layout surrounding the tower or in a polar layout on one side of the tower. These heliostats are exposed to atmospheric wind which imposes unsteady loads on them. The wind loads induce forces on the heliostat normal to the mirror panel, which can be decomposed into two components parallel to wind direction and perpendicular to it, so called a drag and a lift force which are illustrated in Figure 1.1. These forces create moments at the hinge and base of the pylon which are important for the design of the drives and foundation, respectively.

Design and development of cost-effective heliostat fields cannot be achieved without the knowledge of wind loads. An accurate evaluation of the maximum wind loads is critical for analysis of survivability of heliostats under highly turbulent wind speeds as underestimation of the peak design wind loads may result in structural failure (Peterka *et al.*, 1987). Overestimation of the wind loads, on the other hand, increases the capital cost of a solar plant significantly since the heliostat field comprises between 40% to 50% of the total capital cost of the plant (Kolb, 2011). Wind loading is a key parameter in design of the support structures and drives of a heliostat which constitute up to 80% of its capital cost (Kolb, 2011). Furthermore, the dynamic loads, induced by the correlation between the temporal variations of the wind loads and the dynamic properties of the heliostat structure, lead to vibrations of the heliostat panel which impact the tracking accuracy of the heliostat field and consequently the optical efficiency of the solar plant. Moreover, assessment of the dynamic response of the heliostats under unsteady wind loading is important for preventing dynamic failure arising from resonance and buffeting (Pfahl *et al.*, 2017), which may result from when the dominant frequencies of the wind loads are close to the natural frequencies of the heliostat structures, which typically lie in the range of 1.6–3 Hz (Griffith *et al.*, 2011; Gong *et al.*, 2012; Vásquez-Arango *et al.*, 2015).

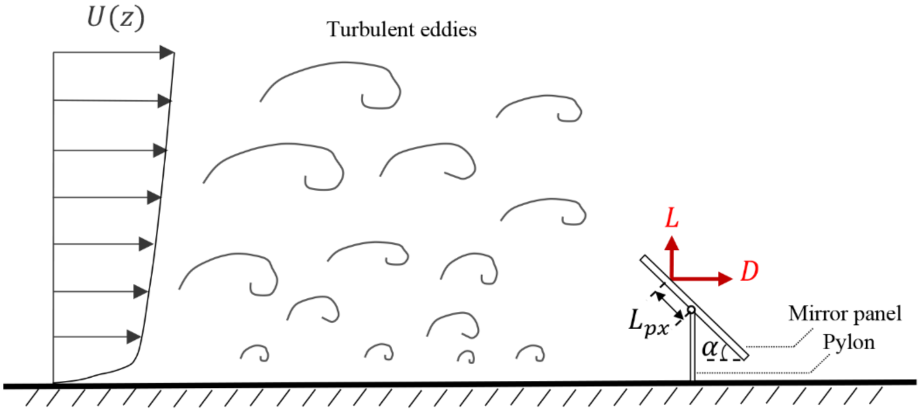

Figure 1.1. A schematic of the lift and drag forces on an operating heliostat within the atmospheric boundary layer.

During their operation, heliostats at different elevation angles, α in Figure 1.1, act as bluff bodies creating a blockage in the flow which leads to vortex shedding at the edges of the mirror panel. The unstable vortices created in the wake are a source of fluctuating lift and drag forces. Another source of the unsteady loads is the turbulence in the atmospheric boundary layer which increases the unsteady wind loads significantly. Turbulence in the atmospheric boundary layer is composed of a range of turbulence structures with various scales which create wind velocity fluctuations of different amplitudes and frequencies. The intensity and scale of these fluctuations impact the wind loads. For instance, Figure 1.2 presents the effect of longitudinal turbulence intensity on the mean and peak drag forces on a vertical heliostat in a study by Peterka *et al.* (1989). As shown in the figure, the peak drag force coefficient almost doubles when the turbulence intensity of the approaching flow increases from 12% to 18%.

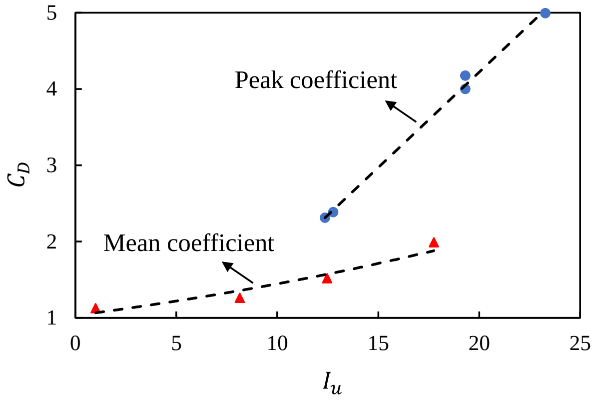

Figure 1.2. The effect of longitudinal turbulence intensity, I_u, on the mean and peak drag force coefficients, C_D, on a heliostat panel normal to the flow. Reproduced by permission from ASME: Solar Energy Engineering, Peterka *et al.* (1989).

During periods of high wind speeds, heliostats are usually stowed by aligning the mirror panel with the direction of the mean flow, i.e., zero-degree elevation angle. While at stow position the mean and peak drag force coefficients are significantly smaller than the coefficients at the operational positions, the turbulent atmospheric flow imposes variations in the distribution and magnitude of differential pressure on the mirror panel creating a highly unsteady lift force. The unsteady lift force at stow position is strongly dependent on turbulence in the approaching flow. The maximum lift force coefficient on a heliostat at stow position is found to increase from 0.46 to 0.59 when longitudinal turbulence intensity in the approaching flow increases from 13% to 21% (Pfahl *et al.*, 2015). Furthermore, Pfahl (2018) discussed that the fluctuating lift force coefficient on a heliostat at stow increases with increasing the vertical turbulence intensity. Moreover, Emes *et al.* (2017) reported that the integral length scale of turbulence is also a key parameter which influences the peak lift force coefficient on a stowed heliostat. The unsteady lift force at stow creates unsteady bending and overturning moments at the heliostat pylon base and hinge. The overturning moment is critical for the design of heliostat foundation since heliostats need to withstand the largest wind speeds at stow position. Furthermore, the positive/negative load cycling can lead to fatigue failure within fewer cycles in comparison to cycling loads of the same sign (Peterka *et al.*, 1987).

The wind loads on heliostats during both operation and stow have been shown to vary with changing intensity and length scales of turbulence in the approaching flow. However, there are discrepancies between the experimental measurements reported in the literature. For example, Peterka *et al.* (1989) found the peak drag force coefficient on a vertical heliostat equal to 4 at an incoming flow turbulence intensity of 18%, while Pfahl *et al.* (2011) found a value of 3.3 for the same turbulence intensity. A better understanding of the key turbulence parameters affecting the wind loads will help explain the differences in the literature. Moreover, the correlation between the turbulence in the flow and the unsteady lift and drag forces is not known. Development of such correlation will enable estimation of the load coefficients for different turbulence conditions of the flow and will contribute to providing a reliable wind load prediction for design of heliostats.

Turbulence in the atmospheric flow is dependent on the features of the terrain and varies based on the site of different heliostat fields. Furthermore, both integral length scale and intensity of turbulence vary with height in the atmospheric boundary layer as shown in Figure 1.3. With increasing the height from the ground, turbulence intensity decreases while the integral length scale of turbulence increases (ESDU85020, 2010). Therefore, based on the height of the heliostats from the ground and the terrain surrounding the heliostat field, the turbulence intensity and length scales can be very different. Hence, it is necessary to establish a correlation between turbulence characteristics of the flow based on the terrain, and the unsteady lift and drag forces on heliostats.

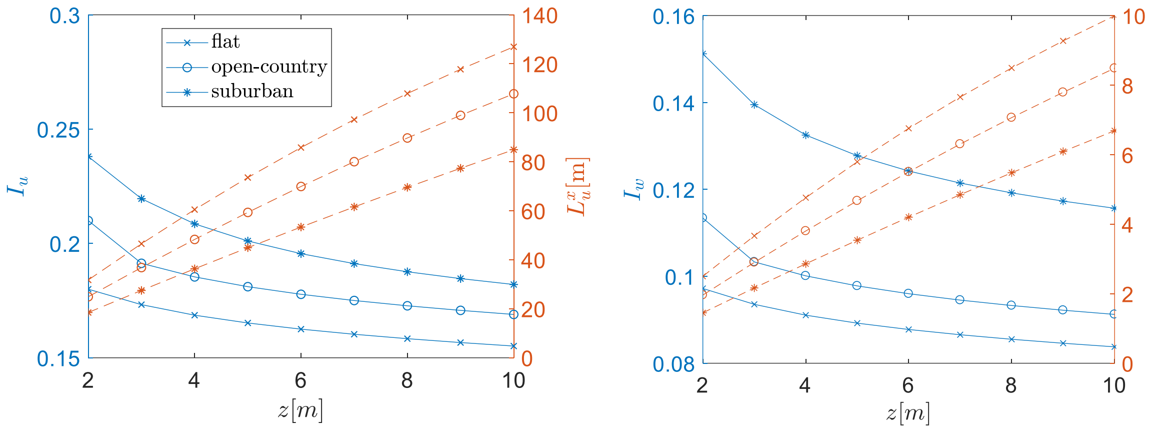

(a) (b)

Figure 1.3. The variations of intensity (the solid blue lines) and length scale (the orange dashed lines) of turbulence with height in the atmospheric boundary layer for different terrains calculated based on ESDU85020 (2010). (a) Longitudinal turbulence intensity and length scale, (b) vertical turbulence intensity and length scale.

The wind-tunnel experiments reported in the literature have been mainly focused on measurement of wind loads on heliostat models in simulated boundary layers. The flow characteristics including the boundary layer height, turbulence intensities and length scales varied in each experiment. These variations have however not been systematic and their effects on the measured wind load coefficients have not been established. This has led to discrepancies in the experimental measurements reported in the literature under seemingly similar conditions. Hence, a systematic analysis of the effect of turbulence parameters on the wind loads is required to explain the differences in the literature. Furthermore, the variations of the unsteady lift and drag forces experienced by heliostats under different turbulent conditions within the atmospheric boundary layer is not known. Development of a relationship between the turbulent properties of the flow and the unsteady lift and drag forces will enable estimation of the wind load coefficients for different turbulence conditions of the flow.

The motivation for the research presented in this thesis is to provide a reliable wind load prediction for design of heliostats. This goal can only be achieved if the effect of flow turbulence on the wind loads is characterised. Hence, the correlation between the turbulence in the atmospheric boundary layer and the wind loads on heliostats in investigated in this study. This knowledge can be employed to determine the unsteady wind loads specific for each terrain regarding the corresponding turbulence conditions. The findings will provide a basis for optimisation of heliostat field and improvement of heliostat design with respect to the wind loads which will contribute to reduction of the capital cost of a heliostat field.

1.2 Aims and objectives

The overall aim of the present research is to develop an understanding of the effect of atmospheric boundary layer turbulence on the unsteady wind loads on heliostats. With wind tunnel experimentation as the method of research, a fundamental requirement for achieving this goal is characterisation of the simulated turbulent boundary layer in the wind tunnel. Hence, the first objective focuses on understanding the turbulence characteristics in atmospheric boundary layer, and wind tunnel boundary layers in order to establish the criteria for modelling atmospheric turbulence in a wind tunnel. This knowledge is essential for wind tunnel measurements of unsteady loads on heliostat models and has been overlooked in the literature. The second objective is targeted at determination of the flow turbulence characteristics that influence the unsteady wind loads and aims to establish a relationship between turbulence intensity and length scales and the unsteady wind loads on stowed and operating heliostats. While the second objective focuses on a single heliostat in an atmospheric boundary layer flow, the third objective aims to characterise the turbulence in the wake of a heliostat placed in an atmospheric boundary layer. This objective seeks to gain an understanding of the interaction between the turbulent structures in the wake of a heliostat and the large-scale turbulence within the atmospheric boundary layer. This knowledge will provide an insight into the flow turbulence in a heliostat field and how it differs from the incoming turbulence in atmospheric boundary layer, which will provide the basis for understanding wind loads in a heliostat field. After developing the correlation between turbulence and unsteady wind loads, the final objective evaluates reduction of the wind loads by manipulation of turbulence in the approaching flow and investigates application of fences as a flow control method for this purpose.

The research objectives are summarised as the following:

- Establishment of the similarity criteria for accurate modelling of turbulence and unsteady wind loads in a wind tunnel.
- Development of the correlation between turbulence length scale and intensity, and the corresponding unsteady wind loads on stowed and operating heliostats.
- Characterisation of turbulence in the wake of a heliostat and its effect on unsteady wind loads in a heliostat field.
- Investigation of a flow control method for reduction of atmospheric turbulence and unsteady wind loads on heliostats.

1.3 Thesis outline

The current thesis comprises of seven distinct chapters. The current chapter provides an overview of the thesis and introduces subject matter and the research objectives. Chapter 2 is an extensive review of the literature in the field of research, highlighting the gaps in knowledge and the significance of the current research. Chapters 3 to 6, which comprise the main body of the thesis, present two conference papers and four manuscripts that have been published or are under review in peer-reviewed journals. The research method and the experimental findings are detailed in these manuscripts. In the final chapter, a summary of the findings and the obtained conclusions, along with recommendations for future work are presented. The following gives a brief description of the contents, scope and influence of each chapter.

Chapter 2 commences with a discussion of the turbulence in the atmospheric boundary layer and its wind tunnel simulations, followed by a review of the effects of turbulence on the unsteady aerodynamic forces on flat plates and heliostats. An extensive literature review is provided discussing turbulence in the wake of flat plates, flow around multiple bluff bodies, and methods for reduction of unsteady wind loads. The literature review is aimed at identifying the key gaps in knowledge which have been addressed in the current research.

In Chapter 3, the turbulence spectra in atmospheric boundary layers simulated in a wind tunnel were analysed and compared with the turbulence spectra from the atmospheric boundary layer. The mismatch of turbulence spectra between the full-scale and the wind tunnel boundary layers when modelling small-scale structures such as heliostats is discussed. To gain an understanding of how inconsistency of turbulence spectra affects the wind tunnel measurements of the unsteady wind loads, the correlation between the turbulence spectra and the measured unsteady lift and drag forces on horizontal and vertical flat plates is determined. The results show that the turbulence structures with reduced frequencies between 0.01 and 1 have the largest contribution to the unsteady wind loads. It is proposed that wind loads on model heliostats in a wind tunnel will closely represent the full-scale loads if this range of reduced frequencies of the turbulence spectrum closely match those of atmospheric boundary layer.

Chapter 4 presents an experimental investigation of the effect that the length scale and intensity of turbulence have on the unsteady wind loads on heliostats at stow and vertical positions. Comprehensive measurements of the unsteady lift and drag forces on heliostats are conducted for heliostat models of different panel dimensions in a range of turbulence intensities and length scales generated in two part-depth atmospheric boundary layers in the wind tunnel. It is shown that the unsteady lift force on a heliostat at stow is dependent on the vertical intensity and length scale of the turbulence. An empirical correlation between the peak lift force and the vertical turbulence intensity and length scale is developed. The results are applied to predict the peak lift force coefficient on full-scale stowed heliostats based on the turbulence characteristics of various terrains. Furthermore, it is demonstrated that the peak drag force on a heliostat with a vertical panel is a function of a turbulence parameter defined by the longitudinal turbulence intensity and length scale.

In Chapter 5, the time-averaged and spectral characteristics of turbulence in the wake of a heliostat are investigated. Extensive velocity measurements are conducted in the wake of heliostat models at three elevation angles in two simulated atmospheric boundary layer flows. Mean velocity and turbulence kinetic energy and spectra in the wake flow are characterised and compared to turbulent atmospheric flow. The results demonstrate an increase in turbulence kinetic energy and a significant change in the distribution of turbulence spectra in the near wake region. Furthermore, the unsteady wind loads on a second heliostat placed in the wake of an upstream heliostat are studied by measurement of the unsteady distribution of differential pressure on the heliostat panel. A significant change in the distribution of large-magnitude pressure regions on the second tandem heliostat is observed in the near wake flow. The findings from the flow field, along with the pressure distributions on the second tandem heliostat, are employed to predict the changes in the unsteady wind loads in high- and low-density regions of a heliostat field.

In Chapter 6, the effectiveness of wire mesh fences in reducing the turbulence within the atmospheric boundary layer that can lead to the reduction of the unsteady wind loads on heliostats is investigated. Turbulence intensity, integral length scale and velocity spectra downstream of fences placed in a simulated turbulent atmospheric boundary layer are characterised and analysed with respect to the turbulence characteristics of the approaching atmospheric flow. Furthermore, the effects of mesh dimensions and porosity of the fence on the variations of the turbulence parameters in the flow behind the fence are analysed. The results show that fence porosity is the key parameter that determines the turbulence reduction performance of a fence. The effectiveness of a wire mesh fence in reducing the peak lift and drag forces on a heliostat is discussed based on the variations of turbulence intensity and integral length scale behind the fence.

In the final chapter, the key conclusions made from the present research are discussed. Furthermore, recommendations for subsequent future work for understanding the wind loads in a heliostat field are presented.

1.4 Publications arising from this thesis

The research presented is this thesis has directly led to generation of four journal manuscripts and three peer-reviewed conference articles, which are listed below:

Journal papers

- Jafari, A., Ghanadi, F., Emes, M. J., Arjomandi, M., and Cazzolato, B. S. 2019. Measurement of unsteady wind loads in a wind tunnel: Scaling of turbulence spectra, *Journal of Wind Engineering and Industrial Aerodynamics*, 193: 103955.
- Jafari, A., Ghanadi, F., Arjomandi, M., Emes, M. J., and Cazzolato, B. S. 2019. Correlating turbulence intensity and length scale with the unsteady lift force on flat plates in an atmospheric boundary layer flow, *Journal of Wind Engineering and Industrial Aerodynamics*, 189: 218-30.
- Jafari, A., Emes, M. J., Cazzolato, B. S., Ghanadi, F., and Arjomandi, M. 2020. Turbulence characteristics in the wake of a heliostat in an atmospheric boundary layer flow, *Physics of Fluids*, 32: 045116.
- Jafari, A., Emes, M. J., Cazzolato, B. S., Ghanadi, F., and Arjomandi, M. 2020. Reduction of turbulence in an atmospheric boundary layer flow by mesh screens. Submitted to *Experiments in Fluids*.

Refereed conference papers

- Jafari, A., Emes, M. J., Cazzolato, B. S., Ghanadi, F., and Arjomandi, M. 2017. The effect of turbulence intensity on the peak wind loads on heliostats. *The Asia Pacific Solar Research Conference 2017*. Melbourne, Australia.
- Jafari, A., Ghanadi, F., Emes, M. J., Arjomandi, M., and Cazzolato, B. S. 2018. Effect of free-stream turbulence on the drag force on a flat plate. *21st Australasian Fluid Mechanics Conference*. Adelaide, Australia.
- Jafari, A., Emes, M. J., Cazzolato, B. S., Ghanadi, F., and Arjomandi, M. 2019. An experimental investigation of unsteady pressure distribution on tandem heliostats. *SolarPaces2019*. Daegu, South Korea.

In addition to the aforementioned papers, the author of the current thesis has also been closely collaborating in developing methods for determination of design wind loads for heliostats leading to the publications listed below. These publications are not included in the current thesis.

- Emes, M. J., Yu, J.S., Jafari, A., Ghanadi, F., and Arjomandi, M. 2017. Experimental investigation of the wind loads on heliostats, *Asia Pacific Solar Research Conference 2017*. Melbourne, Australia.

- Emes, M. J., Jafari, A., and Arjomandi, M. 2018. Estimating the turbulence length scales from cross-correlation measurements in the atmospheric surface layer. *21st Australasian Fluid Mechanics Conference*. Adelaide, Australia.
- Emes, M. J., Jafari, A., Ghanadi, F., and Arjomandi, M. 2019. A method for the calculation of the design wind loads on heliostats, *AIP Conference Proceedings*, 2126: 030020.
- Emes, M. J., Jafari, A., Ghanadi, F., and Arjomandi, M. 2019. Hinge and overturning moments due to unsteady heliostat pressure distributions in a turbulent atmospheric boundary layer, *Solar Energy*, 193: 604-17.
- Emes, M. J., Jafari, A., and Arjomandi, M. 2019. Wind load design considerations for the elevation and azimuth drives of a heliostat, *SolarPaces. Daegu*, South Korea.
- Arjomandi, M., Emes, M. J., Jafari, A., Yu, J.S., Ghanadi, F., Kelso, R., Cazzolato, B. S., Coventry, J., and Collins, M., 2019. Experimental study of heliostat wind loads. *SolarPaces2019*. Daegu, South Korea.
- Emes, M. J., Jafari, A., and Arjomandi, M. 2019. Wind load design considerations and stowing strategies for a heliostat field, *Asia Pacific Solar Research Conference 2019*. Canberra, Australia.
- Emes, M. J., Jafari, A., Coventry, J., and Arjomandi, M. 2020. The influence of atmospheric boundary layer turbulence on the design wind loads and cost of heliostats, *Solar Energy*, 207: 796-812.

1.5 Thesis format

The current thesis has been submitted as a portfolio of the publications in accordance with the University of Adelaide's formatting criteria. The printed and online versions of this thesis are identical, and the electronic version is available in PDF format.

1.6 References

Emes, M. J., Arjomandi, M., Ghanadi, F., and Kelso, R. M. 2017. Effect of turbulence characteristics in the atmospheric surface layer on the peak wind loads on heliostats in stow position, *Solar Energy*, 157: 284-97.

ESDU85020. 2010. Characteristics of atmospheric turbulence near the ground - part ii: Single point data for strong winds (neutral atmosphere), *Engineering Sciences Data Unit*.

Gong, B., Li, Z., Wang, Z., and Wang, Y. 2012. Wind-induced dynamic response of heliostat, *Renewable Energy*, 38: 206-13.

Griffith, D. T., Moya, A. C., Ho, C. K., and Hunter, P. S. 2011. Structural dynamics testing and analysis for design evaluation and monitoring of heliostats. *ASME 2011 5th International Conference on Energy Sustainability*, 567-76.

Kolb, G. J., Ho, C.K., Mancini, T.R., and Gary, J.A. 2011. Power tower technology roadmap and cost reduction plan, *SAND2011-2419, Sandia National Laboratories*.

Peterka, J. A., Tan, L., Bienkiewcz, B., and Cermak, J. E. 1987. Mean and peak wind load reduction on heliostats, *Technical Report for Colorado State University*.

Peterka, J. A., Tan, Z., Cermak, J. E., and Bienkiewicz, B. 1989. Mean and peak wind loads on heliostats, *Journal of Solar Energy Engineering*, 111: 158-64.

Pfahl, A. 2018. *Wind loads on heliostats and photovoltaic trackers*, Doctoral Thesis, Technische Universiteit Eindhoven.

Pfahl, A., Buselmeier, M., and Zaschke, M. 2011. Wind loads on heliostats and photovoltaic trackers of various aspect ratios, *Solar Energy*, 85: 2185-201.

Pfahl, A., Coventry, J., Röger, M., Wolfertstetter, F., Vásquez-Arango, J. F., Gross, F., Arjomandi, M., Schwarzbözl, P., Geiger, M., and Liedke, P. 2017. Progress in heliostat development, *Solar Energy*, 152: 3-37.

Pfahl, A., Randt, M., Meier, F., Zaschke, M., Geurts, C. P. W., and Buselmeier, M. 2015. A holistic approach for low cost heliostat fields, *Energy Procedia*, 69: 178-87.

Vásquez-Arango, F. J., Buck, R., and Pitz-Paal, R. 2015. Dynamic properties of a heliostat structure determined by numerical and experimental modal analysis, *Journal of Solar Energy Engineering*, 137: 051001-01-5.

Chapter 2

Literature Review

In this chapter, an overview of the literature on wind loads and aerodynamics of heliostats in a turbulent flow is provided. The chapter starts with a description of wind characteristics in the atmospheric boundary layer in Section 2.1. Methods for generation of an atmospheric boundary layer flow in a wind tunnel and the requirements for wind load measurements are discussed in Section 2.2. A review of the literature on the effect of the turbulence on wind loads on a single heliostat is provided in Section 2.3. The wind loads in a heliostat array and the flow around multiple heliostats are reviewed in Section 2.4. In Section 2.5, reducing the turbulence within the atmospheric boundary layer which can lead to reducing the wind loads is discussed. The chapter concludes with a summary of the research gaps and the objectives of the thesis in Section 2.6.

2.1 Turbulence in the atmospheric boundary layer

The depth of the atmospheric boundary layer is dependent on wind speed and terrain roughness and can vary between a few hundred metres to several kilometres (Xu, 2013). The lower 50–100 m of the atmospheric boundary layer, where heliostats and other land-structures including buildings and bridges are placed, is known as the atmospheric surface layer (ASL). In the surface layer, the rotation of Earth has no effect on the flow, and surface friction and vertical temperature gradient are two important parameters which influence wind structure in the ASL (Kaimal and Finnigan, 1994). Temperature gradient creates buoyancy forces in the boundary layer which affect its stability. To establish a fundamental understanding of wind loads, the focus in this thesis is on wind conditions in a neutrally stratified ASL, in which the vertical temperature gradient is negligible, and the shear resultant from surface fiction is the dominant mechanism. The neutrally stratified boundary layer is typically used as a reference case for wind load studies since at high wind speeds, thermal effects are less significant (Xu, 2013).

Wind speed in the surface layer is expressed in terms of a time-averaged mean speed and the turbulent fluctuating components. The time-averaged wind speed in the neutrally stratified surface layer matches the logarithmic law for the mean velocity in a canonical boundary layer, which is expressed as,

$$U(z) = \left(\frac{u_*}{\kappa}\right) \ln\left(\frac{z - z_d}{z_0}\right) \tag{2.1}$$

where $U(z)$ is the mean wind velocity at height z, u_* is the surface friction velocity, κ is von Kármán's constant equal to 0.4, z_0 and z_d represent the aerodynamic surface roughness and the zero-plane displacement, respectively. The aerodynamic surface roughness determines the roughness characteristics of a terrain and depends on the height and distribution of roughness elements (Simiu and Scanlan, 1996). Typical values of z_0 for different terrain types are given in Table 2.1. The zero-plane displacement is negligible for small surface roughness lengths, such as flat and open-country terrains (Cook, 1985), where heliostats are usually located.

Table 2.1. Aerodynamic surface roughness values corresponding to different terrain types based on ESDU85020 (2010).

Terrain type	Flat	Open country	Suburban	Dense urban
Aerodynamic surface roughness length, z_0 (m)	0.001–0.003	0.01–0.03	0.1–0.3	0.7

The profile of mean wind speed in ASL can also be expressed as a power law function as,

$$U(z) = U_\infty (\frac{z}{\delta})^\alpha \tag{2.2}$$

where U_∞ and δ represent the freestream velocity and boundary layer depth, respectively. The power law exponent, α, is dependent on surface roughness. While the power law provides a good representation of the mean velocity profile at heights between 30 m and 300 m (Xu, 2013), the logarithmic law has been found to provide a better fit for empirical data at heights below 100 m (Cook, 1997; Li *et al.*, 2010; Sun *et al.*, 2014). The logarithmic law provides an accurate velocity profile independent of atmospheric stability for heights below 10 m very close to the ground (Kaimal and Finnigan, 1994), and is therefore more appropriate for modelling the mean velocity profile for study of wind loads on heliostats.

The ASL consists of a series of coherent structures or eddies of various length scales, which create fluctuations in wind speed through continuous energy exchange with one another and with the mean flow. The turbulence structure in the ASL on a low-roughness terrain can resemble a zero-pressure gradient boundary layer formed over a flat plate. An important parameter which affects the flow and turbulence structure within the boundary layer is the Reynolds number. The Reynolds number based on boundary layer thickness, δ, and friction velocity, u_*, defined as $Re_\tau = u_*\delta/\nu$, in the atmospheric boundary layer is in the order of 10^6, which is three orders of magnitude larger than the low-Reynolds number flow of a boundary layer formed over a flat plate in a laboratory with $Re_\tau \sim 10^3$ (Marusic and Hutchins, 2008). The low-Reynolds number flat plate boundary layer is known to be characterised by regions of high- and low-speed fluid, known as streaks, in its near wall region. Turbulence generation in a turbulent boundary layer is dominated by a series of sweep and ejection events. As described by Corino and Brodkey (2006), the inrush of high-speed fluid from above into the near wall region, known as a sweep event, moves low-speed streaks away from the wall creating an ejection, which is followed by instability of the streaks leading to another sweep and ejection. These events transfer energy between the near wall and the outer region of the boundary layer. Similarly, sweeps and ejections have been found in the ASL. Högström *et al.* (2002) identified sweeps and ejections with mean durations of approximately 4 to 5 seconds with intervals of 10 to 14 seconds from the atmospheric measurements at near-neutral conditions at heights between 1.6 m to 14 m. These events whose time interval was independent of wind speed were found to contribute to more than 90% of the momentum flux.

Adrian *et al.* (2000) associated the streaks observed in the canonical boundary layer with legs of hairpin vortices. As described by Adrian *et al.* (2000), the coherent structures consist of packets of hairpin vortices of variuos scales inclined at approximately 45° to the wall, which join together to form large-scale inclined ramp structures. Figure 2.1(a) shows a schematic of the hairpin vortex packet model by Adrian *et al.* (2000). According to Adrian (2007), the hairpin vortex packets also exist in high Reynolds number flows including ASL, and the turbulence structure is ASL similar to that of a low-Reynolds number turbulent boundary layer on a flat plate. This similarity has been evidenced by smoke visualisations in the lower 2 m of neutral ASL near the ground in a flat desert in Utah (Hommema and Adrian, 2003), which showed the inclined ramp structures formed by large-scale hairpin packets, illustrated in Figure 2.1(b).

LIBRARY NOTE:

This image has been removed to comply with copyright.

(a)

(b)

Figure 2.1. (a) A schematic of the hairpin vortex packets growing from the wall. Reprinted from Adrian *et al.* (2000), (b) smoke visualisation of the near wall region in neutral ASL showing the large-scale ramp-like turbulence structures. The white solid lines mark the extent of the large-scale structures. Reprinted by permission from Springer: Boundary Layer Meteorology, Hommema and Adrian (2003).

Some of the studies in the literature, on the other hand, suggest that the turbulence structure in high-Reynolds ASL is different from the low-Reynolds turbulent boundary layer. Hunt and Carlotti (2001) described the eddy motion mechanism in high-Reynolds ASL as “top-down”. Based on this theory, through the “top-down” motion, eddies originating from above the surface layer move down into ASL and impinge onto the ground, where internal boundary layers are generated due to the zero tangential velocity at the Earth’s surface. The theory describes that smaller eddies are developed in the internal boundary layers, which have been evidenced as near-surface plumes in the literature (Wilczak and Tillman, 1980; Shaw and Businger, 1985), and as cat’s paws on water surface by Hunt and Morrison (2000). The inner shear layer then grows until the interaction of two streamwise vortices on its sides generate an ejection, which transports some of the turbulence energy back into the upper layers. The "top-down" theory has been supported by the observations by Drobinski and Foster (2003), which show traces of occasional propagation of waves from upper layers into the ASL.

Statistical properties of turbulence in the ASL are typically used to determine wind velocity fluctuations. These statistical properties include turbulence intensity, integral length scale of turbulence, and power spectral density of velocity fluctuations, which will be discussed in the following. Turbulence intensity is representative of the amplitude of velocity fluctuations compared to the mean velocity and is given by,

$$I_i = \frac{\sigma_i}{U} \tag{2.3}$$

where σ_i is the velocity variance and i refers to the streamwise or longitudinal, lateral and vertical velocity components, i.e., u, v, and w, respectively. Turbulence in the ASL is anisotropic and is largest in the streamwise direction. According to the empirical relationships derived from atmospheric data given in ESDU85020 (2010), I_v/I_u and I_w/I_u in the ASL are approximately equal to 0.78 and 0.54. Turbulence intensity decreases as the height from the ground increases and is dependent on the surface roughness of the terrain. An example of the variations of streamwise and vertical turbulence intensities with height in different terrains are given in Figure 1.3.

The power spectral density function can be used to describe the distribution of turbulence energy with frequency of the turbulence structures described by the energy cascade in a turbulent boundary layer. The large eddies which contain the majority of kinetic energy are responsible for most of the energy transport from the mean flow. Due to the instabilities, large eddies break up into smaller eddies until they become sufficiently small for viscosity to directly influence them and dissipate their energy into heat. The power spectral density function provides critical information about the scales of turbulent eddies, which is important for evaluation of unsteady wind loads on structures. Empirical and mathematical models have been developed in the literature to describe the wind spectrum in the ASL. The most commonly used model is the von Kármán form, which expresses the power spectral density of streamwise, and vertical velocity components as follows (von Kármán, 1948):

$$\frac{fS_{uu}}{\sigma_u^2} = \frac{4n_u}{(1 + 70.8n_u^2)^{5/6}} \tag{2.4}$$

$$\frac{fS_{ww}(f)}{\sigma_w^2} = \frac{n_w(1 + 755.2\, n_w^2)}{(1 + 283.2\, n_w^2)^{11/6}} \tag{2.5}$$

where S_{uu} and S_{ww} are the power spectral density functions of the fluctuating streamwise and vertical velocity components, σ_u^2 and σ_w^2 show the variance of streamwise and vertical velocity components. Also, $n_u = fL_u^x/U$ and $n_w = fL_w^x/U$, where L_u^x is the longitudinal integral length scale of turbulence, and L_w^x is the vertical integral length scale. The integral length scale of turbulence is representative of the average size of the most energetic eddies within a turbulent boundary layer. The longitudinal and vertical integral length scales, L_u^x and L_w^x indicate the largest distance at which streamwise and vertical velocity components at two points are well-correlated. The integral length scale corresponds to the turbulent eddies at the peak of the turbulence spectrum and can be determined from different methods: semi-empirically from the frequency of the peak of the spectrum, from the value of the spectrum at zero frequency, or from the auto-correlation function of the fluctuating velocity component (Farell and Iyengar, 1999). These methods are discussed in detail in Chapter 4. Furthermore, typical variations of longitudinal and vertical integral length scales with height from the ground in different terrains are presented in Figure 1.3. The length scales of turbulent eddies are important for dynamic wind loads on structures since eddies with a length scale comparable with the length scale of the structure can create a well correlated pressure distribution on the structure (Mendis, 2007). Hence, knowledge of the length scales of turbulence within the ASL is necessary for estimation of wind loads.

Recent measurements of wind velocity in the lower heights of the ASL near the ground, particularly at the lower 10–15 m, have shown differences in the turbulence spectrum from a typical turbulent boundary layer spectrum. Figure 2.2 shows the power spectral densities of streamwise and vertical velocity components from the velocity measurements by a high-resolution Doppler lidar at different heights, between 1.5 m and 20 m, in a flat terrain in Kansas by Drobinski *et al.* (2004). Three spectral ranges were identified in the spectrum of the streamwise velocity component at heights below 10 m, as shown in Figure 2.2: (i) the Kolmogrov inertial subrange where $S_{uu} \propto f^{-5/3}$; (ii) the self-similar or surface eddy subrange where $S_{uu} \propto f^{-1}$, i.e., the quasi-equilibrium state where fS_{uu} is constant; (iii) the lower frequency range where S_{uu} is independent of f, i.e., giving rise to the +1 slope for fS_{uu}. Comparison of the spectrum at heights below and above 10 m shows that the self-similar subrange only exists at heights below 10 m, Figure 2.2(a–b), while the other two subranges are representative of turbulent boundary layer turbulence (Högström *et al.*, 2002). The vertical velocity spectrum as shown in Figure 2.2 at heights below 10 m consists of two subranges: the higher frequency range where $S_{ww} \propto f^{-5/3}$; and the lower frequency range where $S_{ww} \propto f$. The latter disappears with increasing the height from the ground and gradually changes to $S_{ww} \propto f^{-1}$ at a height of 30 m (not given in Figure 2.2). Existence of the +1 slope in vertical velocity spectrum in the same frequency range of self-similar behaviour in the streamwise velocity spectrum shows anisotropic elongated eddies at the lower heights. Hunt and Carlotti (2001) and Högström *et al.* (2002) associate the different turbulence structure in the proximity of the ground with the "top-down" eddy motion theory explaining that blocking of eddies as they impinge onto the ground leads to formation of elongated streamwise eddies and reduction of vertical velocity near the ground. Based on these differences, it has been proposed that the near neutral ASL is structured from two sublayers; a lower sublayer at heights below approximately 10–15 m, named as eddy surface layer (ESL) where blocking plays an important role, and an intermediate sublayer, referred to as the shear surface layer (SSL). The wind data measurements of Richards *et al.* (1997) and the theoretical model of Hunt and Carlotti (2001) suggest that the depth of the ESL increases with increasing the surface roughness of a terrain. Furthermore, large variances in wind velocity are found in the ESL due to existence of different scales of eddies (Drobinski *et al.*, 2007), which is critical to wind loading on structures placed in the ESL.

2.2 Measurement of wind loads in a wind tunnel

An important requirement for experimental measurement of wind loads on scale model heliostats is simulation of atmospheric boundary layer turbulence in a wind tunnel. In this section, the developed methods in the literature for generation of an ABL in a wind tunnel are reviewed followed by a discussion on the similarity requirements for wind load measurements.

2.2.1 Wind tunnel modelling of atmospheric boundary layer

Natural growth of an ABL in a wind tunnel requires a long rough surface. As the scale of the developed boundary layer depends strongly on the length of the roughness fetch, a very long test section is needed. Therefore, natural development of boundary layer is only applicable to wind tunnels with a test section length of about 10 times the tunnel height (Cermak, 1984), and is not applicable to wind tunnels with shorter test sections. Hence, different methods have been developed to artificially thicken the boundary layer by application of turbulence generation devices, such as spires, fences, and barriers (Cermak, 1984), which are followed by a shorter length of surface roughness to maintain the generated turbulence in the vicinity of the ground (Kozmar, 2011a). Two sets of turbulence generation devices, as showed in Figure 2.3, have been commonly used in wind tunnel experiments in the literature; flat triangular spires, known as Irwin’s method (Irwin, 1981), and elliptic vortex generators, which were first proposed by Counihan (1969). Both turbulence generators have been widely used, with and without barriers, for full-depth simulations of ABLs in different terrains including rural and urban terrains (Iyengar and Farell, 2001; Kozmar, 2008; Lopes *et al.*, 2008; Varshney and Poddar, 2011; Kozmar, 2012). De Paepe *et al.* (2016) compared the application of both methods for simulation of a suburban ABL. Evaluation of the mean velocity profiles, longitudinal turbulence intensities and power spectrum of the velocity in the generated boundary layers by both methods showed a good agreement with the standard ABL profiles, indicating the similarity of the simulated flows with ABL. Therefore, De Paepe *et al.* (2016) recommended triangular spires for wind tunnel experiments due to the simplicity of their fabrication.

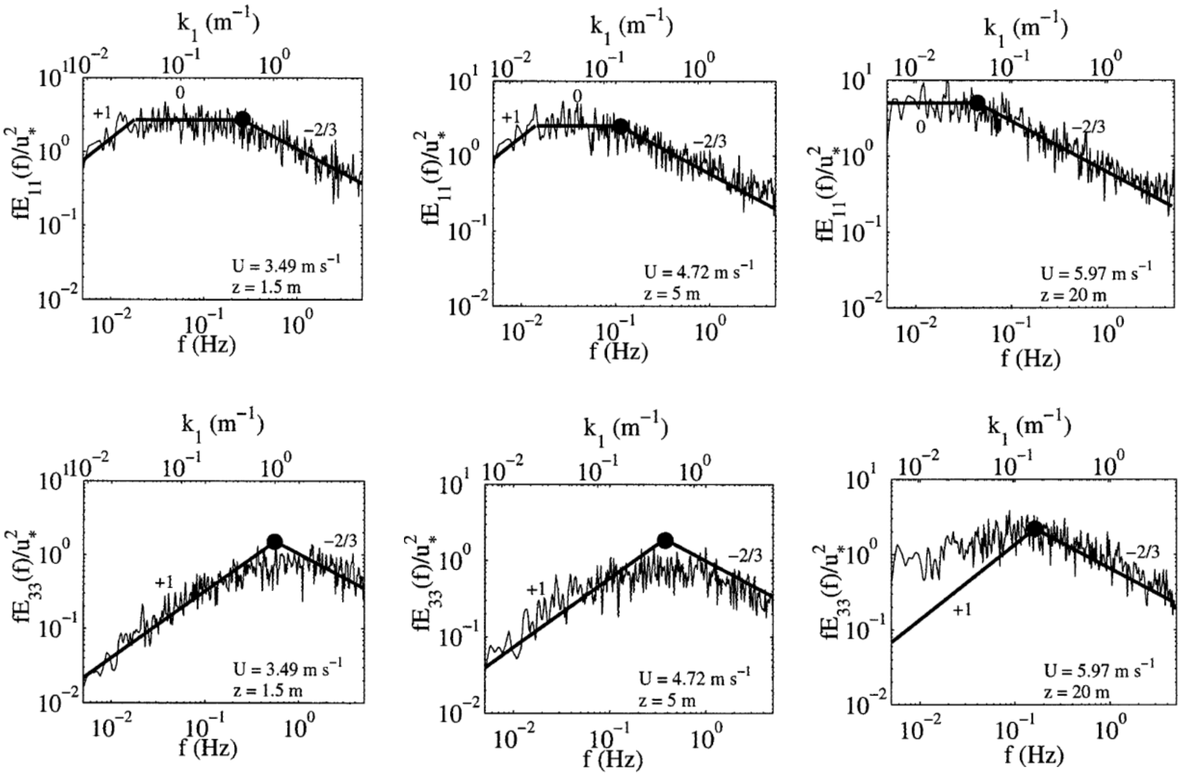

(a) (b) (c)

Figure 2.2. Normalised spectral density of streamwise (top) and vertical (bottom) velocity components in neutral ASL at heights of (a) 1.5 m, (b) 5 m, and (c) 20 m calculated from velocity measurements in Kansas. Reprinted by permission from American Meteorological Society: Boundary-Layer Meteorology, Drobinski *et al.* (2004).

De Bortoli *et al.* (2002) and Kozmar (2011b) proposed a modified design for the turbulence generation devices. In this method, the turbulence generators were truncated to model only the lower part of the ABL instead of the whole depth of the boundary layer, known as part-depth modelling of an ABL. Evaluation of the mean velocity and turbulence intensity profiles generated by the part-depth method also showed similarity of the flow with the ABL. Furthermore, it was found that larger turbulence length scales were generated in the part-depth simulation in comparison with a full-depth modelling with a similar power law exponent (De Bortoli *et al.*, 2002). An advantage of part-depth modelling is that by modelling only the lower part of the boundary layer, a larger simulation scaling factor can be achieved in a given wind tunnel compared to a full-depth modelling in the same tunnel. This is particularly beneficial for study of wind loads on structures of smaller full-scale dimensions, such as heliostats, since it allows modelling them at larger dimensions in the wind tunnel.

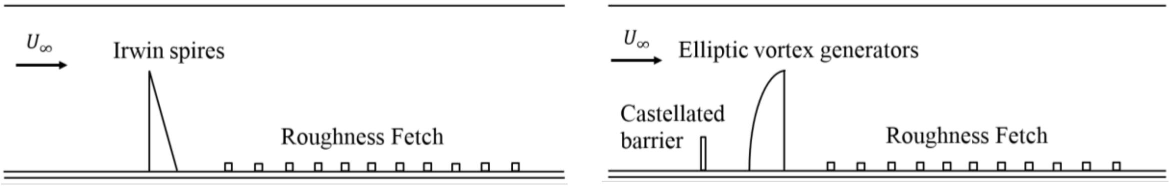

Figure 2.3. Turbulence generation devices for simulation of atmospheric boundary layer in a wind tunnel: (a) Triangular spires, (b) elliptic vortex generators with castellated barrier.

2.2.2 Similarity criteria for wind tunnel experiments

Similarity of the generated boundary layer in a wind tunnel with the ABL is determined in terms of mean velocity profile, and turbulence characteristics, including turbulence intensity, integral length scales, and turbulence spectra (Holmes, 2007). However, similarity of the flow is not sufficient for wind load measurements. According to Plate (1982), in addition to ABL similarity, it is necessary for the structural model to be geometrically similar to the full-scale structure, and the structural model and the boundary layer should be scaled down by an identical scaling ratio.

Large-scale boundary layer wind tunnels are commonly designed for experimental measurements of wind loads on large civil structures, such as tall buildings and bridges. The depth of a boundary layer generated in these wind tunnels is typically between 1 m and 3 m. With the depth of the neutral ABL varying between 275 m and 550 m (Davenport, 1960), the generated boundary layer in a typical wind tunnel is scaled down by a factor varying between

1:100 and 1:500. Therefore, to achieve similarity of the geometric scaling ratios of the structure and the boundary layer in a wind tunnel experiment, it is required to scale down the structure dimensions by a factor between 1:100 and 1:500. Such geometric scaling ratios are achievable for tall buildings and bridges. However, for small-scale structures, such as low-rise buildings, solar panels and heliostats, the geometric dimensions of these structures are much smaller compared to the depth of ABL, for instance, typical heliostats are elevated at heights between 2 m and 10 m above the ground. It is therefore not feasible to fabricate models of the small-scale structures with a geometric scaling factor as large as 1:100. Hence, larger scaling ratios between 1:10 to 1:50 are in practice used for these structures, such as the experiment by (Peterka and Derickson, 1992; Tieleman, 2003; Pfahl and Uhlemann, 2011; Emes *et al.*, 2017). Consequently, the criterion of identical scaling ratios for the structure and ABL is violated.

Lack of similarity of geometric scaling ratios leads to mismatch of the Reynolds number and mismatch of scales of turbulence in a wind tunnel experiment from the full-scale conditions. According to Tieleman (2003), lack of similarity of Reynolds number in a wind tunnel does not affect the wind load measurements for sharp-edged models if the Reynolds numbers is larger than 50,000, where $Re = Uc/\nu$ with c representing the characteristic length of the structure model in the wind tunnel experiment. However, similarity of turbulence scales is important for similarity of unsteady wind loads. As Cook (1978) explains, mismatch of the geometric scaling ratios of the structure and the boundary layer leads to mismatch of the scales of turbulent structures in the flow and the structure-generated turbulence. Hence, the unsteady loads on the model will differ from those corresponding to the prototype in full scale.

In order to resolve the mismatch of turbulence scales in a wind tunnel, Dyrbye and Hansen (1996) recommended to conduct a wind tunnel experiments at a lower turbulence intensity compared to its corresponding full-scale value, in contrast to the commonly used method where turbulence intensity in the wind tunnel is matched with the ABL. As shown in Figure 2.4(a), when turbulence intensity is matched but the geometric scaling factors of the structure model and the boundary layer differ, the turbulence spectrum in the wind tunnel does not match the full-scale spectrum. Dyrbye and Hansen (1996) discussed that by reducing turbulence intensity in a wind tunnel experiment, the high frequency range of the spectrum can be matched with the full-scale, as shown in Figure 2.4(b). Tieleman (2003) suggests that for wind tunnel modelling of low-rise buildings, the high-frequency range of the turbulence spectrum should be matched with the full-scale ABL spectrum. He explains that the base pressure coefficient on a building model is mainly influenced by separation of flow at its edges and proposes that the inflow turbulence of smaller scales and higher frequencies interact with the separated shear layers (Tieleman, 1992). Hence, the higher frequency turbulence structures of the spectrum are suggested to be more important for measurement of pressure on the building models. Richards *et al.* (2007) measured the pressure distribution on the roof of a cube in a simulated atmospheric boundary layer flow in a wind tunnel and compared it to the surface pressure measurements obtained on the full-scale structure within the ABL. The full-scale cube had a height of 6 m and the streamwise turbulence intensity at the roof height was approximately 20%. In their wind tunnel model, only the mid- to high-frequency ranges of the turbulence spectra matched the full-scale atmospheric spectra, and turbulence intensity at the roof height was lower than its full-scale value (I_u =12%). They found that the pressure distribution on the 1:40 model was similar to that at full-scale. The mean pressure coefficients at the cube roof in the wind tunnel model were also similar to those on the full-scale cube. However, the magnitude of the peak pressure coefficients in full-scale measurements were up to 3-times larger than the wind tunnel measurements. Hence, the recommended method of matching the high frequencies of the turbulence spectrum at a reduced turbulence intensity in a wind tunnel, has been shown not to be effective in achieving similarity of peak wind loads.

Figure 2.4. (a) Mismatch of turbulence spectrum in wind tunnel measurements of small-scale structures when turbulence intensity is matched, (b) matching high frequencies of turbulence spectrum by reducing turbulence intensity in the wind tunnel. Reproduced from Dyrbye and Hansen (1996).

The mismatch of scaling ratios is an issue in wind tunnel modelling of heliostats due to their small dimensions compared to ABL. The effect of this mismatch on the wind load measurements however has not been well established in the literature. Figure 2.5 schematically presents the geometric scaling of a heliostat in a typical wind tunnel study and compares the dimensions of a full-scale heliostat with a model heliostat in a wind tunnel experiment. Three sets of experimental studies investigating the wind loads on heliostats have been conducted in the literature (Peterka *et al.*, 1989; Pfahl *et al.*, 2011; Emes *et al.*, 2017). These studies measured wind loads, in terms of coefficients of lift, C_L, and drag forces, C_D, as well as the moments induced at the hinge, C_{MHy}, and foundation, C_{My}, shown in Figure 2.5(b), on heliostat models at different elevation angles at operating and stow positions. In their experiments, the heliostat models were placed in a simulated boundary layer with the mean velocity profile and turbulence intensity matched with an ABL in an open-country terrain. In Peterka's experiments (1989), the heliostat model was built at a scale of 1:40. The boundary layer thickness in Peterka's wind tunnel simulation was about 1 m which when compared to the average ABL thickness in open terrains suggests a scaling factor of 1:350 for the ABL. The same issue exists in Pfahl's experiments (2011), and the heliostat model was scaled at 1:20 which was much larger than the scaling ratio of the ABL. The scaling factors were similar in the experiments of Emes *et al.* (2017). The violation of scaling ratios, demonstrated in Figure 2.5, has led to differences in their reported wind load coefficients as shown in Table 2.2, which compares their peak operational and stow load coefficients. These variations thus raise the question on how reliable the wind load measurements are and whether they correspond to the full-scale wind loads. In a later study, Pfahl (2018) discusses the scaling violations in wind load measurements of heliostats and proposes that for a stowed heliostat matching the vertical turbulence intensity, in spite of mismatch of streamwise turbulence spectrum, is sufficient. This argument is however not well established, and dependency of the wind loads on stowed heliostats on only vertical turbulence intensity needs to be further investigated. Hence, the correlation between the turbulence spectrum and the wind loads, and its influence on the accuracy of the wind load remains a gap.

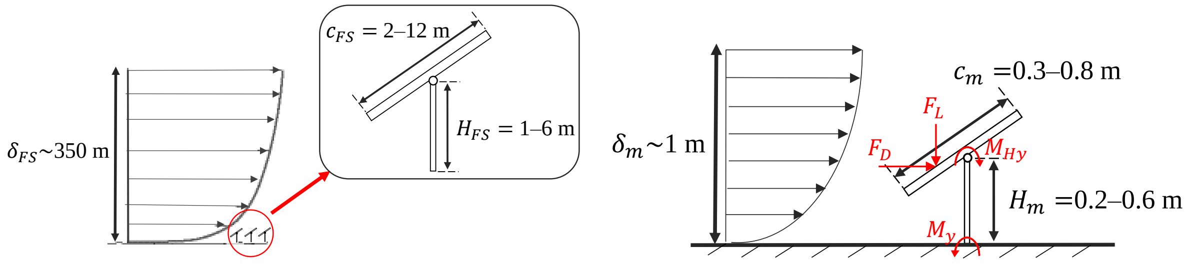

(a) (b)

Figure 2.5. A schematic showing the dimensions of: (a) a full-scale heliostat in the atmospheric boundary layer, (b) a model heliostat in a wind tunnel experiment, and the forces and moments on the

heliostat model. The dimensions of model heliostat are based on the studies in the literature (Peterka *et al.*, 1989; Pfahl, 2011; Emes *et al.*, 2017). δ is boundary layer thickness. c and H show the characteristic length of heliostat panel and the heliostat hinge height. The subscripts FS and m represent full scale and model.

Table 2.2. Comparison of peak operational and stow wind load coefficients reported in the literature. The peak coefficients present the sum of the time-averaged coefficient and three-times the standard deviation of the measured coefficient.

	Operation				Stow				
	C_L	C_D	C_{My}	C_{MHy}	C_L	C_D	C_{My}	C_{MHy}	I_u (%)
Peterka *et al.* (1989)	2.8	4	4.35	0.6	0.9	0.6	1	0.2	18
Pfahl *et al.* (2011), Pfahl *et al.* (2015)	2.1	3.3	3.2	0.55	0.43	0.38	0.53	0.18	18
Emes et al. (2017)	---	---	---	---	0.4	---	---	0.1	12.5

2.3 Effect of turbulence on wind loads

As described in Section 2.2, the distribution of energy over the range of frequencies of the turbulent eddies, as described by turbulence spectrum, in a wind tunnel boundary layer is required to be similar to that in the ASL. In the following section, the effect of turbulence spectrum on heliostat wind loads is discussed in terms of two quantitative parameters: the intensity of velocity fluctuations and the integral length scale of turbulent eddies.

2.3.1 Turbulence intensity

Turbulence intensity in the approaching flow is one of the parameters that is found to affect the wind loads on both operating and stowed heliostats. Peterka et al. (1989) conducted experimental measurements of the wind loads on heliostat models at different elevation angles in simulated boundary layers at longitudinal turbulence intensities, I_u =14% and I_u =18%. It was found that with increasing I_u, the peak lift and drag force coefficients increased regardless of the elevation angle of the panel, α, as shown in Figure 2.6. For instance, the peak drag force coefficient on a heliostat at α=90° increased from 3 to 4, and the peak lift force coefficient at α=30° increased from 1.7 to 2.7 by increasing I_u from 14% to 18%. Furthermore, according to Peterka *et al.* (1987), the peak lift force coefficient on a heliostat at stow increased from 0.5 to 0.9 when I_u increases from 14% to 18%. Peterka et al. (1989) mentions that the reason behind the increase in the wind loads was not determined in their experiments but it was likely to be associated with the interaction of turbulence with the separated shear layers at the edge of the plate.

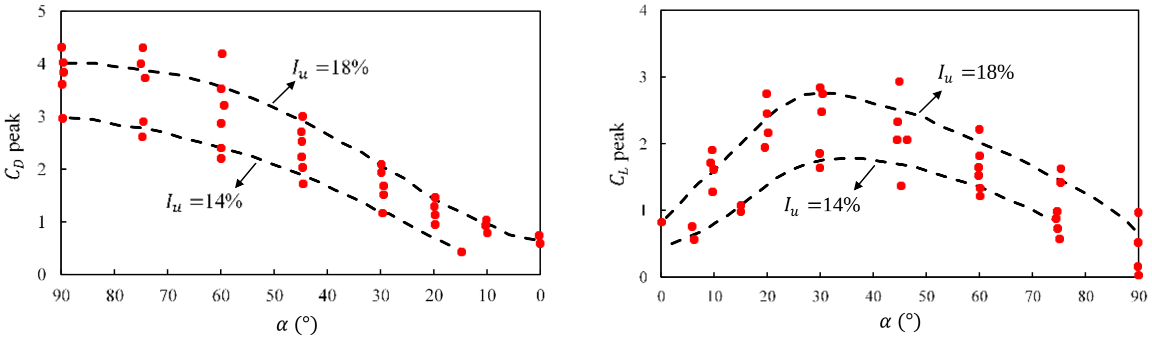

(a) (b)

Figure 2.6. (a) Peak drag force and (b) lift force coefficients on a heliostat at different elevation angles, α, at I_u=14% and I_u=18%. Reproduced by permission from ASME: Solar Energy Engineering, Peterka et al. (1989).

Emes *et al.* (2017) investigated the effect of turbulence intensity on the wind loads on a stowed heliostat by measuring the loads on models of different mirror panel dimensions at different heights in a wind tunnel boundary layer. As the height of the heliostat model varied, it was exposed to longitudinal turbulence intensities between 6% and 14%. Emes *et al.* (2017) reported that the peak lift force and hinge moment coefficients on the stowed heliostat models increased with increasing longitudinal turbulence intensity, showing a linear trend for I_u between 10% and 14%.

Due to the anisotropic nature of atmospheric turbulence and depending on the orientation of the heliostat panel, both streamwise and vertical turbulence parameters can be of significance for the wind loads. While, in the previous experiments by Peterka et al. (1989) and Emes *et al.* (2017), all components of turbulence intensity varied during the experiments, the observed effects on the wind load coefficients were only correlated with longitudinal turbulence intensity and the variations of vertical turbulence components were not differentiated. Pfahl (2018) proposed that at stow position, vertical velocity is more decisive for the pressure forces on the panel as it acts normal to it and therefore the lift force on a heliostat at stow position was suggested to be more closely correlated with vertical turbulence intensity, I_w. A series of experiments were conducted to measure the lift force on a stowed heliostat model in a simulated boundary layer, and in the vortex street generated in the wake of cylinders of different diameters. Figure 2.7 shows the peak and root mean square (RMS) lift force coefficients as a function of I_u and I_w. Pfahl (2018) discusses that the curve-fitted coefficients show a better match as a function of I_w, and therefore, I_w has a stronger effect on the lift force than I_u. This conclusion, however, needs further investigation as both longitudinal and vertical turbulence intensities were varied simultaneously in the experiments of Pfahl (2018). A systematic study to distinguish the effect of each parameter is needed to determine which component more effectively contributes to the unsteady forces. Furthermore, turbulence in the wake of a cylinder is dominated by quasi-static vortex shedding which has different properties from turbulence in an ABL. As described in Section 2.1, turbulence in an ABL is described by its specific power spectrum, which differs from the turbulence spectrum in the cylinder wake. Pfahl (2018) discusses that the differences of the turbulence spectrum do not impact the lift force coefficient, but only affect the pressure distribution on the panel. This conclusion has been drawn from comparison of the lift force coefficients for two cases in the cylinder wake with that for a heliostat model in a simulated boundary layer, where the vertical turbulence intensity in all three cases was approximately 10%. However, further investigation about the effect of the turbulence spectrum on the forces is needed to support this conclusion.

Figure 2.7. Peak and RMS lift force coefficients on a stowed heliostat as a function of: (a) longitudinal turbulence intensity, I_u, (b) vertical turbulence intensity, I_w. Reproduced from Pfahl (2018).

2.3.2 Integral length scale of turbulence

Another important parameter which affects the wind loads is the integral length scale of turbulence in the boundary layer. Bearman (1971) measured the drag force on flat plates of various dimensions which were placed normal to a grid-generated turbulent flow at I_u=8% and a uniform flow. In the turbulent flow, the RMS drag force coefficient was found to be larger for the plates with smaller dimensions, while it remained almost constant for different flat plates in a uniform flow, as shown in Figure 2.8(a). Bearman (1971) discussed that the observed effect is due to the variations in the ratio of the integral length scale of the turbulent flow to the chord length of the plates, L_u^x/c. Decreasing the plate chord length increased L_u^x/c from 0.375 to 1.5, which led to increasing the drag force coefficient. Furthermore, it was found that the effect of L_u^x/c was dependent on turbulence intensity such that the base pressure coefficient on the flat plate increased logarithmically by increasing $I_u(L_u^x/c)^2$, Figure 2.8(b).

Figure 2.8. The effect of turbulence length scale and intensity on the forces on a square flat plate normal to a turbulent flow: (a) the RMS drag force coefficient as a function of the chord length of the plate, (b) the base pressure coefficient as a function of turbulence intensity and integral length scale. Reproduced from Bearman (1971).

Similarly, Humphries and Vincent (1976) found that the base pressure coefficient on flat disks normal to a grid-generated turbulent flow was a function of both turbulence intensity and length scale ratio. The base pressure on flat disks of different diameters positioned at different distances behind a grid were obtained from experimental measurements. The values of inflow turbulence intensities and integral length scales in the experiments were not given, however, $I_u(L_u^x/c)$ varied between 0.002 and 0.004. According to Humphries and Vincent (1976), when the level of turbulence increased, the magnitude of base pressure coefficient increased. The observed effect was correlated with enhanced mixing in the shear layers in the wake of the disk. Consequently, suction at the rear of the disk increases leading to a larger negative base pressure coefficient on the rear surface and ultimately an increase in drag force. Humphries and Vincent (1976) found that the mean base pressure coefficient was a function of a turbulence parameter defined as $I_u(L_u^x/c)$, which is different from the parameter determined by Bearman (1971) discussed above. Despite the difference in the exponent of L_u^x/c between the turbulence parameters defined in the two studies, the results from both show that the pressure coefficient was correlated with both turbulence intensity and integral length scale.

The ratio of the integral length scale was also found to affect the wind loads on a stowed heliostat. Emes *et al.* (2017) investigated the effect of variations in L_u^x/c by measurement of the lift force on stowed heliostat models of different chord length dimensions in an atmospheric boundary layer flow in a wind tunnel. They found that the peak lift force coefficient increased with increasing L_u^x/c. In their experiments, both L_u^x/c and L_w^x/c varied simultaneously by changing the chord length dimensions. However, the possible effect of variations of L_w^x/c was not considered. Hence, further investigation is required to determine whether the observed effect is due to L_u^x or L_w^x.

The effect of the length scale of turbulence on the lift force can be associated with the interaction of turbulent structures with the structure. Chen and Chiou (1998) studied the interactions of a spanwise vortex, generated with a flapping air foil, with a horizontal flat plate, chord length to thickness ratio of 20. Smoke visualisation of the flow around the flat plate and measurements of pressure on the plate surface showed that when the vortex approached the leading edge of the flat plate, at a distance less than the chord length, an upwash effect increased the angle of attack leading to formation of a circulation around the plate in the opposite direction of the vortex. The upwash effect created an increase in the pressure on the bottom surface of the plate and a decrease in the pressure on the top surface which created an increase in the lift force acting on the plate. As the vortex hit the leading edge of the plate, pressure on the top surface reached its lowest, and consequently the lift force reached its maximum. When the vortex passed over the leading edge, reaching to approximately to a distance of 0.3-times the chord length, pressure started to increase on the top surface and to decrease on the bottom surface, leading to reduction of lift force. As the vortex moved over the plate approaching the trailing edge, a downwash effect at the leading edge resulted in a change in the angle of attack leading to a larger pressure over the top surface compared to the bottom surface creating a negative lift force. The variations of lift force and pressure distribution on the flat plate caused by the vortex-induced upwash and downwash effects described by Chen and Chiou (1998), suggest that the unsteady variations of the lift force on a heliostat panel at stow are correlated with the interactions of the turbulent eddies within the boundary layer with the panel. The variations of the lift force are a result of the variations of the pressure distribution on the panel which depend on the distance of eddies from the plate and their length scale.

While the studies in the literature show that the wind loads increase with increasing turbulence intensity and length scale ratio, their mutual effects on heliostat wind loads have not been considered and a correlation between these parameters and the wind loads has not been established. In the studies on heliostat wind loads, the effect of turbulence anisotropy in the ASL has been neglected and the majority of the studies interpreted the variations of wind loads with respect to streamwise turbulence components, despite the simultaneous variations of all turbulence components in their experiments. This can have significant impacts since the level of anisotropy in the wind tunnel experiments and its possible dissimilarity to the turbulence in the ASL has not been analysed. Hence, the effect of turbulence anisotropy and specifically the effect of vertical turbulence components at stow position, where the heliostat panel is aligned with the streamwise flow direction, needs to be further studied. Whether streamwise or vertical turbulence is more dominant on stow wind loads remains a gap which needs further investigation.

2.4 Wind loads and flow behaviour around heliostats in an array

Heliostats in a solar field are arranged in rows surrounding a receiver in a radial, Figure 2.9(a), or a polar design, Figure 2.9(b). For optimum optical performance, the spacing between the subsequent rows in a field increases from a value slightly larger than the chord length dimension of the mirror panel, $D/c>1$, to about 8-times the chord length dimension, $D/c=8$, as the distnace the from the central tower increases (Hui, 2011). As wind flows over a heliostat, a region of disturbed flow is created downstream in its wake. Heliostats within a field are positioned in the wake of other heliostats and/or the receiver tower. Hence, based on the arrangement of heliostats in a field and the spacing between the rows, both the mean and turbulent properties of the flow within the field can vary significantly from the inflow atmospheric boundary layer. For instance, measurements of wind speed by ultrasonic anemometers within a five-row array of heliostats showed that turbulence intensity increased from 10% within the ABL to 50% downstream of the first and second rows of heliostats, when the elevation angle of the heliostats was 45° and 90° (Sment and Ho, 2014). The different flow and turbulence characteristics within a field alter the wind loads on heliostats placed within a field from those on a single heliostat. Hence, knowledge of variations of mean and turbulence characteristics of the flow in a heliostat field can provide a basis for estimation of the wind loads on heliostats at different locations of a field which is essential for the design of a heliostat field. As a first step towards understanding the flow characteristics in a heliostat field, this thesis focuses on the flow around a single heliostat and the flow around multiple heliostats in an array. In the following sections, first, the flow in the wake of a single heliostat is described in Section 2.4.1, starting with a general description of the wake of a flat plate and continuing with a discussion of the parameters differentiating the wake of a heliostat from a simple flat plate. Section 2.4.2 focuses on aerodynamics of multiple heliostats. This section starts with a discussion of flow behaviour around multiple flat plates and continues with a review of wind loads on multiple heliostats.


(a) (b)

Figure 2.9. Different layouts of a heliostat field. (a) A radial heliostat field, Noor III in Morocco. Image from www.masen.ma, (b) a polar heliostat field, PS10 in Spain. Image from www.eusolaris.eu.

2.4.1 Wake of a single heliostat

The flow around a heliostat, if excluding the support structure and the pylon resembles the flow around a thin flat plate. As the flow passes around a thin flat plate, it separates from the plate at its edges forming a low-pressure region immediately downstream of the plate. The separated shear layers then roll up into large scale vortices shedding into the wake. Blockage of the flow by the plate and vortex shedding in the wake lead to a reduction of mean velocity and an increase in turbulence intensity, as shown in Figure 2.10, which illustrates the mean flow characteristics in the wake of a thin flat plate normal to a uniform flow at Re=6600 (Mohebi, 2016). The velocity deficit region and the recirculation zone can be seen up to x/c =4, and regions of expansion where the free-stream velocity is increased are seen above and below the plate top and bottom edges in Figure 2.10(a). The increase in streamwise turbulence intensity in the wake is also evident in Figure 2.10(b). One of the most important features of the wake flow is vortex shedding. The alternating shedding of the rolled-up shear layers into the wake creates oscillations in the flow, which are characterised by the dominant frequency of vortex shedding, typically reported in terms of Strouhal number, $St = fc/U_\infty$, where c is the chord length of the flat plate and f is frequency. The Strouhal number for a flat plate normal to a uniform flow is reported between 0.12 and 0.16 in the literature (Fage and Johansen, 1927; Kiya and Matsumura, 1988; Najjar and Balachandar, 1998; Mohebi, 2016).

Figure 2.10. (a) Time-averaged streamwise velocity, U/U_∞, and (b) turbulence intensity, σ_u/U_∞, in the wake of a flat plate, aspect ratio of 39, normal to a uniform flow at Re=6600. Reprinted from Mohebi (2016).

The wake of a heliostat has more complexities than the flat plate described above due to its geometric specifications and inflow conditions. The geometric parameters which affect the wake are the shape of the mirror panel, its aspect ratio, the elevation angle of the mirror panel and its proximity to the ground. It must be noted that the effect of support structures at the back of the panel on the flow properties in the wake, except in the immediate downstream of the panel, are assumed to be negligible due to their small dimensions compared to the panel chord length. Another parameter which significantly affects the flow around a heliostat and its wake is turbulence in the atmospheric boundary layer. The effect of the geometric and inflow parameters on the mean flow and turbulence properties in the wake are discussed in the following sections.

2.4.1.1 Effect of heliostat geometric specifications on its wake properties

Heliostat panels are typically rectangular in shape with the majority of heliostat panels being square. The aspect ratio of the panel, defined by the ratio of its chord to span, is one of the parameters which affects the wake flow properties. While in most of the studies on wakes of flat plates in the literature, a flat plate with a very large or infinite aspect ratio is studied, a flat plate with a low aspect ratio has a more complex wake structure compared to an infinite-span flat plate due to the additional separation of flow on the spanwise edges of the plate. The wake of a finite aspect ratio flat plate is 3D in contrast to the 2D wake of an infinite span plate. Hemmati *et al.* (2015) studied the wake of a 3D flat plate with an aspect ratio of 3.2 by Direct Numerical Simulation and compared it to the wake of a 2D flat plate. As shown in Figure 2.11, due to the increased entrainment, the recirculation region was shorter and the wake was narrower in the case of the 3D flat plate. As the length of the recirculation region decreased, the mean drag force coefficient on the plate decreased from 2.13 for the 2D plate to 1.16 for the 3D plate. Mean flow and turbulence properties in the wake of the two plates were found to be different. Comparison of profiles of mean velocity along the wake centre line for the two plates, Figure 2.12(a), shows a faster recovery of velocity deficit in the wake of the 3D flat plate. Turbulence kinetic energy, $k = \frac{1}{2}({\sigma_u}^2 + {\sigma_v}^2 + {\sigma_w}^2)$, along the wake centre line, Figure 2.12(b), was an order of magnitude smaller for the 3D plate. The reduction of turbulence kinetic energy in the wake was attributed to the different vortex shedding topology. It was found that the vortices shed from the chord-wise edges were carried out by the vortices created from the separation of the flow from the span-wise edges which led to a reduced turbulence kinetic energy for the 3D flat plate. Furthermore, the Strouhal number increased from 0.158 for the 2D plate to 0.317 for the 3D plate.

Figure 2.11. Streamlines in the wake of a flat plate normal to the flow at Re=1200. (a) 3D flat plate with aspect ratio of 3.2, (b) 2D flat plate. Reprinted from Hemmati *et al.* (2015).

Figure 2.12. Profiles of (a) mean streamwise velocity, U, and (b) turbulence kinetic energy, k, normalised with freestream velocity, U_{∞}, along the wake centreline for the 2D and 3D flat plate in Figure 2.11. Reprinted from Hemmati *et al.* (2015).

A heliostat during its operation is elevated at different angles, α in Figure 1.1, based on its position in the field and the time of the day. Hence, during different times of its operation, the angle of the flow to the heliostat panel, i.e., the angle of attack, varies affecting its wake. While the wake of a flat plate normal to a uniform flow is symmetric, as shown in Figure 2.10, with inclination of the plate, the wake changes to asymmetric. In the case of the normal flat plate, the vortices shed alternately from the edges of the plate are of similar strength resulting in the symmetry of the flow along the centreline. In contrast, the vortices shed from the leading and trailing edges of an inclined flat plate are of different strengths resulting in an asymmetric wake (Lam and Leung, 2005; Yang *et al.*, 2012). For the inclined flat plate, the trailing edge vortices have larger circulation than the leading edge vortices in the near wake region (Lam and Leung, 2005). Mohebi *et al.* (2017) studied the effect of the elevation angle varying between 20° and 90° on the characteristics of a flat plate wake developed in a uniform flow at Re=6600. The mean streamlines and turbulence kinetic energy in the wake at different elevation angles are shown in Figure 2.13. As the angle of attack decreases from α =90° to α =20°, the wake width decreases, and the recirculation zone becomes smaller. Furthermore, with decrease of the angle of attack, regions of maximum turbulence kinetic energy, which are located downstream of the recirculation zone, shrink significantly and move closer to the plate, from $x/c \cong 4$ for α =90°, Figure 2.13(a), to $x/c \cong 1$ for α =20°, Figure 2.13(f). It was also found that the Strouhal number increased from 0.119 at α =90° to 0.437 at α =20°.

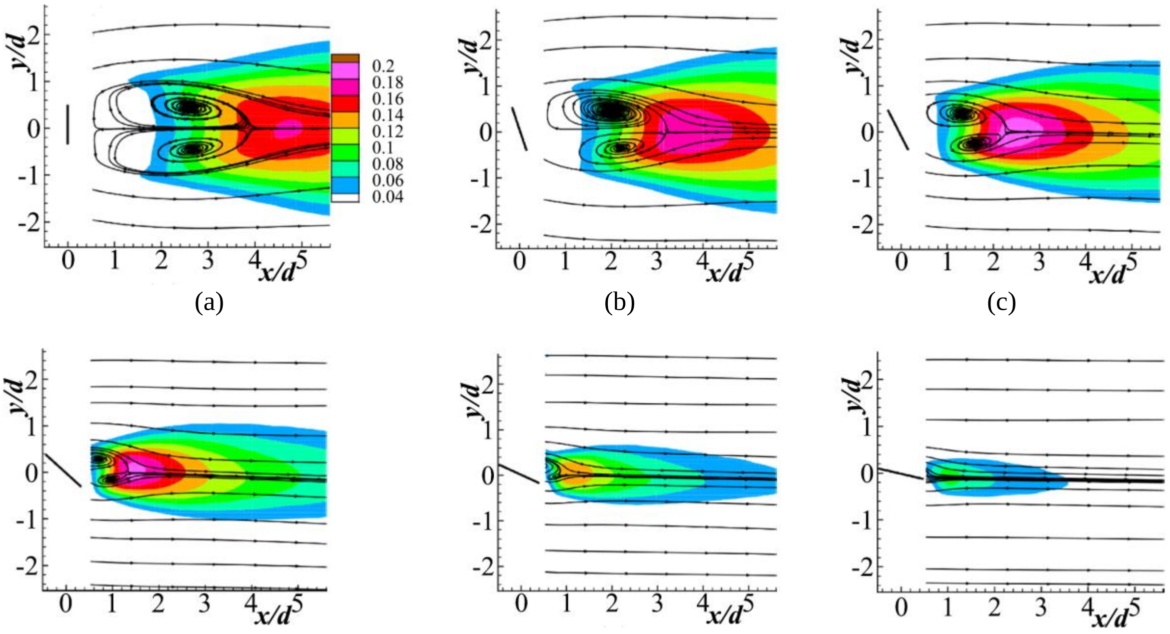

(a) (b) (c)

(d) (e) (f)

Figure 2.13. Streamlines and turbulence kinetic energy in the wake of a flat plate, aspect ratio of 39, in a uniform flow at Re=6600 at different elevation angles. (a) α =90°, (b) α =75°, (c) α =60°, (d) α =40°, (e) α =30°, (f) α =20°. Reprinted by permission from Springer: Experiments in Fluids, Mohebi *et al.* (2017).

When inclined at different angles, there is a gap between the bottom edge of the heliostat panel and the ground. This gap is typically equal to $0.15c$, where c is the chord length of the heliostat panel, at an elevation angle of 90° (Pfahl, 2018), and increases when the elevation angle decreases. The presence of the ground bounds the flow altering it from the case of a flat plate immersed in a uniform flow with free boundaries. The studies on bluff bodies show that at very small gaps from the ground, lower than a certain threshold, vortex shedding on the leading edge is suppressed (Bearman and Zdravkovich, 1978; Bosch *et al.*, 1996). For circular cylinders, this critical gap height is found to be a function of the boundary layer thickness, δ, and independent of the Reynolds number. However, different values for the critical gap height have been reported in the literature. For example, Lei *et al.* (1999) reported that the critical gap ratio, h_g/D where h_g and D are the gap height and the cylinder diameter, decreased from 0.4 to 0.2 when δ/D increased from 0.14 to 2.89, while Taniguchi and Miyakoshi (1990) found that h_g/D increased from 0.3 to 0.9 as δ/D increased from 0.34 to 1.05. For square cylinders, the presence of the wall has been found to have no effect on the wake for $h_g/D \geq 1$, while for $h_g/D < 1$, the strength of vortex shedding decreased, which dependent on h_g/D resulted in different flow regimes (Martinuzzi *et al.*, 2003). Furthermore, no significant effect of boundary layer thickness on the critical gap height has been found for square cylinders.

A few studies in the literature have investigated the effect of wall proximity on the wake of a flat plate but a critical gap ratio has not been determined for flat plates. Krampa-Morlu and Balachandar (2007) and Shinneeb and Balachandar (2016) studied the effect of the gap on the wake of a sharp-edged flat plate suspended in a water channel. The immersed plate was placed normal to the flow with a gap from the channel bed. The water depth in the channel, H, was 100 mm, and the plate, which was chamfered at its bottom edge on the downstream side, had a height of 110 mm, and a thickness of 6 mm. Two gap ratios $h_g/H =$0.05 and $h_g/H =$0.1 were studied and compared to a case with no gap from the bed. The experimental results showed that a wall jet was created at the location of the gap which interacted with the wake flow. It was found that for $h_g/H =$0.05, the reverse flow in the wake of the plate reduced and moved downstream. With increase of the strength of the jet flow at $h_g/H =$0.1, no reverse flow was formed in the wake. The wake recovery length was found to be shorter when a gap existed between the plate and the channel bed compared to the case with no gap.

Furthermore, as shown in Figure 2.14, with the presence of a gap at $h_g/H =$0.1, streamwise turbulence intensity in the wake was lower and vertical turbulence intensity was higher compared to the case where no gap existed. This indicates a transfer of turbulence kinetic energy from the streamwise to the vertical component at the presence of the gap (Shinneeb and Balachandar, 2016b). As shown in Figure 2.14(b), the jet flow creates a region of large turbulence intensity close to the bed in the near wake, up to $x/H =$0.5. The effect of the jet flow reduced further downstream and the flow was mainly dominated by the quasi-steady vortex shedding resulting from separation at the edges of the plate (Krampa-Morlu and Balachandar, 2007). No information about the effect of the gap on the Strouhal number and the length scales of turbulence in the wake was given.

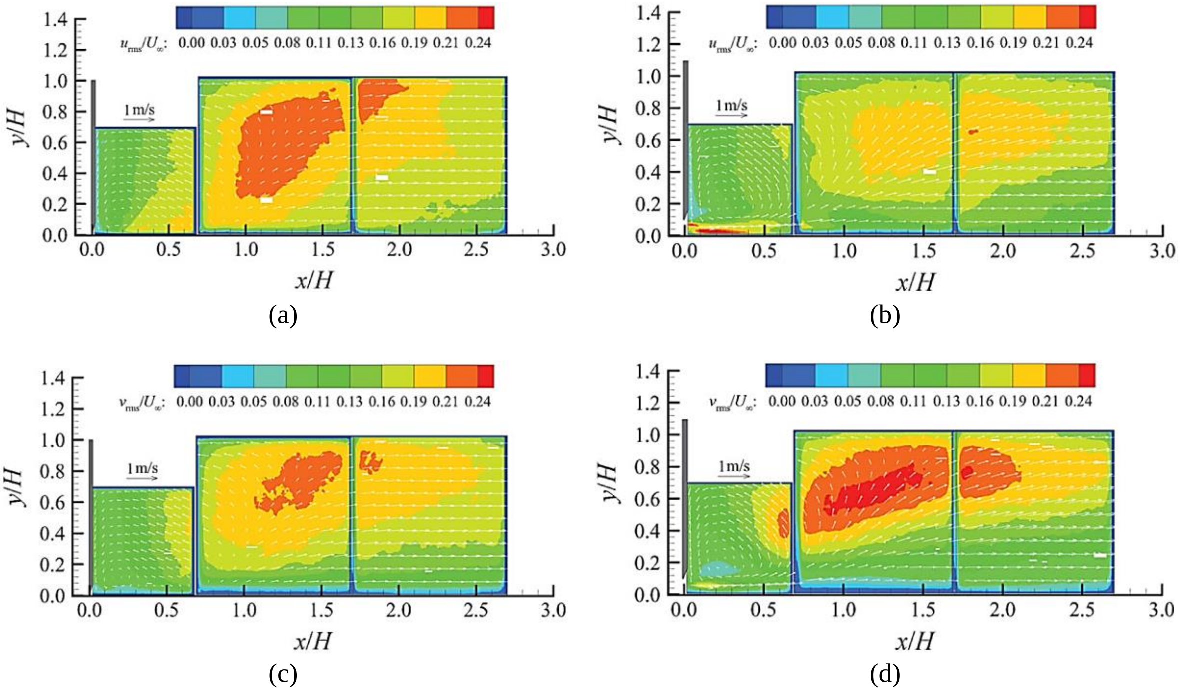

(a) (b) (c) (d)

Figure 2.14. Streamwise, I_u, and vertical, I_w, turbulence intensities in the wake of a suspended flat plate in a water channel with and without a gap from the channel bed. (a) I_u at $h_g/H = 0$, (b) I_u at $h_g/H = 0.1$, (c) I_w at $h_g/H = 0$, (d) I_w at $h_g/H = 0.1$. h_g and H are the gap height and water depth, respectively. The plate is placed at $x/H = 0$. The three domains are the fields of view of PIV measurements. Reprinted from Shinneeb and Balachandar (2016).

2.4.1.2 Effect of atmospheric boundary layer inflow on the wake properties

Heliostats operate within the turbulent atmospheric boundary layer. The shear and turbulence in the boundary layer affect the development of the wake of a heliostat and its turbulence structure significantly. The effect of the inflow atmospheric boundary layer on the flow around a wall-mounted cube was studied by Castro and Robins (1977). They compared the velocity measurements in the wake and the pressure distributions on the cube surface when placed in a uniform flow and in a simulated atmospheric boundary layer flow. It was found that within the turbulent boundary layer, in contrast to the uniform inflow, the separated shear layers reattached to the sides and top surfaces of the cube creating a nearly zero base pressure on these surfaces. Furthermore, a larger velocity deficit was found in the uniform inflow compared to the atmospheric inflow. In a more recent study, Hearst *et al.* (2016) investigated the wake of a wall-mounted cube within boundary layers with different turbulence intensities, I_u between 5.4% and 9%, and L_u^x/c between 0.4 and 0.18. It was found that the stagnation point on the upstream face of the cube and the reattachment point in the wake were not dependent on the inflow turbulence intensity. Comparison of mean streamwise velocity for the four inflow cases showed that for the cases with similar shear level at the cube height, $\tau_H = (H/U_H)(\partial U/\partial z)|_H$, increasing inflow turbulence intensity led to a reduction of the wake recovery length. Turbulence intensity was increased over a larger region in the wake of the cube when the inflow turbulence intensity was lower. Variations of both mean velocity and turbulence intensity in the wake showed that with increase of inflow turbulence intensity, entrainment of flow into the wake increased resulting in a shorter wake recovery length. Furthermore, it was also found that with an increase of inflow turbulence intensity, vortex shedding was suppressed and the shedding frequency, corresponding to the Strouhal number for the case with lower inflow turbulence intensity I_u =5.4%, became less prominent in the turbulence spectrum.

Amoura *et al.* (2010) studied the wake of a sphere subjected to homogenous isotropic turbulence by laser doppler anemometry. Four inflow cases with Reynolds numbers, $Re = U_\infty d/\nu$, between 110 and 1080, I_u =15%–26% and L_u^x/d =3–4, where d is the sphere diameter, were investigated. They found that the inflow turbulence had a greater impact on the wake flow dynamics in the far wake compared to mean shear, such that in the far wake the mean velocity reduction scaled with the inflow turbulence intensity. In the near wake up to a distance of three times the sphere radius, the velocity deficit was found to scale with the mean velocity showing the prominence of mean velocity only in this region. Amoura *et al.* (2010) concluded that the inflow turbulence altered the wake flow structure such that turbulence within the wake was generated from the distorted inflow turbulence and not the instability of mean velocity profiles. Furthermore, analysis of power spectral density of the streamwise and transverse velocity fluctuations in the wake of the sphere showed no significant shedding peak and revealed suppression of vortex shedding, which was attributed to the incident inflow turbulence. Furthermore, Rind and Castro (2012) studied the wake of a disk normal to a grid-generated turbulent flow at I_u =0.8%–4.3% and L_u^x/d = 3–14. The strength of vortex shedding was found to be significantly reduced in the presence of the freestream turbulence, such that at high levels of inflow turbulence intensity, vortex shedding was not evident anymore. Rind and Castro (2012) concluded that inflow turbulence, particularly at high intensities, significantly affects the development and structure of the wake such that turbulence within the far wake eventually reaches the freestream levels. The studies in the literature demonstrate that inflow turbulence affects the wake properties. However, the correlation between the observed effects and intensity and integral length scale of inflow turbulence is not known.

The review of the studies in the literature presented in this section shows that flow around a heliostat despite its fundamental similarity to a flat plate is not well known. The geometric specifications of the heliostat structure and the turbulence in the atmospheric surface layer can significantly influence the flow properties as outlined in this section. Hence, in order to provide a better understanding of the flow properties in a heliostat field, it is necessary to first characterise how the mean and turbulence flow properties, including mean velocity, turbulence intensity and integral length scale, in the wake of a heliostat differ from the wind properties in the atmospheric boundary layer.

2.4.2 Aerodynamics of multiple heliostats

The aerodynamics of multiple heliostats differ from a single heliostat due to the interference of their wakes with each other and the interaction of the downstream heliostats with the wakes. The flow around multiple heliostats depends on their arrangement and the spacing between them. Two different shedding regimes have been found in the flow around two tandem flat plates in a uniform flow: single body, and dual body shedding (Nakamura, 1996; Auteri *et al.*, 2008). Single body shedding corresponds to the case where the two plates are close enough such that the separated shear layers from the upstream plate overshoot the second plate creating a wide wake downstream of the second plate. The dual body shedding regime occurs when the two bodies are spaced sufficiently apart that the vortices shed off the upstream plate roll up inside the spacing between the two plates. Figure 2.15 shows the mean velocity vectors in the flow around two tandem flat plates normal to a uniform flow at two gap ratios, D/c =0.9, and D/c =1.2, where D is the streamwise distance between the two plates and c is the chord length of the plate (Auteri *et al.*, 2009). At D/c =0.9, Figure 2.15(a), two large recirculation regions are formed downstream of the second plate extending beyond the plate edges. Furthermore, two weak recirculation regions are observed between the two plates in which the rotation of the flow is in the opposite direction to that in the wake of the second plate. Flow behaviour around the two plates at D/c =0.9 describes the single body shedding mode as the separated shear layers from the edges of the first plate do not penetrate into the gap between the plates. As the gap ratio enlarges to D/c =1.2, Figure 2.15(b), dual body shedding occurs. At this gap ratio, two distinct recirculation regions are observed both between the two plates and downstream of the second plate resulting from roll-up of vortices behind both first and second plates. Comparison of the mean flow patterns at D/c =1.2 and D/c =0.9 shows that the recirculation regions formed downstream of the second plate are smaller in the dual body mode and the wake is narrower compared to the single body mode.

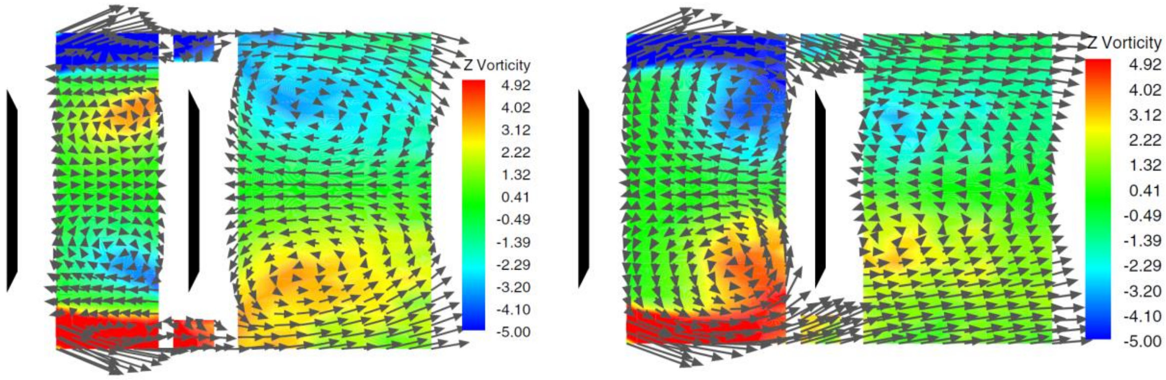

(a) (b)

Figure 2.15. Mean velocity vectors and vorticity, $\omega_z = \frac{\partial v}{\partial x} - \frac{\partial u}{\partial y}$, in the flow around two tandem plates normal to a uniform flow at Re =46800 determined from laser doppler anemometry measurements. (a) Single body shedding at a gap ratio, D/c =0.9, (b) dual body shedding at D/c =1.2. D and c represent the streamwise distance between the two plates and the chord length of the plate, respectively. Reprinted by permission from Springer: Journal of Visualization, Auteri *et al.* (2009).

The gap between the two plates affects the distribution and magnitude of turbulence intensity in the wakes of the flat plates in the two shedding regimes. Auteri *et al.* (2009) found that in the single body shedding mode at D/c =0.9, turbulence kinetic energy downstream of the second plate was increased by one order of magnitude compared to its value between the two plates. Furthermore, the maximum turbulence kinetic energy occurred at the location of the recirculation regions downstream of the second plate. Teimourian *et al.* (2017) studied the flow around two tandem inclined flat plates at α =45° in a uniform flow and compared the turbulence kinetic energy downstream of the second plate for the two shedding modes. They found that the peak turbulence kinetic energy production downstream of the second plate at x/c =4 was up to 50% larger when the gap ratio between the two inclined flat plates decreased from D/c =1.5 to D/c =0.5 changing from dual body to single body shedding mode. The larger turbulence kinetic energy downstream of the second plate for the single body shedding mode was attributed to the roll-up of separated shear layers from the edges of the first plate downstream of the second plate.

Furthermore, the Strouhal number of the tandem normal flat plates have been found to vary significantly based on the shedding mode and the gap between the two plates (Auteri *et al.*, 2009). As shown in Figure 2.16, which presents the Strouhal number for two tandem flat plates normal to a uniform flow, when the gap between the two plates is smaller than the plate chord length, D/c <1, the Strouhal number of the tandem plate is similar to that of an isolated flat plate. A sharp rise in the Strouhal number is indicated as the gap between the two plates increases to slightly more than a plate's chord length followed by a rapid decline as the gap further increases. The jump in the Strouhal number occurs at a threshold distance above which the dual body shedding mode exists. A similar trend for the Strouhal number of two tandem inclined plates at angles of attack between 45° and 75° was also found by Teimourian *et al.* (2017).

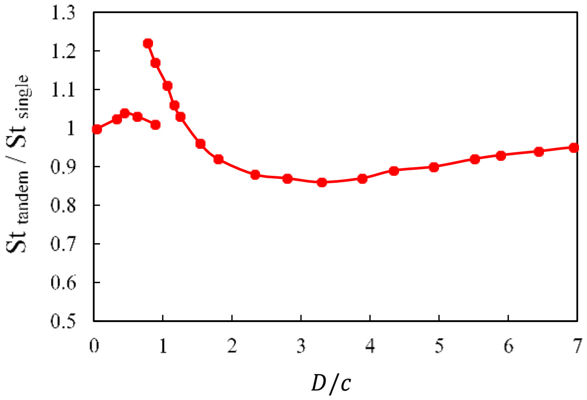

Figure 2.16. Strouhal number for two tandem plates normalised against that for a single plate versus gap ratio, D/c, between two tandem plates normal to uniform flow for Re =22400 to Re =78500. Reproduced by permission from Springer: Journal of Visualization, Auteri *et al.* (2009).

The wake interaction of multiple bluff bodies is not limited to tandem arrangements, and the vortices shed by bodies positioned side by side in a row interact with each other as well. Different flow patterns were found by Hayashi *et al.* (1986) between a row of three flat plates normal to a uniform flow, Re=1.3×10^4–1.9×10^4. Figure 2.17(a) schematically illustrates the gap flow patterns around three plates. At very small gap ratios between the plates, D/c <1, Pattern (I) in Figure 2.17(a), the separated shear layers from the edges of the outer plates joined together to form a large vortex street behind the plates. The wake in Pattern (I) was similar to the wake of a single flat plate with weak gap flows between the plates. When the gaps enlarged, D/c <2, Pattern (II), vortex shedding occurred distinctively for the two outer plates. The gap flows in Pattern (I) were deflected to the same side, while in Pattern (II), the gap flows were deflected in opposite directions. The biasing of the gap flows was attributed to the interaction of vortices shed by the plates. When the gap was sufficiently large, each plate shed vortices, and biasing occurred due to the engulfment of the gap flow by the stronger vortices. According to Hayashi *et al.* (1986), at very small ratios, the vortex shedding of each plate was weak, and biasing seemed to be due to the interaction of the jet flow between the plates and the flow outside them. At larger gap ratios, D/c >2, Pattern (III) in Figure 2.17(a), there was no more interaction between the wake of the plates and each plate formed its own vortex street. No information about the variations of turbulence intensity in the three flow patterns was given. However, the interactions of the wakes of the three plates with one other at different gap ratios is expected to affect turbulence in the wake of the plates.

The mean drag force coefficient as a function of the gap ratio for Pattern (II) is demonstrated in Figure 2.17(b) which indicates that the drag force coefficients on the plates on the biased sides were higher than that on the middle plate, due to the stronger vortices resulting in lower base pressure on this side. It was also found that the Strouhal number was higher for Pattern (II). As the gap ratio enlarged, the vortex of the middle plate strengthened and the Strouhal number was approximately double its value for Pattern (I).

Figure 2.17. (a) Directions of gap flow between a row of three flat plates normal to a uniform flow with varying gap ratios, D/c, (b) the variations of mean drag force coefficient, C_D, with the gap ratio, D/c, between three normal flat plates for Pattern (II). Reproduced from Hayashi *et al.* (1986).

The review of the flow properties around tandem flat plates and side-by-side flat plates shows that mean and turbulence properties in the flow around multiple heliostats can be different from those for a single heliostat based on the gap between the heliostats. Consequently, the wind loads on multiple heliostats will vary. A few wind tunnel experiments in the literature have investigated the wind loads on heliostats in an array. Emes *et al.* (2018) investigated the variations of the stow wind loads on two tandem heliostats and reported that the peak lift force coefficient on the second tandem stowed heliostat was up to 7% larger than that for the single stowed heliostat for D/c >1.5. Furthermore, Peterka *et al.* (1987) measured the wind loads on an operating heliostat in the fourth row of a four-row arrangement for two different gap ratios between consecutive rows, D/c =3.07 and D/c =6.4, representing high- and low-density zones of a heliostat field. It was found that for a heliostat in the fourth row at D/c =3.07, the mean drag force coefficient was 12% lower than that for a heliostat in the front row. For a higher field density, the reduction in the mean drag coefficient increased reaching 32% of that in the first row. In contrast, the peak drag force coefficient on the heliostat in the fourth row was found to be 40% larger than that of the heliostat in the front row when the gap ratio was 6.4. The increase in the peak drag coefficient may be correlated with an increase in turbulence intensity of the flow. Therefore, it suggests the effect of turbulence in the wake of upstream heliostats on the unsteady drag force and highlights the importance of characterisation of turbulence in the wake of heliostats and its effect on the wind loads in a field.

2.5 Flow control for reduction of wind loads

As discussed in the review of the literature presented in the previous sections, wind loads on heliostats are correlated with the properties of the approaching flow. Therefore, in order to reduce the wind loads, flow control methods can be utilised to manipulate the flow properties, including mean velocity, turbulence intensity and integral length scales. A potential candidate for this purpose is application of mesh screens in form of a perimeter fence. Fences are typically used around a field of heliostats and solar panels for protective roles including dust control, prevention of unauthorised access to the field, and protection of animals and trespassers from an exposed danger. In addition to their main purpose, fences can affect the flow properties. Fences decrease the wind speed and can therefore reduce the mean wind loads. They can also alter the turbulence properties of the flow by disrupting the energy cascade in the atmospheric surface layer. An example of the application of screens for reduction of turbulence is in wind tunnels where they are commonly used along with honeycombs for constraining the lateral and vertical velocity components and enhancing turbulence dissipation rate (Groth and Johansson, 1988). As the unsteady and peak wind load coefficients on heliostats are strongly dependent on the turbulence properties, there is a potential to reduce these loads if the fences can effectively reduce turbulence intensity and integral length scales. Therefore, it may be possible to utilise the fences around a heliostat field with a modification in their design as a passive flow control method to reduce the wind loads on heliostats. However, the effectiveness of fences in reduction of turbulence and ultimately reduction of unsteady wind loads is not well known. Hence, in the following section, a description of mean flow and turbulence properties behind fences and screens is provided, which is followed by a review of the application of fences for reduction of wind loads on heliostats in the literature.

2.5.1 Flow control by a porous fence

Flow behind a porous fence is influenced by two effects: blockage and flow separation at the top edge of the fence, and the jets formed as flow passes through the mesh openings, known as the bleed flow. The interaction of the displaced flow and the bleed flow, which is determined by the level of porosity of a fence, significantly affects the flow properties downstream of a fence. Hence, porosity of a fence, ϕ, defined as the ratio of the open area to the total area of the fence, is an important parameter affecting flow structure around a fence. An example of mean flow streamlines around a fence with a porosity of ϕ =0.1, are shown in Figure 2.18, which displays the recirculation zone formed in the wake of the fence and the bleed flow zone in the immediate downstream of the fence. With increase of porosity of the fence, the blockage effect and the displacement of approaching flow decrease, and the bleed flow increases. Hence, the flow properties downstream of the fence vary significantly. Other parameters which affect the flow downstream of a porous fence are the height of the fence, H, the geometry of mesh openings, and the inflow properties, including mean velocity and turbulence intensity. The effects of these parameters on mean velocity and turbulence properties of the flow are discussed in the following.

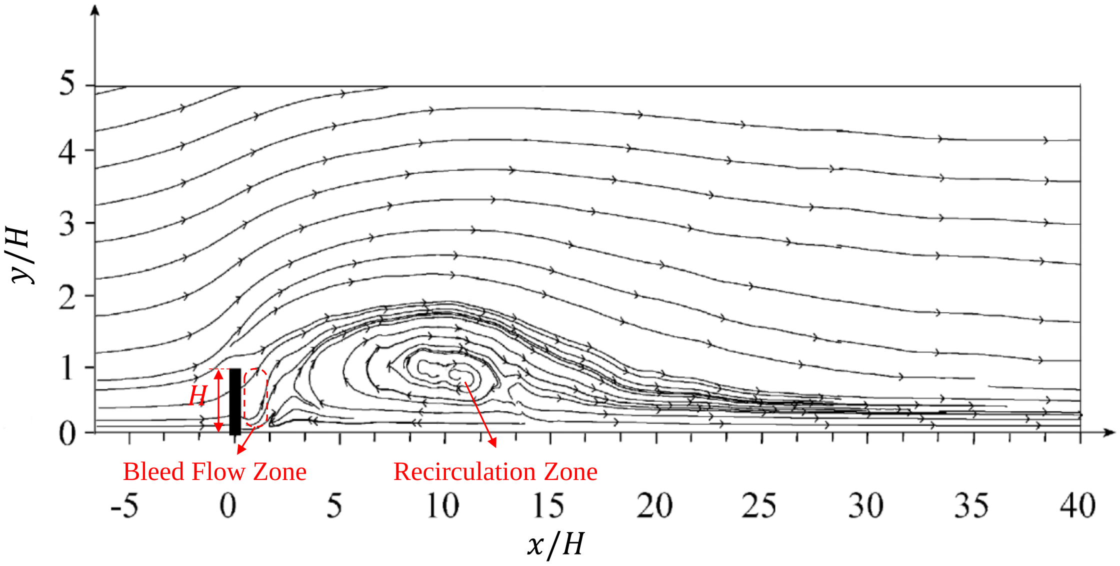

Figure 2.18. Streamlines around a porous fence, with a porosity of ϕ =0.1, at a freestream velocity U_∞ =10 m/s and Re =6.9×10^4, showing the bleed flow and recirculation zones. Reproduced by permission from Elsevier: Agricultural and Forest Meteorology, Dong *et al.* (2007).

The flow patterns shown in Figure 2.18 strongly depend on the porosity of the fence. Fences with higher porosities create less blockage and therefore less pressure drop in the flow. Furthermore, the bleed flow is stronger for higher porosities. Lee and Kim (1999) used PIV to study the flow downstream of perforated plates with porosities of ϕ =0, 0.2, 0.4 and 0.65 in a uniform flow in a water channel. They found that for porosities of 0.4 and 0.65, due to the strong bleed flow, no recirculation zone was formed. Furthermore, a comparison of mean velocity distributions downstream of the fence of ϕ =0.2 with the solid fence, ϕ =0 showed that the recirculation region was shifted downstream and the magnitude of the maximum reverse velocity was 28% lower. A similar result was found by Dong *et al.* (2010) in a wind tunnel experiment on fences with porosities between ϕ =0 and ϕ =0.8. The vertical profiles of mean streamwise velocity at various downstream locations for the different fences are presented in Figure 2.19. As shown in Figure 2.19, no reverse flow was observed for fences with porosities larger than 0.2. Porosity was found to affect both velocity deficit and recovery length. The reduction in mean velocity downstream of the fences increased when the porosity of the fence decreased. Furthermore, with decrease of porosity, the recovery length over which the mean velocity returned to its inflow level increased.

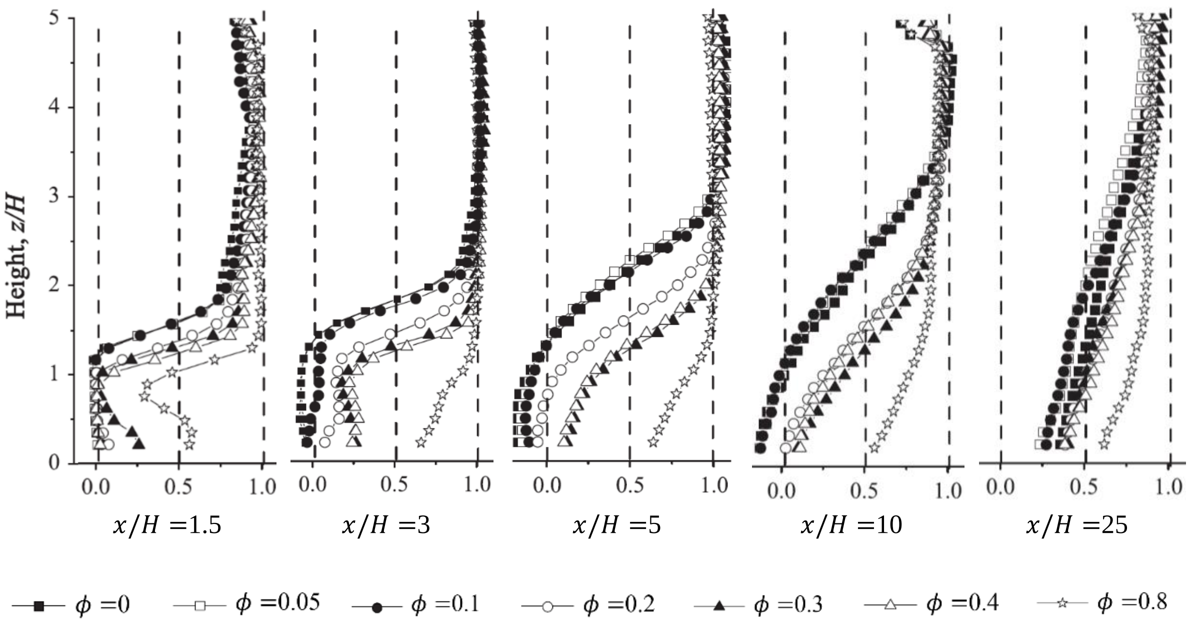

Figure 2.19. Vertical profiles of mean streamwise velocity downstream of vertical slat fences of different porosities, ϕ. The horizontal axis shows mean streamwise velocity normalised with freestream velocity, U/U_∞, where U_∞ =10 m/s. The vertical axis shows height normalised with the fence height, H. Reprinted by permission from Elsevier: Journal of Arid Environments, Dong *et al.* (2010).

Another parameter of interest for design of fences is turbulence intensity in the flow downstream of fences. While a less porous fence creates a larger mean velocity deficit, turbulence intensity in its wake is also larger (Lee and Kim, 1999), which could therefore make it less effective in reduction of wind loads. Figure 2.20 shows the streamwise turbulence intensity downstream of a solid, ϕ =0, and a porous fence, ϕ =0.5, in an atmospheric boundary layer flow in a wind tunnel (Raine and Stevenson, 1977). As shown in Figure 2.20, there were two regions of low and high streamwise turbulence intensity downstream of both solid and porous fences. In the immediate downstream of the fences, streamwise turbulence intensity was lower than the inflow level, and larger turbulence intensities existed at the top edge of the fence at the location of the separated shear layers.

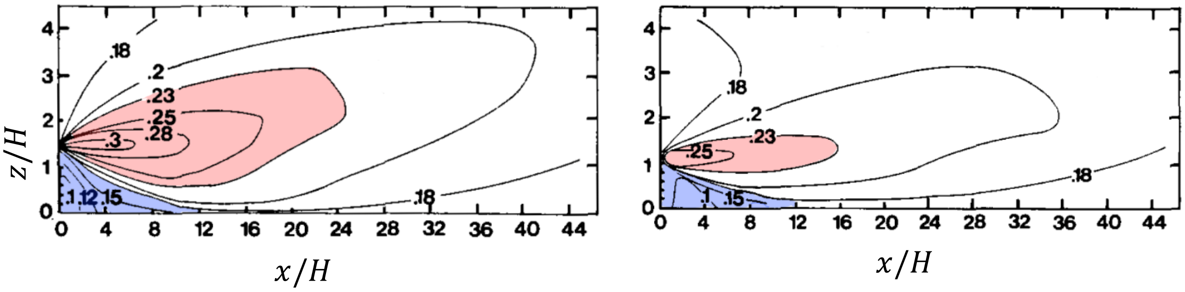

(a) (b)

Figure 2.20. Distribution of turbulence intensity, $I_u = \frac{\sigma_u}{U_H}$, downstream of a fence: (a) ϕ =0, (b) ϕ =0.5. U_H is the mean streamwise velocity at the fence height, and x/H is the downstream distance normalised with fence height. The red and blue shaded regions show regions where turbulence intensity is higher and lower than the inflow level of 0.2. Reproduced by permission from Elsevier: Journal of Wind Engineering and Industrial Aerodynamics, Raine and Stevenson (1977).

Dong *et al.* (2010) investigated the effect of porosity on turbulence intensity downstream of fences placed in a wind tunnel boundary layer with an inlet streamwise turbulence intensity, I_u, of approximately 10% at the fence height. Vertical profiles of streamwise and vertical turbulence intensities at various downstream distances are shown in Figure 2.21. According to Figure 2.21(a), for fences with ϕ ≤0.2, the maximum turbulence intensity was significantly larger than that for ϕ >0.2. At x/H <10, two local maximum points of I_u existed for ϕ ≤0.2; one in the near wall region near the ground and another one at the height of the top edge of the fence. For larger porosities, ϕ =0.3 and ϕ =0.4, the maximum point at the fence height was only observed at x/H =1.5, showing that separation of flow at the top edge was weaker. Furthermore, the profiles of vertical turbulence intensity, Figure 2.21(b), show that there was only one local maximum located at the fence height, which is corelated with the separated flow at top edge. The values of vertical turbulence intensity were generally less than streamwise turbulence intensity for all porosities at downstream distances between 1.5H and 25H. Concentration of maximum turbulence intensities at the height of the fence implies that the fence height should be larger than the heliostat panel height to avoid subjecting heliostats to an increased turbulence intensity.

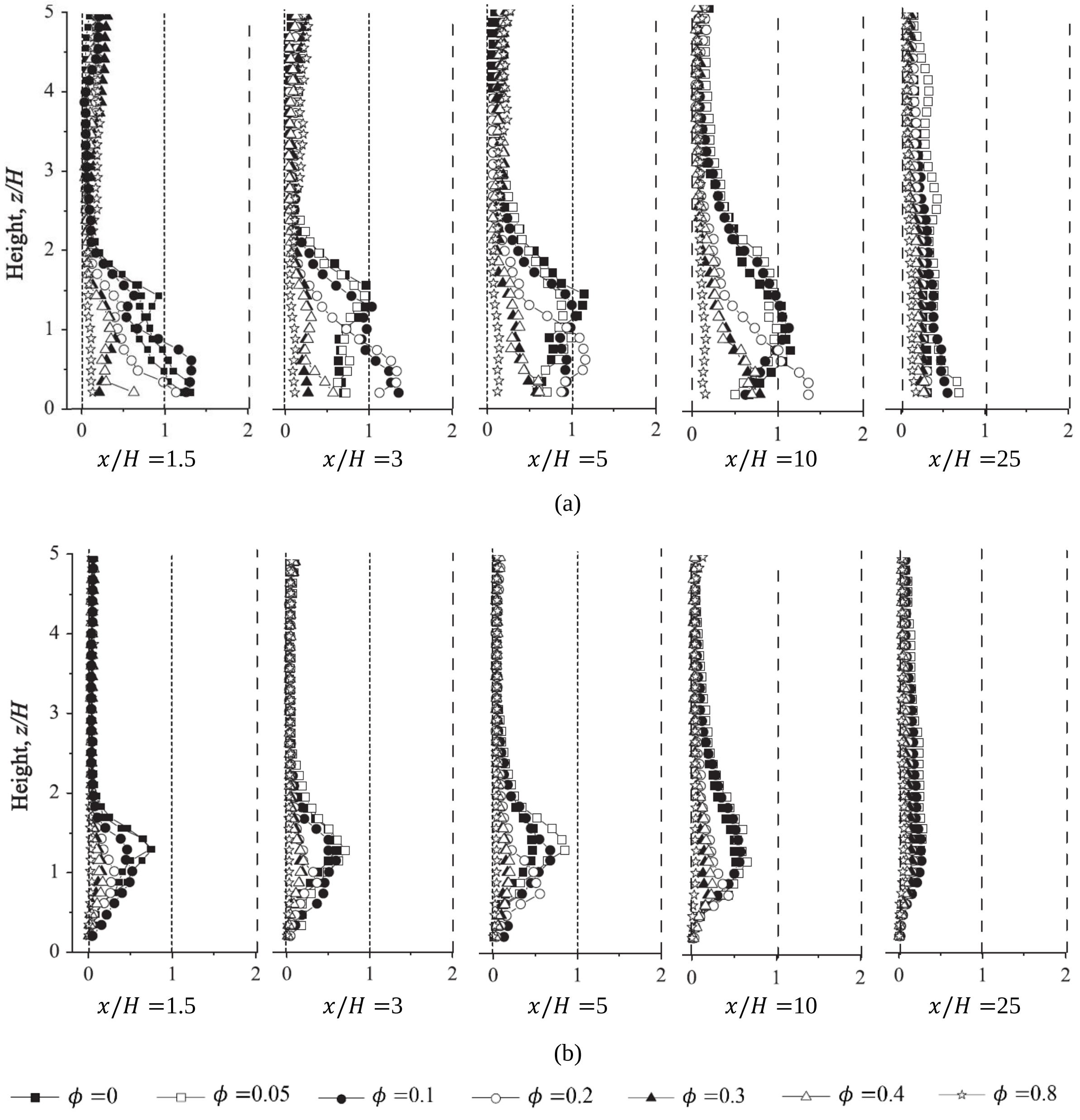

(a)

(b)

Figure 2.21. Vertical profiles of (a) streamwise, and (b) vertical turbulence intensities downstream vertical slat fences of different porosities, ϕ. The horizontal axis shows streamwise turbulence intensity, $I_u = \frac{\sigma_u}{U_\infty}$, on top and vertical turbulence intensity, $I_w = \frac{\sigma_w}{U_\infty}$, in bottom. The vertical axis shows height normalised with the fence height, H. Reprinted by permission from Elsevier: Journal of Arid Environments, Dong *et al.* (2010).

The findings of the above-mentioned studies show that the distance downstream of a fence over which mean velocity and turbulence intensity are reduced mainly depends on the fence height and porosity. Fences with different geometries have been investigated in the literature including horizontal and vertical slats, mesh grids and perforated metals, which are shown in Figure 2.22. The geometry of mesh openings however has been found to affect the flow properties only over a short distance downstream of a fence. Perera (1981) compared the mean streamwise velocity downstream of fences of different opening geometries with an identical porosity, ϕ =0.1. Three fence geometries including a perforated plate with circular openings, vertical and horizontal slat fences were studied. Differences in the mean velocity values were only found at x/H <2. Furthermore, Kim and Lee (2001) investigated the effect of opening geometry of fences with identical porosity and found differences in the mean velocity and turbulence intensity variations up to x/H =4. They studied flow downstream of three perforated metal fences with circular openings of diameters d =1.4 mm, 2.1 mm, and 2.8 mm and a porosity of ϕ =0.38, using PIV in a uniform flow in a water channel. It was found that the fence with the smallest opening size, d =1.4 mm, created more blockage in the flow and thus had the largest mean velocity reduction. The fence with d =2.8 mm had larger mean velocity reduction compared to d =2.1 mm. Furthermore, the largest values of turbulence kinetic energy in the wake up to x/H =4, existed for d =2.8 mm, followed by d =1.4 mm and d =2.4 mm. Larger turbulence kinetic energy for the fence with d =2.8 mm was attributed to the effect of jet coalescence and bleed flow mixing. Jet coalescence has been observed in flow through porous grids with porosities less than 0.5, which occurs when the jets formed through individual openings merge together. The jet coalescence creates instabilities in the mean flow giving rise to turbulence production (Loehrke and Nagib, 1972).

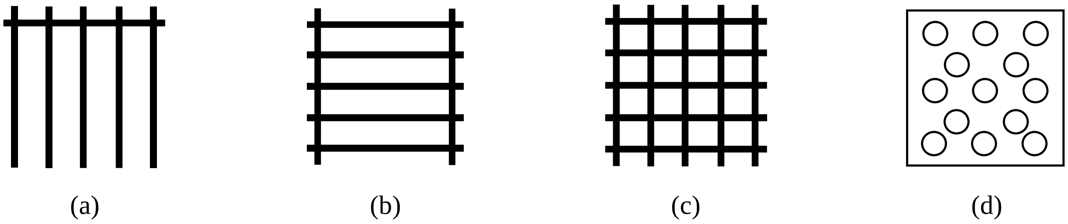
(a) (b) (c) (d)

Figure 2.22. Different fence geometries: (a) vertical slats, (b) horizontal slats, (c) mesh grid, (d) perforated plate.

In order to reduce the unsteady wind loads on heliostats, in addition to reducing turbulence intensity, reducing the integral length scale of turbulence and suppression of prominent eddies within the atmospheric surface layer is necessary. As this is not a general requirement for design of windbreaks and fences in other applications, variations of the length scales of turbulence in the flow downstream of a porous fence have not been extensively studied in the literature. One of the few studies in which these variations were reported is the wind tunnel experiment by Raine and Stevenson (1977). Power spectral density of the streamwise velocity fluctuations downstream of a fence with ϕ =0.2 and ϕ =0.5 in an atmospheric boundary layer flow are shown in Figure 2.23. A shift of the turbulence spectrum to higher frequencies compared to the inflow spectrum was found for both porosities at x/H =2. Further downstream at x/H =15, the turbulence spectrum was similar to the inflow, although not fully recovered. Similarly, from analysis of power spectral density of pressure measured downstream a full-scale fence, 50 m long and 2 m high and ϕ =0.5, Richardson (1989) found that low frequencies were significantly attenuated downstream of the fence, at x/H =5 and x/H =10.

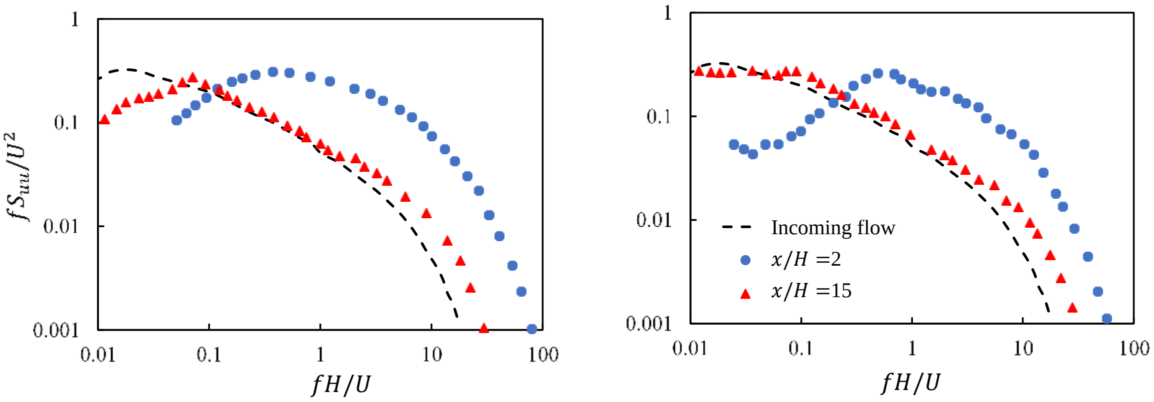

(a) (b)

Figure 2.23. Normalised spectra of streamwise velocity fluctuations downstream horizontal slat fences of different porosities: (a) ϕ =0.2, and (b) ϕ =0.5. The dashed line shows the inflow spectrum for a reference upstream point. x/H is the downstream distance normalised with fence height. Reproduced by permission from Elsevier: Journal of Wind Engineering and Industrial Aerodynamics, Raine and Stevenson (1977).

The inflow properties can affect the turbulence properties downstream of a porous fence. However, as the mean wind speed has a less significant effect on the velocity deficit downstream of a porous fence than the fence porosity (Li and Sherman, 2015), and since the main purpose for general applications of fences is typically reduction of mean wind speed, the effects of inflow conditions on the turbulence properties downstream of a porous fence have not been well established in the literature. Screens are commonly used in wind tunnels in order to reduce turbulence in the flow. Therefore, the effect of inflow conditions on the variations of turbulence downstream of screens in wind tunnels has been the subject of several studies. The effectiveness of a mesh in turbulence manipulation has been found to depend on the inflow velocity and turbulence. Two different flow regimes have been found based on $Re_d = Ud/\nu$, which is the Reynolds number based on the wire diameter of a mesh screen, d: a subcritical regime for Re_d <40, and a supercritical regime for Re_d >40 (Loehrke and Nagib, 1972). Figure 2.24 shows turbulence intensity downstream of a screen covering the cross-section of the test section in a wind tunnel (Tan-Atichat *et al.*, 1982) for different inflow mean velocities and different values of Re_d. While for Re_d <40, the downstream turbulence intensity remained below the inflow level, in the supercritical regime, turbulence intensity increased immediately downstream of the screen and then decreased further downstream. The increase in turbulence intensity in the supercritical regime is due to generation of new turbulence by separated shear layers and vortex shedding, which were absent in the subcritical regime. According to Tan-Atichat *et al.* (1982), the initial decay rate of turbulence in the subcritical regime varies with the freestream velocity, thus making this regime unfavourable as the turbulence reduction performance of the screen is dependent on freestream velocity. In supercritical regime, however, the turbulence decay rate, although lower than subcritical regime, is independent of freestream velocity. Fences that are used around a heliostat field typically operate in the supercritical regime due to the large wind speeds and Reynolds number.

Figure 2.24. Streamwise turbulence intensity, $I_u = \frac{\sigma_u}{U_\infty}$, downstream of a screen in a grid-generated turbulent inflow for different freestream velocities. The horizontal dashed line shows the inflow turbulence intensity. Reproduced from Tan-Atichat *et al.* (1982).

Groth and Johansson (1988) studied application of cross-sectional screens of different mesh sizes with porosities between ϕ =0.58 and ϕ =0.71 operating at both subcritical and supercritical regimes for reduction of an isotropic grid-generated turbulence, I_u =5.5% at the screen position, in a wind tunnel. They found that in the region immediately downstream of a screen in supercritical regime, the flow was dominated by mesh-generated turbulence with the peak frequency of the turbulence spectrum at length scales in the order of a few mesh widths. Throughout the first 15–25 mesh widths, which was called the initial decay region, the intensity of turbulence decreased quickly to less than the inflow level, which was accompanied with prominence of the mesh-generated turbulence at the peak of the spectrum and suppression of larger inflow length scales. Analysis of the turbulence spectrum in the subcritical regime showed a strong suppression of turbulence energy in all frequencies. Furthermore, in both regimes, anisotropy of turbulence was evident downstream of the fence, particularly in the initial decay region, which was attributed to stretching of turbulence structures in the streamwise direction as the flow passed through the screen.

Although in the supercritical regime, the mesh itself creates shear layer instabilities and turbulence, if composed of high frequencies, the generated turbulence dissipates rapidly (Loehrke and Nagib, 1972). Thus, the intensity and scale of the generated turbulence by the mesh affects its overall turbulence reduction performance. The mesh is more effective if its generated turbulence is of smaller scales than the inflow turbulence, which is desired to be reduced, but it should not be of significantly smaller scales so that it can enhance energy transfer from large scales to the smaller ones (Tan-Atichat *et al.*, 1982). Hence, the performance of the mesh depends on the structure of both the inflow and the screen-generated turbulence. Tan-Atichat *et al.* (1982) investigated the interaction between the two parameters by studying the flow downstream screens and perforated plates in different freestream conditions. They found that turbulence decay rate downstream of the screen was significantly dependent on the scale and intensity of freestream turbulence. When the freestream turbulence was of low turbulence intensity and contained no large scales compared to the mesh size, turbulence decay rate was higher in comparison with the inflow cases with large turbulence scales. A relationship between the two parameters which can be used to determine the critical threshold was however not established.

The review of the literature on flow downstream of mesh screens used in wind tunnels shows that turbulence properties downstream of screens depend on the inflow turbulence. This implies that a similar behaviour exists for flow downstream of porous fences, which has not been investigated in the literature. Understanding the effect of inflow conditions on turbulence intensity and length scales in the flow downstream of a porous fence and determination of the effect of fence geometric parameters on these variations is therefore a gap of knowledge in the literature. This knowledge provides a foundation for design of fences for the purpose of reducing the unsteady and peak wind loads on heliostats.

2.5.2 Applications of fences for reducing the wind loads on heliostats

Wind tunnel experiments have been conducted in the literature to investigate the effect of the fences on the wind loads on heliostats. Peterka *et al.* (1986) conducted a series of wind tunnel experiments to measure the wind loads on a heliostat placed in an array with perimeter and in-field fences. The configuration of the heliostat array was chosen based on different regions of a field with different densities. Fences with porosities of 0.4, 0.5 and 0.6 and two heights, equal to 0.9 and 1.35 times the heliostat hinge height, were investigated. They found that with the addition of the fence, the mean drag force coefficient on a heliostat at α =90° and a wind direction of 250° in the third row of an array was reduced from approximately 1 to 0.45. The results were presented as a function of a factor named as generalised blockage area (GBA), which was defined as the ratio of the area of the upstream blockage projected to the plane normal to the wind direction, including external and internal fences and upstream heliostats, over the field ground area, Figure 2.25(c). Peterka *et al.* (1989) reports the ratio of the peak drag and lift force coefficients in a field as a function of GBA as shown in Figure 2.25(a–b). The results show cases where the peak coefficients are larger than a single heliostat, shaded by red in Figure 2.25(a–b). The reason for increase of wind loads was not explained by Peterka *et al.* (1986). Furthermore, the elevation angles and heliostat configurations for the presented results were not provided, and it is not clear for which conditions the wind loads were larger than a single heliostat. Moreover, the results were only presented as a function of GBA which included the effects of both fence and blockage by upstream heliostats, and the influence of fence on the wind loads was not distinguished. Hence, a clear conclusion about the effectiveness of the fences in wind load reduction cannot be achieved based on the results.

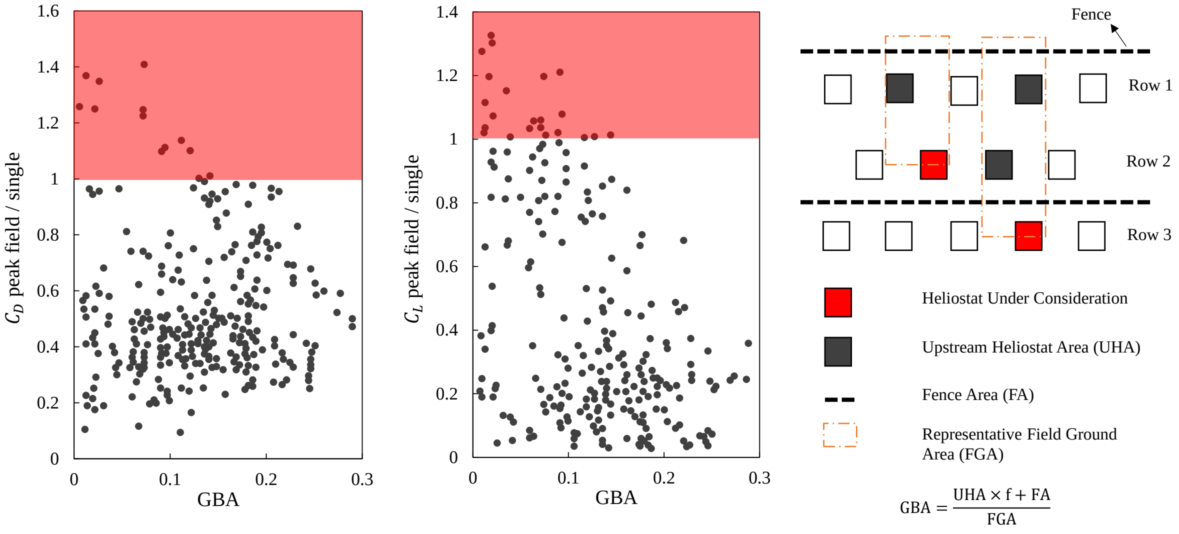

(a) (b) (c)

Figure 2.25. (a) Peak drag, C_D, and (b) peak lift, C_L, force coefficients in an array with perimeter and in-field fences normalised with the peak force coefficients on a single heliostat as a function of generalised blockage area, GBA. The red shaded regions show cases where the peak wind load coefficients are larger compared to a single heliostat. (c) A schematic of the heliostat array demonstrating the calculation of GBA. Reproduced by permission from ASME: Solar Energy Engineering, from Peterka *et al.* (1989).

In a similar experiment, Pfahl (2018) measured the wind loads on a heliostat in the fourth row of an array in presence of a fence upstream of the first row. The fence had a porosity of 40% and height equal to 1.25 times the heliostat hinge height. Different cases with varied distances between the heliostat rows and between the fence and the front row were investigated, through which GBA varied between 0.053 and 0.46. Their results in general showed that the maximum wind load coefficients at operating elevation angles were less than a single heliostat for the investigated range of GBA. Furthermore, it was found that the peak lift force coefficient on a stowed heliostat was up to 25% larger than a single heliostat for GBA values less than 0.1. The increase in the stow lift force coefficient was suggested to be related to an increase in vertical velocity component downstream of the fence. No velocity measurements were however provided. According to Pfahl (2018), application of fences therefore may not be beneficial due to the increase of the lift force at stow position. As the results were presented as a function of GBA, the effect of fence was not differentiated from the effect of blockage by upstream heliostats. Pfahl (2018) mentions that the uncertainty in the reported results was large due to the limited measurement cases. Furthermore, the inflow turbulence properties were not reported.

The review of the literature shows that the studies on application of fences in a heliostat field have been limited. Scarce information is provided about the test conditions and the effect of fence on the wind loads has not been well established. The effectiveness of a fence barrier on reduction of the unsteady and peak wind loads on a heliostat at operating and stow conditions therefore requires further investigations in future to be well understood. Furthermore, understanding the effects of geometric parameters of a porous fence and the effect of inflow turbulence on its performance is necessary for the development of a fence design for the purpose of wind load reduction.

2.6 Concluding remarks and perspectives

As discussed in the Section 2.2, an important aspect missing from the literature is determination of the degree of similarity of the simulated turbulence in a wind tunnel to the atmospheric boundary layer. Lack of similarity of the scaling ratio of the heliostat structure and the boundary layer accompanied with the existing discrepancies in the measurements of heliostat wind loads raises a concern on accuracy of the wind load coefficients reported in the literature to date. Hence, one of the important gaps in the knowledge of heliostat wind loads is determination of reliability of wind tunnel measurements. To achieve similarity of the unsteady wind loads in a wind tunnel model and the full-scale structure, the effect of mismatch of geometric scaling ratios and turbulence spectrum must be determined. This issue is addressed in Chapter 3 which aims to establish the necessary similarity criteria for modelling turbulence and unsteady wind loads in a wind tunnel.

The literature review presented in this chapter shows that turbulence significantly affects the unsteady wind loads on operating and stowed heliostats. This effect while partly described in the literature of heliostat wind loads, has not been well established. The existing literature on heliostat wind loads mainly considered streamwise turbulence intensity as the major effective parameter on the unsteady wind loads. A systematic approach which identifies key turbulence parameters for unsteady wind loads is lacking is the literature. The mutual effects of the intensity and integral length scale of the turbulence in the atmospheric boundary layer on the wind loads and the correlation between the key parameters is yet to be determined. Furthermore, the turbulence parameters, streamwise or vertical components, which have a more prominent effect on the stow and operating wind loads must be established. Hence, Chapter 4 presents a systematic study aimed to develop a correlation between the turbulence characteristics of the flow and the heliostat wind loads.

A significant lack of knowledge about the flow properties and wind loads in a heliostat field is indicated from the literature reviewed in Section 2.4. While the wind tunnel experiments have more commonly investigated wind loads on a single heliostat, how the unsteady wind loads in different regions of a field differ from those on a single heliostat remains unknown. As the wind loads are directly correlated with approaching flow properties, understanding the mean and turbulence characteristics of the flow in a heliostat field is a primary step towards understanding the variations of wind loads in a heliostat field. This knowledge is lacking in the literature. As a first step for development of this knowledge, flow and turbulence properties in the wake of a heliostat must be well understood. However, a significant gap exists regarding the wake of a heliostat. Variations of turbulence intensity and integral length scale at different downstream positions in the wake of an operating heliostat from those in the atmospheric boundary layer are not well known. Hence, the research presented in Chapter 5 investigates flow properties in the wake of a single heliostat. Based on the developed knowledge of the heliostat wake, an estimation of the variations of turbulence properties in a heliostat field is provided. Finally, the effect of the wake on the wind loads on downstream heliostats is studied through investigation of wind loads on tandem heliostats.

Extensive research gaps exist regarding reduction of heliostat wind loads, which can lead to reduction of the cost of heliostats. As highlighted in the literature review, reduction of turbulence intensity and integral length scale is necessary for reducing unsteady wind loads. While fences are commonly used for protective roles, their effectiveness in manipulation of the anisotropic atmospheric turbulence has not been investigated. However, application of mesh screens for reducing turbulence in wind tunnels shows a potential for reducing turbulence in a heliostat field by mesh fences. Whether it is worthwhile to employ mesh fences for reduction of turbulence intensity and integral length scale and ultimately unsteady wind loads needs to be determined. Therefore, in Chapter 6, manipulation of atmospheric turbulence by application of mesh fences is investigated in order to provide an understanding of the effectiveness of this method for reduction of heliostat wind loads. Furthermore, the effects of mesh geometric properties and the incoming turbulence properties on the effectiveness of a fence for reducing turbulence are studied.

2.7 References

Adrian, R. J. 2007. Hairpin vortex organization in wall turbulence, *Physics of Fluids,* 19: 041301.

Adrian, R. J., Meinhart, C. D., and Tomkins, C. D. 2000. Vortex organization in the outer region of the turbulent boundary layer, *Journal of Fluid Mechanics*, 422: 1-54.

Amoura, Z., Roig, V., Risso, F., and Billet, A.-M. 2010. Attenuation of the wake of a sphere in an intense incident turbulence with large length scales, *Physics of Fluids*, 22: 055105.

Auteri, F., Belan, M., Cassinelli, C., and Gibertini, G. 2009. Interacting wakes of two normal flat plates an investigation based on phase averaging of LDA signals, *Journal of Visualization*, 12: 307-21.

Auteri, F., Belan, M., Gibertini, G., and Grassi, D. 2008. Normal flat plates in tandem: An experimental investigation, *Journal of Wind Engineering and Industrial Aerodynamics*, 96: 872-79.

Bearman, P. W. 1971. An investigation of the forces on flat plates normal to a turbulent flow, *Journal of Fluid Mechanics*, 46: 177-98.

Bearman, P. W., and Zdravkovich, M. M. 1978. Flow around a circular cylinder near a plane boundary, *Journal of Fluid Mechanics*, 89: 33-47.

Bosch, G., Kappler, M., and Rodi, W. 1996. Experiments on the flow past a square cylinder placed near a wall, *Experimental Thermal and Fluid Science*, 13: 292-305.

Castro, I. P., and Robins, A. G. 1977. The flow around a surface-mounted cube in uniform and turbulent streams, *Journal of Fluid Mechanics*, 79: 307-35.

Cermak, J. E. 1984. Wind-simulation criteria for wind-effect tests, *Journal of Structural Engineering*, 110: 328-39.

Chen, J. M., and Chiou, C. C. 1998. Experimental investigation of a parallel vortex-plate interaction, *Journal of Fluids and Structures*, 12: 295-314.

Cook, N. J. 1978. Determination of the model scale factor in wind-tunnel simulations of the adiabatic atmospheric boundary layer, *Journal of Wind Engineering and Industrial Aerodynamics*, 2: 311-21.

Cook, N. J. 1985. *The designer's guide to wind loading of building structures*, Building Research Establishment, Watford.

Cook, N. J. 1997. The Deaves and Harris ABL model applied to heterogeneous terrain, *Journal of Wind Engineering and Industrial Aerodynamics*, 66: 197-214.

Corino, E. R., and Brodkey, R. S. 2006. A visual investigation of the wall region in turbulent flow, *Journal of Fluid Mechanics*, 37: 1-30.

Counihan, J. 1969. An improved method of simulating an atmospheric boundary layer in a wind tunnel, *Atmospheric Environment (1967)*, 3: 197-214.

Davenport, A. G. 1960. Rationale for determining design wind velocities, *ASCE Journal of the Structural Division*, 86: 39-68.

De Bortoli, M. E., Natalini, B., Paluch, M. J., and Natalini, M. B. 2002. Part-depth wind tunnel simulations of the atmospheric boundary layer, *Journal of Wind Engineering and Industrial Aerodynamics*, 90: 281-91.

De Paepe, W., Pindado, S., Bram, S., and Contino, F. 2016. Simplified elements for wind-tunnel measurements with type-iii-terrain atmospheric boundary layer, *Measurement,* 91: 590-600.

Dong, Z., Luo, W., Qian, G., Lu, P., and Wang, H. 2010. A wind tunnel simulation of the turbulence fields behind upright porous wind fences, *Journal of Arid Environments*, 74: 193-207.

Dong, Z., Luo, W., Qian, G., and Wang, H. 2007. A wind tunnel simulation of the mean velocity fields behind upright porous fences, *Agricultural and Forest Meteorology*, 146: 82-93.

Drobinski, P., Carlotti, P., Newsom, R. K., Banta, R. M., Foster, R. C., and Redelsperger, J.-L. 2004. The structure of the near-neutral atmospheric surface layer, *Journal of the Atmospheric Sciences*, 61: 699-714.

Drobinski, P., Carlotti, P., Redelsperger, J.-L., Masson, V., Banta, R. M., and Newsom, R. K. 2007. Numerical and experimental investigation of the neutral atmospheric surface layer, *Journal of the Atmospheric Sciences*, 64: 137-56.

Drobinski, P., and Foster, R. C. 2003. On the origin of near-surface streaks in the neutrally-stratified planetary boundary layer, *Boundary-Layer Meteorology*, 108: 247-56.

Dyrbye, C., and Hansen, S. O. 1996. *Wind loads on structures*, John Wiley & Sons.

Emes, M. J., Arjomandi, M., Ghanadi, F., and Kelso, R. M. 2017. Effect of turbulence characteristics in the atmospheric surface layer on the peak wind loads on heliostats in stow position, *Solar Energy*, 157: 284-97.

Emes, M. J., Ghanadi, F., Arjomandi, M., and Kelso, R. M. 2018. Investigation of peak wind loads on tandem heliostats in stow position, *Renewable Energy*, 121: 548-58.

ESDU85020. 2010. Characteristics of atmospheric turbulence near the ground - part ii: Single point data for strong winds (neutral atmosphere), *Engineering Sciences Data Unit*.

Fage, A., and Johansen, F. C. 1927. On the flow of air behind an inclined flat plate of infinite span, *Proceedings of the Royal Society of London. Series A, Containing Papers of a Mathematical and Physical Character*, 116: 170-97.

Groth, J., and Johansson, A. V. 1988. Turbulence reduction by screens, *Journal of Fluid Mechanics*, 197: 139-55.

Hayashi, M., Sakurai, A., and Ohya, Y. 1986. Wake interference of a row of normal flat plates arranged side by side in a uniform flow, *Journal of Fluid Mechanics*, 164: 1-25.

Hearst, R. J., Gomit, G., and Ganapathisubramani, B. 2016. Effect of turbulence on the wake of a wall-mounted cube, *Journal of Fluid Mechanics*, 804: 513-30.

Hemmati, A., Wood, D. H., and Martinuzzi, R. J. 2015. Direct numerical simulation of the wake of a normal thin flat plate: Infinite vs. Finite width. *International Symposium on Turbulence and Shear Flow Phenomena (TSFP-9)*. Melbourne, Australia.

Högström, U., Hunt, J. C. R., and Smedman, A.-S. 2002. Theory and measurements for turbulence spectra and variances in the atmospheric neutral surface layer, *Boundary-Layer Meteorology*, 103: 101-24.

Holmes, J. D. 2007. *Wind loading of structures*, Taylor & Francis.

Hommema, S. E., and Adrian, R. J. 2003. Packet structure of surface eddies in the atmospheric boundary layer, *Boundary-Layer Meteorology*, 106: 147-70.

Hui, T. M. 2011. Design and optimization of heliostatt field using spinning-elevation sun tracking method based on computational analysis, Master of Engineering Thesis, Universiti Tunku Abdul Rahman.

Humphries, W., and Vincent, J. H. 1976. Experiments to investigate transport processes in the near wakes of disks in turbulent air flow, *Journal of Fluid Mechanics*, 75: 737-49.

Hunt, J. C. R., and Carlotti, P. 2001. Statistical structure at the wall of the high reynolds number turbulent boundary layer, *Flow, Turbulence and Combustion*, 66: 453-75.

Hunt, J. C. R., and Morrison, J. F. 2000. Eddy structure in turbulent boundary layers, *European Journal of Mechanics - B/Fluids*, 19: 673-94.

Irwin, H. P. A. H. 1981. The design of spires for wind simulation, *Journal of Wind Engineering and Industrial Aerodynamics*, 7: 361-66.

Iyengar, A. K. S., and Farell, C. 2001. Experimental issues in atmospheric boundary layer simulations: Roughness length and integral length scale determination, *Journal of Wind Engineering and Industrial Aerodynamics*, 89: 1059-80.

Kaimal, J. C., and Finnigan, J. J. 1994. *Atmospheric boundary layer flows: Their structure and measurement,* Oxford University Press.

Kim, H.-B., and Lee, S.-J. 2001. Hole diameter effect on flow characteristics of wake behind porous fences having the same porosity, *Fluid Dynamics Research*, 28: 449-64.

Kiya, M., and Matsumura, M. 1988. Incoherent turbulence structure in the near wake of a normal plate, *Journal of Fluid Mechanics*, 190: 343-56.

Kozmar, H. 2008. Influence of spacing between buildings on wind characteristics above rural and suburban areas, *Wind and Structures*, 11: 413-26.

Kozmar, H. 2011a. Physical modeling of complex airflows developing above rural terrains, *Environmental Fluid Mechanics*, 12: 209-25.

Kozmar, H. 2011b. Truncated vortex generators for part-depth wind-tunnel simulations of the atmospheric boundary layer flow, *Journal of Wind Engineering and Industrial Aerodynamics*, 99: 130-36.

Kozmar, H. 2012. Improved experimental simulation of wind characteristics around tall buildings, *Journal of Aerospace Engineering,* 25: 670-79.

Krampa-Morlu, F. N., and Balachandar, R. 2007. Flow recovery in the wake of a suspended flat plate, *Journal of Hydraulic Research*, 45: 270-78.

Lam, K. M., and Leung, M. Y. H. 2005. Asymmetric vortex shedding flow past an inclined flat plate at high incidence, *European Journal of Mechanics - B/Fluids*, 24: 33-48.

Lee, S.-J., and Kim, H.-B. 1999. Laboratory measurements of velocity and turbulence field behind porous fences, *Journal of Wind Engineering and Industrial Aerodynamics*, 80: 311-26.

Lei, C., Cheng, L., and Kavanagh, K. 1999. Re-examination of the effect of a plane boundary on force and vortex shedding of a circular cylinder, *Journal of Wind Engineering and Industrial Aerodynamics,* 80: 263-86.

Li, B., and Sherman, D. J. 2015. Aerodynamics and morphodynamics of sand fences: A review, *Aeolian Research*, 17: 33-48.

Li, Q. S., Zhi, L., and Hu, F. 2010. Boundary layer wind structure from observations of a 325 m tower, *Journal of Wind Engineering and Industrial Aerodynamics*, 98: 818-32.

Loehrke, R. I., and Nagib, H. M. 1972. Experiments on management of free-stream turbulence, *Technical Report AGARD Report No. 598*.

Lopes, M. F. P., Glória Gomes, M., and Ferreira, J. G. 2008. Simulation of the atmospheric boundary layer for model testing in a short wind tunnel *Experimental Techniques*, 32: 36-43.

Marusic, I., and Hutchins, N. 2008. Study of the log-layer structure in wall turbulence over a very large range of reynolds number, *Flow, Turbulence and Combustion*, 81: 115-30.

Martinuzzi, R. J., Bailey, S. C. C., and Kopp, G. A. 2003. Influence of wall proximity on vortex shedding from a square cylinder, *Experiments in Fluids,* 34: 585-96.

Mendis, P., Ngo, T., Haritos, N., Hira, A., Samali, B. and Cheung, J. 2007. Wind loading on tall buildings, *EJSE Special Issue: Loading on Structures*, 3: 41-54.

Mohebi, M. 2016. *Influence of thickness and angle of attack on the dynamics of rectangular cylinder wakes*, Doctoral Thesis, University of Calgary.

Mohebi, M., Wood, D. H., and Martinuzzi, R. J. 2017. The turbulence structure of the wake of a thin flat plate at post-stall angles of attack, *Experiments in Fluids,* 58: 67.

Najjar, F. M., and Balachandar, S. 1998. Low-frequency unsteadiness in the wake of a normal flat plate, *Journal of Fluid Mechanics,* 370: 101-47.

Nakamura, Y. 1996. Vortex shedding from bluff bodies and a universal Strouhal number, *Journal of Fluids and Structures*, 10: 159-71.

Perera, M. D. A. E. S. 1981. Shelter behind two-dimensional solid and porous fences, *Journal of Wind Engineering and Industrial Aerodynamics*, 8: 93-104.

Peterka, J. A., and Derickson, R. G. 1992. Wind load design methods for ground-based heliostats and parabolic dish collectors, *Technical Report for Sandia Laboratories*.

Peterka, J. A., Hosoya, N., Bienkiewicz, B., and Cermak, J. E. 1986. Wind load reduction for heliostats, *Technical Report for Colorado State University*.

Peterka, J. A., Tan, L., Bienkiewcz, B., and Cermak, J. E. 1987. Mean and peak wind load reduction on heliostats, *Technical Report for Colorado State University*.

Peterka, J. A., Tan, Z., Cermak, J. E., and Bienkiewicz, B. 1989. Mean and peak wind loads on heliostats, *Journal of Solar Energy Engineering*, 111: 158-64.

Pfahl, A. 2018. *Wind loads on heliostats and photovoltaic trackers*, Doctoral Thesis, Technische Universiteit Eindhoven.

Pfahl, A., Buselmeier, M., and Zaschke, M. 2011. Wind loads on heliostats and photovoltaic trackers of various aspect ratios, *Solar Energy*, 85: 2185-201.

Pfahl, A., Buselmeier, M. Zaschke, M. 2011. Determination of wind loads on heliostats. *Proceedings of the 17th SolarPACES Conference*. Spain.

Pfahl, A., Randt, M., Meier, F., Zaschke, M., Geurts, C. P. W., and Buselmeier, M. 2015. A holistic approach for low cost heliostat fields, *Energy Procedia*, 69: 178-87.

Pfahl, A., and Uhlemann, H. 2011. Wind loads on heliostats and photovoltaic trackers at various reynolds numbers, *Journal of Wind Engineering and Industrial Aerodynamics*, 99: 964-68.

Plate, E. J. 1982. *Engineering meteorology, studies in wind engineering and industrial aerodynamics*, Elsevier.

Raine, J. K., and Stevenson, D. C. 1977. Wind protection by model fences in a simulated atmospheric boundary layer, *Journal of Wind Engineering and Industrial Aerodynamics*, 2: 159-80.

Richards, P. J., Fong, S., and Hoxey, R. P. 1997. Anisotropic turbulence in the atmospheric surface layer, *Journal of Wind Engineering and Industrial Aerodynamics*, 69-71: 903-13.

Richards, P. J., Hoxey, R. P., Connell, B. D., and Lander, D. P. 2007. Wind-tunnel modelling of the Silsoe cube, *Journal of Wind Engineering and Industrial Aerodynamics*, 95: 1384-99.

Richardson, G. M. 1989. A permeable windbreak: Its effect on the structure of the natural wind, *Journal of Wind Engineering and Industrial Aerodynamics*, 32: 101-10.

Rind, E., and Castro, I. P. 2012. On the effects of free-stream turbulence on axisymmetric disc wakes, *Experiments in Fluids*, 53: 301-18.

Shaw, W. J., and Businger, J. A. 1985. Intermittency and the organization of turbulence in the near-neutral marine atmospheric boundary layer, *Journal of the Atmospheric Sciences*, 42: 2563-84.

Shinneeb, A. M., and Balachandar, R. 2016. Effect of gap flow on the shallow wake of a sharp-edged bluff body – mean velocity fields, *Journal of Turbulence*, 17: 94-121.

Simiu, E., and Scanlan, R. H. 1996. *Wind effects on structures*, John Wiley & Sons.

Sment, J., and Ho, C. K. 2014. Wind patterns over a heliostat field, *Energy Procedia*, 49: 229-38.

Sun, H., Gong, B., and Yao, Q. 2014. A review of wind loads on heliostats and trough collectors, *Renewable and Sustainable Energy Reviews*, 32: 206-21.

Tan-Atichat, J., Nagib, H. M., and Loehrke, R. I. 1982. Interaction of free-stream turbulence with screens and grids: A balance between turbulence scales, *Journal of Fluid Mechanics*, 114: 501-28.

Taniguchi, S., and Miyakoshi, K. 1990. Fluctuating fluid forces acting on a circular cylinder and interference with a plane wall, *Experiments in Fluids*, 9: 197-204.

Teimourian, A., Hacisevki, H., and Bahrami, A. 2017. Experimental study on flow past two inclined flat plates in tandem arrangement, *Journal of Wind Engineering and Industrial Aerodynamics*, 169: 1-11.

Tieleman, H. W. 1992. Problems associated with flow modelling procedures for low-rise structures, *Journal of Wind Engineering and Industrial Aerodynamics*, 42: 923-34.

Tieleman, H. W. 2003. Wind tunnel simulation of wind loading on low-rise structures: A review, *Journal of Wind Engineering and Industrial Aerodynamics*, 91: 1627-49.

Varshney, K., and Poddar, K. 2011. Experiments on integral length scale control in atmospheric boundary layer wind tunnel, *Theoretical and Applied Climatology*, 106: 127-37.

von Kármán, T. 1948. Progress in the statistical theory of turbulence, *Proceedings of the National Academy of Sciences*, 34: 530-39.

Wilczak, J. M., and Tillman, J. E. 1980. The three-dimensional structure of convection in the atmospheric surface layer, *Journal of the Atmospheric Sciences*, 37: 2424-43.

Xu, Y. 2013. *Wind effects on cable-supported bridges*, John Wiley & Sons.

Yang, D., Pettersen, B., Andersson, H. I., and Narasimhamurthy, V. D. 2012. Vortex shedding in flow past an inclined flat plate at high incidence, *Physics of Fluids*, 24: 084103.

Chapter 3

Turbulence modelling for wind load measurements

3.1 Chapter overview

If scale-model testing in wind tunnels is to accurately reproduce the unsteady wind loads on full scale heliostats, it is essential that the appropriate turbulence parameters are reproduced. However, as discussed in Section 2.2.2, similarity of turbulence spectra cannot be achieved for small-scale structures in a wind tunnel due to the inevitable mismatch of the scaling ratios of the structure and the boundary layer. The effect of this mismatch on the wind loads measured in a wind tunnel experiment has been overlooked in the literature and remains unknown. Hence, this chapter aims to develop an understanding of how the differences of the turbulence spectra in a wind tunnel affect the wind load measurements on scale-model heliostats. First, an analysis of the similarities and differences between the turbulence characteristics of a simulated boundary layer in a wind tunnel and an atmospheric surface layer is provided. Then, through analysis of the measured unsteady forces on heliostat models with different scaling ratios, a correlation between turbulence spectra and lift and drag forces is developed.

The results show the existence of a direct correlation between turbulence spectrum with the spectra of the lift and drag forces over a certain range of reduced frequencies. It is proposed that modelling this range of reduced frequencies of the turbulence spectrum in a wind tunnel experiment is essential for elimination of scaling effects on the measured wind loads, and the similarity of turbulence intensity between a wind tunnel and the full-scale is not sufficient for similarity of the wind loads on the model-scale heliostat and the full-scale structure. Although the geometric scaling ratio of a heliostat model in practice cannot be identical to the scaling ratio of the atmospheric surface layer, by choosing a scaling ratio, for which the turbulence spectrum over the determined range of reduced frequencies is a close match to that at full-scale, a more reliable estimate of the wind loads on the full-scale heliostat can be achieved. It is however important to interpret the measured forces on scale-model heliostats in a wind tunnel with respect to the turbulence properties of the approaching flow noting the differences with the full-scale conditions within the atmospheric surface layer.

This chapter consists of the following published journal article:

Jafari, A., Ghanadi, F., Emes, M. J., Arjomandi, M., and Cazzolato, B. S. 2019. Measurement of unsteady wind loads in a wind tunnel: Scaling of turbulence spectra, ***Journal of Wind Engineering and Industrial Aerodynamics*****, 193: 103955.**

The article is identical to its published format with the following exceptions:

- The numbering of figures, tables and equations have been altered to include the chapter number.
- The position of some figures and tables have been changed to improve legibility.

The article in its published format is available at:
https://doi.org/10.1016/j.jweia.2019.103955

Statement of Authorship

Title of Paper	Measurement of unsteady wind loads in a wind tunnel: Scaling of turbulence spectra.
Publication Status	■ Published ☐ Accepted for Publication ☐ Submitted for Publication ☐ Unpublished and Unsubmitted work written in manuscript style
Publication Details	Jafari, A., Ghanadi, F., Emes, M. J., Arjomandi, M., and Cazzolato, B. S. 2019. Measurement of unsteady wind loads in a wind tunnel: Scaling of turbulence spectra, *Journal of Wind Engineering and Industrial Aerodynamics*, 193: 103955.

Principal Author

Name of Principal Author (Candidate)	Azadeh Jafari		
Contribution to the paper	Developed ideas, conducted experiments, performed data analysis and interpreted results, wrote manuscript, and acted as corresponding author.		
Overall percentage (%)	75		
Certification	This paper reports on original research I conducted during the period of my Higher Degree by Research candidature and is not subject to any obligations or contractual agreements with a third party that would constrain its inclusion in this thesis. I am the primary author of this paper.		
Signature		Date	25/05/2020

Co-Author Contributions

By signing the Statement of Authorship, each author certifies that:

i. the candidate's stated contribution to the publications is accurate (as detailed above);

ii. permission is granted for the candidate in include the publication in the thesis; and

iii. the sum of all co-author contributions is equal to 100% less the candidate's stated contribution.

Name of Co-Author	Farzin Ghanadi		
Contribution to the paper	Supervised the development of the research, helped in developing ideas, contributed in academic discussion and manuscript review.		
Signature		Date	26/05/2020

Name of Co-Author	Matthew Emes		
Contribution to the paper	Helped in the development of the research, contributed in academic discussion and manuscript review.		
Signature		Date	26/05/2020

Name of Co-Author	Maziar Arjomandi		
Contribution to the paper	Supervised the development of the research, participated in developing ideas and concepts, helped in interpretation of results, provided critical revision of manuscript.		
Signature		Date	25/05/2020

Name of Co-Author	Benjamin Cazzolato		
Contribution to the paper	Supervised the development of the research, helped in developing ideas, contributed in academic discussion and manuscript review.		
Signature		Date	26/5/2020

Measurement of unsteady wind loads in a wind tunnel: scaling of turbulence spectra

Azadeh Jafari, Farzin Ghanadi, Matthew J. Emes, Maziar Arjomandi, Benjamin S. Cazzolato

Abstract

Mismatch of turbulence spectra from the corresponding full-scale conditions is a common challenge in wind tunnel modelling of unsteady wind loads on small-scale structures, such as solar panels, heliostats and low-rise buildings. Understanding the effect of this mismatch on the unsteady wind loads is necessary for providing an accurate estimation of wind loads on full-scale structures. The correlation between the turbulence spectra and the unsteady wind loads in wind tunnel measurements is investigated in this study through measurement of unsteady lift and drag forces on horizontal and vertical flat plates. It was found through spectral analysis that the turbulent eddies in the range of reduced frequencies between 0.01 and 1 contributed the most to the unsteady wind loads. An approach for wind tunnel modelling was proposed in which the geometric scaling ratio of each model is determined based on the analysis of the turbulence power spectrum as a function of reduced frequency. The suitable geometric scaling ratio should be then chosen such that the turbulence spectrum as a function of reduced frequency is the closest match to that at full-scale for reduced frequencies between approximately 0.01 and 1.

Keywords: Unsteady wind load, turbulence spectrum, wind tunnel modelling, atmospheric boundary layer.

Nomenclature

A_D	aerodynamic admittance of the drag force
A_L	aerodynamic admittance of the lift force
c	characteristic length dimension (m)
C_D	drag coefficient
C_L	lift coefficient
$C_{L,0}$	lift coefficient at zero angle of attack
C_L'	slope of the lift curve near zero angle of attack (rad^{-1})
F	lift force (N)
f	frequency (Hz)

I_u	longitudinal turbulence intensity (%)
I_w	vertical turbulence intensity (%)
L_u^x	longitudinal integral length scale (m)
L_w^x	vertical integral length scale (m)
R	autocorrelation of velocity
S_{C_D}	power spectral density of the drag force coefficient (s)
S_{C_L}	power spectral density of the lift force coefficient (s)
S_{uu}	power spectral density of the longitudinal velocity fluctuation (m^2/s)
S_{ww}	power spectral density of the vertical velocity fluctuation (m^2/s)
t	time (s)
τ_u^x	longitudinal integral time scale (s)
u'	fluctuating velocity component (m/s)
U	mean velocity (m/s)
u, v, w	velocity components in the stream-wise, lateral and vertical directions (m/s)
x, y, z	distance in the stream-wise, lateral and vertical directions (m)
z_0	aerodynamic surface roughness (m)
z_{WT}	height in the wind tunnel (m)
z_{FS}	height in full scale (m)
Symbols	
α	angle of attack (°)
σ_u	standard deviation of longitudinal velocity fluctuations (m/s)
ρ	density (kg/m^3)

3.2 Introduction

Accurate estimation of the unsteady wind loads on structures is necessary for assessment of structural survivability under extreme conditions and prediction of the dynamic response. Several studies in the literature have used boundary layer wind tunnel testing for investigation of the wind loads on large civil structures such as buildings, bridges, as well as small-scale structures such as solar panels. While the common practice in wind tunnel testing is to generate a boundary layer with a logarithmic mean velocity profile similar to that of the atmospheric surface layer (ASL), similarity of the turbulence characteristics of the flow is also important for an accurate prediction of the unsteady wind loads (Holmes, 2007). For wind tunnel experiments of large civil structures such as tall buildings and bridges, achieving similarity of the turbulence spectra, length scales and intensity is possible. However, for small-scale structures such as low-rise buildings, solar panels, billboards and heliostats, similarity of the turbulence characteristics is often compromised by the technical challenges. These challenges arise due to the much smaller dimensions of the structure compared to the atmospheric surface layer height. Boundary layer wind tunnels are typically built for testing large-scale buildings and structures, and allow generation of a boundary layer with a depth of 1–3 m. The essential depth of the neutral ASL for wind engineering applications is between 275 m and 550 m (Davenport, 1960), which is the gradient height where the wind speed reaches a maximum and is dependent on the wind speed and terrain roughness. Therefore, the boundary layer is typically scaled by a factor in the order of 1:100 and 1:500 in wind tunnels. It is not technically feasible to model the small-scale structures with such scaling ratios due to the challenges in modelling the structural details and difficulty of measurement of the pressure and forces on the model. Furthermore, the interference effects of the measurement devices are a problem for such models. Therefore, these structures are, in practice, modelled at larger scaling ratios between 1:10 to 1:50. As a result of the larger model scales, the Reynolds number and the turbulence spectra in the experiments differ from the full-scale condition. While it has been shown that the Reynolds number equality in wind tunnel experiments can be circumvented for sharp-edged models as long as the Reynolds number is above 50,000 (Tieleman, 2003), the turbulence characteristics of the flow affect the wind loads, especially the fluctuating component, significantly.

The mismatch of the turbulence spectra due to the violation of the geometric scaling has led to a large variability in the reported wind load measurements from different wind tunnel experiments. For instance, a comparison of the maximum pressure coefficients on a cubic building model reported from six wind tunnel studies (Hölscher and Niemann, 1998), as displayed in Figure 3.1(a), shows a deviation of up to 12% between the peak pressure coefficients. All the six studies used a similar method for simulation of a neutral suburban boundary layer with an average power law exponent α=0.22, and the wind loads were measured at similar turbulence intensity (I_u =12%). However, the geometric scaling factors were different and the model height varied between 100 mm and 250 mm among the six studies. A similar comparative study was conducted to measure the pressure distribution on low-rise building models in an open-country (z_0=0.03 m) and a suburban terrain (z_0=0.3 m) in six wind tunnels (Fritz *et al.*, 2008). The peak pressure coefficient reported from the six studies varied between 1.2 and 3 for the open-country terrain and between 1.5 and 2.1 for the suburban terrain.

This large variability was attributed to the difference in the ratio of the turbulence length scales and the model dimensions, as well as the measurement techniques (Fritz *et al.*, 2008). Furthermore, Stathopoulos and Surry (1983) found that changing the scaling ratio of a building model from 1:500 to 1:100 led to a reduction of the peak local pressure coefficient on the walls of the model by 30% for the same flow conditions. Another example of the discrepancies is the wind load coefficients on heliostats reported by two wind tunnel experiments (Peterka *et al.*, 1989; Pfahl *et al.*, 2011) with a similar mean velocity profile and a similar turbulence intensity (I_u =18%). The main difference between the two studies was the geometric scaling ratio of the model, 1:40 and 1:20 for Peterka *et al.* (1989) and Pfahl *et al.* (2011), respectively. As shown in Figure 3.1(b), for instance the measured peak drag coefficient from the two studies differ by 30%. Furthermore, Emes *et al.* (2017) found that the peak lift coefficient on a heliostat at zero elevation angle increased from 0.3 to 0.83 as the model characteristic length decreased from 0.8 m to 0.3 m at a constant turbulence intensity (I_u =12.5%). The increase in the peak lift coefficient was attributed to the increase of the ratio of turbulent integral length scale to the model dimension (Emes *et al.*, 2017). Moreover, as demonstrated in Figure 3.1(c), a comparison between the measured peak pressure coefficients on a rooftop solar panel in a wind tunnel study (at scaling factor of 1:24) and a full-scale measurement shows that the peak pressure coefficients are underestimated in the wind tunnel experiment (Stathopoulos *et al.*, 2012). Therefore, the geometric scaling ratio of the wind tunnel models is the main reason of the discrepancies in wind tunnel studies with similar mean flow conditions. Since wind tunnel experimentation is the primary tool for prediction of unsteady wind loads and due to the importance of an accurate estimation of the loads for the design of the structures, it is necessary to develop a standard method for accurate estimation of unsteady wind loads on small-scale structures.

Reduction of turbulence intensity in wind tunnel tests has been proposed as a method to alleviate the mismatch of turbulence spectra (Dyrbye and Hansen, 1996). The common practice of matching turbulence intensity in the wind tunnel experiments to that at full-scale leads to a shift of the power spectra to higher frequencies. Dyrbye and Hansen (1996) recommended that by reducing turbulence intensity in the wind tunnel experiments, the high frequency range of the spectrum can be matched to that of the full-scale. However, similarity of the whole spectrum cannot be achieved. Hence, the remaining argument is whether the whole turbulence spectrum needs to be matched or similarity of a specific frequency range is sufficient for measurement of the wind loads in the wind tunnel experiments. In other words, the frequency range of the turbulence power spectrum which is more effective in generating the unsteady wind loads needs to be determined.

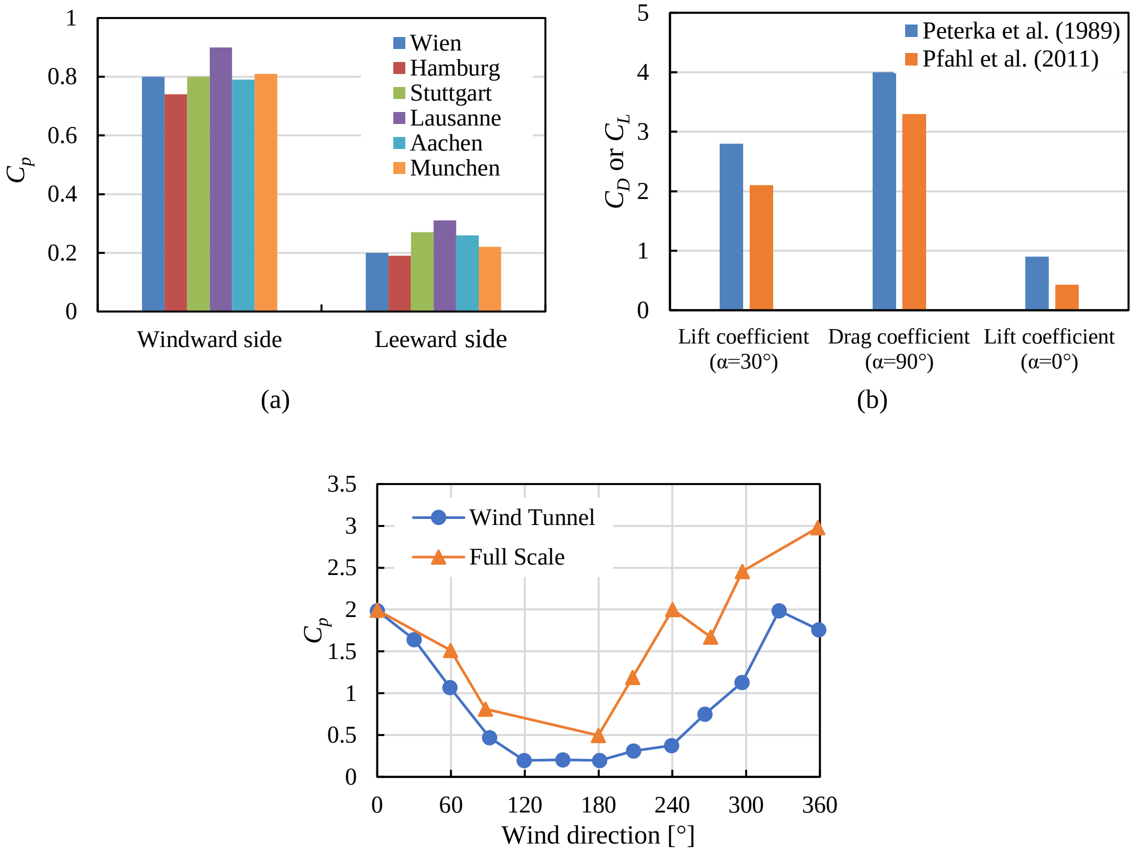

(a)

(b)

(c)

Figure 3.1. (a) Comparison of absolute maximum pressure coefficients, $C_p = P/0.5\rho U^2$, for a cubic building model from different wind tunnel studies, conducted at wind tunnels at six cities, with a similar mean velocity profile and an average turbulence intensity of 12% reproduced from Hölscher and Niemann (1998), (b) comparison of peak lift and drag coefficient at different elevation angles of heliostats from two wind tunnel studies (Peterka *et al.*, 1989; Pfahl *et al.*, 2011), (c) comparison of absolute maximum pressure coefficients, $C_p = P/0.5\rho U^2$, for a solar panel on a 30-degree hipped roof reproduced from Stathopoulos *et al.* (2012).

The peak of the turbulence spectrum containing the most energetic eddies, which is represented by the integral length scale of turbulence, is nominated as an important parameter which contributes significantly to the wind loads in the literature. For instance, the drag coefficient on a flat plate normal to a turbulent flow with a longitudinal turbulence intensity I_u=8% is found to be strongly dependent on the ratio of the longitudinal integral length scale to the characteristic length of the plate, L_u^x/c, such that the root-mean-square (RMS) of the drag coefficient increases dramatically by increasing L_u^x/c (Bearman, 1971). A similar trend is found for a flat plate normal to a simulated atmospheric boundary layer showing that the RMS of the drag coefficient increases by 37% when L_u^x/c increases from 1.5 to 4 at I_u=26%, and by 70% when L_u^x/c increases from 0.97 to 2.3 at I_u=13% (Jafari *et al.*, 2018). The mean drag force on a rectangular prism is also found to be dependent on L_u^x/c (Lee, 1975). Furthermore, L_u^x/c is reported to be the factor responsible for the differences in the measured pressure distribution on cubic models of different scaling ratios (Holdø *et al.*, 1982). The area-averaged pressure coefficients on the leeward and windward faces of cubic building models of different scaling ratios in a boundary layer wind tunnel experiment are found to increase by 50% when L_u^x/c increased from 1 to 4 (Hunt, 1982). Roy and Holmes (1988) on the other hand correlated the fluctuating wind loads on models of low-rise buildings with the lateral integral length scale, L_u^y. The vertical integral length scale is also found to dominate the wind loads on a horizontal thin flat plate showing that the fluctuating wind loads increase with increasing L_w^x/c (Jafari *et al.*, 2019).

On the other hand, Tieleman (2003) argues that the integral length scale is not of primary influence on the peak pressure coefficient on low-rise buildings, but the high-frequency range of the spectrum needs to be matched in the wind tunnel modelling. The high frequency turbulence affects the flow separation and reattachment but the effect of the low frequency turbulence, which is of much larger length scale than the structure, is similar to the effect of changing the mean velocity vector (Tieleman, 2003). Furthermore, the pressure coefficients on a cube model in a wind tunnel boundary layer, in which the high frequency range of the turbulence spectrum was a close match to the full-scale, were found to be close to the full-scale pressure measurements on the Silsoe cube (Richards *et al.*, 2007). It was proposed that turbulence over the range of the non-dimensional frequencies fz/U>0.05 directly interacts with the local flow field and is therefore important to be modelled accurately in the wind tunnel. The results of this study show that the scale of turbulence in relation to the mean velocity and the structure dimensions are important. Furthermore, Aly and Bitsuamlak (2013) measured the pressure coefficient on ground-mounted solar panels of different scaling ratios and recommended that by matching the turbulence spectra at high frequencies and calculating the average of peak pressure coefficients for measurement periods of 3 seconds, the 3-second pressure coefficients for the models with different scaling ratios will be similar. A quantitative analysis of the effect of the lower frequencies on the peak pressure is however not given.

A review of the existing literature shows that the correlation between the turbulence power spectrum of the flow and the fluctuating wind loads is not known. While some of the studies in the literature (Lee, 1975; Holdø *et al.*, 1982; Hunt, 1982; Roy and Holmes, 1988) indicate the peak of the turbulence power spectra to be more important for the unsteady wind loads, other studies (Tieleman, 2003; Richards *et al.*, 2007) propose that the high frequency range to be dominant. Determination of the critical frequency range of the spectrum which contributes to the generation of the unsteady wind loads is required for wind tunnel modelling of the small-scale structures. Hence, the aim of this study is to develop an understanding of the correlation between the turbulence spectra and the unsteady wind loads by spectral analysis of the turbulence of wind tunnel boundary layers and the fluctuating forces on flat plate models of various geometric scaling ratios. The flat plate is studied as a fundamental geometry to establish a standard method. The implemented method is described in Section 2, followed by analysis of the turbulence characteristics of the simulated atmospheric boundary layers in the wind tunnel in Section 3. Their resemblance to the atmospheric turbulence and the existing mismatch of the spectra for modelling the small-scale structures are then described. In Section 4, the experimental measurements of the forces on horizontal and vertical flat plates in the wind tunnel boundary layers are presented, and the correlation between the turbulence spectra and the unsteady forces on the plates is investigated by determination of the aerodynamic admittance function. A case study is then discussed in Section 5 to demonstrate how the results of this study can be applied for wind tunnel modelling of a flat-plate-like structure. The results of this study can be applied for a more accurate wind tunnel modelling of small-scale structures such as solar panels, heliostats and billboards.

3.3 Methodology

Wind loads on thin square flat plates of different characteristic lengths, resembling different geometric scaling ratios, in vertical and horizontal configurations were measured in simulated boundary layers in the large-scale wind tunnel at the University of Adelaide. The rectangular test section of the boundary layer wind tunnel has a cross-sectional area of 3 m × 3 m, and the level of turbulence intensity in the empty tunnel is between 1% and 3% outside the boundary layer. Two wind tunnel boundary layers (WTBL) with different intensities and length scales of turbulence were generated using two sets of spires and roughness elements. For each WTBL, three spires with identical dimensions, shown in Figure 3.2(a), were placed at a centre-line distance of 0.9 m in the lateral (y) direction followed by a 10 m stream-wise fetch of wooden roughness elements (90 mm × 90 mm cross section and 45 mm height). The sizing and spacing of the roughness elements were determined using the empirical equations by (Wooding *et al.*, 1973). The elements were placed with a spacing of 500 mm in all directions covering approximately 24% of the floor area over the fetch length. The spires were designed based on Kozmar's part-depth method (Kozmar, 2011) for part-depth simulation of the atmospheric boundary layer. The flat plates were placed downstream of the spires at a distance equal to 6 times the spire height which is expected to be sufficient for flow development (Irwin, 1981). Square flat plates with chord length dimensions between 0.2 m and 0.7 m with a thickness of 3 mm were mounted on a post of constant height (0.3 m). The forces on the horizontal and vertical flat plates were measured by three three-axis ME load cells (K3D50), each with a capacity of 50 N which were calibrated for a range of forces between 0-25 N. A schematic of the wind engineering test section of the tunnel containing spires and roughness elements and the flat plate model is shown in Figure 3.2(b).

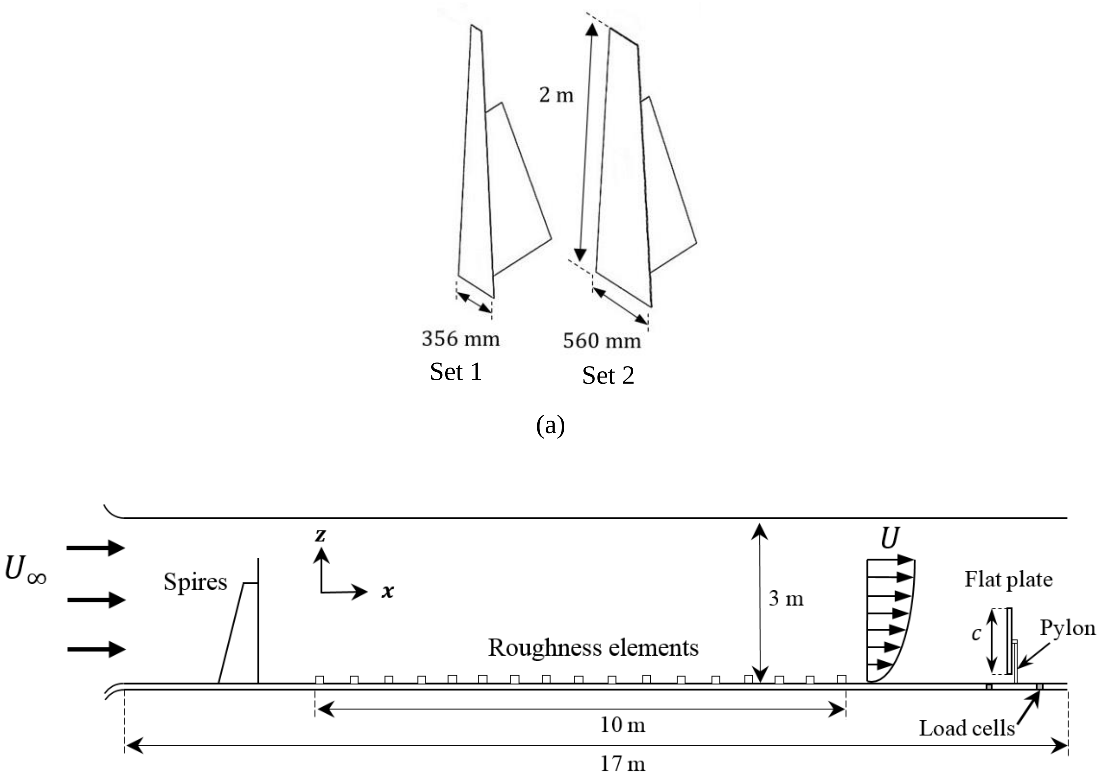

(a)

(b)

Figure 3.2. (a) Dimensions of the two spire sets, (b) Schematic of the test section containing spires and roughness elements and the flat plate model.

3.3.1 Calculation of turbulence characteristics within the WTBL

Three components of velocity (u, v, w) were measured by a Turbulent Flow Instrumentation (TFI) multi-hole pressure probe, with an accuracy of ±0.5 m/s, downstream of the roughness fetch over an area of 1 m^2 in both vertical and lateral directions, with a longitudinal spacing of 500 mm in order to investigate flow development. Data were measured for a duration of 150 s at each location at a sampling rate of 1 kHz. In order to reduce the experimental errors, the velocity measurements were repeated for five times and the average of the five measurements was calculated. Turbulence intensity was calculated from the following:

$$I_i = \frac{\sigma_i}{U}, i = u, w \tag{3.6}$$

The power spectral densities of the velocity fluctuations were found using the *pwelch*-function in MATLAB.

3.3.2 Calculation of wind load coefficients

The forces on the flat plates were sampled at 1 kHz and were measured over a sampling period of 120 seconds, which was found to be sufficient as the calculated root mean square (RMS) of the fluctuating forces varied by less than 2% when the sampling period increased above 120 seconds. Only the dominant unsteady wind-induced force, which is the force acting normal to the plate, the drag force for the vertical flat plate and the lift force for the thin horizontal flat plate, were reported for all cases. Since the turbulence characteristics of the flow mainly impact the unsteady wind loads, only the unsteady wind load coefficients are reported in this study.

The fluctuating drag and lift coefficients were calculated from the following:

$$C_{i,RMS} = \frac{F_{i,RMS}}{\frac{1}{2}\rho U^2 c^2}\ , \quad i = L, D \tag{3.7}$$

where $F_{i,RMS}$ represents the RMS of the fluctuating component of lift and drag forces, ρ represents the air density, U is the mean velocity at pylon height and c represents the characteristic length of the flat plate.

3.4 Characterisation of the WTBLs

The mean velocity profile at the centre-line (y=0) as a function of height in the wind tunnel boundary layers generated by the two sets of spires and roughness elements, hereafter referred to as WTBL1 and WTBL2, at a freestream velocity of 11.5 m/s is shown in Figure 3.3, which match the logarithmic profiles corresponding to the atmospheric surface layer. The aerodynamic surface roughness lengths were determined by fitting the mean velocity profile of each simulation to the logarithmic law. As shown in Figure 3.3, the velocity profile of WTBL1 matches a logarithmic profile with a roughness height of 0.018 m in full scale, with a maximum error of 2.3%, and represents an open country terrain. The mean velocity profile of WTBL2 matches a logarithmic profile with a roughness height of 0.35 m and a displacement height of 0.02 m in full scale, with a maximum error of 5% (for heights up to 0.7 m), and is representative of a suburban terrain. It must be noted that the displacement height is negligible for terrains whose surface roughness value is low (such as flat and open country terrains), while for suburban and urban terrains, the displacement height is non-zero (Holmes, 2007; Kozmar, 2012; De Paepe *et al.*, 2016). Therefore, the displacement height (equal to 0.02 m in full scale) is found for the logarithmic profile fit of the mean velocity profile of WTBL2 with z_0=0.35 m.

The longitudinal and vertical turbulence intensities within WTBL1 and WTBL2 are shown in Figure 3.4. Longitudinal turbulence intensity within the WTBLs decrease with height. According to Figure 3.4, the longitudinal turbulence intensity reduces from 15% to 9% in WTBL1 and from 34% to 20% in WTBL2 as the height from the ground increases to 1 m. The variation of turbulence intensity with height from the ground is larger in WTBL2 since the aerodynamic surface roughness is larger, whereas for WTBL1, which resembles an open-country terrain with lower surface roughness, the change in turbulence intensity with height is less. At the model height at 0.5m, the longitudinal turbulence intensity is approximately 11% and 26%, and the vertical turbulence intensity is approximately 9% and 21% within WTBL1 and WTBL2, respectively.

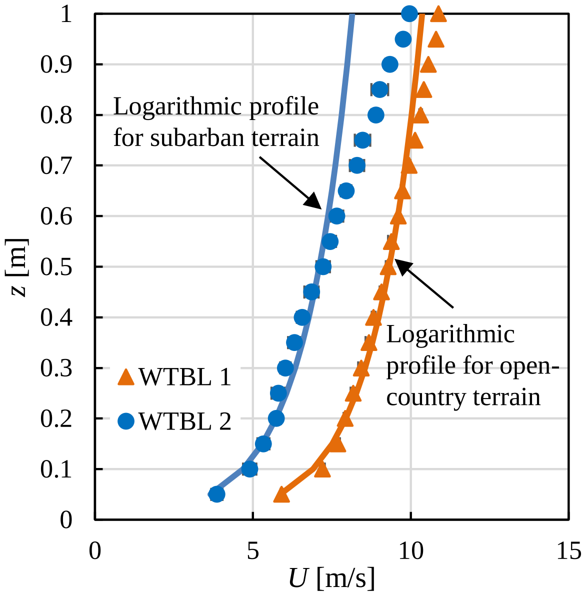

Figure 3.3. Mean velocity profile of the wind tunnel boundary layers compared with logarithmic profiles. The error bars show the standard deviation calculated from five measurements.

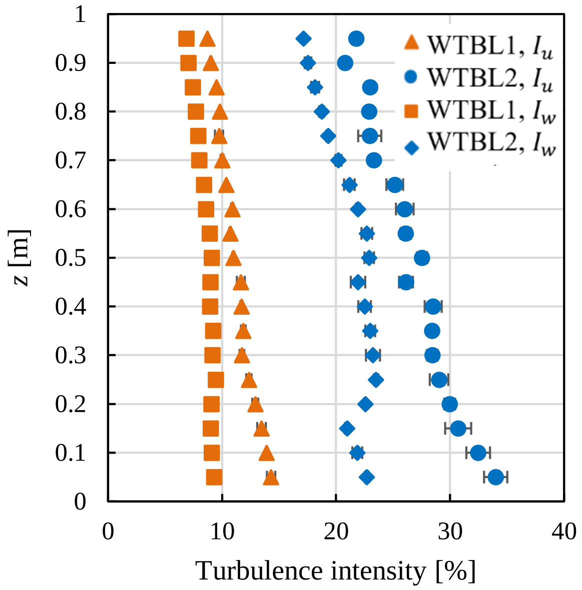

Figure 3.4. Longitudinal turbulence intensity profiles for WTBL1 and WTBL2. The error bars show the standard deviation calculated from five measurements.

The longitudinal and vertical velocity spectra at different heights of 0.1 m, 0.3 m in WTBL1 and WTBL2 are shown in Figure 3.5, which shows that turbulence tends to be locally isotropic for fz/U above 0.3 in both boundary layers. The spectral distribution of vertical turbulence energy follows the same trends as those in the atmosphere having the +1 and -2/3 slopes. Three distinctive spectral ranges can be seen in the longitudinal power spectra in the wind tunnel boundary layers at the lower height, z= 0.1 m: The inertial subrange where $fS_{uu} \propto f^{-2/3}$; the lower frequency range, where S_{uu} is independent of f (the +1 slope for fS_{uu}/U^2); and a self-similar range, where fS_{uu}/U^2 is constant which extends over fz/U of about 0.02 to 0.06 (Högström *et al.*, 2002; Drobinski *et al.*, 2004). By increasing the height from the ground to z=0.3 m, the self-similar region almost disappears. The self-similar range has also been identified in the lower 10–20 m of the ASL, known as the eddy surface layer, from the measured atmospheric data from different sites (Högström *et al.*, 2002; Drobinski *et al.*, 2004). The self-similar range of the eddy surface layer represents the anisotropic eddies formed due to the blockage by the ground (Högström *et al.*, 2002). Therefore, the distribution of the turbulence energy in the wind tunnel boundary layers is similar to the lower part of ASL. It must be noted that the power spectral density is normalised by mean velocity and measurement height as recommended by Richards *et al.* (2007). This method of normalising the spectral density demonstrates the differences between the simulated boundary layers more clearly compared to normalising with turbulence dependant variables such as variance and integral length scale (Richards *et al.*, 2007).

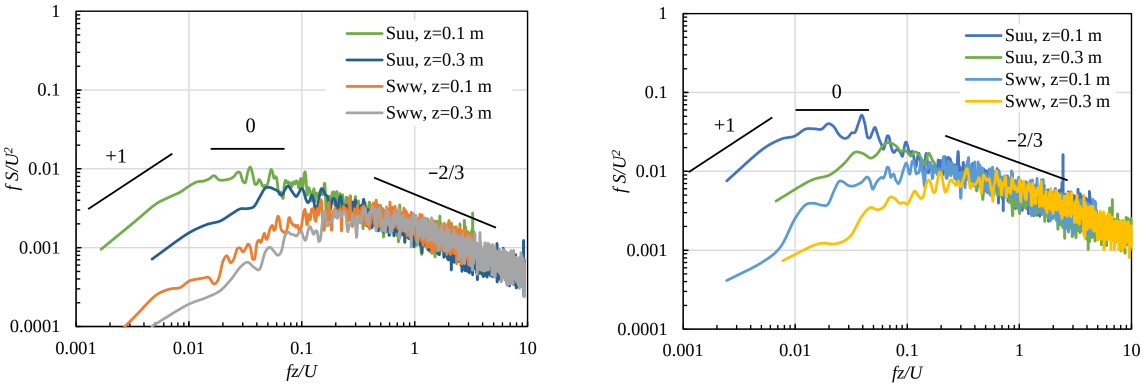

(a)

(b)

Figure 3.5. Normalised longitudinal velocity spectrum, fS_{uu}/U^2, and normalised vertical velocity spectrum, fS_{ww}/U^2, as a function of fz/U, at different heights in (a) WTBL1 and (b) WTBL2.

3.4.1 Mismatch of turbulence spectra in modelling small-scale structures

The mismatch of turbulence spectra usually occurs when a small-scale structure is modelled in the wind tunnel as a result of the larger geometric scaling ratio of the model compared to that of the simulated boundary layer. The difference in the geometric scaling ratio of the structure and the boundary layer leads to a difference in the scale of flow turbulence in relation to the structure's characteristic length. The consequences of such violation of the similarity of geometric scaling ratio are further elaborated by an example. The simulation length scale factor for the wind tunnel boundary layers is calculated using Cook's method (Cook, 1978) from the aerodynamic surface roughness length and integral length scales at different heights within each boundary layer. The length scale factor for WTBL1 and WTBL2 was determined as the average of the calculated values from Cook's method for different heights. Hence, the simulation length scale factor was found to equal 1:151 and 1:90 for WTBL1 and WTBL2, respectively. A flat-plate-like structure with a characteristic length of 12 m at a height of z_{FS}=6 m in the full-scale is considered as an example. This flat plate could resemble an industrial heliostat or solar tracker. An accurate model of this flat plate in WTBL1 is required to be scaled down by a factor of 1:151, i.e., identical to the scaling ratio of the simulated boundary layer. The model is thus required to be composed of a plate of approximately 0.08 m by 0.08 m placed at a height of approximately 0.04 m in the wind tunnel. There are however several technical challenges for such small-scale wind tunnel testings such as interference effects of the measurement devices and requirement of very sensitive low-range force sensors. Therefore, the model is usually built at a larger scaling ratio, typically about 1:10 to 1:50, as done in the literature such as (Radu *et al.*, 1986; Peterka *et al.*, 1989; Bronkhorst *et al.*, 2010; Pfahl *et al.*, 2011; Ruscheweyh and Windhövel, 2011; Saha *et al.*, 2011; Emes *et al.*, 2017). Taking a model scaling ratio of 1:20, the model will be composed of a plate of 0.6 m by 0.6 m placed at a height of 0.3 m. Figure 3.6 shows the longitudinal and vertical turbulence intensity profiles of WTBL1 converted to full-scale (by a factor of 1:151) along with the estimations of the atmospheric turbulence intensities given by ESDU85020 (2010) for a terrain with a similar surface roughness. The solid lines showing the ESDU range are represented as ±20% from the calculated mean values which is suggested as the allowable bandwidth (ESDU85020, 2010). The two horizontal lines show the full-scale height of the structure within the ASL (z_{FS}=6 m) and the corresponding full-scale height of the model in the wind tunnel (z_{WT}=0.3 m) which equals 45.3 m. As shown in Figure 3.6, with the model being placed at a larger height within the boundary layer (45.3 m opposed to z_{FS}=6 m), turbulence intensity at the model height is less than those given by ESDU85020 (2010) for z_{FS}=6 m.

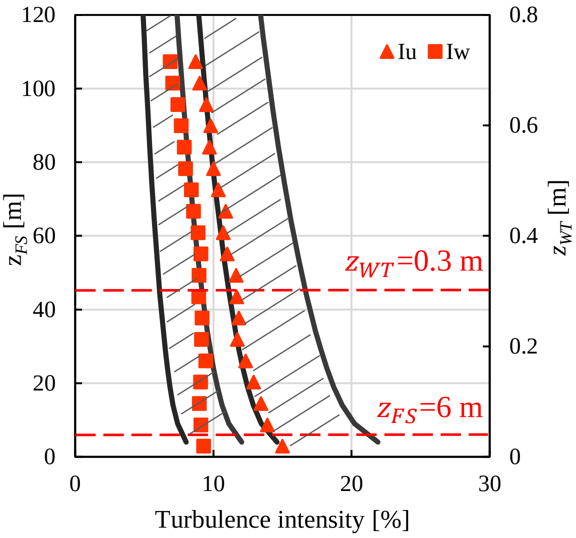

Figure 3.6. Longitudinal and vertical turbulence intensity profiles for WTBL 1 at the wind tunnel scale and at full-scale (scaling ratio 1:151). The shaded areas show the estimations by ESDU 85020 for z_0=0.018 m.

Furthermore, the spectral distribution of turbulence at the model position is very different from that at full-scale. This is shown by comparison of the normalised spectra at z_{WT}=0.3 m in WTBL1 with the full-scale spectra at z_{FS}=6 m and 45.3 m in Figure 3.7(a–b). The ASL spectra are estimated from the spectral equations given by ESDU85020 (2010) which provide a modified version of Von Karman's model. The ESDU spectral equations correct for the underestimation of the integral length scales and the overestimation of the peak of the spectra by the Von Karman model at lower heights near the ground (ESDU85020, 2010), and are therefore applied in this study to predict the turbulence spectra. According to Figure 3.7(a), the longitudinal turbulence spectrum at z_{WT}=0.3 m in WTBL1 almost matches that at 45.3 m in full-scale. However, it deviates from the spectrum at z_{FS}=6 m over the mid and low frequencies. The peak of the longitudinal power spectrum at z_{WT}=0.3 m occurs at higher frequencies compared to the spectrum at z_{FS}=6 m, which indicates the integral length scale is smaller. Although, the higher frequency range, fz/U>0.1, at z_{WT}=0.3 m matches that at z_{FS}=6 m, the large-scale eddies in the wind tunnel contain lower turbulence energy than the full-scale z_{FS}=6 m. Furthermore, according to Figure 3.7(b), there is a distinctive shift to higher frequencies in the vertical power spectrum of WTBL1 at z_{WT}=0.3 m compared to the full-scale vertical spectrum at z_{FS}=6 m. Furthermore, according to Figure 3.7(b), there is a distinctive shift to higher frequencies in the vertical power spectrum of WTBL1 at z_{WT}=0.3 m compared to the full-scale vertical spectrum at z_{FS}=6 m. The peak of the vertical power spectrum at

z_{WT}=0.3 m, occurs at fz/U=0.4 compared to the peak of the spectrum at z_{FS}=6 m at fz/U=0.02. Therefore, as shown in Figure 3.7(b), the vertical turbulence energy in the wind tunnel is composed of eddies of higher frequencies and relatively smaller length scales compared to the corresponding full-scale height.

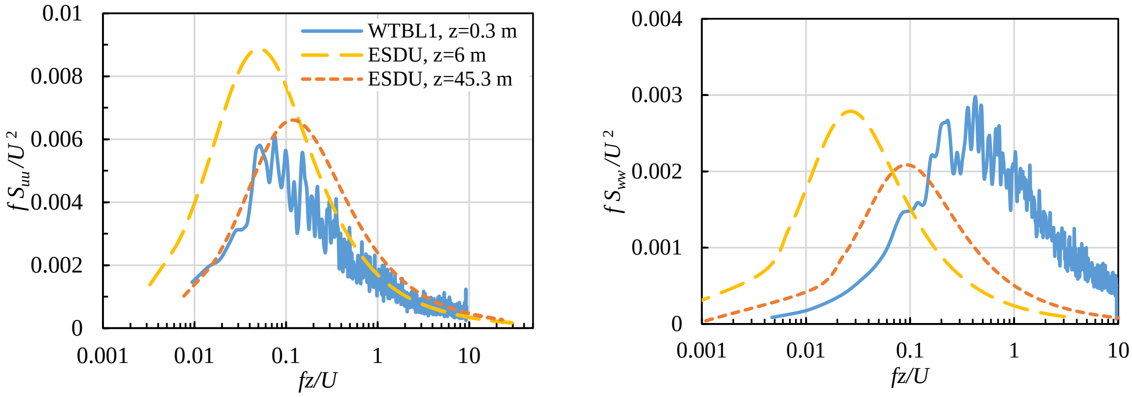

(a) (b)

Figure 3.7. Comparison of normalised spectral densities as a function of fz/U at z=0.3 m in WTBL1 with the ESDU estimations for the ASL spectra at a terrain with similar terrain roughness at two heights, (a) normalised longitudinal velocity spectrum, fS_{uu}/U^2, (b) normalised vertical velocity spectrum, fS_{ww}/U^2.

3.5 Experimental results

The unsteady wind loads on horizontal (α=0°) and vertical (α=90°) square flat plates of different characteristic length dimensions between 0.2 m and 0.7 m, resembling different geometric scaling ratios, were measured within WTBL1 and WTBL2. Figures 3.8 shows the RMS of the unsteady lift coefficient on the horizontal plates and the unsteady drag coefficient on vertical plates, respectively. Both the unsteady lift and drag force coefficients are found to decrease with increasing the characteristic length of the plate, which shows that the measured wind forces in wind tunnel experiments vary significantly when the size of the model and its geometric scaling ratio change. For example, according to Figure 3.8(a), in WTBL2, increasing the characteristic length dimension of the plate from 0.2 m to 0.7 m reduces the fluctuating lift coefficient from 0.6 to 0.19. Similarly, Increasing c from 0.2 m to 0.7 m leads to a reduction in the fluctuating drag coefficient from approximately 0.39 to 0.22 and from 0.8 to 0.53 within WTBL1 and WTBL2, respectively.

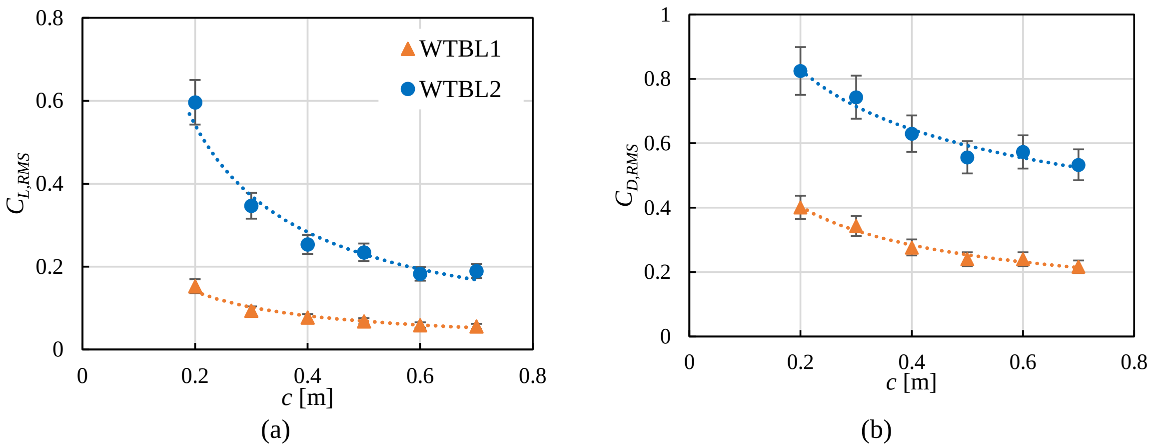

(a) (b)

Figure 3.8. The effect of the characteristic length dimension of the flat plate on the unsteady wind loads in two simulated wind tunnel boundary layers, (a) The fluctuating lift coefficient, $C_{L,RMS}$, on a horizontal flat plate, (b) The fluctuating drag coefficient, $C_{D,RMS}$, on a vertical flat plate (WTBL1: I_u=11%, L_u^x=0.57 m, I_w=8.9%, L_w^x=0.236 m; WTBL2, I_u=26%, L_u^x=0.81 m, I_w=21.1%, L_w^x=0.333 m).

In order to understand the correlation between the incoming turbulence and the forces on the flat plates of different characteristic lengths, the aerodynamic admittance function of the lift and drag force is evaluated. The aerodynamic admittance represents a measure of the effectiveness of a body in extracting energy from the oncoming turbulence at different frequencies (Larose and Livesey, 1997), and correlates the power spectrum of velocity with the power spectrum of the transverse force on the body. While in a quasi-steady situation the contribution of velocity fluctuations of all wavelengths is assumed equal in generation of aerodynamic forces, in reality, different scales of turbulence are not equally effective in producing aerodynamic forces (Sankaran and Jancauskas, 1992). The frequency-dependency of the aerodynamic forces is expressed by the aerodynamic admittance. The aerodynamic admittance of the transverse force on a flat plate is found from the following equation (Drabble *et al.*, 1990):

$$|A_i(f)|^2 = \frac{U^2 S_{C_i}(f)}{C_i^2\, S_{jj}(f)}, \quad i = L, D, \;\; j = u, w \tag{3.8}$$

where $S_{jj}(f)$ and $S_{C_i}(f)$ represent the power spectra of the transverse velocity component, and transverse fluctuating force coefficient on the flat plate. For the vertical flat plate, the aerodynamic admittance correlates the power spectrum of the drag force coefficient with the power spectrum of the longitudinal velocity, i.e. $|A_D(f)|^2 = \frac{U^2 S_{C_D}(f)}{C_D^2\, S_{uu}(f)}$ (Bearman, 1971).

For the horizontal flat plate, Larose and Livesey (1997) gives the aerodynamic admittance of the lift force as $|A_L(f)|^2 = \frac{U^2 S_{C_L}(f)}{4C_L^2\, S_{uu}(f)+C'^2_L\, S_{ww}(f)}$, where C_L and $C_L' = \partial C_L/\partial\alpha$ represent the lift coefficient at zero angle of attack and the rate of change of the lift coefficient with the angle of attack (the slope of the lift curve for α=0), respectively. The experimental results, however, show that C_L is much smaller than C_L' (Larose *et al.*, 1998; Rasmussen *et al.*, 2010). Similarly, by measuring the lift force on the flat plates at low angles of attack near zero (between ±5°), in this study, C_L and C_L' were found to be -0.11 and 2.9, respectively. As given in the denominator of the equation given by Larose and Livesey (1997), the longitudinal velocity spectrum is weighed by $C_{L,0}^2$ and the vertical velocity spectrum is weighed by C'^2_L. Since $C_{L,0}^2$ is two orders of magnitude smaller than C'^2_L, the first term in the denominator (i.e., $4C_{L,0}^2\, S_{uu}(f)$) is much smaller than the second term (i.e., $C'^2_L\, S_{ww}(f)$). Hence, the equation given by Larose and Livesey (1997) can be simplified to the form given in Equation (3.3), as $|A_L(f)|^2 = \frac{U^2 S_{C_L}(f)}{C'^2_L\, S_{ww}(f)}$. This simplification of the aerodynamic admittance of the lift force is in agreement with the findings in the literature (Rasmussen *et al.*, 2010; Jafari *et al.*, 2018; Pfahl, 2018) reporting that the fluctuating lift force on the horizontal flat plate is mainly induced by the vertical velocity component of the turbulent eddies. In the present study, the aerodynamic admittance of the lift force has been calculated from the equation given by Larose and Livesey (1997) considering both longitudinal and vertical velocity spectra.

The aerodynamic admittance of the unsteady transverse forces on the flat plates are presented in Figure 3.9 as a function of reduced frequency, fc/U, where c is the characteristic length of the plate. The aerodynamic admittance of the lift force on the horizontal flat plates within the two WTBLs are shown in Figure 3.9(a–b), and the aerodynamic admittance of the drag force on the vertical flat plates are presented in Figure 3.9(c–d). According to Figure 9, as the reduced frequency increases, the aerodynamic admittance tends to zero which indicates that the higher frequencies of the turbulence spectrum contribute little to the overall force. The fluctuating transverse force is mainly induced by the lower reduced frequencies for which the admittance function is largest. For instance, according to Figure 3.9(a), the aerodynamic admittance of the lift force varies between 0.5 and 2 for c=0.2 m, between 0.6 and 1.5 for c=0.5 m, and between 0.4 and 1 for c=0.7 m, for reduced frequencies below 0.5. The aerodynamic admittance decreases with further increase of the reduced frequency. A similar trend is found for the aerodynamic admittance of the forces for the plates in WTBL2. Reduction of the admittance function from its peak shows smaller correlation between the velocity of the turbulent eddies and the generated transverse force.

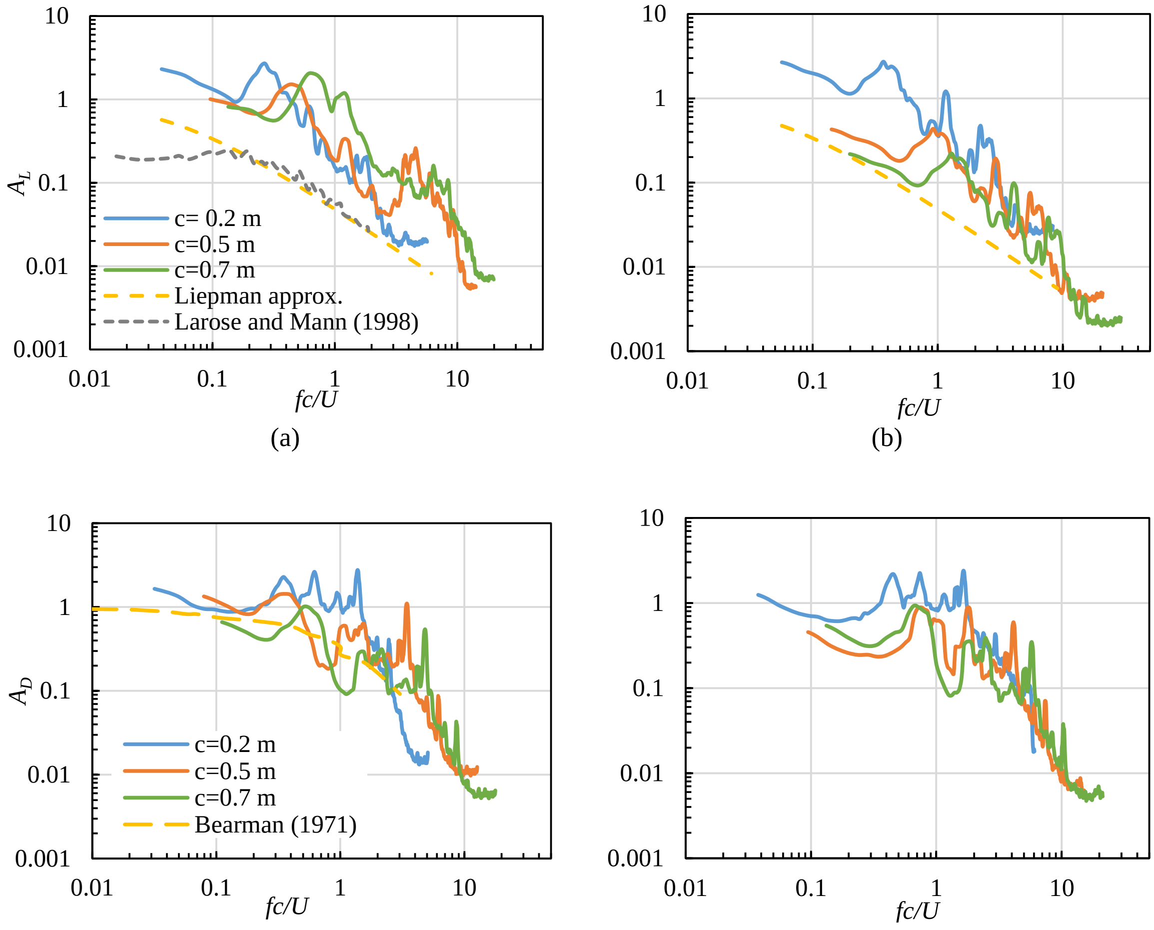

(a) (b)

(c) (d)

Figure 3.9. The aerodynamic admittance of the transverse force as a function of reduced frequency, fc/U, for different chord length dimensions of the flat plate, (a–b) lift force on the horizontal flat plate in WTBL1 and WTBL2, respectively, (c–d) the drag force on the vertical flat plate in WTBL1 and WTBL2, respectively (WTBL1: I_u=11%, L_u^x=0.57 m, I_w=8.9%, L_w^x=0.236 m; WTBL2, I_u=26%, L_u^x=0.81 m, I_w=21.1%, L_w^x=0.333 m).

The observed trend is in agreement with that reported in the literature (Bearman, 1971; Drabble *et al.*, 1990; Larose *et al.*, 1998; Rasmussen *et al.*, 2010). For comparison of the calculated aerodynamic admittance in this study with the literature, the theoretical approximation of the aerodynamic admittance of the lift force for a flat plate in a fully correlated sinusoidal gust by Liepmann, calculated according to Fung (2002), is shown in Figure 3.9(a–b). The calculated aerodynamic admittance functions of the flat plates in the wind tunnel boundary layers show a similar trend to Liepmann's approximation, although larger in magnitude. Rasmussen *et al.* (2010) also reports that the admittance measured in wind tunnel experiments with spire-roughness-generated boundary layers is generally larger than Liepmann's approximation. Furthermore, the experimental results for a bridge deck model in a turbulent boundary layer with I_w=8% from Larose and Mann (1998) are shown in Figure 3.9(a), which demonstrate a similar decreasing trend with increasing fc/U, as observed for the flat plates in this study. Moreover, The aerodynamic admittance reported by Bearman (1971) for the drag force on a vertical flat plate in a grid-generated turbulence with I_u=8% and L_u^x/c=1.5 is also given in Figure 3.9(c). The aerodynamic admittance of the drag force found in this study follows the same trend as that given by Bearman (1971).

According to Figure 3.9, the aerodynamic admittance decreases sharply from its peak as the reduced frequency increases to values of above approximately 1. This trend holds true for all the flat plates in both WTBLs despite the difference in the magnitude of the aerodynamic admittance for flat plates of different characteristic length dimensions. Since the peak of the aerodynamic admittance (which has a magnitude near 1) shows the strongest correlation between the transverse force and the turbulence spectra, it can be concluded that turbulence eddies with reduced frequencies lower than 1 are more effective in generating the transverse force. The reason is that turbulence fluctuations with reduced frequencies above 1 are less spatially correlated. Hence, the critical reduced frequencies, which are the major contributors to the fluctuating force are approximately below 1 for all the investigated cases. This is in agreement with the findings by Drabble *et al.* (1990) who compared the aerodynamic admittance of the drag force on a vertical flat plate in a turbulent flow with that in a fully coherent fluctuating flow. It was found that in the turbulent flow, the aerodynamic admittance decreased rapidly for reduced frequencies above approximately 0.5, while the admittance increased with increasing frequency in the fully coherent fluctuating flow (Drabble *et al.*, 1990).

It must be noted that the minor peaks observed at higher frequencies are due to the body-induced turbulence as also noted by Rasmussen *et al.* (2010). Furthermore, the lower band of the calculated values shown in Figure 3.9 is limited to half of the sampling frequency of the force and velocity measurements, which is identical for all the cases. However, the different low bands for fc/U in Figure 3.9 are due to normalising this frequency with c and U, which differ for the different flat plate and the WTBLs, respectively.

The difference in the magnitude of the aerodynamic admittance of flat plates with different characteristic length dimensions, seen in Figure 3.9, shows the effect of the ratio of the turbulence length scales to the plate's characteristic length. As more clearly demonstrated in Figure 3.9(b), the magnitude of the lift force aerodynamic admittance, especially at low frequencies, is largest for c=0.2 m, for which the ratio of length scale of turbulence over c is the largest. Similarly, the magnitude of the aerodynamic admittance of the drag force is largest for c=0.2 m (see Figure 3.9(d)). This is due to the stronger correlation of the turbulent fluctuations over the plate's characteristic length. Larose *et al.* (1998) also found that the aerodynamic admittance of lift force on bridge decks was larger for decks with larger ratio of vertical integral length scale over the deck's characteristic length (L_w^x/c). Hence, as shown in Figures 3. (8–9), the fluctuating transverse force and its aerodynamic admittance are larger on the flat plate with a smaller characteristic length dimension. As evaluation of the aerodynamic admittance function shows that reduced frequencies below 1 are responsible for the generation the fluctuating force, the larger transverse force on the flat plate with a smaller characteristic length dimension is related to the larger magnitude of the turbulence energy over this spectral range, compared to the larger plates. This is demonstrated in Figure 3.10 which presents the velocity power spectra normalised by the mean velocity as a function of reduced frequency, fc/U, for chords of c=0.2 m, c=0.5 m and c=0.7 m. As shown in the Figure 3.10, there is a shift to lower reduced frequencies for flat plates with smaller characteristic length dimension. Larger longitudinal and vertical turbulence energy over the critical reduced frequency range for c=0.2 m lead to increasing the fluctuating drag and lift force, respectively. Hence, an accurate estimation of the fluctuating force on a horizontal flat-plate-like structure in a wind tunnel experiment can be achieved if the distribution of vertical power spectrum as a function of reduced frequency is a close match to that of the full scale over the critical reduced frequency range below 1. Similarly, for an accurate estimation of the fluctuating drag force on a vertical flat plate, an appropriate characteristic length for the model should be chosen such that the distribution of longitudinal turbulence spectrum over the critical reduced frequency range is a close match to that at the full scale.

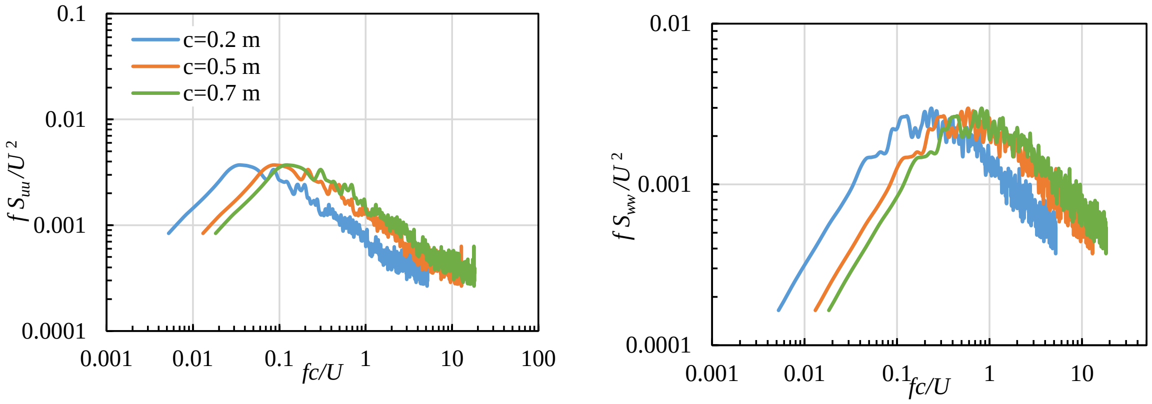

(a) (b)

Figure 3.10. The normalised power spectral density of turbulence energy as a function of reduced frequency, fc/U, for different characteristic length dimensions of the flat plate in WTBL1 at z=0.3 m (a) normalised longitudinal power spectrum, fS_{uu}/U^2, (b) normalised vertical power spectrum, fS_{ww}/U^2.

3.6 Discussion

The spectral analysis presented in Section 4 shows the existence of a range of reduced frequencies, which are critical to the generation of the unsteady wind loads. This indicates that the critical turbulence frequency range, and the corresponding critical length scales of turbulence which influence the fluctuating wind loads, are dependent on the characteristic length of the model. This relationship is expressed by normalising the turbulence frequency with the characteristic length of the structure, in terms of reduced frequency. The results from the wind tunnel experiments on horizontal and vertical flat plates of various dimensions, given in Section 4, show that the wind loads are mainly generated by the turbulence length scales over the range of reduced frequencies below 1, i.e., $fc/U \leq 1$, which represents turbulent eddies which are of approximately the same length scale of the structure. The reason for this is that the turbulent eddies which are much smaller than the flat plate's characteristic length do not correlate over the structure's length and therefore do not produce large loads. The eddies which are of approximately the same order as the plate produce large unsteady loads on it.

On the other hand, the studies in the literature suggest that the eddies which are much larger than the structure, $fc/U \ll 1$, do not produce significant loads on it either. According to the studies in the literature (Lee, 1975; Holdø *et al.*, 1982; Bearman and Morel, 1983), when the turbulence length scale is much larger than the characteristic length of the structure, free-stream turbulence acts like a correlated unsteady mean flow and the flow behaviour around the body is quasi-static. The turbulence scales which interact with the local flow field, not the eddies with very larger scales, produce the unsteady wind loads (Richards *et al.*, 2007). However, the effect of the very large scales could not be investigated in the performed analysis as the results from the wind tunnel experiments are limited at the low frequency range due to the sampling frequencies and the restriction in generation of the low-end of the spectrum in the wind tunnel. Consequently, the smallest reduced frequency for which the aerodynamic admittance was calculated was approximately 0.03 (as shown in Figure 3.9). Therefore, it can be concluded from the experimental results of this study and the studies in the literature that turbulent length scales corresponding to a range of reduced frequencies between 0.01 and 1, are most effective in generation of the unsteady wind loads. Hence, it is proposed that this range of reduced frequencies of the turbulence spectrum should be correctly modelled in wind tunnel experiments in order to minimise the scaling effects. The suitable geometric scaling ratio of the structure should then be determined based on the scaling ratio for which the turbulence spectrum as a function of reduced frequency is the closest match to that at full-scale.

The critical reduced frequency range determined in this study is in agreement with the experimental results in the literature. For instance, Richards *et al.* (2007) compared the pressure distribution on a cubic model in a wind tunnel experiment with the data collected on the full-scale Silsoe cube, and reported that when the mid- to high-frequency ranges of the turbulence spectra in the wind tunnel matched the full-scale spectra, the obtained pressure coefficients from the wind tunnel experiment were a close match to the full-scale data. The frequency range, referred to as the mid- to high-frequency range by Richards *et al.* (2007), corresponds to $fc/U >$0.05 for the longitudinal spectrum (Figure 3.11(a)). This range contains the critical frequency range obtained from the results of the present study, 0.01$< fc/U <$1, (shaded in Figure 3.11(a)) which shows that by matching the spectra in the wind tunnel to the full-scale over this reduced frequency range, the wind tunnel experimental results provided a good match to the full-scale pressure measurements. This is in agreement with the concluded result in the present study that the critical reduced frequency range is the major contributor to the wind loads. Furthermore, comparison of the pressure distribution on a cubic model, measured from six wind tunnel studies with similar simulated boundary layers (Hölscher and Niemann, 1998), with the full-scale pressure measurements from Silsoe cube showed that the results were the closest to the full-scale pressure coefficients for two wind tunnel experiments, for which the turbulence spectrum was a closer match to the full-scale spectrum for reduced frequencies above approximately 0.1 (Figure 3.11(b) based on the spectra given by (Richards *et al.*, 2007)).

Moreover, a similar partial simulation approach was recommended by Irwin (2008) for wind tunnel modelling of bridge decks is in agreement with the results of this study. Irwin (2008) suggested matching only a higher frequency range of the turbulence spectrum with the full-scale. The recommended high-frequency range for the bridge decks corresponds to reduced frequencies between approximately 0.1 and 1 which is in agreement with matching the critical reduced frequency range found in the present study. As discussed above, the critical turbulence length scales and frequencies are a function of the characteristic dimension of the structure. This explains the reason why the recommended critical frequencies for the bridge decks by Irwin (2008) contain higher frequencies as follows. Due to the larger characteristic length of the bridge decks, the critical reduced frequency range, 0.01$< fc/U <$1, contains mainly the high-end frequency of the turbulence spectrum. For small-scale structures, such as solar panels, due to the smaller characteristic length, this range of reduced frequencies will shift to slightly larger length scales of turbulence containing mid- to high-frequencies.

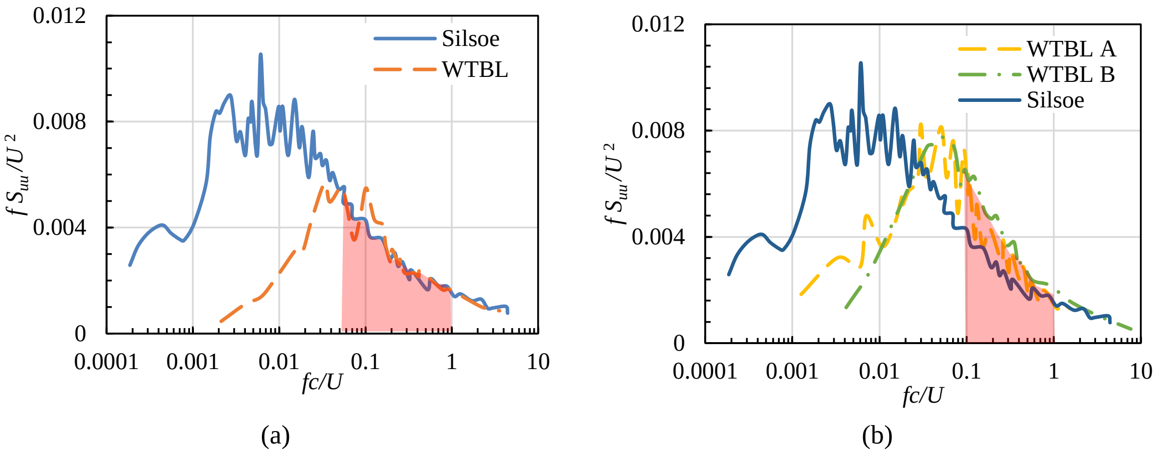

(a) (b)

Figure 3.11. The turbulence power spectra as a function of reduced frequency compared with the Silsoe site, for (a) The Auckland wind tunnel (Richards *et al.*, 2007), (b) Two different wind tunnel experiments (Hölscher and Niemann, 1998) reproduced from (Richards *et al.*, 2007). The red shaded area represents the critical reduced frequency range.

In order to demonstrate an example of the application of the results, the case of the flat plate mentioned in Section 3.1 is considered. Figure 3.12 shows the turbulence spectra of WTBL1 as a function of reduced frequency for different scaling ratios of the model compared to the full-scale spectra. The full-scale spectra were estimated from the modified Von Karman model by ESDU85020 (2010) and for an open-country terrain with a surface roughness of approximately 0.02 m and a mean velocity of 20 m/s. According to Figure 3.12(a), for model scaling ratios of 1:24 and 1:17 (a characteristic length dimension of 0.5 m and 0.7 m for the plate, respectively), a close match to the longitudinal spectrum for fc/U of between 0.1 and 1 is achieved, while a smaller model scaling ratio of 1:60 leads to a noticeable mismatch in the turbulence spectrum. Therefore, geometric scaling ratios of 1:24 and 1:17 can be used for measurement of the unsteady drag on the vertical flat plate. For the horizontal configuration of the flat plate, however, the vertical turbulence spectrum is more important. According to Figure 3.12(b), the closest match to the vertical turbulence spectrum can be achieved for the scaling ratio of 1:60. Using larger geometric scaling for the model leads to underestimation of the unsteady lift force on the stowed flat plate. Hence, for measurement of the unsteady drag force on the vertical flat plate, larger model scales can be used, while measurement of the unsteady lift force on the horizontal flat plate requires smaller model scales which is mainly due to the restricted generation of the vertical turbulence structures in the wind tunnel. The model scale should therefore be chosen according to the full-scale conditions and the WTBL turbulence characteristics for each case.

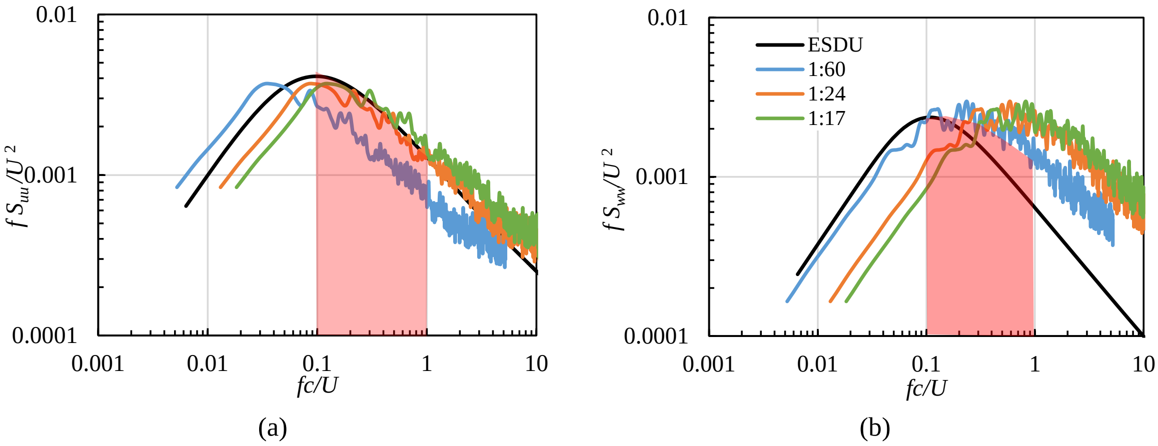

Figure 3.12. The effect of model scale on the mismatch of turbulence spectra, (a) The normalised power spectral density of longitudinal turbulence energy, fS_{uu}/U^2, (b) The normalised power spectral density of vertical turbulence energy, fS_{ww}/U^2, as a function of reduced frequency, fc/U. The red shaded area represents the critical reduced frequency range.

The effect of the turbulence spectrum on the unsteady wind loads and the dependency of the drag and lift coefficients on the critical reduced frequency range of the longitudinal and vertical turbulence spectra show the importance of matching the turbulence parameters in the wind tunnel experiments to those at full-scale. The obtained results suggest the possibility of achieving a unified wind load coefficient valid for all geometric scales by normalising the wind force with the turbulence characteristics of the flow. A similar approach was used by Richards *et al.* (2007) to normalise the pressure coefficient by the peak dynamic pressure instead of the mean dynamic pressure, and in this way, the effect of turbulence intensity was taken into account. However, further wind load measurements on full-scale structures are required to assess the applicability of normalisation of the forces with turbulence intensity and length scales.

3.7 Conclusion

The effect of mismatch of turbulence spectra on the unsteady wind loads in wind tunnel modelling of small-scale structures was investigated in this study. Wind loads on horizontal and vertical flat plates were measured in two simulated atmospheric boundary layers in a large-scale wind tunnel. The results showed that wind loading is frequency-dependant. It was found through spectral analysis that the turbulent eddies within a range of reduced frequencies between approximately 0.01 and 1 contributed the most to the unsteady wind loads on the flat plates. Based on the experimental results, it was proposed that this range of reduced frequencies of the turbulence spectrum should be correctly modelled in a wind tunnel experiment in order to minimise the scaling effects. The suitable geometric scaling ratio of the structure should then be determined based on the scaling ratio for which the turbulence spectrum as a function of reduced frequency is the closest match to that at full-scale.

The results were applied for determination of a suitable scaling ratio for wind tunnel modelling of a flat-plate like structure such as a solar tracker or heliostat as a case study. It was found that larger model dimensions could be used for measurement of the unsteady drag force on the vertical flat plate, while measurement of the unsteady lift force on the horizontal plate required models scaled down to smaller dimensions.

Acknowledgements

Financial support for the project has been provided by the Australian Government Research Training Program, the University of Adelaide Scholarship and the Australian Solar Thermal Research Initiative (ASTRI). The authors would like to acknowledge the School of Mechanical Engineering and the workshop at the University of Adelaide.

3.8 References

Aly, A. M., and Bitsuamlak, G. 2013. Aerodynamics of ground-mounted solar panels: Test model scale effects, *Journal of Wind Engineering and Industrial Aerodynamics*, 123: 250-60.

Bearman, P. W. 1971. An investigation of the forces on flat plates normal to a turbulent flow, *Journal of Fluid Mechanics*, 46: 177-98.

Bearman, P. W., and Morel, T. 1983. Effect of free stream turbulence on the flow around bluff bodies, *Progress in Aerospace Sciences*, 20: 97-123.

Bronkhorst, A., Franke, J., Geurts, C., van Bentum, C., and Grépinet, F. 2010. Wind tunnel and CFD modelling of wind pressures on solar energy systems on flat roofs. In *The fifth International Symposium on Computational Wind Engineering*.

Cook, N. J. 1978. Determination of the model scale factor in wind-tunnel simulations of the adiabatic atmospheric boundary layer, *Journal of Wind Engineering and Industrial Aerodynamics*, 2: 311-21.

Davenport, A. G. 1960. Rationale for determining design wind velocities, *ASCE Journal of the Structural Division*, 86: 39-68.

De Paepe, W., Pindado, S., Bram, S., and Contino, F. 2016. Simplified elements for wind-tunnel measurements with type-III-terrain atmospheric boundary layer, *Measurement*, 91: 590-600.

Drabble, M. J., Grant, I., Armstrong, B. J., and Barnes, F. H. 1990. The aerodynamic admittance of a square plate in a flow with a fully coherent fluctuation, *Physics of Fluids A: Fluid Dynamics*, 2: 1005-13.

Drobinski, P., Carlotti, P., Newsom, R. K., Banta, R. M., Foster, R. C., and Redelsperger, J.-L. 2004. The structure of the near-neutral atmospheric surface layer, *Journal of the Atmospheric Sciences*, 61: 699-714.

Dyrbye, C., and Hansen, S. O. 1996. *Wind Loads on Structures*, John Wiley & Sons.

Emes, M. J., Arjomandi, M., Ghanadi, F., and Kelso, R. M. 2017. Effect of turbulence characteristics in the atmospheric surface layer on the peak wind loads on heliostats in stow position, *Solar Energy*, 157: 284-97.

ESDU85020. 2010. Characteristics of atmospheric turbulence near the ground - Part II: single point data for strong winds (neutral atmosphere), *Engineering Sciences Data Unit*.

Fritz, W. P., Bienkiewicz, B., Cui, B., Flamand, O., Ho, T. C., Kikitsu, H., Letchford, C. W., and Simiu, E. 2008. International comparison of wind tunnel estimates of wind effects on low-rise buildings: Test-related uncertainties, *Journal of Structural Engineering*, 134: 1887-90.

Fung, Y. C. 2002. *An Introduction to the Theory of Aeroelasticity*, Dover Publications.

Högström, U., Hunt, J. C. R., and Smedman, A.-S. 2002. Theory and measurements for turbulence spectra and variances in the atmospheric neutral surface layer, *Boundary-Layer Meteorology*, 103: 101-24.

Holdø, A. E., Houghton, E. L., and Bhinder, F. S. 1982. Some effects due to variations in turbulence integral length scales on the pressure distribution on wind-tunnel models of low-rise buildings, *Journal of Wind Engineering and Industrial Aerodynamics*, 10: 103-15.

Holmes, J. D. 2007. *Wind Loading of Structures*, Taylor & Francis.

Hölscher, N., and Niemann, H.-J. 1998. Towards quality assurance for wind tunnel tests: A comparative testing program of the Windtechnologische Gesellschaft, *Journal of Wind Engineering and Industrial Aerodynamics*, 74-76: 599-608.

Hunt, A. 1982. Wind-tunnel measurements of surface pressures on cubic building models at several scales, *Journal of Wind Engineering and Industrial Aerodynamics*, 10: 137-63.

Irwin, H. P. A. H. 1981. The design of spires for wind simulation, *Journal of Wind Engineering and Industrial Aerodynamics*, 7: 361-66.

Irwin, P. A. 2008. Bluff body aerodynamics in wind engineering, *Journal of Wind Engineering and Industrial Aerodynamics*, 96: 701-12.

Jafari, A., Ghanadi, F., Arjomandi, M., Emes, M. J., and Cazzolato, B. S. 2018. The effect of turbulence intensity and length scale on the peak lift force on flat plates in longitudinal flows, *Journal of Wind Engineering and Industrial Aerodynamics (Under review)*.

Jafari, A., Ghanadi, F., Arjomandi, M., Emes, M. J., and Cazzolato, B. S. 2019. Correlating turbulence intensity and length scale with the unsteady lift force on flat plates in an atmospheric boundary layer flow, *Journal of Wind Engineering and Industrial Aerodynamics*, 189: 218-30.

Jafari, A., Ghanadi, F., Emes, M. J., Arjomandi, M., and Cazzolato, B. S. 2018. Effect of free-stream turbulence on the drag force on a flat plate. In *21st Australasian Fluid Mechanics Conference*. Adelaide, Australia.

Kozmar, H. 2011. Truncated vortex generators for part-depth wind-tunnel simulations of the atmospheric boundary layer flow, *Journal of Wind Engineering and Industrial Aerodynamics*, 99: 130-36.

Kozmar, H. 2012. Physical modeling of complex airflows developing above rural terrains, *Environmental Fluid Mechanics*, 12: 209-25.

Larose, G. L., and Livesey, F. M. 1997. Performance of streamlined bridge decks in relation to the aerodynamics of a flat plate, *Journal of Wind Engineering and Industrial Aerodynamics*, 69-71: 851-60.

Larose, G. L., and Mann, J. 1998. Gust loading on streamlined bridge decks *Journal of Fluids and Structures*, 12: 511-36.

Larose, G. L., Tanaka, H., Gimsing, N. J., and Dyrbye, C. 1998. Direct measurements of buffeting wind forces on bridge decks, *Journal of Wind Engineering and Industrial Aerodynamics*, 74-76: 809-18.

Lee, B. E. 1975. Some effects of turbulence scale on the mean forces on a bluff body, *Journal of Wind Engineering and Industrial Aerodynamics*, 1: 361-70.

Peterka, J. A., Tan, Z., Cermak, J. E., and Bienkiewicz, B. 1989. Mean and peak wind loads on heliostats, *Journal of Solar Energy Engineering*, 111: 158-64.

Pfahl, A. 2018. Wind loads on heliostats and photovoltaic trackers, *Eindhoven: Technische Universiteit Eindhoven*.

Pfahl, A., Buselmeier, M., and Zaschke, M. 2011. Wind loads on heliostats and photovoltaic trackers of various aspect ratios, *Solar Energy*, 85: 2185-201.

Radu, A., Axinte, E., and Theohari, C. 1986. Steady wind pressures on solar collectors on flat-roofed buildings, *Journal of Wind Engineering and Industrial Aerodynamics*, 23: 249-58.

Rasmussen, J. T., Hejlesen, M. M., Larsen, A., and Walther, J. H. 2010. Discrete vortex method simulations of the aerodynamic admittance in bridge aerodynamics, *Journal of Wind Engineering and Industrial Aerodynamics*, 98: 754-66.

Richards, P. J., Hoxey, R. P., Connell, B. D., and Lander, D. P. 2007. Wind-tunnel modelling of the Silsoe Cube, *Journal of Wind Engineering and Industrial Aerodynamics*, 95: 1384-99.

Roy, R. J., and Holmes, J. D. 1988. The effects of scale distortion on total wind loads on a low rise building model, *Journal of Wind Engineering and Industrial Aerodynamics*, 29: 273-82.

Ruscheweyh, H., and Windhövel, R. 2011. Wind loads at solar and photovoltaic modules for large plants. In *13th International Conference on Wind Engineering (ICWE)*. Amsterdam, Netherlands.

Saha, p. K., Yoshida, A., and Tamura, Y. 2011. Study on wind loading on solar panel on a flat-roof building: Effects of locations and inclination angles. In *13th International Conference on Wind Engineering (ICWE)*. Amsterdam, Netherlands.

Sankaran, R., and Jancauskas, E. D. 1992. Direct measurement of the aerodynamic admittance of two-dimensional rectangular cylinders in smooth and turbulent flows, *Journal of Wind Engineering and Industrial Aerodynamics*, 41: 601-11.

Stathopoulos, T., and Surry, D. 1983. Scale effects in wind tunnel testing of low buildings, *Journal of Wind Engineering and Industrial Aerodynamics*, 13: 313-26.

Stathopoulos, T., Zisis, I., and Xypnitou, E. 2012. Wind loads on solar collectors: A review. in, *Proceedings of Structures Congress 2012*.

Tieleman, H. W. 2003. Wind tunnel simulation of wind loading on low-rise structures: A review, *Journal of Wind Engineering and Industrial Aerodynamics*, 91: 1627-49.

Wooding, R. A., Bradley, E. F., and Marshall, J. K. 1973. Drag due to regular arrays of roughness elements of varying geometry, *Boundary-Layer Meteorology*, 5: 285-308.

Chapter 4

Effect of turbulence in the atmospheric boundary layer on wind loads

4.1 Chapter overview

As discussed in Section 2.3, an increase in turbulence intensity and/or length scale increases the wind loads on heliostats. Turbulence intensity and integral length scale in the neutral atmospheric boundary layer are dependent on terrain type and vary with surface roughness, such that for terrains with higher values of surface roughness the turbulence intensity is larger, while the integral length scale of turbulence is smaller, as shown in Figure 1.3. Therefore, heliostats are exposed to different values of turbulence intensity and length scale based on the surrounding terrain of the field. Furthermore, both the intensity and length scale of the turbulence vary with height from the ground. As the height from the ground increases, turbulence intensity decreases, while the integral length scale of turbulence increases (Figure 1.3). The hinge height of industrial heliostats from the ground is typically a function of the panel size and varies from approximately 1 m to 6 m. Hence, wind loads on heliostats depend on the turbulence characteristics at their corresponding height and surrounding terrain. A correlation between these two turbulence parameters and the wind loads is therefore of significance for the determination of design wind loads on heliostats that vary in size from 2 m^2 to 150 m^2 at industrial scale. Furthermore, such correlation can be used to establish a link between the measurements on scale-model heliostats in a wind tunnel and the wind loads on full-scale heliostats. As elaborated in Chapter 3, due to the differences between the turbulence properties in a wind tunnel experiment and the full-scale atmospheric surface layer, the measured wind loads on scale-model heliostats do not accurately represent the wind loads on full-scale heliostats. A relationship between the turbulence properties of the approaching flow and the wind loads can help to evaluate the wind loads on any given full-scale heliostat with respect to the turbulence properties in its surrounding terrain, eliminating the need to reproduce the specific atmospheric turbulence conditions for each full-scale case.

In this chapter, through experimental measurement of wind loads on heliostat models at various intensities and length scales of turbulence, a correlation between the turbulence intensity and integral length scale of the approaching flow and the peak lift and drag forces on heliostats is developed. The chapter consists of two sections, each focusing on a critical wind loading case for design of heliostats. In Section 4.2, the peak lift force on a heliostat at stow position, which represents the maximum survival load, is investigated, and in Section 4.3, the peak drag force on a vertical heliostat, which is the maximum drag force that a heliostat experiences during its operation, is studied.

A comprehensive analysis of the unsteady and peak lift force on a stowed heliostat over a range of intensities and length scales of turbulence in the approaching flow is presented in Section 4.2. An answer is provided to the question as to which turbulence component, streamwise or vertical, has a more dominant effect on the stow lift force. Through analysis of the effects of both streamwise and vertical turbulence components on the lift force, it is demonstrated that the lift force at stow position is a function of vertical intensity and integral length scale of the turbulence. The results show that the peak lift force on a stowed heliostat increases logarithmically with increasing the vertical turbulence intensity and vertical integral length scale. A correlation between these two turbulence parameters and the peak lift force is developed which can be used to determine the peak stow lift force coefficient based on the intensity and integral length scale of the vertical fluctuating velocity component. Furthermore, the developed correlation is used to predict the wind loads on full-scale heliostats at various heights in different terrains. The results show that by decreasing the height of the heliostat panel at stow position, due to the simultaneous changes in the integral length scale and intensity of the turbulence, the peak lift force coefficient decreases independent of the terrain type.

The drag force on a heliostat with vertical orientation of the mirror panel is investigated in Section 4.3. It is demonstrated that the unsteady and peak drag forces on a vertical heliostat are directly correlated with the intensity and integral length scale of the streamwise fluctuating velocity component. An empirical relationship is developed which describes the peak drag force as a function of the streamwise turbulence intensity and the longitudinal integral length scale. The established correlations in this chapter can be used to provide an evaluation of the peak lift and drag forces on full-scale industrial heliostats according to the heliostat size and the intensity and integral length scale of the turbulence in their surrounding terrain. This is of particular benefit for determination of the design wind loads as reliable wind load estimations can be obtained without the need to conduct a wind tunnel experiment for each specific full-scale condition.

4.2 Peak lift force on a stowed heliostat

This section consists of the following published journal article:

Jafari, A., Ghanadi, F., Arjomandi, M., Emes, M. J., and Cazzolato, B. S. 2019. Correlating turbulence intensity and length scale with the unsteady lift force on flat plates in an atmospheric boundary layer flow, *Journal of Wind Engineering and Industrial Aerodynamics*, 189: 218-30.

The article is identical to its published format with the following exceptions:

- The numbering of figures, tables and equations have been altered to include the chapter number.
- The position of some figures and tables have been changed to improve legibility.

The article in its published format is available at:
https://doi.org/10.1016/j.jweia.2019.03.029

Statement of Authorship

Title of Paper	Correlating turbulence intensity and length scale with the unsteady lift force on flat plates in an atmospheric boundary layer flow.	
Publication Status	■ Published ☐ Submitted for Publication	☐ Accepted for Publication ☐ Unpublished and Unsubmitted work written in manuscript style
Publication Details	Jafari, A., Ghanadi, F., Arjomandi, M., Emes, M. J., and Cazzolato, B. S. 2019. Correlating turbulence intensity and length scale with the unsteady lift force on flat plates in an atmospheric boundary layer flow, *Journal of Wind Engineering and Industrial Aerodynamics*, 189: 218-30	

Principal Author

Name of Principal Author (Candidate)	Azadeh Jafari		
Contribution to the paper	Developed ideas, conducted experiments, performed data analysis and interpreted results, wrote manuscript, and acted as corresponding author.		
Overall percentage (%)	75		
Certification	This paper reports on original research I conducted during the period of my Higher Degree by Research candidature and is not subject to any obligations or contractual agreements with a third party that would constrain its inclusion in this thesis. I am the primary author of this paper.		
Signature		Date	25/05/2020

Co-Author Contributions

By signing the Statement of Authorship, each author certifies that:

i. the candidate’s stated contribution to the publications is accurate (as detailed above);

ii. permission is granted for the candidate in include the publication in the thesis; and

iii. the sum of all co-author contributions is equal to 100% less the candidate’s stated contribution.

Name of Co-Author	Farzin Ghanadi		
Contribution to the paper	Supervised the development of the research, helped in developing ideas, contributed in academic discussion and manuscript review.		
Signature		Date	26/05/2020

Name of Co-Author	Maziar Arjomandi		
Contribution to the paper	Supervised the development of the research, participated in developing ideas and concepts, helped in interpretation of results, provided critical revision of manuscript.		
Signature		Date	25/05/2020

Name of Co-Author	Matthew Emes		
Contribution to the paper	Helped in the development of the research, contributed in academic discussion and manuscript review.		
Signature		Date	26/05/2020

Name of Co-Author	Benjamin Cazzolato		
Contribution to the paper	Supervised the development of the research, helped in developing ideas, contributed in academic discussion and manuscript review.		
Signature		Date	26/5/2020

Correlating turbulence intensity and length scale with the unsteady lift force on flat plates in an atmospheric boundary layer flow

Azadeh Jafari, Farzin Ghanadi, Maziar Arjomandi, Matthew J. Emes, Benjamin S. Cazzolato

Abstract

The correlation between turbulence intensity and length scale and the lift force on a horizontal flat plate in an atmospheric boundary layer flow is investigated in this study. Experiments were conducted in a large-scale wind tunnel to measure the peak loads on flat plate models of various chord length dimensions at different heights within simulated atmospheric boundary layers. The peak lift force coefficient on the flat plates was correlated with both turbulence intensity and length scale. The results show that the peak lift force coefficient on the flat plate is a function of vertical integral length scale (L_w^x) and vertical turbulence intensity (I_w) in terms of a parameter defined as $I_w(\frac{L_w^x}{c})^{2.4}$, where c is the chord length of the plate. An increase in this turbulence parameter from 0.005 to 0.054, increases the peak lift force coefficient from 0.146 to 0.787. The established relationship is then used to predict the peak wind loads on full-scale heliostats within the atmospheric surface layer as a case study. It is found that decreasing the ratio of heliostat height to the chord length dimension of the mirror panel from 0.5 to 0.2 leads to a reduction of 80% in the peak stow lift force coefficient, independent of the terrain roughness.

Keywords: Wind load, turbulence intensity, integral length scale, atmospheric boundary layer, Heliostat.

Nomenclature

A	plate area (m^2)
c	plate chord length dimension (m)
$C_{L,p}$	peak lift force coefficient
$C_{L,p(0.5)}$	peak lift force coefficient for H/c=0.5
F_L	lift force (N)
f	frequency (Hz)
H	height (m)
I_u	longitudinal turbulence intensity (%)
I_w	vertical turbulence intensity (%)

L_u^x	longitudinal integral length scale (m)
L_w^x	vertical integral length scale (m)
p	pressure (Pa)
R	autocorrelation of velocity
S_u	power spectral density of the longitudinal velocity fluctuation (m^2/s)
t	time (s)
τ_u^x	longitudinal integral time scale of turbulence (s)
U_∞	free-stream velocity (m/s)
u, v, w	absolute velocity components in the $x-, y-, z-$ flow directions, respectively (m/s)
U, V, W	time averaged mean velocity components in the $x-, y-, z-$ flow directions, respectively (m/s)
u', v', w'	fluctuating velocity components in the $x-, y-, z-$ flow directions, respectively (m/s)
x, y, z	distance in the stream-wise, lateral and vertical directions (m)
z_0	aerodynamic surface roughness length (m)
Symbols	
σ_u	standard deviation of longitudinal velocity fluctuations (m/s)
η	turbulence parameter
ρ	density (kg/m^3)
φ	angle of attack (rad)

4.2.1 Introduction

The turbulence within the atmospheric boundary layer (ABL) induces highly fluctuating aerodynamic loads on the structures within the ABL. An accurate estimation of the wind loads on structures is of high significance for their design. Wind loads on large civil structures such as buildings and bridges have been studied thoroughly in the literature. However, their design guidelines are not applicable to small-scale structures such as solar panels and heliostats. While these structures, which are placed at lower 10–20 m within the atmospheric surface layer (ASL), are exposed to highly turbulent wind conditions, the effect of atmospheric turbulence on their wind loads is not well known. With the increasing popularity of solar energy and the growth of solar panels and concentrating solar power plants, it is important to provide an accurate prediction of the wind loads on them since underestimation of the peak loads in the design process will lead to overstressing and consequently structural failure (Peterka, Tan, *et al.*, 1987). A common practice for reducing wind loads during extreme wind gusts is stowing the heliostats and solar trackers by aligning the mirror panel horizontally. In a turbulent flow such as the ASL, the significant force on stowed heliostats and solar trackers is the lift force which is caused by the variations in the pressure distribution on the upper and lower faces of the mirror panel as a turbulent eddy passes over it, as shown schematically in Figure 4.1. The lift force then induces a bending moment at the base of the pylon which is important for the design of solar trackers and heliostats. This study aims to investigate the effect of turbulence on the peak lift force on stowed heliostats and solar trackers, which can be represented by horizontal flat plates with a large ratio of characteristic length to thickness.

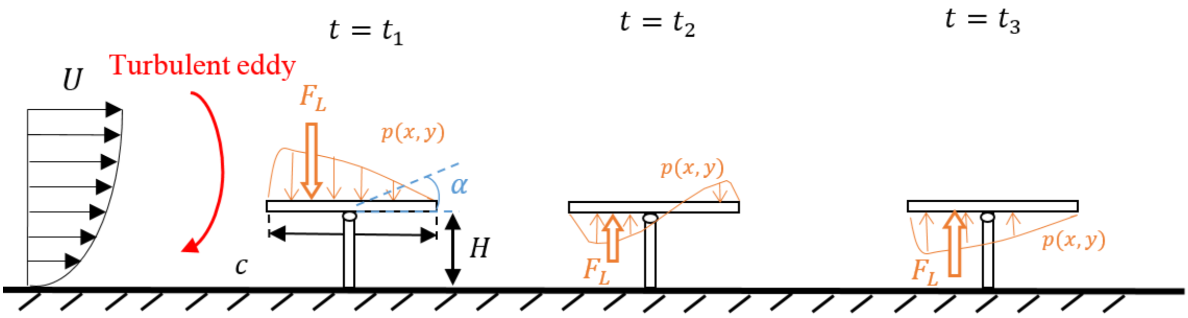

Figure 4.1. Fluctuating pressure distribution on a stowed heliostat within the atmospheric boundary layer based on the pressure measurements from (Emes et al., 2017; Gong et al., 2013) (Instantaneous pressure distributions at three random time steps are shown).

Wind loads on flat plates in boundary layer flows are found to increase dramatically with increasing turbulence intensity as indicated by wind tunnel experiments presented in the literature (Emes *et al.*, 2017; Emes *et al.*, 2018; Peterka *et al.*, 1989; Pfahl *et al.*, 2011). Peterka, Tan, *et al.* (1987) measured the wind loads on heliostat models within a simulated boundary layer in a wind tunnel, and found that the peak lift force coefficient on a stowed heliostat almost doubles when longitudinal turbulence intensity increases from 14% to 18%. Furthermore, it has been reported that the peak lift force coefficient on a stowed heliostat increases by 28% and 77% when the longitudinal turbulence intensity increases from 13% to 21% (Pfahl *et al.*, 2015) and from 7% to 26% (Jafari *et al.*, 2017), respectively. Emes *et al.* (2017) found that the peak lift force coefficient increases linearly as the longitudinal turbulence intensity increases from 10% to 14%. The reason for this dramatic effect is not yet known. Furthermore, there are discrepancies between the peak lift force coefficients on stowed heliostats reported by the different studies which were measured at similar turbulence intensities. As the peak lift force coefficient on a stowed heliostat at I_u=18% is reported to be 0.9 by Peterka, Tan, *et al.* (1987), in contrast to 0.49 by Pfahl *et al.* (2015). Also, according to Pfahl *et al.* (2015), the peak lift coefficient equals 0.46 at I_u=13%, while Emes *et al.* (2017) reports a coefficient of 0.83 at

I_u=12.5%. On the other hand, Pfahl (2018) proposed that that the peak and fluctuating lift force coefficients on a stowed heliostat depend on the vertical turbulence intensity, not the longitudinal one. This argument is, however, not well-established as both longitudinal and vertical turbulence intensities varied in the experiments by Pfahl (2018). Since in all the mentioned studies, both longitudinal and vertical turbulence intensities changed simultaneously, it not clear whether the observed effects were due to longitudinal turbulence intensity or vertical turbulence intensity. Therefore, this study aims to provide a deeper understanding of the effect of turbulence intensity on the peak lift force coefficient on a horizontal flat plate in terms of determination of the dominant turbulence component, i.e. longitudinal or vertical.

Another parameter which is found to affect the wind loads is the integral length scale of turbulence which expresses the average size of the most energetic eddies within the turbulent flow and is a key factor influencing the loads on bluff bodies within a turbulent flow (Bearman and Morel, 1983). The drag coefficient on a flat plate normal to a turbulent flow is found to be strongly dependent on the relative size of the longitudinal integral length scale to the chord length dimension of the plate (Bearman, 1971). The root-mean-square (RMS) of the drag coefficient increases dramatically by decreasing the plate’s chord length, which as taken equal to increasing L_u^x/c (Bearman, 1971). Measurement of the spectra of the unsteady longitudinal velocity component upstream of the stagnation point and its comparison with the spectra in the absence of the plate shows distortion of turbulence along the stagnation line, such that the small scale turbulence is amplified and the large scales are attenuated (Bearman and Morel, 1983). The distortion of turbulence when approaching a bluff body is postulated to depend on L_u^x/c. According to Holdø et al. (1982), when the integral length scale is much larger than the chord length of the plate, the flow behaviour is quasi-static and the effect of the bluff body on the turbulence is similar to its effect on the mean flow. Therefore, the energy of the fluctuating longitudinal velocity component is transferred to the vertical and lateral components as the flow approaches the plate. Holdø et al. (1982) proposes that when the integral length scale is much smaller than the chord length, stretching of the vortex lines is the dominant mechanism. Hence, the fluctuating longitudinal velocity component and thereby the longitudinal turbulence intensity increase and turbulence is amplified along the stagnation line, while the vertical and lateral components remain almost constant (Holdø et al., 1982). If the integral length scale is in the same order of the body’s crossflow dimension, a combination of both effects occurs (Bearman, 1971; Holdø *et al.*, 1982). The behaviour of a flow over a thin flat plate is however different from bluff bodies. Emes *et al.* (2017) reported that the peak lift force coefficient on a stowed heliostat increases by increasing the relative size of the longitudinal integral length scale of turbulence, L_u^x, to the chord length of the heliostat panel (L_u^x/c). However, in their experiments, both longitudinal and vertical integral length scales varied, and therefore it is not clear whether the observed increase in the peak lift force coefficient is due to the effect of L_u^x or L_w^x. The vertical length scale, L_w^x, seems to be important for a thin horizontal flat plate since the fluctuating lift is mainly dependent on the vertical velocity component (Rasmussen *et al.*, 2010). In order to provide a better understanding of the effect of longitudinal and vertical integral length scales on the lift force, it is necessary to distinguish their effects by further experimentation. Therefore, one of the aims of this study is to develop an understanding of the major contributor to the lift force, L_u^x or L_w^x, and to determine the correlation between the peak load on a horizontal flat plate in a with the integral length scale of turbulence.

Turbulence intensity and integral length scale vary with the height from the ground within the ASL. As the height in the ASL increases, the longitudinal integral length scale tends to get larger while turbulence intensity decreases (ESDU85020, 2010). Moreover, the effects of turbulence intensity and integral length scale are interrelated and cannot be separated. For instance, the peak and fluctuating pressures on a horizontal blunt flat plate (α=0°) are found to be strongly dependent on both turbulence intensity and length scale ratio such that the effect of L_u^x/c on the peak pressure is greater at higher turbulence intensities (Li and Melbourne, 1999; Shu and Li, 2017). The peak pressure on the plate which occurs near separation is found to increase with the parameter $I_u(L_u^x/c)^{0.15}$ (Li and Melbourne, 1995) where I_u and L_u^x are the turbulence intensity and integral length scale, respectively. Furthermore, the pressure coefficient on a normal flat plate (α=90°) is also a function of both turbulence intensity and L_u^x/c and increases logarithmically with the turbulence parameter $I_u(L_u^x/c)^2$ (Bearman, 1971). Hence, in order to provide an accurate prediction of wind loads on flat-plate-like structures, it is necessary to establish a correlation between the aerodynamic lift force coefficient on flat plates and both turbulence intensity and integral length scale.

The studies in the literature suggest the increase in the unsteady lift force on a horizontal flat plate with increasing turbulence intensity and integral length scales. However, none of the studies developed a strong argument, and no conclusion about the effect of turbulence was reached. While Emes *et al.* (2017); Peterka *et al.* (1989); Pfahl *et al.* (2011) proposed the longitudinal turbulence intensity to be important, Pfahl (2018) proposed the increase of the lift force to be due to the effect of vertical turbulence intensity. The main problem in the literature is that their results are simultaneously affected by both turbulence intensity and integral length scale, and both longitudinal and vertical components. For example, Emes et al. (2017) reported that increasing L_u^x/c led to increasing the peak lift coefficient. This result was obtained by measuring the forces on flat plates of different chord length dimensions at a constant flow condition, i.e. changing c to change L_u^x/c. However, it was not noted that L_w^x/c was also increasing, and the observed increase in the lift coefficient could be due to the increase of L_w^x/c. A similar limitation applies to the reported effect of I_u by Emes et al. (2017), as I_w and the integral length scales did not remain constant. As another example, Pfahl (2018) proposed that the peak lift coefficient on a stowed heliostat increased with increasing the vertical turbulence intensity, but could not differentiate the observed effect from the possible effect of longitudinal turbulence intensity as I_u increased as well. Furthermore, the integral length scales were not constant in the reported results by Pfahl (2018). Therefore, it is not yet known which turbulence component is of main impact on the fluctuating lift force on a horizontal flat plate. Hence, the objective of the present study is to develop a better understanding of the effect of turbulence intensity and length scale on the peak lift force on horizontal flat plate-like structures in the ASL. It aims to establish a correlation between the lift force with both turbulence intensity and integral length scale. To do so, the lift force on flat plates of different dimensions were measured at different heights within two simulated boundary layers in wind tunnel experiments. The turbulence characteristics of the wind tunnel boundary layers are described in Section 2. In Section 3, the experimental results are presented and a correlation between the turbulence characteristics and the wind loads is developed. The developed correlation is then used in Section 4 to predict the lift force on stowed heliostats within the ASL as a case study. Furthermore, the possibility of reduction of the lift force on a stowed heliostat by decreasing the stow height is discussed. The results of this study will contribute to a better understanding of wind loads on structures such as heliostats, solar trackers, and solar panels, and can be used to reduce wind loads on them.

4.2.2 Experimental method

Experiments were conducted in a large-scale wind tunnel at the University of Adelaide. The rectangular test section of the boundary layer wind tunnel has a cross-sectional area of 3 m × 3 m. The wind tunnel is designed for a maximum air speed of 33 m/s, and a boundary layer thickness of 0.2 m in the smooth flow at the heliostat location. The level of turbulence intensity in the empty tunnel is between 1% and 3% outside the boundary layer. As an initial stage, ABL was simulated in the wind tunnel by use of spires and roughness elements. Two sets of spires were first designed as non-truncated based on the desired power law exponent and boundary layer height using the empirical formula given by Irwin (1981). The design was then modified for part-depth simulation of the ABL based on Kozmar's part-depth method (Kozmar, 2011). In each set, three spires with identical dimensions, shown in Figure 4.2, were used placed at a centre-line distance of 0.9 m in the lateral direction. The flat plate model was placed downstream at a distance equal to 6 times the spire height which is expected to be sufficient for flow development (Irwin, 1981). The spires were followed by a 10 m fetch of wooden roughness elements of 90 mm × 90 mm cross section and 45 mm height. The sizing and spacing of the roughness elements were determined using the empirical equations by (Wooding *et al.*, 1973). The elements were placed with a spacing of 500 mm in all directions covering approximately 24% of the floor area over the fetch length. The experimental test setup is illustrated in Figure 4.3.

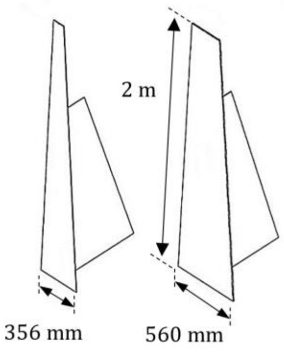

(a) (b)

Figure 4.2. Dimensions of the two spire sets: (a) Set 1, (b) Set 2.

The flat plate models comprise a square aluminium plate mounted on a pylon. In order to investigate the effect of height, pylons with heights of 0.14 m to 0.64 m, with an increment of 0.1 m, were built. Plates with chord lengths of 0.5 m, 0.6 m and 0.7 m and a thickness of 3 mm were used. This range of plate chord lengths and pylon heights delivered H/c ratios between 0.2 and 1.3. H/c =0.2 was the smallest ratio used in the experiments due to the technical challenges of building models with smaller H/c ratios and measuring forces on them. Heliostats and solar trackers are conventionally designed for height to chord length ratio, H/c, of about 0.5 (Téllez *et al.*, 2014). Hence, a range of H/c between 0.2 and 1.3 allowed investigation of the wind loads for higher and lower ratios.

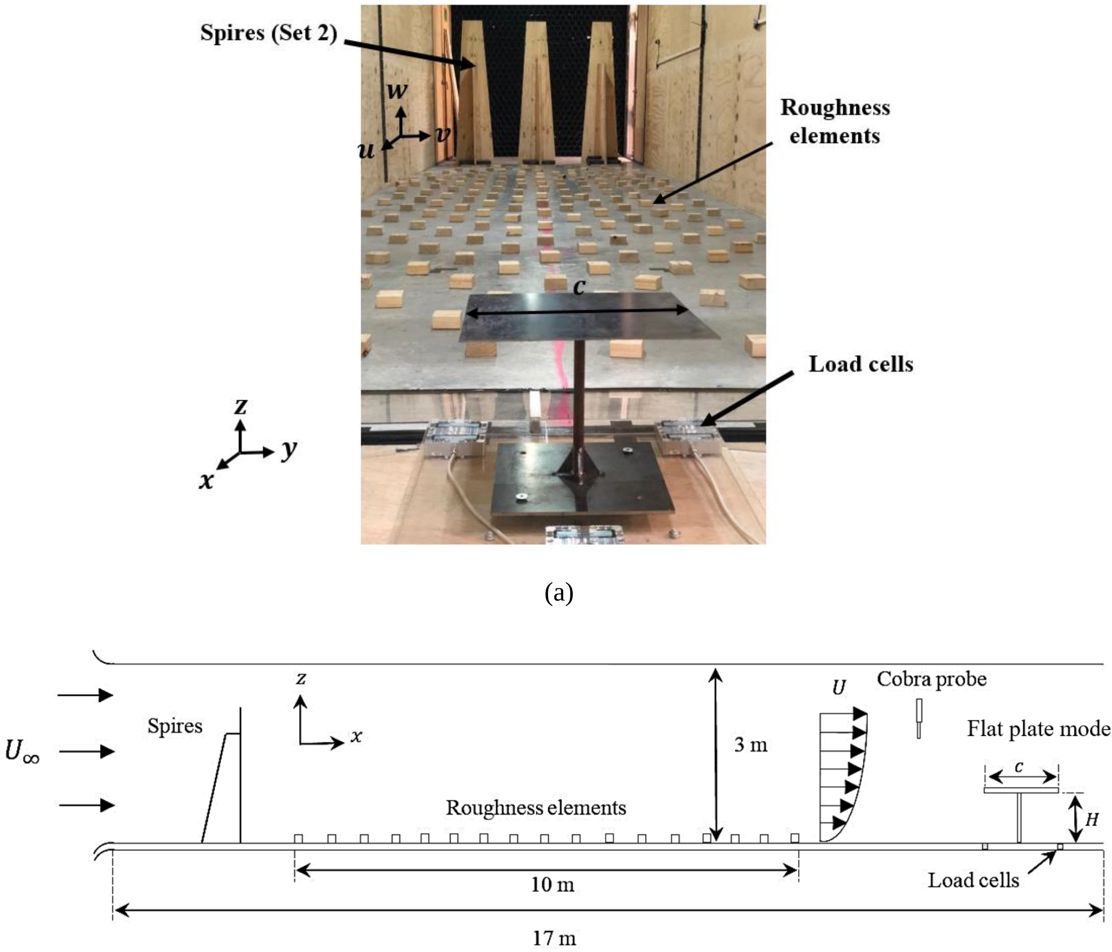

(a)

(b)

Figure 4.3. (a) Experimental test setup, (b) Schematic of the test section containing spires and roughness elements and the flat plate model.

The forces on the flat plate models were measured by three three-axis Bestech load cells (K3D50), each with a capacity of 50 N. The load cells were calibrated for a range of forces between 0-25 N. The measurement errors are found to be approximately 1.5% of the measured forces. Forces on the model were measured over a sampling period of 120 seconds, sampled at 1 kHz. It was determined through extreme value analysis that the estimated peak loads vary by less than 2% if the sampling period increases above 120 seconds. Therefore, this period was found to be sufficient. The peak values were determined based on extreme value analysis and the assumption of a Gaussian distribution as the sum of the mean value and three-times the root-mean-square of the fluctuating forces (Simiu and Scanlan, 1996). This method is used to predict the peak value from a set of data collected over a sampling time with 99.7% probability that forces will not exceed this value.

The lift force coefficient is found by the following equation:

$$C_L = \frac{F_L}{\frac{1}{2}\rho U^2 A} \tag{4.9}$$

where F_L represents the lift force on the plate, ρ is the air density, U is the mean velocity at plate height and $A = c^2$ represents the plate area. It must also be noted that absolute values for the lift force coefficient are given.

4.2.2.1 Simulation of the atmospheric boundary layer

Three components of velocity (u, v, w) were measured by a Turbulent Flow Instrumentation (TFI) multihole probe (Cobra probe), with an accuracy of ±0.5 m/s. The velocity measurements were taken downstream of the roughness fetch, with a longitudinal spacing of 500 mm up to the model position, over an area of 1 m^2 in both vertical and lateral directions, in order to investigate flow development. The flow characteristics at the model position and in the absence of the flat plate model are reported in this section. Data were sampled at a rate of 1 kHz for a duration of 150 s at each location. In order to reduce the experimental errors, the velocity measurements were repeated for five times and the average of five measurements was calculated.

Figure 4.4 shows the mean velocity profile as a function of height at three lateral locations in the wind tunnel boundary layers using the two spire sets (hereafter referred to as WTBL1 and WTBL2) at a freestream velocity of 11.5 m/s. The shaded areas in Figure 4.4 show the heights where the flat plate models were placed within the wind tunnel (z=0.14 m to 0.64 m). The mean velocity at the centre line (y=0) shows a maximum of 9% and 14% deviation from the side lines (y=$-$0.5, y=0.5) at the position of the heliostat model for WTBL1 and WTBL2, respectively. The velocity profiles of WTBL1 show a better lateral homogeneity than WTBL2 which is due to the higher separation and turbulence produced by the spires of Set 2. As the flat plate models are placed at a maximum lateral distance of 0.3 m from the centre line, the lateral homogeneity of both simulated boundary layers is acceptable and the measured velocity at the centre line is used for calculation of wind loads.

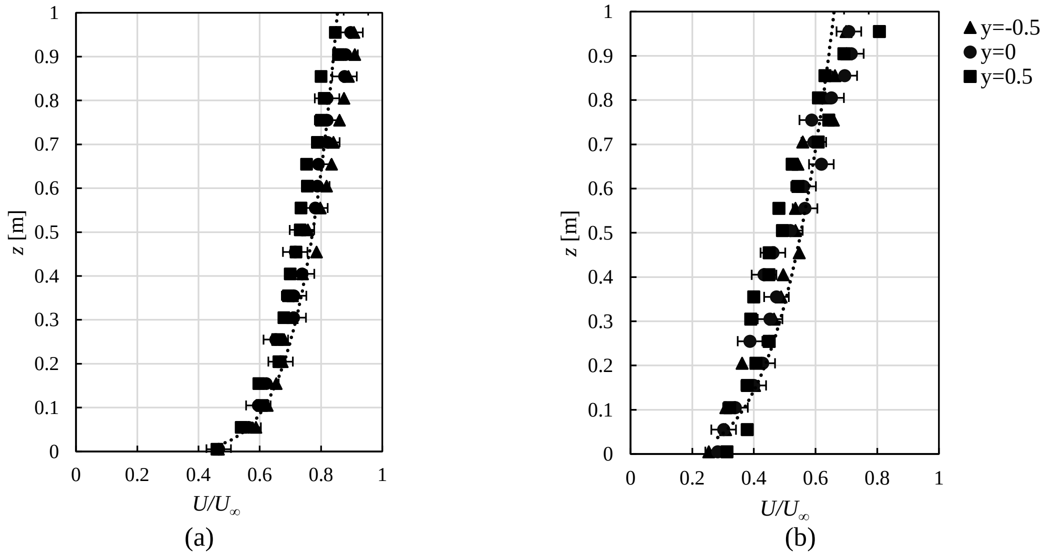

(a) (b)

Figure 4.4. Mean velocity profiles normalised with respect to the reference velocity (U_{∞}=11.5 m/s) at three lateral locations for: (a) WTBL1, Spire Set 1, (b) WTBL2, Spire Set 2, in model scale (The shaded area shows the height of the flat plate models in the wind tunnel).

Figure 4.5(a) shows the mean velocity profiles at the centre-line (y=0) of the wind tunnel measured at heights up to 1 m compared to the logarithmic profiles of the mean wind velocity within the ABL. The velocity profile of the boundary layer generated by Spire Set 1 matches a logarithmic profile with a roughness height of 0.018 m in full scale, with a maximum error of 2.3%. The mean velocity profile of WTBL2 represents a logarithmic profile with a roughness height of 0.35 m and a displacement height of 0.02 m in full scale, with a maximum error of 5% at the model position. Therefore, the mean velocity profiles of WTBL1 and WTBL2 provide a good representation of the mean wind velocity for z_0=0.018 m and z_0=0.35 m, respectively. The aerodynamic surface roughness lengths were determined from fitting the mean velocity profile of each simulation to the logarithmic law. It must be noted that as suggested by (De Paepe *et al.*, 2016; Holmes, 2007; Kozmar, 2012) the displacement height is negligible for flat and open country terrains whose surface roughness value is low while for suburban and urban areas with larger surface roughness, the displacement height must be taken into account. Therefore, the displacement height is only considered in the log law profile for WTBL2 with z_0=0.35 m, and it is considered negligible for WTBL1 which represents an open country terrain with z_0=0.018 m. Comparison of the mean velocity profiles with the power law profiles, as shown in Figure 4.5(b), also indicates that the boundary layer generated by Spire Set 1 matches a power law for α=0.18 and WTBL2 represents a power law profile for α=0.3. The power-law profiles in Figure 4.5(b) were determined by assuming a reference height within each boundary layer. According to De Paepe et al. (2016), an arbitrary height within the simulated boundary layer can be used as the reference for part-depth simulated boundary layers. the reference height was chosen as z_{ref} =1 m, as it is not in the vicinity of the ground or the ceiling of the tunnel, and is therefore not affected by the local effects of the roughness elements or the secondary boundary layer formed over the ceiling (De Paepe et al., 2016). Furthermore, this height is larger than the height of the flat plate models in the wind tunnel. The mean velocity obtained at different heights of each boundary layer are then normalised with the mean velocity at the reference height, which equals 10.87 m/s and 9.95 m/s for WTBL1 and WTBL2, respectively.

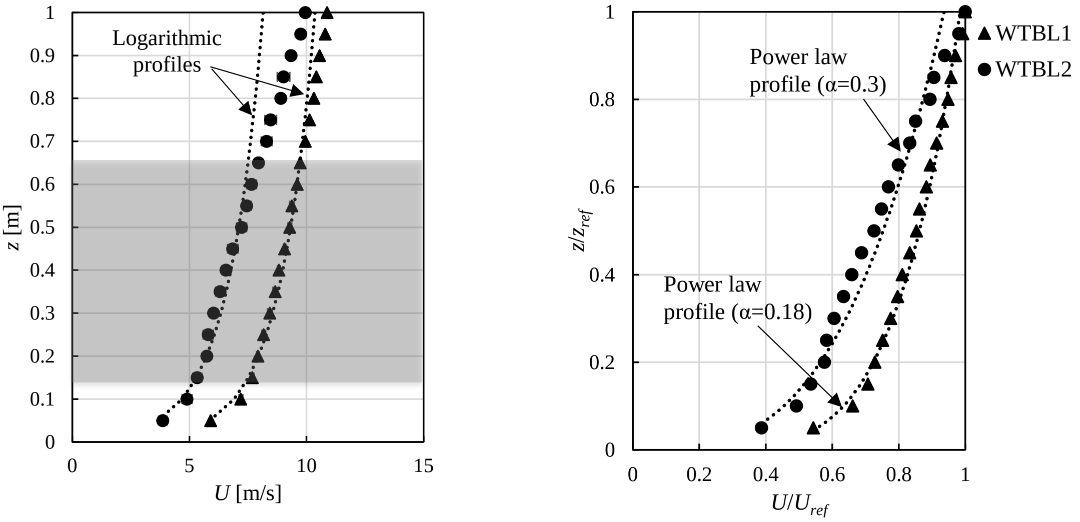

(a) (a)

Figure 4.5. Mean velocity profile of the boundary layers generated by the two spire sets in the wind tunnel in model scale, (a) comparison with logarithmic profiles. The error bars show the standard deviation calculated from five measurements, (b) comparison with power law profiles (The shaded area shows the height of the flat plate models in the wind tunnel).

In order to compare the characteristics of the wind tunnel boundary layers with the ASL, the simulation length scale factor was calculated for each boundary layer. The length scale factor was calculated using Cook’s method (Cook, 1978) from the aerodynamic surface roughness length and integral length scales at different heights within each boundary layer. The length scale factor of each boundary layer was then determined as the average of the calculated values for different heights. Hence, the simulation length scale factor was found to equal 1:151 and 1:90 for WTBL1 and WTBL2, respectively.

The turbulence characteristics of the flow in the two wind tunnel boundary layers including turbulence intensity, power spectral density and integral length scales are determined.

The turbulence intensity is calculated based on the measured velocity for heights up to 1 m in the wind tunnel for WTBL1 and WTBL2. Figure 4.6 shows the longitudinal and vertical turbulence intensity profiles achieved in WTBL1 and WTBL2 in the wind tunnel scale. The longitudinal turbulence intensity at the heights where the flat plate model is positioned (z=0.14 m to 0.64 m) in the wind tunnel is between 11% and 13% and between 24% and 28% for the WTBL1 and WTBL2, respectively. The vertical turbulence intensity at the model height in the wind tunnel is about 9% for the WTBL1, and is about 19% for the WTBL2. Turbulence intensity profiles from the wind tunnel measurements for heights up to 1 m are converted to match the full scale height using the simulation length scale factors, 1:151 and 1:90 for WTBL1 and WTBL2, respectively. Turbulence intensity for a similar terrain type to each WTBL was estimated according to ESDU85020 (2010) and (ESDU74031, 1974). The longitudinal and vertical turbulence intensity profiles from WTBL1 and WTBL2 are shown in Figure 4.6(b-c) and Figure 4.6(d-e), respectively. The solid and dashed lines show the upper and lower bounds of the ESDU 74031 and ESDU 85020 ranges, respectively, which are represented as ±20% from the calculated mean values which is suggested as the allowable bandwidth (ESDU85020, 2010). According to Figure 4.6(b-d), both longitudinal and vertical turbulence intensity profiles of WTBL1, and the longitudinal turbulence intensity in WTBL2 are within the ESDU range. The vertical turbulence intensity for WTBL2 is, however, larger than the ESDU estimations (Figure 4.6(e)).

The longitudinal and vertical power spectral density functions of the two wind tunnel boundary layers, at z=0.3 m, are shown in Figures 4.7(a) and 4.7(b), respectively. The non-dimensional power spectral density is compared with the spectra predicted by the theoretical models of von Kármán (1948) which is also recommended by ESDU85020 (2010) to compare the distribution of turbulence energy in the wind tunnel with that at the ASL. The power spectra of both wind tunnel boundary layers show a similar distribution to that of von Kármán which indicates that the turbulence energy distribution in both boundary layers at the model heights is similar to the ASL. Figure 4.7(b) shows a noticeable shift in the frequency of the peak of the vertical power spectra to higher frequencies. The shift in the peak of power spectra to smaller length scales, which is also reported by Pfahl *et al.* (2015), is due to the different mechanism of turbulence generation in the tunnel compared to the ABL. Furthermore, the larger magnitude of the vertical power spectra for WTBL2 indicates the larger vertical turbulence intensity in the wind tunnel compared to the estimations of the ASL.

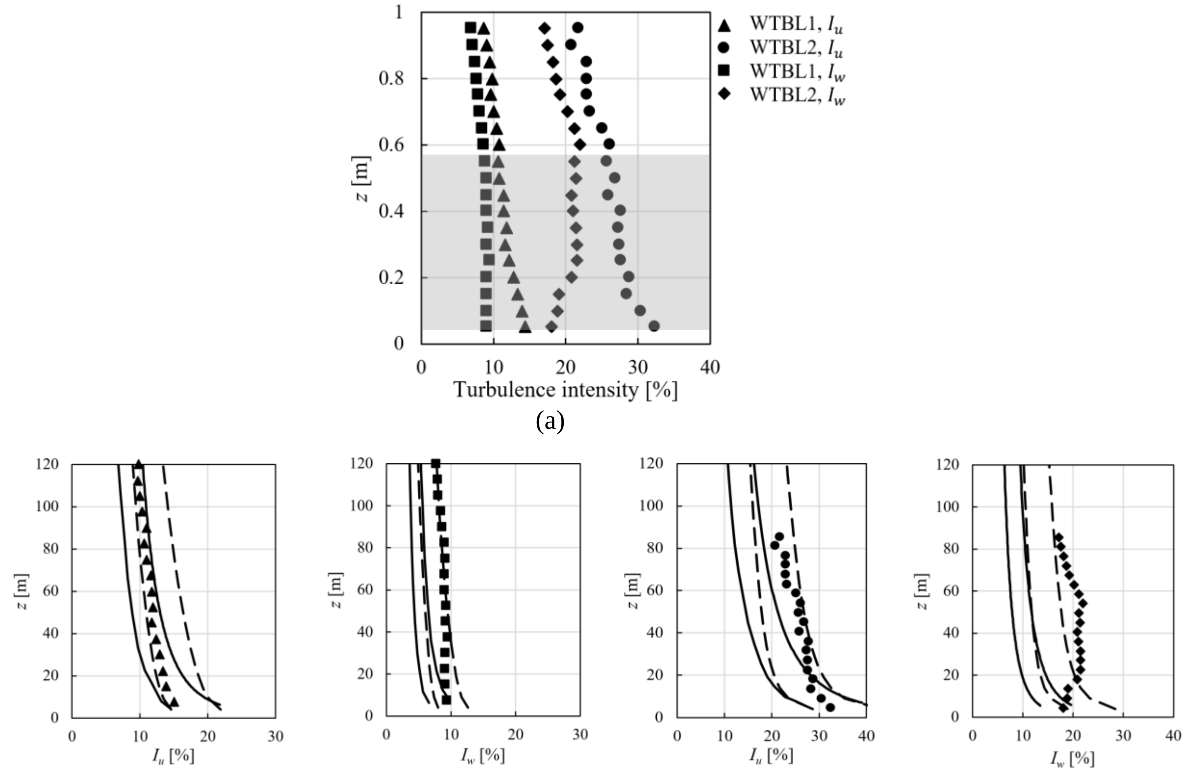

(a)

(b) (c) (d) (e)

Figure 4.6. (a) Longitudinal and vertical turbulence intensity profiles for WTBL1 and WTBL2 in the wind tunnel scale (The shaded area shows the height of the flat plate models in the wind tunnel), (b–c) Full-scale longitudinal and vertical turbulence intensity profiles in 1:151 ABL simulations for WTBL1 compared with ESDU 85020 and ESDU 74031 profiles, (d–e) Full-scale longitudinal and vertical turbulence intensity profiles in 1:90 ABL simulations for WTBL2 compared with ESDU 85020 and ESDU 74031 profiles (The solid and dashed lines show the upper and lower bound of the estimated range from ESDU 74031 and ESDU 85020, respectively).

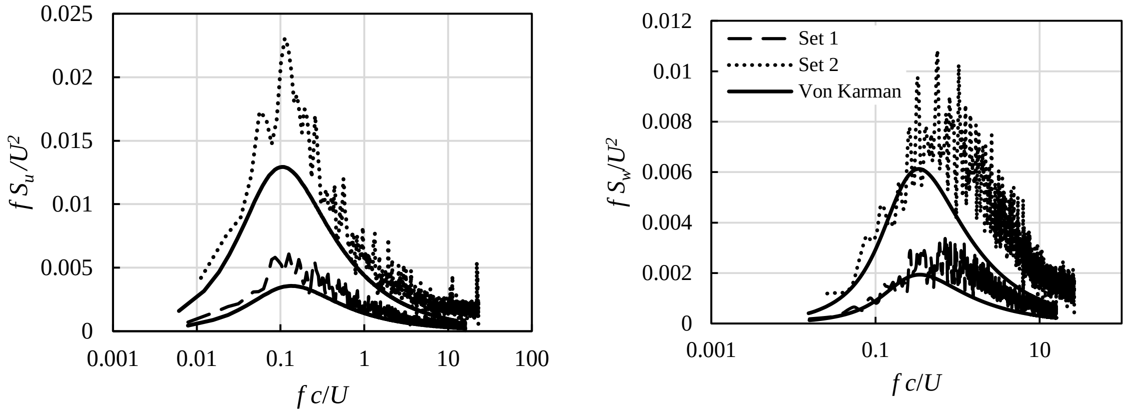

(a) (b)

Figure 4.7. Power spectral density of (a) longitudinal and (b) vertical velocity fluctuation of WTBL1 and WTBL2 as a function of non-dimensional frequency, fc/U, at z=0.3 m, for c=0.5 m (U is the mean velocity at z=0.3 m).

The longitudinal and vertical integral length scales were calculated based on Taylor’s hypothesis assuming that the eddies are transported by the mean velocity. In this method, the integral time scale of turbulence is calculated from equation (4.2) by integration of the auto-correlation of fluctuating longitudinal or vertical velocity components given by equation (4.3). The length scale is then found by multiplying the integral time scale by the mean velocity as given in equation (4.4) (Farell and Iyengar, 1999). This method for calculation of integral length scales produces smaller errors compared to other methods, i.e. determination of the value of the spectrum at zero frequency, and semi-empirically from the location of the spectral peak. The former involves significant errors due to lack of adequate resolution at low frequencies (Iyengar and Farell, 2001). Determination of the central peak also leads to errors due to the noise (De Paepe et al., 2016). Therefore, the integral length scales were calculated from the auto-correlation method in this study.

$$\tau_i^x = \int R_i(\tau)d, \quad i = u, w \tag{4.2}$$

$$R_u(\tau) = \frac{\overline{u'(t)u'(t+\tau)}}{\sigma_u^2} \tag{4.3}$$

$$L_i^x = \tau_i^x\, U \tag{4.4}$$

The longitudinal and vertical integral length scales, L_u^x and L_w^x, in the wind tunnel scale for the two boundary layers are shown in Figure 4.8. There is some scatter in the length scale values which is also reported in the literature (De Paepe *et al.*, 2016; Emes *et al.*, 2018; Kozmar, 2011; Watkins *et al.*, 2006) and is due to limited sampling time and measurement techniques. However, in order to reduce the scatter in the data and to eliminate the error in the determination of the integral length scales, velocity measurements in the wind tunnel were repeated for five times and the average (and standard deviation) of five measurements is reported in Figure 4.8.

According to Figure 4.8, the vertical length scale generally decreases as the height in the wind tunnel decreases. In contrast, at heights below 0.2 m, the longitudinal length scale becomes larger as the ground is approached. Above 0.2 m, the longitudinal length scale overall increases as the height from the ground increases. This is due to the turbulence generation technique in the wind tunnel. The spires generate larger turbulence structures close to the ground due to their larger width near the ground. As the height from the ground increases, the width of the spires decreases and smaller turbulence structures are developed. The generated eddies then grow over the longitudinal development length. While at heights below 0.2 m, the development of the eddies is influenced by the ground effect, as the height from the ground further increases, the eddies grow and get larger. The growth and development of the eddies is nevertheless restrained due to the limited cross-section of the wind tunnel as noted in other wind tunnel simulations of the ABL (Banks, 2011; De Paepe *et al.*, 2016; Iyengar and Farell, 2001; Kozmar, 2012; Leitch *et al.*, 2016; Peterka *et al.*, 1998) which reported that the length scales did not increase with height at the same increasing rate observed in the atmosphere. Experimental results in the literature show that the integral length scales in the wind tunnel increase with height but remain almost constant as the height from the ground further increases to reaching towards the ceiling of the tunnel (De Paepe *et al.*, 2016; Iyengar and Farell, 2001; Kozmar, 2011). Unlike the longitudinal length scales, the vertical length scales do not get larger with the increasing width of the spires near the ground since the vertical structures are restrained by the ground. Despite the different mechanism of turbulence generation in the wind tunnel and the atmosphere, the increase in L_u^x and the decrease in L_w^x near the ground is also observed in the lower part of the ASL which is due to the elongation of the turbulent eddies near the ground. In the lower 10 m to 20 m of the ASL, at near-neutral conditions, the eddies, which originate in the lower parts of the middle layer above the surface layer, get stretched and blocked by the ground as they impinge upon it. Consequently, the vertical velocity tends to zero near the ground (Högström *et al.*, 2002; Hunt and Carlotti, 2001).

According to Figure 4.8, the longitudinal and vertical integral length scales in WTBL2 are larger than those for the WTBL1. The longitudinal integral length scales at the heliostat positions are between 0.66 m to 0.75 m for WTBL2, while they are about 0.52 m to 0.67 m for WTBL1. According to Figure 4.8, the vertical length scales at the heliostat positions are between 0.2 m to 0.25 m for WTBL1 and between 0.27 m to 0.35 m for WTBL2. Therefore, the flat plate models can be exposed to different scales of turbulence within the two simulated boundary layers which allows investigation of the effect of the relative size of the integral length scale to the chord length on the loads. Figure 4.8(b–e) show the longitudinal and vertical integral length scales within the two wind tunnel boundary layers converted to full scale in comparison with the recommended ESDU 74031 and ESDU 85020 ranges for the corresponding open country and suburban terrains. The integral length scales are in general within the ranges predicted by ESDU 85020 and ESDU 74031.

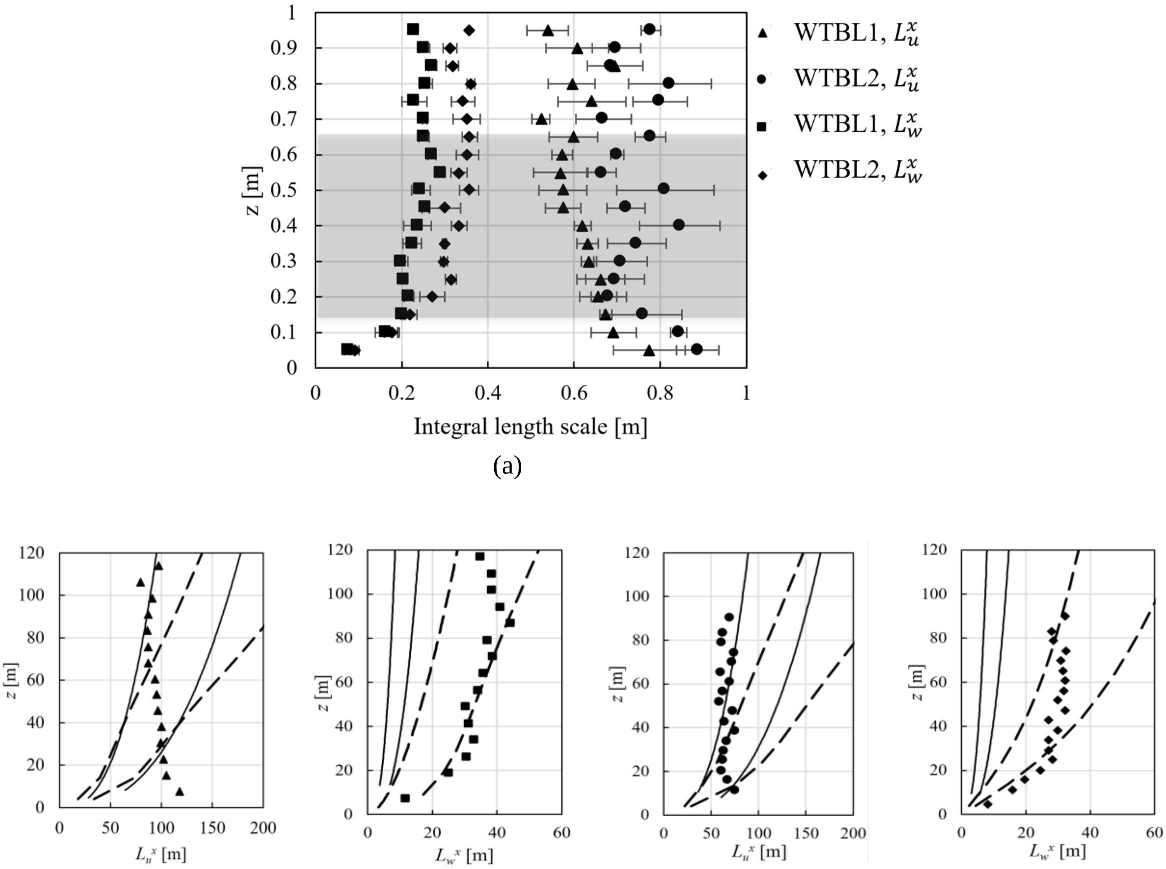

(a)

(b) (c) (d) (e)

Figure 4.8. (a) Longitudinal and vertical integral length scales for WTBL1 and WTBL2 in the wind tunnel scale (The error bars show the standard deviation calculated from five measurements), (b-c) Full-scale longitudinal and vertical integral length scales in 1:151 ABL simulations for WTBL1 compared with ESDU 85020 and ESDU 74031 profiles, (d-e) Full-scale longitudinal and vertical integral length scales in 1:90 ABL simulations for WTBL2 compared with ESDU 85020 and ESDU 74031 profiles (The solid and dashed lines show the upper and lower bound of the estimated range from ESDU 74031 and ESDU 85020, respectively).

A summary of the velocity and turbulence characteristics of the two wind tunnel boundary layers is given in Table 4.1.

Table 4.1. Summary of the characteristics of the two wind tunnel boundary layers (the turbulence intensity and length scales are given for the heights of the heliostat models). The aerodynamic surface roughness and the integral length scale are given in model scale.

	Length scale factor	z_0**(mm)**	I_u**(%)**	I_w**(%)**	L_u^x **(m)**	L_w^x **(m)**
WTBL1	1:151	0.12	11	9	0.52–0.67	0.2–0.25
WTBL2	1:90	3.88	26	19	0.66–0.75	0.27–0.35

4.2.3 Results

In order to find the effect turbulence characteristics on the wind loads, forces on horizontal flat plate models with varying pylon heights (with H/c ratios between 0.2 and 1.3) were measured. The measurements were undertaken at longitudinal turbulence intensities of approximately 11% and 26% and vertical turbulence intensities of approximately 9% and 21% produced within the wind tunnel boundary layers using the two spire sets. Furthermore, three square plates with chord length dimensions of 0.5, 0.6 and 0.7 m were used to achieve different ratios of L_u^x/c and L_w^x/c. Figure 4.9 shows the variations of the peak lift force coefficient on the horizontal flat plates with changing the flat plate heights as a function of H/c. It is found that $C_{L,p}$ decreases linearly with reducing H/c, which agrees with the results reported by Emes et al. (2017) who found a similar trend for the peak lift force coefficient on stowed heliostats for H/c values between 0.5 and 1.3. The results reported by Emes et al. (2017) were limited to H/c=0.5 and lower turbulence intensity (I_u=6–12.5%). The results of the present study shown in Figure 4.9 indicate that $C_{L,p}$ on a stowed heliostat is further reduced by decreasing H/c to below 0.5. According to Figure 4.9, reducing H/c from 0.5 to 0.2 reduces $C_{L,p}$ from approximately 0.3 to 0.2 at an average vertical turbulence intensity of 9%, and from 0.65 to 0.48 at an average vertical turbulence intensity of 19%. Furthermore, as shown in Figure 4.9, the rate of reduction of $C_{L,p}$ with reducing H/c is larger in WTBL2, where the turbulence intensity and integral length scales are larger than those in WTBL1, such that the slope of the linear trend for WTBL2 is three times larger than WTBL1 ($\frac{dC_{L,p}}{d(H/c)}$=0.18 and 0.67 for WTBL1 and WTBL2, respectively).

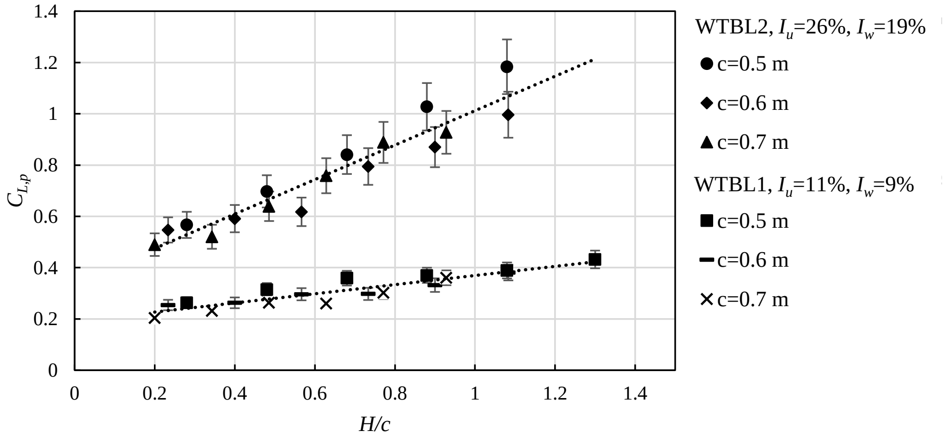

Figure 4.9. The effect of height to chord length ratio, H/c, on the peak lift force coefficient on a horizontal flat plate, $C_{L,p}$, for WTBL1, $I_u = 11\%$ and I_w =9%, and WTBL2, $I_u = 26\%$ and I_w =19%.

Reduction of the peak lift force coefficient with the reduction of the height of the flat plate shown in Figure 4.9 is due to the effect of turbulence. As the height of each flat plate within each boundary layer is reduced from 0.64 m to 0.14 m, it is exposed to a different turbulence condition. According to Figure 4.6 and as shown in Table 4.1, longitudinal and vertical turbulence intensity remain almost constant (varying by less than 2%) over the range of heights between 0.14 m and 0.64 m. Therefore, the reduction of $C_{L,p}$ with height for each plate in each boundary layer is not related to turbulence intensity. On the other hand, the integral length scales of turbulence vary with height in each boundary layer. Therefore, the reduction of $C_{L,p}$ is due to the effect of the integral length scale of turbulence. According to Figure 4.8, as the height reduces from 0.64 m to 0.14 m in each boundary layer, L_w^x decreases while L_u^x does not consistently decrease and increases at some heights. Hence, reduction of $C_{L,p}$ for a single flat plate (constant c) as H reduces is due to the reduction of L_w^x. The effect of L_w^x on the peak lift force coefficient is shown in Figure 4.10, which presents the change in the peak lift force coefficient as a function of L_w^x/c, for each flat plate (constant chord length dimension) as the height of the pylon changes. As the height of the plates from the ground reduces, the vertical length scales and consequently L_w^x/c for each plate size decrease, which results in the reduction of the peak lift force coefficient as shown in Figure 4.10. For instance, reducing L_w^x/c from 0.7 to 0.54 reduces the peak lift force coefficient from approximately 1.18 to 0.57 for c=0.5 m and I_w =19%. Similarly, $C_{L,p}$ reduces from 0.43 to 0.26 by reducing L_w^x/c from 0.51 to 0.43 for c=0.5 m and I_w =9%. The results in Figure 4.10 show that $C_{L,p}$ increases as a power function of L_w^x/c, with an exponent between 2.2 and 2.5.

As the height within the simulated boundary layers decreases, the vertical velocity component is reduced due to the no-slip effect of the ground. According to Figure 4.8, with the decrease of the height within the boundary layer, L_w^x decreases and the vertical to longitudinal length scale ratio, L_w^x/L_u^x reduces, which represents how the eddies are more elongated in the longitudinal direction at the lower heights near the ground resulting in smaller magnitude of the vertical velocity component. As the eddy hits the plate, the vertical velocity component, which is normal to the flat plate, produces the vertical lift force by generating pressure and suction on the plate surface. L_w^x represents the longitudinal distance over which the vertical velocity components are well correlated. L_w^x/c is indicative of the extent to which the eddies engulf the plate. Therefore, less lift is produced on larger plates with smaller L_w^x/c since a smaller area of the plate is impacted by the vertical velocity component of the eddy. Therefore, the reduction of the vertical length scales at lower heights close to the ground leads to the reduction of the fluctuating component of the lift force coefficient.

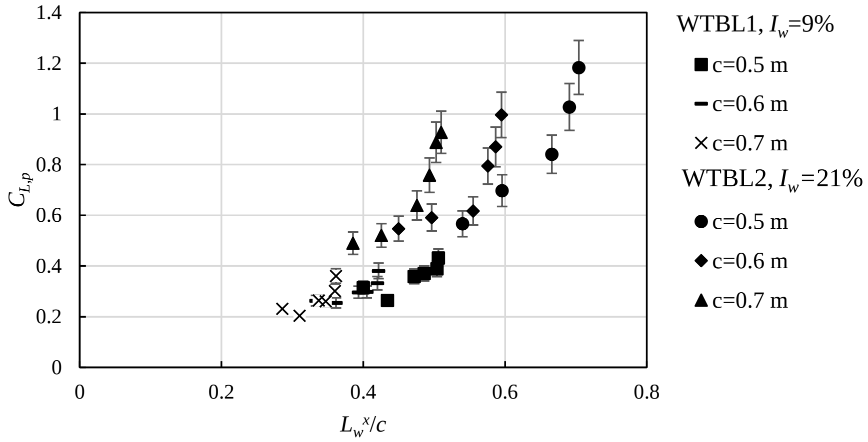

Figure 4.10. The effect of vertical integral length scale to chord length ratio, L_w^x/c, on the peak lift force coefficient, $C_{L,p}$, on a horizontal flat plate within WTBL1, I_w =19%, and WTBL2, I_w =9%.

Emes *et al.* (2017) proposed that the peak lift force coefficient on a stowed heliostat increases linearly with L_u^x/c. The trend reported by Emes *et al.* (2017) was achieved by measuring the lift force coefficient on flat plates of different chord length dimensions at a constant height and constant L_u^x and L_w^x. The ratio of L_u^x/c was varied by changing only c while L_u^x was constant. While c increased, both L_u^x/c and L_w^x/c decreased. However, the effect of variation of L_w^x/c was not taken into account. Therefore, the reported results by Emes *et al.* (2017) were simultaneously affected by both longitudinal and vertical turbulence length scales. The method used in the present study is different from Emes *et al.* (2017) as the effect of integral length scale is investigated by exposing a single flat plate with a constant c to different turbulence length scales by changing the height of the plate in the boundary layer. To achieve a larger set of data, flat plates of different dimensions were used in two boundary layers. In the results of the present study shown in Figure 4.10, L_u^x and L_w^x are varied for a constant value of c by changing the height of each plate in the two boundary layers. Although both L_u^x/c and L_w^x/c are varied in the current experiments, the results show that $C_{L,p}$ is more strongly correlated with L_w^x/c (Figure 4.10). Therefore, the vertical integral length scale, L_w^x, is the major contributor to the lift force on the horizontal flat plate, not L_u^x. This is further supported by comparison of $C_{L,p}$ for cases with similar L_u^x/c and different L_w^x/c, as presented in Figure 4.11. For instance, the peak lift force coefficient increases from 0.62 to 1.18 as L_w^x/c increases from 0.55 to 0.7 although L_u^x/c remains constant at approximately 1.4. Another example is increase of $C_{L,p}$ from approximately 0.54 to 0.99 when L_w^x/c increases from 0.45 to 0.59 at L_u^x/c=1.1. Hence, the results show that the peak lift force coefficient increases with increasing L_w^x/c.

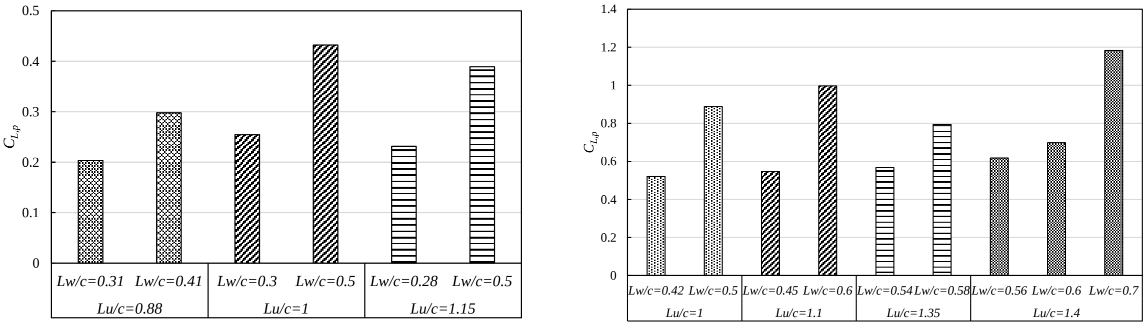

(a) (b)

Figure 4.11. Comparison of the peak lift force coefficient for cases with similar L_u^x/c and different L_w^x/c, (a) WTBL1, I_u =11% and I_w =19%, (b) WTBL2, I_u =26% and I_w =21%.

The dependency of the fluctuating lift force on the fluctuating vertical velocity component found in the present study is in agreement with that reported by (Larose and Livesey, 1997; Pfahl, 2018; Rasmussen *et al.*, 2010). Assuming quasi-steady aerodynamics, the lift force coefficient can be defined as a linear function of the angle of attack (φ) (Rasmussen *et al.*, 2010),

$$C_L(\varphi) = C_{L,0}(\varphi = 0) + \frac{\partial C_L}{\partial \varphi}\varphi \tag{4.5}$$

where the instantaneous angle of attack is given by $\varphi = \frac{w}{U+u'}$. Rasmussen *et al.* (2010) shows that the lift force on a horizontal flat plate caused by the fluctuating wind can be expressed as,

$$F_L = \frac{\rho U A}{2}\left(2C_{L,0}u' + \frac{\partial C_L}{\partial \varphi}w'\right) \tag{4.6}$$

where $C_{L,0}$ and $\frac{\partial C_L}{\partial \varphi}$ represent the lift force coefficient at $\varphi = 0$ and the slope of the lift force coefficient at near zero angle of attack, respectively. $C_{L,0}$ and $\frac{\partial C_L}{\partial \varphi}$ can be determined through static tests by measuring the lift force on flat plates at small elevation angles according to the method given by Cigada *et al.* (2002), and were measured to be equal to -0.11 and 2.90 respectively. The experimental values of $C_{L,0} = -0.11$ and $\frac{\partial C_L}{\partial \varphi}$=2.9 are in agreement with those reported for bridge decks (Larose *et al.*, 1998) showing that $\frac{\partial C_L}{\partial \varphi}$ is much larger compared to $C_{L,0}$. Based on Equation (4.6) and since $\frac{\partial C_L}{\partial \varphi}$ is much larger in magnitude compared to $C_{L,0}$, the lift force is mainly influenced by the vertical velocity component.

The effect of vertical turbulence intensity can also be seen in Figure 4.10, as at similar values of L_w^x/c, $C_{L,p}$ is larger for the WTBL2 where the turbulence intensity is larger. For example, at L_w^x/c=0.5, $C_{L,p}$ equals approximately 0.43 and 0.6 for I_w =9% and I_w =19%, respectively. Therefore, the peak lift force coefficient is a function of both integral length scale and turbulence intensity. This relationship can be expressed in terms of the turbulence parameter represented by $\eta = I_w(\frac{L_w^x}{c})^{2.4}$. Similar parameters defined by longitudinal turbulence intensity and length scale have been correlated with the pressure coefficient on a flat plate normal to the flow in terms of $I_u(\frac{L_u^x}{c})^2$ by Bearman (1971), and a thick blunt horizontal plate as $I_u(\frac{L_u^x}{c})^{0.15}$ by Li and Melbourne (1995) in which the flow is different from the case of a thin horizontal flat plate in an atmospheric boundary layer flow. As described earlier, the fluctuating lift force on the flat plate is induced by the vertical velocity component resulting from the variations in the angle of attack of the flow induced by the turbulent eddies (see Equation (4.6)). The turbulence parameter is calculated for the three chord length dimensions (c=0.5, 0.6, 0.7 m) of the plates within WTBL1 and WTBL2 and the investigated H/c ratios between 0.2 and 1.3. For the flat plate in a boundary layer flow, the current experimental data suggest the best fit for $C_{L,p}$ is achieved for $\eta = I_w(\frac{L_w^x}{c})^{2.4}$. Figure 4.12 shows the peak lift force coefficient as a function of η. According to Figure 4.12, $C_{L,p}$ increases logarithmically with the turbulence parameter, which can be described by the following correlation:

$$C_{L,p} = 0.267\ln(\eta) + 1.566 \tag{4.7}$$

This finding is in agreement with that found by Bearman (1971) reporting that the pressure coefficient on a plate normal to the turbulent flow increases logarithmically with the turbulence parameter, $I_u(\frac{L_u^x}{c})^2$. The turbulence parameter can be interpreted as an expression of the entrainment of the turbulence energy (Bearman, 1971). The dependency of the lift force on the turbulence parameter indicates that the force is the result of both spatial and temporal coherence of vertical turbulence energy. The determined relationship in terms of the turbulence parameter indicates that the peak lift force coefficient is more sensitive to L_w^x/c than to turbulence intensity, I_w. Therefore, the effect of the spatial distribution of vertical turbulence energy on the peak lift force coefficient on a stowed heliostat is more significant than the temporal release of turbulent energy.

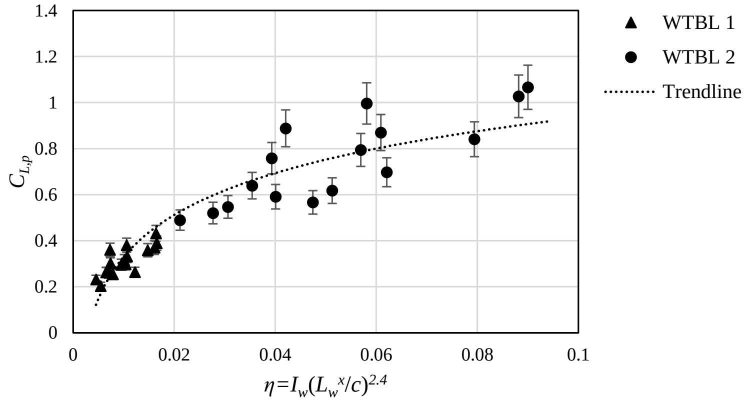

Figure 4.12. Variations of the peak lift force coefficient on horizontal flat plates, $C_{L,p}$, with the turbulence parameter, η.

4.2.4 Case study: Lift force on stowed heliostats

The results presented in the previous section indicate that the effect of free-stream turbulence on the peak lift force coefficient on a thin horizontal flat plate is predominantly affected by the turbulence parameter. In this section, the correlation between the lift force and the turbulence parameter developed from the wind tunnel experiments is used to predict the lift force on stowed heliostats as a case study. Heliostats with square mirror panels with a chord length dimension between 2 m and 10 m, and with pylon heights between 0.2 c and 0.5 c are considered. First, the turbulence parameter for the heliostats within ASL is calculated from equation $\eta = I_w(\frac{L_w^x}{c})^{2.4}$ using estimations of the integral length scales and turbulence intensity at terrains with different surface roughness values. Then the lift force coefficient is predicted as a function of the turbulence parameter from Equation (4.7).

To estimate the turbulence parameter for heliostats within the ASL, the vertical turbulence intensity and integral length scale were calculated for different terrain roughness values and heights within the ASL using the empirical relationships given by ESDU85020 (2010), and are given in Figure 4.13(a). The turbulence parameter was then calculated for heliostats with chord lengths of the mirror panel between 2 m to 10 m and for different pylon heights, from the equation, $= I_w(\frac{L_w^x}{c})^{2.4}$, using the turbulence intensity and length scales corresponding to each height. An example of the calculations is given in Table 4.2 for a terrain roughness of 0.1 m. Similar calculations were carried out for different surface roughness values between 0.01 m and 0.3 m. The results showed that the turbulence parameters for heliostats with different pylon heights and chord length dimensions of the panel, which have an identical H/c, are similar and can be expressed as a single value with a maximum standard deviation of 15%. Therefore, the average value of the turbulence parameter can be given for heliostats of constant H/c ratio at each terrain roughness, and the turbulence can be expressed as a function of terrain roughness and H/c, i.e. $\eta = f(z_0, \frac{H}{c})$. This is due to the dependence of the turbulence intensity and length scale on height and the relationship between the height and chord length of the mirror panel of heliostats. The turbulence parameter for different roughness values (z_0 =0.01 m to 0.3 m) as a function of H/c is shown in Figure 4.13(b). The error bars in Figure 4.13(b) show the standard deviation from the average values for a specific H/c. According to Figure 4.13(b), the turbulence parameter is larger for smaller values of surface roughness. For instance, at H/c=0.5, the turbulence parameter increases from approximately 0.016 to 0.054 when the surface roughness decreases from 0.3 m to 0.01 m. This is because the vertical integral length scales tend to decrease with increase in surface roughness at heights below 10 m where heliostats are positioned within the ASL, according to ESDU85020 (2010). Furthermore, according to Figure 4.13(b), at a specific terrain, the turbulence parameter increases with a power function with increasing H/c. Decreasing H/c from 0.5 to 0.2 leads to a reduction of the turbulence parameter to below 0.01 for the considered range of surface roughness values. It must be mentioned that the values of the turbulence parameter within the ABL shown in Figure 4.13 are calculated for heights above 3 m since the relationships for integral length scale and turbulence intensity given by ESDU85020 (2010) hold true for a minimum height of 3 m.

Table 4.2. Estimations of the vertical turbulence intensity, vertical length scale and the turbulence parameter for heliostats with different chord length dimensions of the mirror panel and pylon heights for a terrain with z_0=0.1 m in full-scale.

H [m]	I_w [%]	L_w^x [m]	c [m]	H/c	L_w^x/c	η
3	25.83	2.164	6	0.5	0.360	0.022
3	25.83	2.164	7.5	0.4	0.288	0.013
3	25.83	2.164	10	0.3	0.216	0.006
4	24.53	2.859	8	0.5	0.357	0.021
4	24.53	2.859	10	0.4	0.285	0.012
4	24.53	2.859	13.3	0.3	0.215	0.006

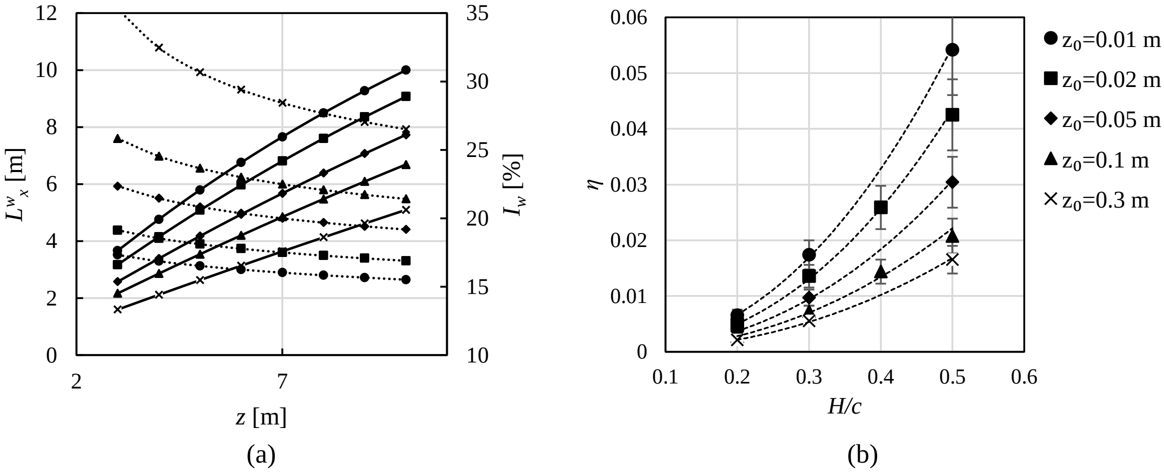

(a) (b)

Figure 4.13. (a) Vertical length scale (solid lines) and turbulence intensity (dotted lines) within the ASL calculated from ESDU85020 (2010) in full-scale (b) The turbulence parameter, η, within the ASL as a function of terrain roughness, z_0, and hinge height to chord length ratio of heliostats, H/c.

According to Figure 4.13(b), for industrial-scale heliostats within the ABL with terrain roughness values between 0.01 m and 0.3 m the turbulence parameter is between 0.005 and 0.054. The peak lift force coefficient on full-scale heliostats within the ABL can then be predicted based on the relationship given by Equation (4.7). According to Equation (4.7), as the turbulence parameter increases from 0.005 to 0.054, the peak lift force coefficient on a stowed heliostat increases from 0.146 to 0.787.

As mentioned in the previous sections, heliostats and solar trackers are conventionally designed H/c of about 0.5 (Téllez *et al.*, 2014). According to Emes *et al.* (2017) the lift force coefficient on a stowed heliostat model, in a wind tunnel boundary layer with a longitudinal turbulence intensity of 6%, decreases by about 80% when H/c from 1.2 to 0.5. Therefore, there seems to be a potential to decrease wind loads at stow position by further reducing H/c. In order to assess this potential, the turbulence parameter for full-scale heliostats within the ASL with different height to chord length ratios are calculated from ESDU85020 (2010) and thereafter, the lift force coefficient is found as a function of the turbulence parameter by Equation (4.7). The corresponding values of the turbulence parameter and the peak lift force coefficient for H/c ratios between 0.2 and 0.5 are presented in Table 4.3 for surface roughness values of 0.02 m and 0.1 m as samples of two terrain types. According to Table 4.3, reducing H/c from 0.5 to 0.2 for a stowed heliostat in a terrain with a surface roughness of 0.02 m, leads to a reduction in turbulence parameter from approximately 0.042 to 0.004 which decreases the $C_{L,p}$ from 0.722 to 0.146. Similarly, stowing at H/c=0.2 instead of H/c=0.5 reduces the peak lift force coefficient from 0.531 to 0.068 at z_0 =0.1 m. The last row in Table 4.3 shows the peak lift force coefficient normalised with that at H/c=0.5, $C_{L,p(0.5)}$, which is chosen for normalising the lift force coefficient since heliostats are usually designed for H/c=0.5.

Table 4.3. The turbulence parameter within the full-scale ASL for different surface roughness values and stow H/c ratios and its effect on the peak lift force coefficient on a full-scale stowed heliostat.

	$\boldsymbol{z_0 = 0.02\ \mathrm{m}}$				$\boldsymbol{z_0 = 0.1\ \mathrm{m}}$			
$\boldsymbol{H/c}$	0.5	0.4	0.3	0.2	0.5	0.4	0.3	0.2
$\boldsymbol{\eta}$	0.042	0.025	0.013	0.004	0.020	0.014	0.007	0.003
$\boldsymbol{C_{L,p}}$	0.722	0.590	0.417	0.146	0.531	0.433	0.249	0.068
$\boldsymbol{C_{L,p}/C_{L,p(0.5)}}$	1	0.816	0.577	0.202	1	0.815	0.468	0.108

The normalised peak lift force coefficient as a function of H/c is shown in Figure 4.14 for different terrain roughness values and H/c between 0.2 and 0.8. According to Figure 4.14, the normalised peak lift force coefficient on stowed heliostats within the ASL is a linear function of H/c, nearly independent of the terrain roughness. This relationship indicates that decreasing H/c from 0.5 to 0.2 reduces the peak lift force coefficient on stowed heliostats by 80% for all of the terrain types.

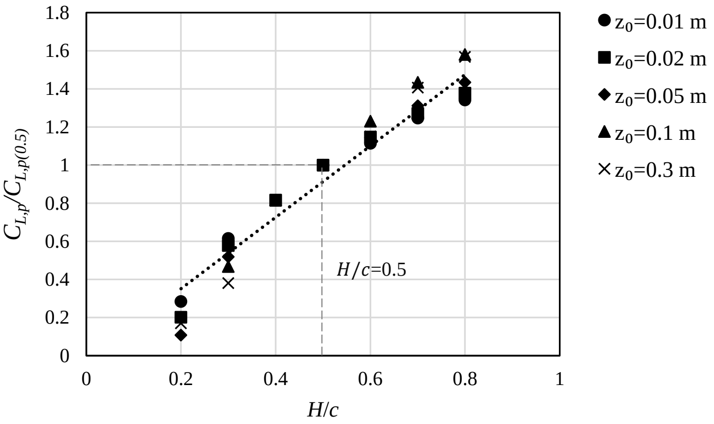

Figure 4.14. The peak lift force coefficient, $C_{L,p}$, of a full-scale stowed heliostat within the ASL normalised with that for H/c=0.5, $C_{L,p(0.5)}$, as a function of heliostat hinge height to chord length ratio, H/c.

The results presented in this section show that the turbulence parameter and the peak lift force coefficient on stowed heliostats depend on H/c and are the same for heliostats of various chord lengths with a similar H/c ratio. Although the peak lift force coefficient is the same for heliostats of different sizes with an identical H/c, the lift force is larger on heliostats with larger chord length of the mirror panel due to the larger panel area. Therefore, peak wind loads at stow position can be reduced by stowing heliostats at lower H/c ratios and by reducing the panel area.

Furthermore, it is noteworthy that the values of turbulence parameter given in Figure 4.13 are calculated for a single heliostat and therefore apply to heliostats in the outermost row of a field exposed to the wind. Mean wind loads on the heliostats in the inner rows of a field are less than the first row due to the shielding effect of the first row (Peterka, Bienkiewicz, *et al.*, 1987; Pfahl, 2011). Therefore, use of a first row of heliostats as a buffer has been proposed. However, heliostats placed within a field are exposed to different scales and intensities of turbulence. The dominant frequency of the fluctuating pressure on a second tandem heliostat in stow is an order of magnitude smaller than that for a single heliostat which indicates that the upstream heliostat breaks up the large energetic eddies within the flow (Emes *et al.*, 2018). Furthermore, turbulence intensity is found to increase dramatically after the second row of heliostats (Sment and Ho, 2014). The dynamic loads are dependent on the turbulence characteristics among the rows of heliostats. Therefore, it is necessary to investigate turbulence characteristics and wind loads for heliostats placed within rows of a field in future studies.

4.2.5 Conclusion

The effect of turbulence intensity and length scales on the peak lift force on a horizontal flat plate in a longitudinal turbulent flow was investigated in this study. Comprehensive experimental investigations were conducted to measure the wind loads on flat plate models at various heights within a part-depth wind tunnel model of the atmospheric surface layer. The following conclusions were reached from the obtained results:

- The peak lift force coefficient on a horizontal flat plate in an atmospheric boundary layer flow increases as a power function, with an exponent between 2.2 and 2.5, of the ratio of vertical integral length scale to the chord length of the plate.
- The peak lift force coefficient on a horizontal flat plate increases with increasing the vertical turbulence intensity.
- Turbulence parameter, which expresses the effect of both vertical turbulence intensity and vertical integral length scales, is the key factor affecting the peak lift force coefficient on horizontal flat plates, such that the peak lift force coefficient increases logarithmically with the turbulence parameter.

The developed correlation between the peak lift force coefficient and the turbulence parameter was used to predict the wind loads on stowed heliostats with square mirror panels as a case study. The results showed that:

- The turbulence parameter for heliostats with a chord length dimension below 10 m is between 0.005 and 0.054 for z_0=0.01 m to 0.3 m and can be expressed as a function of terrain roughness and heliostat height to chord length ratio.
- The peak lift force coefficient on stowed heliostats can be expressed as a linear function of the pylon height to chord length ratio of a heliostat. Its value is identical for heliostats regardless of the mirror panel chord length as long as H/c is the same, but it is dependent on the terrain roughness.
- Reducing H/c at stow position from 0.5 to 0.2 decreases the peak lift force coefficient on stowed heliostats by approximately 80%, independent of the terrain roughness.

Hence, the results of this study show that decreasing the heliostat height and thereby height to chord length ratio at stow position leads to reduction of the peak lift force at stow. It is recommended to stow heliostats at lower H/c ratios by adjustment of the pylon design, as for instance, lowering H/c to 0.2 or 0.3 will lead to a reduction of the peak lift force coefficient and thereby the lift force by approximately 50% and 80%, accordingly, for all terrain surface roughness values. Therefore, there is a great potential for reduction of the cost of heliostats since the overall required mass and strength of the structure can be decreased. This can be achieved by design of telescopic pylons with adjustable height to allow heliostats to be stowed at lower heights while operating at larger H/c values. An example of a heliostat design with adjustable height is the DLR carousel heliostat in which the panel is lowered to the ground during stow (Pfahl *et al.*, 2017). In order to provide an estimation of the potential cost reduction, it is necessary to further investigate the cost of the new pylon design in the future studies. Furthermore, investigation of the hinge and overturning moments at stow position is required since they must be considered for the survivability of the structure, and they are dependent on the centre of pressure in addition to the lift force. Moreover, comparison of the wind tunnel results with measurements of wind loads on full-scale heliostats will be done in future.

Acknowledgements

Financial support for the project has been provided by the Australian Government Research Training Program, the University of Adelaide Scholarship and the Australian Solar

Thermal Research Initiative (ASTRI). The authors would like to acknowledge the School of Mechanical Engineering and the workshop at the University of Adelaide.

4.2.6 References

Banks, D. 2011. Measuring peak wind loads on solar power assemblies. In *13th International Conference on Wind Engineering*. Amsterdam, Netherlands.

Bearman, P. W. 1971. An investigation of the forces on flat plates normal to a turbulent flow, *Journal of Fluid Mechanics*, 46: 177-98.

Bearman, P. W., and Morel, T. 1983. Effect of free stream turbulence on the flow around bluff bodies, *Progress in Aerospace Sciences*, 20: 97-123.

Cigada, A., Diana, G., and Zappa, E. 2002. On the response of a bridge deck to turbulent wind: a new approach, *Journal of Wind Engineering and Industrial Aerodynamics*, 90: 1173-82.

Cook, N. J. 1978. Determination of the model scale factor in wind-tunnel simulations of the adiabatic atmospheric boundary layer, *Journal of Wind Engineering and Industrial Aerodynamics*, 2: 311-21.

De Paepe, W., Pindado, S., Bram, S., and Contino, F. 2016. Simplified elements for wind-tunnel measurements with type-III-terrain atmospheric boundary layer, *Measurement*, 91: 590-600.

Emes, M. J., Arjomandi, M., Ghanadi, F., and Kelso, R. M. 2017. Effect of turbulence characteristics in the atmospheric surface layer on the peak wind loads on heliostats in stow position, *Solar Energy*, 157: 284-97.

Emes, M. J., Ghanadi, F., Arjomandi, M., and Kelso, R. M. 2018. Investigation of peak wind loads on tandem heliostats in stow position, *Renewable Energy*, 121: 548-58.

ESDU74031. 1974. Characteristics of atmospheric turbulence near the ground - Part II: single point data for strong winds (neutral atmosphere), *Engineering Sciences Data Unit*.

ESDU85020. 2010. Characteristics of atmospheric turbulence near the ground - Part II: single point data for strong winds (neutral atmosphere), *Engineering Sciences Data Unit*.

Farell, C., and Iyengar, A. K. S. 1999. Experiments on the wind tunnel simulation of atmospheric boundary layers, *Journal of Wind Engineering and Industrial Aerodynamics*, 79: 11-35.

Gong, B., Wang, Z., Li, Z., Zang, C., and Wu, Z. 2013. Fluctuating wind pressure characteristics of heliostats, *Renewable Energy*, 50: 307-16.

Högström, U., Hunt, J. C. R., and Smedman, A.-S. 2002. Theory and measurements for turbulence spectra and variances in the atmospheric neutral surface layer, *Boundary-Layer Meteorology*, 103: 101-24.

Holdø, A. E., Houghton, E. L., and Bhinder, F. S. 1982. Some effects due to variations in turbulence integral length scales on the pressure distribution on wind-tunnel models of low-rise buildings, *Journal of Wind Engineering and Industrial Aerodynamics*, 10: 103-15.

Holmes, J. D. 2007. *Wind Loading of Structures*, Taylor & Francis.

Hunt, J. C. R., and Carlotti, P. 2001. Statistical structure at the wall of the high Reynolds number turbulent boundary layer, *Flow, Turbulence and Combustion*, 66: 453-75.

Irwin, H. P. A. H. 1981. The design of spires for wind simulation, *Journal of Wind Engineering and Industrial Aerodynamics*, 7: 361-66.

Iyengar, A. K. S., and Farell, C. 2001. Experimental issues in atmospheric boundary layer simulations: Roughness length and integral length scale determination, *Journal of Wind Engineering and Industrial Aerodynamics*, 89: 1059-80.

Jafari, A., Emes, M. J., Ghanadi, F., and Arjomandi, M. 2017. The effect of turbulence intensity on the peak wind loads on heliostats. In *The Asia Pacific Solar Research Conference 2017*. Melbourne, Australia.

Kozmar, H. 2011. Truncated vortex generators for part-depth wind-tunnel simulations of the atmospheric boundary layer flow, *Journal of Wind Engineering and Industrial Aerodynamics*, 99: 130-36.

Kozmar, H. 2011. Wind-tunnel simulations of the suburban ABL and comparison with international standards, *Wind and Structures*, 14: 15-34.

Kozmar, H. 2012. Physical modeling of complex airflows developing above rural terrains, *Environmental Fluid Mechanics*, 12: 209-25.

Larose, G. L., and Livesey, F. M. 1997. Performance of streamlined bridge decks in relation to the aerodynamics of a flat plate, *Journal of Wind Engineering and Industrial Aerodynamics*, 69-71: 851-60.

Larose, G. L., Tanaka, H., Gimsing, N. J., and Dyrbye, C. 1998. Direct measurements of buffeting wind forces on bridge decks, *Journal of Wind Engineering and Industrial Aerodynamics*, 74-76: 809-18.

Leitch, C. J., Ginger, J., and Holmes, J. 2016. Wind loads on solar panels mounted parallel to pitched roofs, and acting on the underlying roof, *Wind and Structures*, 22: 307-28.

Li, Q. S., and Melbourne, W. H. 1995. An experimental investigation of the effects of free-stream turbulence on streamwise surface pressures in separated and reattaching flows, *Journal of Wind Engineering and Industrial Aerodynamics*, 54-55: 313-23.

Li, Q. S., and Melbourne, W. H. 1999. The effect of large-scale turbulence on pressure fluctuations in separated and reattaching flows, *Journal of Wind Engineering and Industrial Aerodynamics*, 83: 159-69.

Peterka, J. A., Bienkiewicz, B., Hosoya, N., and Cermak, J. E. 1987. Heliostat mean wind load reduction, *Energy*, 12: 261-67.

Peterka, J. A., Hosoya, N., Dodge, S., Cochran, L., and Cermak, J. E. 1998. Area-average peak pressures in a gable roof vortex region, *Journal of Wind Engineering and Industrial Aerodynamics*, 77-78: 205-15.

Peterka, J. A., Tan, L., Bienkiewcz, B., and Cermak, J. E. 1987. Mean and peak wind load reduction on heliostats, *Technical Report for Colorado State University*.

Peterka, J. A., Tan, Z., Cermak, J. E., and Bienkiewicz, B. 1989. Mean and peak wind loads on heliostats, *Journal of Solar Energy Engineering*, 111: 158-64.

Pfahl, A. 2018. Wind loads on heliostats and photovoltaic trackers, *Eindhoven: Technische Universiteit Eindhoven*.

Pfahl, A., Buselmeier, M., and Zaschke, M. 2011. Wind loads on heliostats and photovoltaic trackers of various aspect ratios, *Solar Energy*, 85: 2185-201.

Pfahl, A., Buselmeier, M. Zaschke, M. 2011. Determination of wind loads on heliostats. In *Proceedings of the 17th SolarPACES Conference*. Spain.

Pfahl, A., Coventry, J., Röger, M., Wolfertstetter, F., Vásquez-Arango, J. F., Gross, F., Arjomandi, M., Schwarzbözl, P., Geiger, M., and Liedke, P. 2017. Progress in heliostat development, *Solar Energy*, 152: 3-37.

Pfahl, A., Randt, M., Meier, F., Zaschke, M., Geurts, C. P. W., and Buselmeier, M. 2015. A holistic approach for low cost heliostat fields, *Energy Procedia*, 69: 178-87.

Rasmussen, J. T., Hejlesen, M. M., Larsen, A., and Walther, J. H. 2010. Discrete vortex method simulations of the aerodynamic admittance in bridge aerodynamics, *Journal of Wind Engineering and Industrial Aerodynamics*, 98: 754-66.

Shu, Z. R., and Li, Q. S. 2017. An experimental investigation of surface pressures in separated and reattaching flows: Effects of freestream turbulence and leading edge geometry, *Journal of Wind Engineering and Industrial Aerodynamics*, 165: 58-66.

Simiu, E., and Scanlan, R. H. 1996. *Wind Effects on Structures*, John Wiley & Sons.

Sment, J., and Ho, C. K. 2014. Wind patterns over a heliostat field, *Energy Procedia*, 49: 229-38.

Téllez, F., Burisch, M., Villasente, Sánchez, M., Sansom, C., Kirby, P., Turner, P., Caliot, C., Ferriere, A., Bonanos, C. A., Papanicolas, C., Montenon, A., Monterreal, R., and Fernández, J. 2014. State of the Art in Heliostats and Definition of Specifications, *STAGE-STE Project, Madrid, Spain*.

von Kármán, T. 1948. Progress in the Statistical Theory of Turbulence, *Proceedings of the National Academy of Sciences*, 34: 530-39.

Watkins, S., Milbank, J., Loxton, B. J., and Melbourne, W. H. 2006. Atmospheric winds and their implications for microair vehicles, *AIAA Journal*, 44: 2591-600.

Wooding, R. A., Bradley, E. F., and Marshall, J. K. 1973. Drag due to regular arrays of roughness elements of varying geometry, *Boundary-Layer Meteorology*, 5: 285-308.

4.3 Peak drag force on an operating heliostat

This section consists of the following published conference paper:

Jafari, A., Ghanadi, F., Emes, M. J., Arjomandi, M., and Cazzolato, B. S. 2018. Effect of free-stream turbulence on the drag force on a flat plate. *21st Australasian Fluid Mechanics Conference*. Adelaide, Australia.

The article is identical to its published format with the following exceptions:

- The numbering of figures, tables and equations have been altered to include the chapter number.
- The position of some figures and tables have been changed to improve legibility.

The article in its published format is available at the proceedings of the 21st Australasian Fluid Mechanics Conference at:

https://people.eng.unimelb.edu.au/imarusic/proceedings/21%20AFMC%20TOC.html

Statement of Authorship

Title of Paper	Effect of free-stream turbulence on the drag force on a flat plate	
Publication Status	■ Published ☐ Submitted for Publication	☐ Accepted for Publication ☐ Unpublished and Unsubmitted work written in manuscript style
Publication Details	Jafari, A., Ghanadi, F., Emes, M. J., Arjomandi, M., and Cazzolato, B. S. 2018. Effect of free-stream turbulence on the drag force on a flat plate. *21st Australasian Fluid Mechanics Conference*. Adelaide, Australia.	

Principal Author

Name of Principal Author (Candidate)	Azadeh Jafari		
Contribution to the paper	Developed ideas, conducted experiments, performed data analysis and interpreted results, wrote manuscript, and acted as corresponding author.		
Overall percentage (%)	75		
Certification	This paper reports on original research I conducted during the period of my Higher Degree by Research candidature and is not subject to any obligations or contractual agreements with a third party that would constrain its inclusion in this thesis. I am the primary author of this paper.		
Signature		Date	25/05/2020

Co-Author Contributions

By signing the Statement of Authorship, each author certifies that:

i. the candidate's stated contribution to the publications is accurate (as detailed above);

ii. permission is granted for the candidate in include the publication in the thesis; and

iii. the sum of all co-author contributions is equal to 100% less the candidate's stated contribution.

Name of Co-Author	Farzin Ghanadi		
Contribution to the paper	Supervised the development of the research, helped in developing ideas, contributed in academic discussion and manuscript review.		
Signature		Date	26/05/2020

Name of Co-Author	Matthew Emes		
Contribution to the paper	Helped in the development of the research, contributed in academic discussion and manuscript review.		
Signature		Date	26/05/2020

Name of Co-Author	Maziar Arjomandi		
Contribution to the paper	Supervised the development of the research, participated in developing ideas and concepts, helped in interpretation of results, provided critical revision of manuscript.		
Signature		Date	25/05/2020

Name of Co-Author	Benjamin Cazzolato		
Contribution to the paper	Supervised the development of the research, helped in developing ideas, contributed in academic discussion and manuscript review.		
Signature		Date	26/5/2020

Effect of free-stream turbulence on the drag force on a flat plate

Azadeh Jafari, Farzin Ghanadi, Matthew J. Emes, Maziar Arjomandi and Benjamin S. Cazzolato

Abstract

The effect of intensity and length scale of turbulence on the mean and fluctuating drag forces on a flat plate normal to a boundary layer flow is investigated. Experiments were conducted at the University of Adelaide large wind tunnel to measure the drag force on flat plates of different areas. Two boundary layers of different depths were generated by spires and roughness elements to achieve a range of longitudinal turbulence intensities between 12% and 26% and integral length scales between 0.4 m and 1.22 m. The root-mean-square of the fluctuating drag coefficient was well correlated with a turbulence parameter defined as a function of turbulence intensity (I_u) and integral length scale (L_u^x). The results showed that both the fluctuating and the peak drag coefficients increased logarithmically with increasing the turbulence parameter such that increasing the turbulence parameter from 0.11 to 0.47 increased the peak drag coefficient from 1.73 to 3.

4.3.1 Introduction

Free-stream turbulence influences the mean and the unsteady aerodynamic loads on bluff bodies. The relative size of the integral length scales to the chord length of the body (L_u^x/c) is a key factor affecting the loads. The mean drag force on a square prism is found to be strongly dependent on the scale of turbulence (Lee, 1975). Measurements of the mean drag force on a prism within grid-generated turbulent flows with different turbulence intensities between 3% and 12% show that the mean drag force reaches a maximum at $L_u^x/c \cong 1$ (Lee, 1975). The mean base pressure on a cubic building model in a non-isotropic boundary layer flow is also found to be dependent on L_u^x/c remaining almost constant for L_u^x/c between 3 and 5 and decreasing afterwards (Holdø *et al.*, 1982). Furthermore, the root-mean-square of the drag force on a flat plate normal to a turbulent flow is found to increase by decreasing the plate's chord length, which is similar to increasing L_u^x/c (Bearman, 1971).

The effect of integral length scales on the loads is suggested to be associated with the distortion of turbulence in the flow around the bluff body (Bearman and Morel, 1983). For the case of a flat plate normal to the flow, the flow behaviour is quasi-static when the integral length scale is much larger than the chord length of the plate, and the effect of the bluff body on the turbulence is similar to its effect on the mean flow. Therefore, the fluctuating longitudinal velocity decreases along the stagnation line, and its energy is transferred to the vertical and lateral components as the flow approaches the plate. On the contrary, stretching of the vortex lines is the dominant effect when the integral length scale is much smaller than the chord length, which leads to an increase in the fluctuating longitudinal velocity component, while the vertical and lateral velocity components remain almost constant. If L_u^x/c is in the order of 1, a combination of both effects occurs (Bearman, 1971; Holdø *et al.*, 1982).

Moreover, the effect of L_u^x/c is also dependent on turbulence intensity. For instance, the base-pressure on a flat plate normal to a turbulent flow is found to be a function of $I_u(L_u^x/c)^2$ (Bearman, 1971). Furthermore, for a blunt flat plate placed horizontally within a turbulent flow, the effect of L_u^x/c on the peak pressure is greater at higher turbulence intensities (Li and Melbourne, 1999; Shu and Li, 2017). The peak pressure on the plate is found to be a function of both turbulence intensity and integral length scale and increases with the parameter $I_u(L_u^x/c)^{0.15}$ (Li and Melbourne, 1995).

Although the effect of turbulence intensity and length scale on the loads has been investigated in the literature, the correlation between these turbulence characteristics and the loads on a flat plate in a boundary layer flow is not known. Hence, this study investigates the effect of turbulence intensity and integral length scale on the mean and fluctuating drag forces on a flat plate normal to a boundary layer flow. It expands upon the findings of Bearman (1971) and differs from it by several aspects. First, a non-isotropic boundary layer flow with the characteristics of the atmospheric boundary layer is simulated. Second, a wide range of intensities and scales of turbulence are investigated. While the experiments of Bearman (1971) were conducted at a turbulence intensity of 8% and an integral length scale of approximately 0.07 m, longitudinal turbulence intensities between 12% and 26% and integral length scales between 0.4 m and 1.22 m are achieved in the current study. The results of this study are important for calculation of the fluctuating wind loads on structures such as solar panels, heliostats and billboards where an accurate estimation of the effects of turbulence within the atmospheric boundary layer on the fluctuating drag force is necessary for their design.

4.3.2 Methodology

Experiments were conducted in the University of Adelaide large-scale wind tunnel. The cross-sectional area of the wind engineering test section is 3 m × 3 m with a development length of 17 m. The wind tunnel is designed for a maximum air speed of 33 m/s, and the level of turbulence intensity in the clear tunnel is between 1% and 3% at different measurement positions. In order to achieve different intensities and length scales of turbulence in the wind tunnel, two boundary layers of different depths were generated in the wind tunnel using spires and roughness elements. Two sets of spires were designed to model the atmospheric boundary layer based on Kozmar's part-depth method (Kozmar, 2011). Each set consisted of three spires with identical dimensions shown in Figure 4.15. The spires were separated by a centre-line distance of 0.9 m in the lateral direction (y), followed by a 10 m fetch of wooden roughness elements of 90 mm × 90 mm cross section and 45 mm height in the x direction.

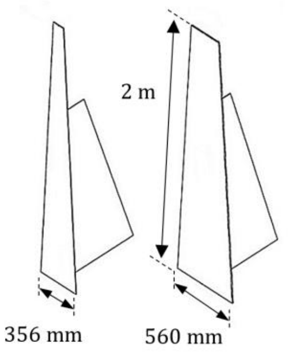

(a) (b)

Figure 4.15. Dimensions of the two spire sets: (a) Set 1, (b) Set 2.

Three components of velocity (u, v, w) were measured over an area of 1 m^2 normal to the flow above the tunnel floor in both vertical and lateral directions (y, z) downstream of the roughness fetch at the position of the flat plate models by a Turbulent Flow Instrumentation (TFI) multi-hole pressure probe which has an accuracy of ±0.5 m/s. Data were measured for a duration of 150 s at a sampling rate of 1 kHz at each location at free-stream velocity of 11.5 m/s. The mean velocity as a function of height at three lateral locations in the generated boundary layers by the two spire sets is presented in Figure 4.16. The mean velocity at the centre line (y=0) shows a maximum of 9% and 14% deviation from the side lines (y=-0.5, y=0.5) for Set 1 and Set 2, respectively. Since the plates span a maximum of 0.4 m from the centre line in the y direction, the lateral homogeneity of both simulated boundary layers is acceptable and the measured velocity at the centre line is used for calculation of wind loads.

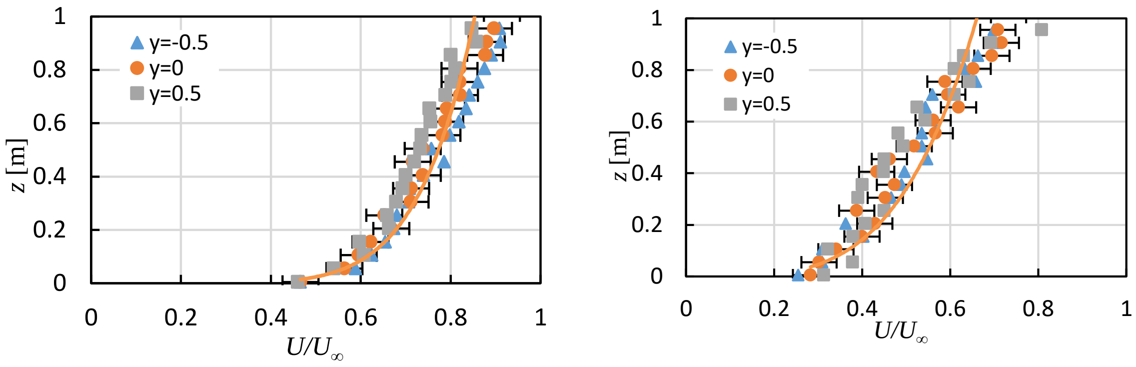

(a)

(b)

Figure 4.16. Mean velocity profiles normalised with respect to the free-stream velocity (U_∞=11.5 m/s) at three lateral locations for: (a) Spire Set 1, (b) Spire Set 2.

Figure 4.17 shows the longitudinal turbulence intensity at different heights in the wind tunnel for the two generated boundary layers. The longitudinal turbulence intensity at the mid-plane height of the flat plate model in the wind tunnel, (z=0.5 m), is approximately 13% and 26% for the boundary layers produced by Set 1 and Set 2, respectively. The longitudinal integral length scales for the two boundary layers are compared in Figure 4.18. The integral length scales were determined by the autocorrelation method which is selected in this study since it produces smaller errors in estimation of the length scales in comparison with the spectral fit methods (Iyengar and Farell, 2001; De Paepe *et al.*, 2016; Emes *et al.*, 2018). In this method, first, the auto-correlation of velocity measurements is found by Equation (4.8). Then, after determination of the time scale of turbulence from Equation (4.9), the length scale is calculated, based on Taylor's hypothesis, as the multiplication of the time scale by the mean velocity from Equation (4.10) (Farell and Iyengar, 1999).

$$R(\tau) = \frac{\overline{u'(t)u'(t+\tau)}}{\sigma_u^2} \tag{4.8}$$

$$\tau_u^x = \int R(\tau)d\tau \tag{4.9}$$

$$L_u^x = \tau_u^x \, U \tag{4.10}$$

where u' and σ_u^2 represent the fluctuating component and the standard deviation of longitudinal velocity. R is the autocorrelation. τ_u^x and L_u^x show the integral time scale and length scale, respectively.

According to Figure 4.18, the integral length scales in the boundary layer generated by Spire Set 2 are larger than those in the generated boundary layer by Spire Set 1 as at z=0.5 m the integral length scale is approximately 0.57 m and 0.70 m for the boundary layers by Set 1 and Set 2, respectively.

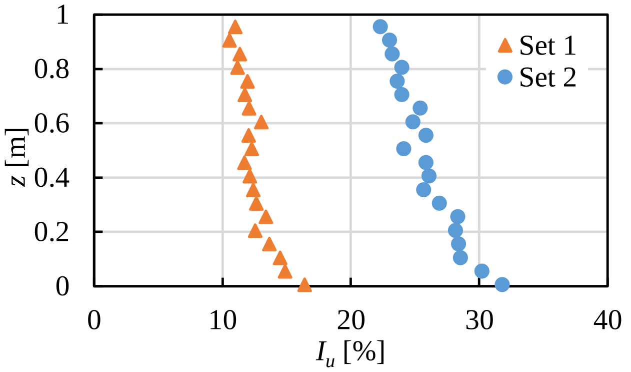

Figure 4.17. Longitudinal turbulence intensity profiles of the generated boundary layers by Set 1 and Set 2 in the wind tunnel.

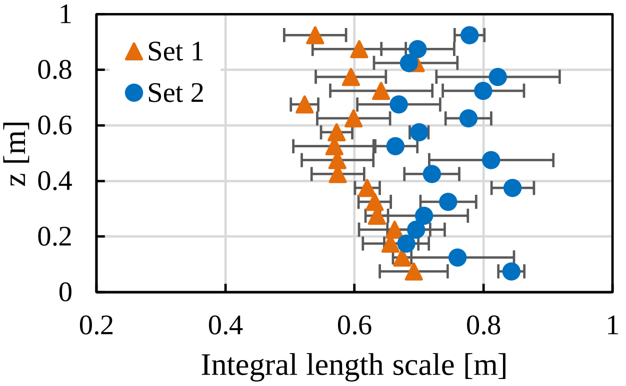

Figure 4.18. Longitudinal integral length scales of turbulence, L_u^x, in the generated boundary layers by the two spire sets in the wind tunnel. (The error bars show the standard deviation calculated from five measurements).

According to Figures 4.17–4.18, a range of turbulence intensities and length scales are generated in the wind tunnel which allows investigation of the effect of turbulence intensity and length scales on the drag on the flat plates by placing the plates in the two simulated boundary layers. Square flat plates of different dimensions with chord lengths between 0.3 m and 0.8 m and a thickness of 3 mm were mounted on a pylon of 0.5 m height placed downstream of the roughness fetch, as shown in Figure 4.19. By using plates of different chord length dimensions, a range of values for L_u^x/c between 0.85 and 4 were achieved in each boundary layer. The drag force on the plates was measured using four load cells, each with a capacity of 500 N which were placed below the test section floor. Calibration of the load cells was done for a range of forces between 0–25 N, and the measurement errors were determined to be approximately 1.5% of the measured forces.

The force on the plate was measured over a period of 120 seconds at a sampling rate of 1 kHz. The mean and the root-mean-square (RMS) of the fluctuating force were found and then the peak force was determined as the sum of the mean value and three-times the RMS of the fluctuating force according to Simiu and Scanlan (1996). The drag coefficient is then found by the following equation:

$$C_D = \frac{F_D}{\frac{1}{2}\rho U^2 c^2} \tag{4.11}$$

where F_D represents the drag force on the plate, U is the mean velocity at a height of 0.5 m corresponding to the mid-plane height of the flat plate models, ρ is air density and c is the chord length of the plate. The calculated drag coefficients are corrected for the wind tunnel blockage effect by the method of Maskell (1987).

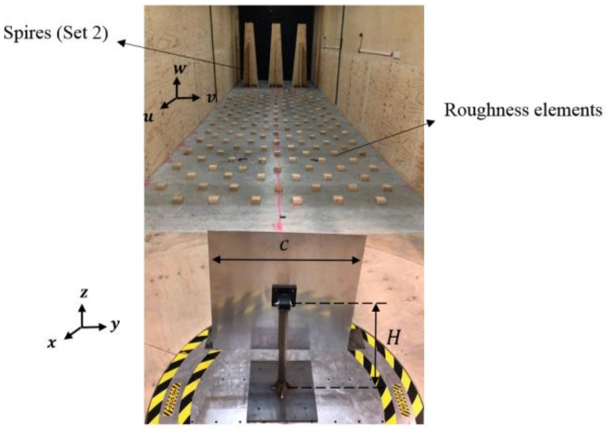

Figure 4.19. Experimental test setup showing the flat plate model, and spires and roughness elements for generation of the turbulent boundary layer.

4.3.3 Results and discussion

The mean and fluctuating drag on flat plates normal to the flow were measured in the two generated boundary layers. Figure 4.20 presents the mean drag coefficient for different values of L_u^x/c within the two boundary layers, which shows that C_D is larger at a turbulence intensity of 26% compared to a turbulence intensity of 13%. According to Figure 4.20, at I_u=13%, the mean drag coefficient remains almost constant for L_u^x/c between 0.97 and 1.36, then followed by a decrease in the mean drag coefficient with a further increase in L_u^x/c. Similarly, at I_u= 26%, the mean drag coefficient is almost constant over a range of L_u^x/c

between 1.5 and 2. Afterwards, as L_u^x/c increases from 2 to approximately 4, the mean C_D decreases from 1.4 to 0.85. The data suggest that the mean drag coefficient is maximum for L_u^x/c between 1 and 2, and is dependent on the turbulence intensity. The reason for the decrease in the mean drag coefficient at large values of L_u^x/c is that when the integral length scales are much larger than the chord length dimension, the flow behaves quasi-statically and turbulence appears as the mean flow to the body (Bearman, 1971; Holdø *et al.*, 1982; Bearman and Morel, 1983).

Measurements of mean drag coefficient on a square prism in an isotropic turbulence field show a similar behaviour over the range of L_u^x/c between 0.5 and 2.5 (Lee, 1975). These results show that the mean drag coefficient reaches a peak at $L_u^x/c \cong 1$ and decreases afterwards with a further increase in L_u^x/c up to about 2. With a further increase in L_u^x/c to over 5, the mean drag coefficient is found to increase again. The trend in the variation of the mean drag coefficient with L_u^x/c over the range of 0.5 to 2.5 found by Lee (1975) is similar to that shown in the present study, although the geometry is different. Furthermore, the turbulence field in the experiments of Lee (1975) is grid-generated and isotropic, whereas in this study anisotropic turbulence within a boundary layer is investigated.

The experimental data of Bearman (1971), which show an almost constant mean drag coefficient over the range of L_u^x/c between 0.37 and 1.5 at I_u= 8%, are also shown in Figure 4.20. It must be noted that the results of Bearman (1971) also correspond to an isotropic grid-generated turbulence.

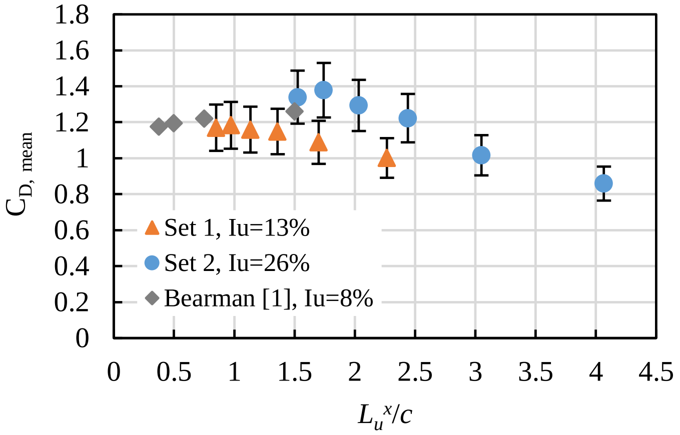

Figure 4.20. The effect of longitudinal integral length scale to chord length ratio, L_u^x/c, on the mean drag coefficient, C_D, on a flat plate normal to a boundary layer flow at two different turbulence intensities, I_u.

The RMS of the fluctuating drag coefficient for different values of L_u^x/c within the two boundary layers are compared in Figure 4.21 with those reported by Bearman (1971). According to Figure 4.21, at I_u=26%, increasing L_u^x/c from 1.5 to 4 increases the RMS of the fluctuating drag coefficient from 0.54 to 0.74. Similarly, at I_u=13%, an increase in L_u^x/c from 0.97 to 2.3 leads to an increase in $C_{D,RMS}$ from 0.2 to 0.34. The reported data by Bearman (1971) show a similar trend as the $C_{D,RMS}$ increases from 0.09 to 0.15 by increasing L_u^x/c from 0.37 to 1.5.

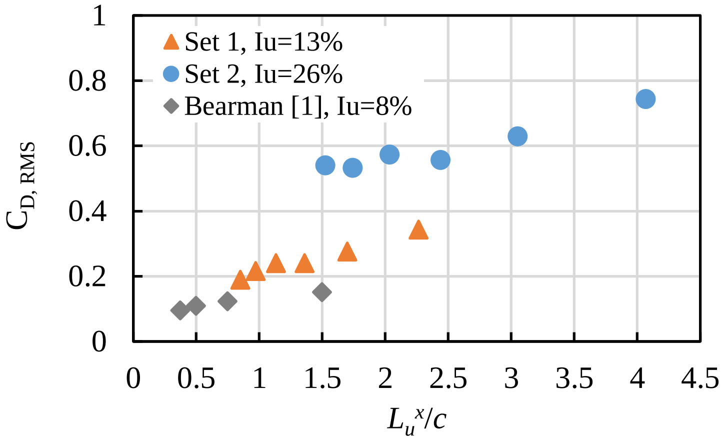

Figure 4.21. The effect of longitudinal integral length scale to chord length ratio, L_u^x/c, on the RMS of the fluctuating drag coefficient, $C_{D,RMS}$, on a flat plate normal to a boundary layer flow at two different turbulence intensities, I_u.

The effect of turbulence intensity on the RMS of the fluctuating drag coefficient is indicated by comparison of $C_{D,RMS}$ at similar values of L_u^x/c. For instance, according to Figure 4.21, at L_u^x/c of 1.7, $C_{D,RMS}$ is approximately 0.53 for I_u=26% while it equals 0.27 at I_u=13%. Therefore, the effect of L_u^x/c on the fluctuating drag is larger when the turbulence intensity is higher. The dependence of the fluctuating drag coefficient on turbulence intensity and integral length scale can be expressed in terms of a turbulence parameter defined as $\eta = I_u(\frac{L_u^x}{c})^{0.48}$. The RMS of the fluctuating drag coefficient as a function of the turbulence parameter is shown in Figure 4.22 which shows that the data from both boundary layers with different turbulence intensities and length scales collapse into a logarithmic function of η.

The turbulence parameter describes both spatial and temporal release of turbulence energy and therefore the effect of turbulence energy on the fluctuating drag coefficient. Similar parameters were suggested to correlate pressure with turbulence intensity and length scale, $\eta =$

$I_u(\frac{L_u^x}{c})^2$ for the base pressure on flat plates normal to a grid-generated turbulence (Bearman, 1971) and $\eta = I_u(\frac{L_u^x}{c})^{0.15}$ for fluctuating pressure on a horizontal flat plate within a grid-generated turbulence (Li and Melbourne, 1995). In the current study, $\eta = I_u(\frac{L_u^x}{c})^{0.48}$ was determined as the best fit for the fluctuating drag data on a flat plate normal to boundary layer flows.

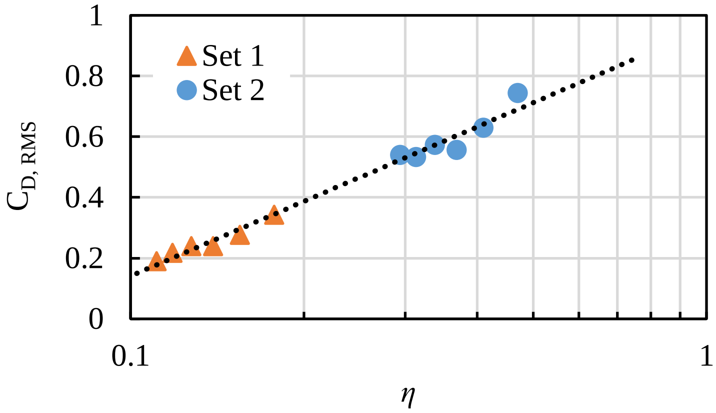

Figure 4.22. Variations of the RMS of the fluctuating drag coefficient, $C_{D,RMS}$, with the turbulence parameter, η.

The peak drag coefficient as a function of the turbulence parameter is given in Figure 4.23, which shows that the peak drag coefficient increases logarithmically with increasing turbulence parameter. According to figure 9, increasing the turbulence parameter from 0.11 to 0.47 increases the peak drag coefficient on the flat plates by 73% (from 1.73 to 3).

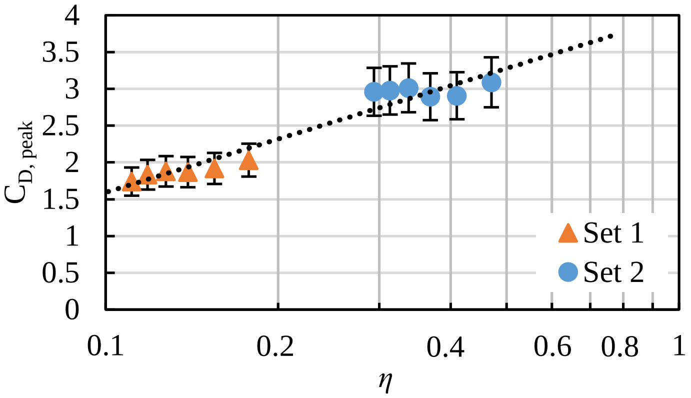

Figure 4.23. Variations of the peak fluctuating drag coefficient, $C_{D,peak}$, with the turbulence parameter, η.

4.3.4 Conclusions

The effect of turbulence intensity and length scale on the mean and fluctuating drag coefficient on a flat plate normal to the flow were investigated in this study. Comprehensive experimental investigations were conducted to measure the drag force on flat plates of different dimensions within two simulated boundary layers in a wind tunnel. The results show that, over the investigated range of L_u^x/c between 0.85 and 4, the mean drag coefficient is maximum for L_u^x/c between 1 and 1.5, and decreases afterwards with increasing L_u^x/c. Furthermore, the RMS of the fluctuating drag coefficient increases with increasing L_u^x/c and turbulence intensity. It is found that the RMS of the fluctuating drag coefficient and the peak drag coefficient are logarithmic functions of a turbulence parameter defined as $\eta = I_u(\frac{L_u^x}{c})^{0.48}$, which expresses the effect of both intensity and length scale of turbulence within a boundary layer.

Acknowledgments

Financial support for the project has been provided by the Australian Government Research Training Program, the University of Adelaide Scholarship and the Australian Solar Thermal Research Initiative (ASTRI). The authors would like to acknowledge the School of Mechanical Engineering and the Mechanical Workshop at the University of Adelaide.

4.3.5 References

Bearman, P. W. 1971. An investigation of the forces on flat plates normal to a turbulent flow, *Journal of Fluid Mechanics*, 46: 177-98.

Bearman, P. W., and Morel, T. 1983. Effect of free stream turbulence on the flow around bluff bodies, *Progress in Aerospace Sciences*, 20: 97-123.

De Paepe, W., Pindado, S., Bram, S., and Contino, F. 2016. Simplified elements for wind-tunnel measurements with type-III-terrain atmospheric boundary layer, *Measurement*, 91: 590-600.

Emes, M. J., Ghanadi, F., Arjomandi, M., and Kelso, R. M. 2018. Investigation of peak wind loads on tandem heliostats in stow position, *Renewable Energy*, 121: 548-58.

Farell, C., and Iyengar, A. K. S. 1999. Experiments on the wind tunnel simulation of atmospheric boundary layers, *Journal of Wind Engineering and Industrial Aerodynamics*, 79: 11-35.

Holdø, A. E., Houghton, E. L., and Bhinder, F. S. 1982. Some effects due to variations in turbulence integral length scales on the pressure distribution on wind-tunnel models of low-rise buildings, *Journal of Wind Engineering and Industrial Aerodynamics*, 10: 103-15.

Iyengar, A. K. S., and Farell, C. 2001. Experimental issues in atmospheric boundary layer simulations: Roughness length and integral length scale determination, *Journal of Wind Engineering and Industrial Aerodynamics*, 89: 1059-80.

Kozmar, H. 2011. Truncated vortex generators for part-depth wind-tunnel simulations of the atmospheric boundary layer flow, *Journal of Wind Engineering and Industrial Aerodynamics*, 99: 130-36.

Lee, B. E. 1975. Some effects of turbulence scale on the mean forces on a bluff body, *Journal of Wind Engineering and Industrial Aerodynamics*, 1: 361-70.

Li, Q. S., and Melbourne, W. H. 1995. An experimental investigation of the effects of free-stream turbulence on streamwise surface pressures in separated and reattaching flows, *Journal of Wind Engineering and Industrial Aerodynamics*, 54-55: 313-23.

Li, Q. S., and Melbourne, W. H. 1999. The effect of large-scale turbulence on pressure fluctuations in separated and reattaching flows, *Journal of Wind Engineering and Industrial Aerodynamics*, 83: 159-69.

Maskell, E. C. 1987. *A theory of the blockage effects on bluff bodies and stalled wings in a closed wind tunnel*, Aeronautical Research Council.

Shu, Z. R., and Li, Q. S. 2017. An experimental investigation of surface pressures in separated and reattaching flows: Effects of freestream turbulence and leading edge geometry, *Journal of Wind Engineering and Industrial Aerodynamics*, 165: 58-66.

Simiu, E., and Scanlan, R. H. 1996. *Wind Effects on Structures*, John Wiley & Sons.

Chapter 5

Effect of wake-induced turbulence on wind loads

5.1 Chapter overview

After establishing a relationship between the incoming turbulence within the atmospheric surface layer and the wind loads on a heliostat in Chapters 3–4, this chapter analyses the flow behaviour in the wake of a heliostat. How the turbulence within the atmospheric surface layer changes in the wake of a heliostat at different operating angles is investigated. This analysis provides a basis for understanding the complex flow behaviour and the turbulence within a heliostat field, which based on the arrangement of a field and the spacings between the heliostats can be different from the incoming flow conditions. Furthermore, the impact of the variations of turbulence on the wind loads on the heliostats within a field is discussed through analysis of how the turbulence in the wake of a heliostat affects the wind loads on a second downstream heliostat. The developed knowledge is important for the evaluation of variations of wind loads in a heliostat field, which can be used to improve the field design with respect to the wind loads. As an example, through identification of the regions of a field where heliostats experience increased wind loads, their design can be improved to increase the structural stiffness.

The chapter consists of two sections: Section 5.2 describes turbulence characteristics in the wake of a heliostat model in a wind tunnel, and Section 5.3 reports an experimental measurement of the wind loads on operating heliostats in tandem. Time-averaged and spectral characteristics of turbulence in the wake are analysed, and variations of the intensity and length scales of turbulence in the wake are determined. Furthermore, a discussion on how the findings can be interpreted to predict the turbulence within a heliostat field and its effect on the wind loads on the heliostats within a field is provided. The predicted patterns are confirmed with the changes in the wind loads on tandem heliostats.

The results in Section 5.2 show a significant increase in turbulence intensity in the wake of a heliostat, such that the streamwise and vertical turbulence intensities are more than four times larger than their inflow levels behind the heliostat at downstream distances of less than three-times the chord length dimension of the mirror panel. Based on the determined characteristics of the turbulence in the wake of a heliostat, it is estimated that a significant increase of turbulence intensity occurs in high-density regions of a field where the spacing between the heliostat rows is between 1–3 times the characteristic length of the mirror panel.

Measurements of the wind loads on a second tandem heliostat placed at varying distances behind an upstream heliostat in Section 5.3, reveal the existence of regions of large-magnitude peak pressure at the leading edge of the mirror panel of the second tandem heliostat. It is demonstrated that the unsteady variations of pressure distribution on the mirror panel lead to an increase of the mean and peak hinge moment coefficients on the second tandem heliostat, which highlight the importance of considering the increased wind loads for the design of the torque tube and drives.

The findings presented in this chapter provide an improved understanding of the wind loads on heliostats within a field, from which a number of inferences for the field design have been drawn. Field density is identified as a key parameter which affects the wind loads in a field, such that heliostats placed in high-density regions of a field are expected to experience increased peak wind loads compared to those in less dense areas. This indicates the necessity of improving the structural design of heliostats in dense regions of a field. Furthermore, opportunities for reducing the structural costs are identified in low-density regions of a field where the wind loads are lower.

5.2 Turbulence characteristics in the wake of a heliostat

This section consists of the following published journal article:

Jafari, A., Emes, M. J., Cazzolato, B. S., Ghanadi, F., and Arjomandi, M. 2020. Turbulence characteristics in the wake of a heliostat in an atmospheric boundary layer flow, *Physics of Fluids*, 32: 045116.

The article is identical to the submitted manuscript with the following exceptions:

- The numbering of figures, tables and equations have been altered to include the chapter number.
- The position of some figures and tables have been changed to improve legibility.
- A list of symbols is added.

The article in its published format is available at:
https://doi.org/10.1063/5.0005594

Statement of Authorship

Title of Paper	Turbulence characteristics in the wake of a heliostat in an atmospheric boundary layer flow	
Publication Status	■ Published	☐ Accepted for Publication
	☐ Submitted for Publication	☐ Unpublished and Unsubmitted work written in manuscript style
Publication Details	Jafari, A., Emes, M. J., Cazzolato, B. S., Ghanadi, F., and Arjomandi, M. 2020. Turbulence characteristics in the wake of a heliostat in an atmospheric boundary layer flow, *Physics of Fluids*, 32: 045116.	

Principal Author

Name of Principal Author (Candidate)	Azadeh Jafari		
Contribution to the paper	Developed ideas, conducted experiments, performed data analysis and interpreted results, wrote manuscript, and acted as corresponding author.		
Overall percentage (%)	75		
Certification	This paper reports on original research I conducted during the period of my Higher Degree by Research candidature and is not subject to any obligations or contractual agreements with a third party that would constrain its inclusion in this thesis. I am the primary author of this paper.		
Signature		Date	25/05/2020

Co-Author Contributions

By signing the Statement of Authorship, each author certifies that:

i. the candidate’s stated contribution to the publications is accurate (as detailed above);

ii. permission is granted for the candidate in include the publication in the thesis; and

iii. the sum of all co-author contributions is equal to 100% less the candidate’s stated contribution.

Name of Co-Author	Matthew Emes		
Contribution to the paper	Helped in the development of the research, contributed in academic discussion and manuscript review.		
Signature		Date	26/05/2020

Name of Co-Author	Benjamin Cazzolato		
Contribution to the paper	Supervised the development of the research, helped in developing ideas, contributed in academic discussion and manuscript review.		
Signature		Date	26/5/2020

Name of Co-Author	Farzin Ghanadi		
Contribution to the paper	Supervised the development of the research, participated in developing ideas, contributed in academic discussion and manuscript review.		
Signature		Date	26/05/2020

Name of Co-Author	Maziar Arjomandi		
Contribution to the paper	Supervised the development of the research, participated in developing ideas and concepts, helped in interpretation of results, provided critical revision of manuscript.		
Signature		Date	25/05/2020

Turbulence characteristics in the wake of a heliostat in an atmospheric boundary layer flow

Azadeh Jafari, Matthew Emes, Benjamin Cazzolato, Farzin Ghanadi, Maziar Arjomandi

Abstract

The mean and spectral characteristics of turbulence in the wake flow of a flat plate model resembling a heliostat in the atmospheric boundary layer flow are investigated in a wind tunnel experiment. Mean velocity and turbulence kinetic energy were characterised in the wake of a heliostat model at three elevation angles up to a distance of eight times the characteristic dimension of the heliostat panel. An increase in turbulence intensity and kinetic energy was found in the wake flow, reaching a peak at a distance equal to approximately twice the characteristic dimension of the heliostat panel. Furthermore, spectral and wavelet analysis of velocity fluctuations in the wake showed that the dominant mechanism in the immediate downstream of the plate was breakdown of large inflow turbulence structures to smaller scales. In the end, the wake-induced turbulence patterns and wind loads in a heliostat field were discussed. It was found that compared to a heliostat at the front row, the heliostats positioned in high-density regions of a field were subjected to a higher turbulence intensity, and consequently larger dynamic wind loading. The results show that it is necessary to consider the increased unsteady wind loads for the design of heliostat in high-density regions of a field, where the gap between the rows is less than three-times the characteristic length of the heliostat panel.

Nomenclature

c	chord length dimension of heliostat panel (m)
C_{MHy}	hinge moment force coefficient
f	frequency (Hz)
H	hinge height of heliostat model (m)
I_u	streamwise turbulence intensity (%)
I_w	vertical turbulence intensity (%)
k	turbulent kinetic energy (J/kg)
L_u^x	longitudinal integral length scale (m)
L_w^x	vertical integral length scale (m)

S_{uu}	power spectral density of the longitudinal velocity fluctuation (m^2/s)
S_{ww}	power spectral density of the vertical velocity fluctuation (m^2/s)
τ_H	non-dimensional shear at heliostat hinge height
u, v, w	absolute velocity components in the $x-, y-, z-$ flow directions, respectively (m/s)
U, W	time averaged mean velocity components in streamwise and vertical directions, respectively (m/s)
U_∞	free-stream velocity (m/s)
u', w'	fluctuating velocity components in streamwise and vertical directions, respectively (m/s)
x, y, z	distance in the streamwise, lateral and vertical directions (m)
Symbols	
α	elevation angle (°)
δ	boundary layer thickness (m)
σ_u	standard deviation of streamwise velocity fluctuations (m/s)
σ_w	standard deviation of vertical velocity fluctuations (m/s)
Subscripts	
H	heliostat hinge height
in	inflow boundary layer

5.2.1 Introduction

Understanding the flow characteristics in the wake of a heliostat is a fundamental step for analysis of the flow turbulence within a heliostat field which has several complexities including its dependence on the field arrangement and density. This knowledge accompanied with measurements of in-field wind loads on full-scale structures can be used to predict the wind loads in a heliostat field, which is important for the field design. As an example, heliostats placed in regions of increased turbulence intensity need to be designed to withstand larger unsteady and dynamic forces requiring higher mechanical impedance of the support structure. Furthermore, by determination of the regions of the field where the mean and unsteady wind loads are lower, the structural stiffness and foundation depth can be decreased. As the heliostat field constitutes between 40% to 50% of the total capital cost of a solar plant (Kolb, 2011), modification of the design of heliostats can help to reduce the capital cost. This study focuses on the wake of a heliostat in an atmospheric boundary layer and aims to develop an understanding of how the statistical and spectral characteristics of turbulence change in the wake of the heliostat. The findings are however are not limited to heliostats and provide an insight into the turbulence in the wake of other flat-plate-like structures in the atmospheric boundary layer including solar photovoltaic panels, billboards and wind barriers.

Heliostats in a solar field are arranged in rows surrounding a receiver in a central or a polar design, with a gap between the subsequent rows which typically varies from a value equal to the characteristic length of the mirror panel to about 8-times the characteristic length as the heliostats are installed further away from the central tower (Hui, 2011). Heliostats within the field are exposed to the turbulence in the wake of other heliostats or the solar tower which alters the approaching turbulence in the atmospheric boundary layer. Based on the field arrangement and the gap between the heliostat rows, both the mean flow and turbulence characteristics inside the field can be very different from the incoming conditions. For instance, wind velocity measurements by ultrasonic anemometers in a five-row array of heliostats in a field found an increase in turbulence intensity from 10% in the approaching flow to 50% in the second row of heliostats (Sment and Ho, 2014). Available field measurements are however very limited due to the complexity of field measurements and the variations of velocity and intensity and length scales of turbulence in a heliostat field are not well known. The increased turbulence in the field is related to the vortex shedding in the wake of heliostats. A large eddy simulation of the flow field around a heliostat, at an elevation angle $\alpha = 25°$, in a uniform inflow showed formation of coherent turbulence structures and counter rotating vortices in the wake (Boddupalli *et al.*, 2018), which subject the downstream structures to dynamic loading. Experimental investigations of the wind loads on multiple heliostats also show the changes in the wind loads from a single heliostat. For instance, measurements of surface pressure distribution on a second heliostat placed in tandem of another one in an atmospheric boundary layer flow showed significant changes in the pressure distribution on the second heliostat, which varied with the gap between the two heliostats (Jafari *et al.*, 2019c). Furthermore, Peterka *et al.* (1987b) measured the wind loads in a four-row arrangement of heliostat models in a wind tunnel experiment and found that while the mean drag force coefficient on a heliostat in the fourth row was lower than that for a heliostat in the first row, the peak drag force coefficient was larger. The increase in the peak drag force suggests an increase in the turbulence intensity in the wake of the upstream heliostats. Hence, understanding how the flow turbulence changes inside the field can help to provide an estimate of the changes in the unsteady wind loads on in-field heliostats.

The flow past a heliostat, if excluding the support structure and the pylon, is similar to the flow past a flat plate at different angles of attack. The wake of a flat plate in a uniform flow, which is a widely studied subject, is characterised by flow separation and vortex shedding. The blockage of the flow by the bluff body creates a velocity deficit in the wake accompanied with periodic velocity fluctuations due to vortex shedding. Three-dimensional and large coherent turbulence structures are formed in the wake. Turbulence intensity in the wake of a square flat plate normal to a uniform flow can increase by up to 16% in the near wake (Nedić *et al.*, 2013). The angle of attack, which resembles the elevation angle of a heliostat panel during its operation, affects the symmetry of the wake. While the wake of a flat plate normal to a uniform flow is symmetric, when inclined at different angles to the flow, the wake becomes asymmetric due to the unequal strength of vortices shed from the leading and trailing edges, resulting in an asymmetric velocity deficit in the wake (Lam and Leung, 2005; Yang *et al.*, 2012).

Inflow turbulence impacts the wake dynamics including structure of turbulence and vortex shedding. Experimental investigation of the wake of flat disks normal to a grid-generated turbulent flow showed the effect of turbulence length scale and kinetic energy in the incoming flow on the flow around the disk (Humphries and Vincent, 1976). Increase of incoming turbulence enhanced mixing in the shear layer and increased entrainment of fluid into the wake, and consequently, decreased the wake recovery length over which the flow properties returned to the undisturbed condition. A large eddy simulation of the wake behind a sphere developed in a turbulent pipe flow also showed that the incoming turbulence resulted in a wider radial expansion of the wake and a faster recovery of velocity deficit along the wake centreline (Legendre *et al.*, 2006). Hearst *et al.* (2016) studied the wake of a wall-mounted cube in four turbulent boundary layers with grid-generated turbulence intensities between 5.4% and 9%. At constant inflow shear level, the wake recovered faster for larger inflow turbulence intensities. In contrast, shear at the cube height was found to have a stronger impact on the flow recovery when comparing wakes with different values of inflow velocity gradient. On the other hand, inflow turbulence is found to have a stronger effect than mean shear at large inflow turbulence intensities (Amoura *et al.*, 2010). An experimental investigation of the effect of inflow turbulence on the wake of a sphere, with inflow turbulence intensities between 15% and 26% and length scales of 3–4 times larger than the sphere diameter, showed that turbulence and velocity deficit in the far wake scaled with the intensity of incoming turbulence (Amoura *et al.*, 2010). It was found that existence of the incoming turbulence altered the wake flow characteristics as the wake instabilities were mainly resulted from the distortion of the incident turbulence, and not the mean velocity, by the sphere. Furthermore, an experimental study of the effect of grid-generated turbulence, with turbulence intensities between 0.8% and 4.3%, on the wake of a disk normal to the flow found that the inflow turbulence weakened vortex shedding in the near wake and reduced its strength (Rind and Castro, 2012). The turbulence decay rate in the far wake was significantly varied by the inflow turbulence such that the wake turbulence evolved towards the inflow characteristics eventually. The observed effects were found to be stronger when the freestream turbulence intensity was larger than 3%. These findings suggest that the inflow turbulence significantly influences the dynamics of wake instabilities and turbulence within the wake flow. Heliostats are placed in the lower the 10 m of the turbulent atmospheric boundary layer and are subjected to large velocity gradients and large-scale turbulence structures. Hence, the inflow turbulent boundary layer alters the wake of a heliostat from a flat plate developed in a uniform flow.

Another parameter, in addition to the inflow turbulence, which affects the wake of a heliostat is the ground effect. The mirror panel of a heliostat is hinged on a pylon such that usually there is a gap between the bottom edge of the panel and the ground which varies with the elevation angle of the panel. The studies on bluff body wakes in a uniform flow show that decreasing the gap from the ground beyond a certain threshold can suppress vortex shedding (Bearman and Zdravkovich, 1978; Bosch *et al.*, 1996). Furthermore, investigation of the effect of the gap flow on the wake of a sharp-edged flat plate suspended in a water channel showed the formation of a wall jet which influenced the near wake significantly (Krampa-Morlu and Balachandar, 2007; Shinneeb and Balachandar, 2016a). It was found that when the gap increased, the reverse flow in the wake was eliminated and the streamwise velocity fluctuations were decreased (Shinneeb and Balachandar, 2016b).

The present study aims to develop an understanding of the turbulence characteristics in the wake of a heliostat in an atmospheric boundary layer flow. Extensive velocity measurements were conducted in the wake of a flat plate model representing a heliostat in two simulated neutral atmospheric boundary layer flows in the University of Adelaide large-scale wind tunnel to characterise turbulence in the wake flow. The remainder of this paper is organised as follows. A description of the experimental method is presented in Section 2. In Section 3, the wake flow and turbulence were characterised by statistical and spectral analysis of the velocity measurements. The findings are then used as a basis for prediction of how wind loads in a heliostat field change in Section 4. Finally, conclusions are given in Section 5.

5.2.2 Methodology

Experimental measurements were performed in the University of Adelaide large-scale wind tunnel. The working section of the boundary layer wind tunnel is 3 m × 3 m × 17 m, and the turbulence intensity in the empty tunnel is between 1% and 3%. Spires and floor roughness elements were used to simulate the atmospheric boundary layer in the wind tunnel. Five spires with identical dimensions were placed at the inlet of the test section with a centre-line distance of 0.5 m in the lateral (y) direction. The spires were followed by a 7.2 m streamwise fetch of wooden roughness elements covering approximately 24% of the floor area over the fetch length. The sizing and spacing of the roughness elements were similar to previous experiment by the authors (Jafari *et al.*, 2019c). In order to minimise the parameters affecting the wake flow, it was attempted to create two boundary layers of a similar height so that the relative position of the models in the boundary layers, H/δ, does not change. Therefore, the spires for the two boundary layers, boundary layer A and B, were designed with an identical height (1.3 m). Figure 5.1(a–b) show the test setup at the test section containing spires, roughness elements and the heliostat model. The heliostat model consists of a pylon (height =130 mm and thickness=10 mm), and a square panel with a characteristic length of 200 mm and a thickness of 2 mm. The heliostat model height to panel characteristic length ratio, H/c, is 0.65, which according to Pfahl (2018) is conventional for heliostats. Furthermore, the blockage ratio, defined as the ratio of the frontal area of the heliostat model panel to the tunnel cross-sectional area, has a maximum value of 0.44% when the heliostat panel is normal to the flow, which is insignificant and hence blockage does not affect the measurements as the maximum allowable blockage ratio is 10% (Barlow *et al.*, 1999).

The inflow conditions and the wake behind the heliostat model were measured using a Turbulent Flow Instrumentation (TFI) multi-hole pressure probe (Cobra probe), which is capable of measuring the three unsteady velocity components and the local static pressure. The accuracy of the measured velocity by the multi-hole pressure probe is within ±0.5 m/s and ±1° in pitch and yaw angles for turbulence intensities of up to 30% according to the manufacturer datasheet. The turbulence intensities in this study are generally below this limit except at very near-wake regions. Furthermore, the measurement error of mean velocity calculated as the standard deviation of five identical measurements was found to be 1.1%. Cobra probes have been found to provide reasonable accuracy for measurement of complex turbulent flows in the literature. Cobra probes have been used in the literature (Vino *et al.*, 2003; Bell *et al.*, 2014; Peng *et al.*, 2016; Gilhome, 2017; Lam and Peng, 2017; Aliferis *et al.*, 2019) for study of both time-averaged and time-resolved velocity and turbulence characteristics in the wake flow. Furthermore, a comparison of the velocity measurements preformed with Cobra probe with those from laser Doppler anemometry and hot wire anemometry in a turbulent pipe flow and in the wake of a wind turbine showed that the maximum error in the mean velocity and turbulence intensity measured by the Cobra probe were 2% and 1%, respectively (Draskovic, 2017).

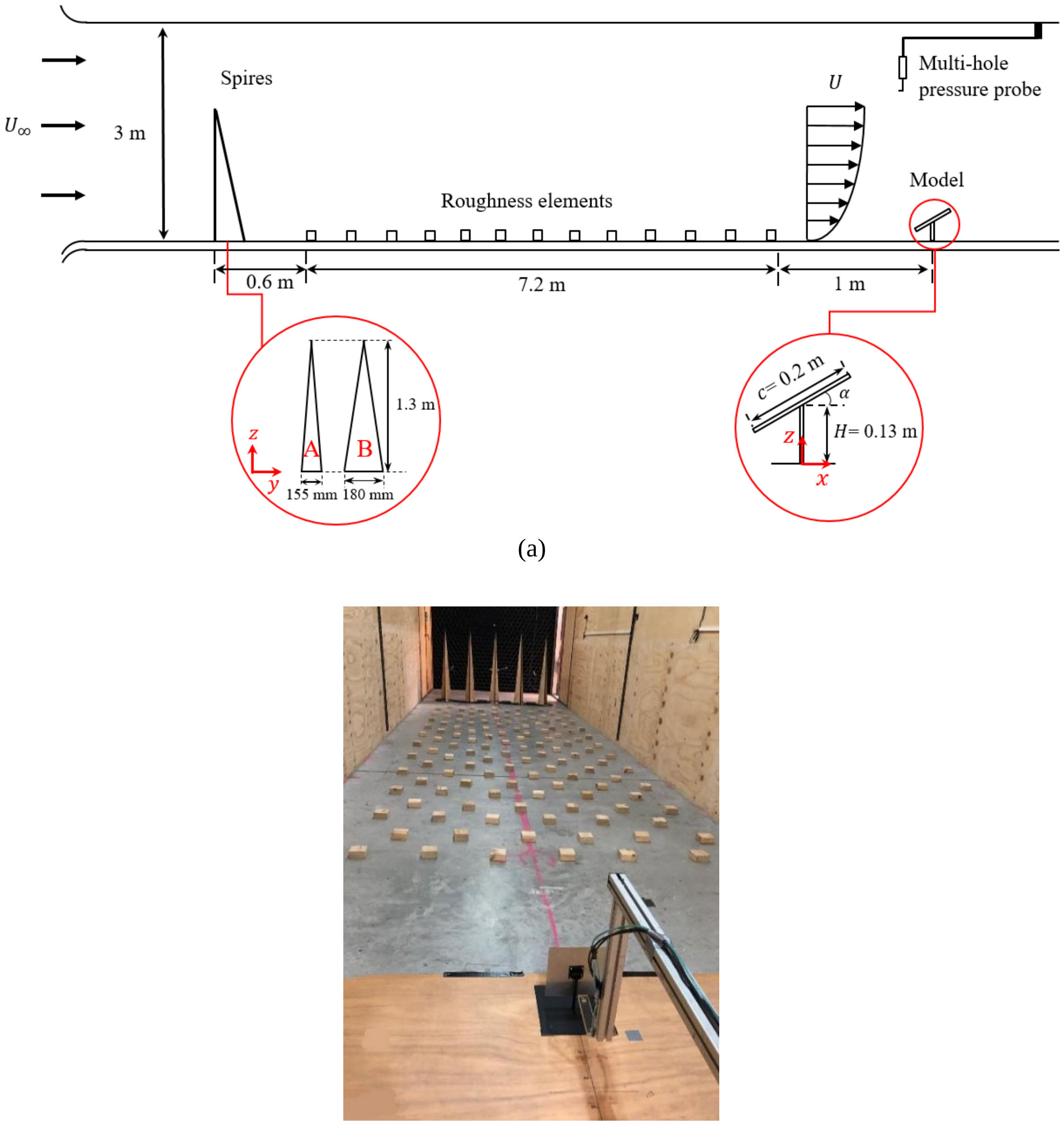

(a)

(b)

Figure 5.1. The experimental setup in the University of Adelaide wind tunnel. (a) Schematic of the setup, (b) photograph of the setup looking upstream from the plate.

5.2.2.1 Incoming Flow Conditions

The two simulated boundary layers in the wind tunnel were characterised and their mean velocity and turbulence characteristics were determined. Velocity was measured, in the absence of the heliostat model, over an area of 1 m^2 in the lateral-wall normal planes at different streamwise locations starting from 1 m downstream of the roughness fetch over a length of 1.6 m (x/c=8) to investigate the boundary layer development. The vertical profiles of mean velocity, U, normalised with the free-stream velocity, U_∞, streamwise and vertical turbulence intensities, $I_u = \sigma_u/U$ and $I_w = \sigma_w/U$, and normalised Reynolds shear stress, $-uw/U_\infty^2$, for the two boundary layers measured at the location of the model (x=0, and y=0) and in its absence are given in Figure 5.2. Figure 5.2(a) shows the non-dimensional mean velocity profiles of the two boundary layers. The boundary layer thickness (δ) was determined as $\delta_{0.99}$ from the mean velocity profile as 0.98 m and 1.1 m for boundary layer A and B, respectively. The mean velocity profiles of the two boundary layers match logarithmic profiles with aerodynamic surface roughness values of 0.002 m and 0.0026 m, respectively. According to Figure 5.2(b), the longitudinal turbulence intensity at the model hinge height (z/c=0.65) is 13% and 15% in boundary layer A and B, respectively. Furthermore, the vertical turbulence intensity at the model hinge height is 8% and 10% in boundary layer A and B, respectively (Figure 5.2(c)). The normalised Reynolds shear stress profiles in Figure 5.2(d) show the largest magnitude of the Reynolds shear stress at z/c=2 in boundary layer B and an approximately constant shear stress between z/c=1 and 3 for boundary layer A. For the analysis of the wake flow characteristics in the current study, only the mean velocity and turbulence characteristics in the simulated wind tunnel boundary layers are presented. A detailed discussion of the similarities and differences of the mean velocity and turbulence intensity profiles, as well as spectral characteristics and length scales of turbulence in the wind tunnel boundary layers and the atmospheric boundary layer is given in Jafari *et al.* (2019c).

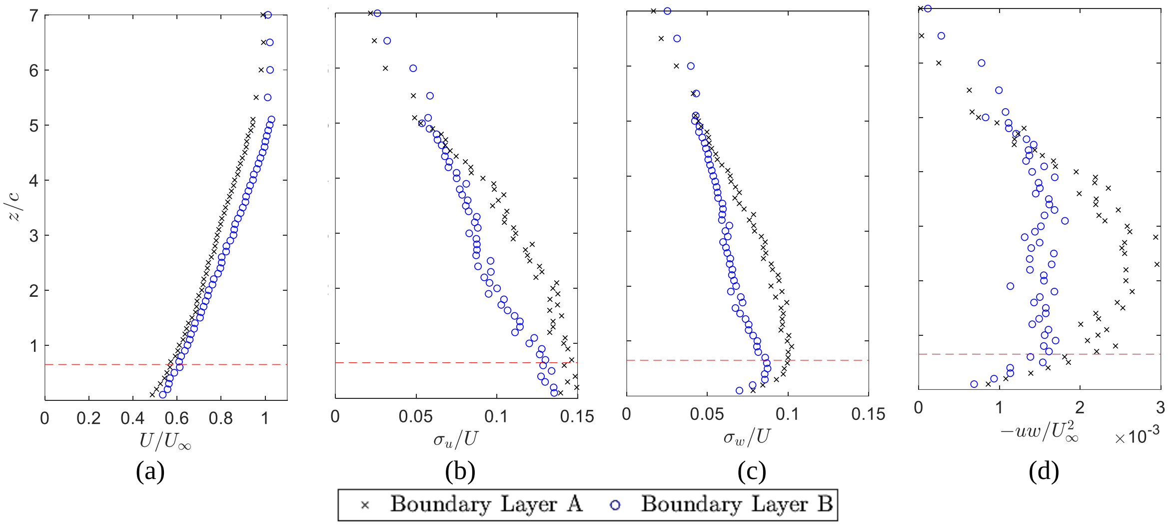

(a) (b) (c) (d)

Figure 5.2. Profiles of the incoming flow in the two wind tunnel boundary layers: (a) normalised mean velocity, (b) longitudinal turbulence intensity, (c) vertical turbulence intensity, and (d) Reynolds shear stress (at U_∞ =11.1 m/s, x=0, and y=0). The horizontal dashed lines show the model hinge height.

Table 5.1 gives a summary of the inflow conditions, including boundary layer height and longitudinal and vertical turbulence intensities at the model location for each boundary layer flow. In addition, the ratio of longitudinal and vertical integral length scales (L_u^x and L_w^x) over the characteristic dimension of the plate are presented. The turbulence intensities and integral length scale ratios are given at the hinge height of the model, H, since this value is constant for all elevation angles, while the height of the plate top edge varies, and hence, provides a comparison for all cases. The non-dimensional shear $\tau_H = (H/U_H)(\partial U/\partial z)|_H$ is also given in Table 5.1. This non-dimensional form of shear is selected as recommended by Hearst *et al.* (2016) as free-stream measurements in the atmospheric surface layer are not usually available. Hence, τ_H is normalised with the time scale of the flow at the hinge height of the model.

Table 5.1. Incoming flow conditions. The characteristics given at the model position were calculated from velocity measurements in the absence of the model.

	δ	H/δ	U_H/U_∞	τ_H	I_{u_H}	I_{w_H}	$(L_u^x/c)_H$	$(L_w^x/c)_H$
Boundary Layer A	0.98	0.133	0.56	0.048	0.13	0.08	2.01	0.42
Boundary Layer B	1.20	0.108	0.61	0.028	0.15	0.10	2.40	0.48

Furthermore, to achieve similarity in the wind tunnel experiments, ideally, both the boundary layer and the heliostat model must be scaled down by an identical length scale factor. However, this similarity cannot be achieved for small-scale structures such as heliostats and solar panels as it requires the model dimensions to be very small. The inevitable consequence of the mismatch of length scale factors is a change in H/δ and a different L_u^x/c and L_w^x/c between the wind tunnel and the full-scale conditions. This scaling issue has been extensively discussed in the literature (Tieleman, 2003; Richards *et al.*, 2007; Jafari *et al.*, 2019c) and its discussion is out of the scope of the current study. However, with consideration of the differences, the results are interpreted with respect to the inflow conditions for characterisation of the wake flow.

5.2.2.2 Wake Measurements

The velocity in the wake of the heliostat model at elevation angles of α=30°, 60°, and 90° were measured within the two boundary layers. These elevation angles are considered to represent a range of operational angles for heliostats. Velocity measurements were performed over streamwise wall normal planes downstream of the heliostat model at y=0 mm. Figure 5.3 shows the measurement grid which was determined based on initial measurements and evaluation of the resolution of the results. The measurement grid ranges from z=10 mm to

z=500 mm in the vertical direction, with a grid spacing Δz=20 mm. In the streamwise direction, the measurements were taken at positions ranging from x=150 mm to x=1600 mm downstream of the model, with Δx increasing from 50 mm in the near wake to a maximum of 200 mm at x=1000–1600 mm. Velocity measurements were performed for a duration of 30 seconds at each point with a sampling frequency of 2 kHz. Some measurements were also taken over a duration of 120 seconds for spectral analysis.

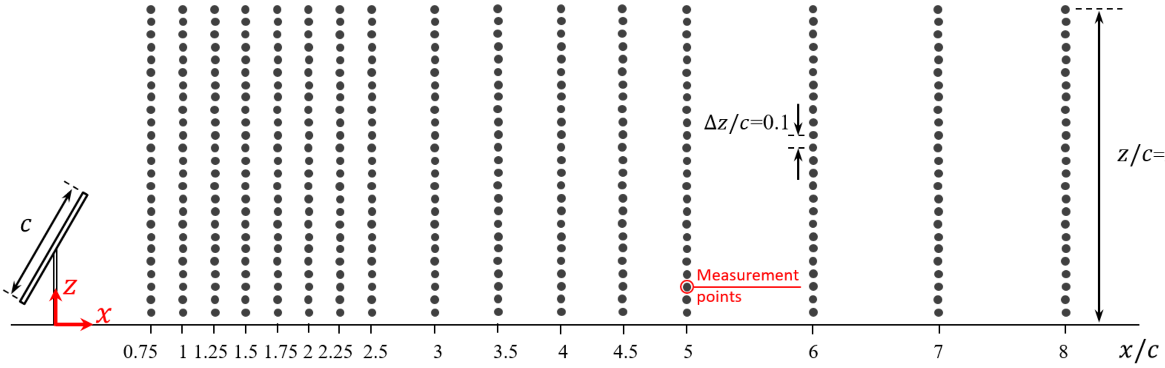

Figure 5.3. A schematic showing the locations of velocity measurements in the wake.

5.2.3 Wake Flow Characteristics

5.2.3.1 Velocity Deficit

Figure 5.4 shows the time-averaged streamwise velocity deficit in the xz-plane in the wake for the three elevation angles and the two inflow conditions. The velocity deficit normalised with the free-stream velocity, $(U_{in} - U)/U_{\infty}$, at the central line, y=0, is presented. A distinct region of velocity deficit exists in the wake of the plates up to x/c=5 for all three elevation angles, with the largest deficit observed when α =90°. Due to proximity to the ground and velocity gradient in the inflow boundary layer, the wakes are asymmetric. The accelerated flow regions, represented by the negative values, are also seen above the plate, z/c >1.5, and further downstream at x/c >6. Furthermore, the comparison of the mean velocity at x/c=8 with the inflow conditions shows that the wake flow has not yet recovered.

Comparison of the flow for the two incoming conditions in Figure 5.4 shows a slightly faster recovery of the wake for the incoming flow with the larger turbulence intensity, which is due to the increased entrainment of fluid into the wake.

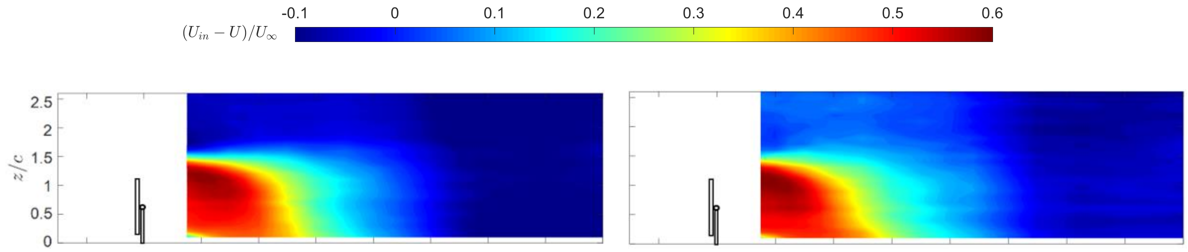

(a) I_u =13%, α =90°

(b) I_u =15%, α =90

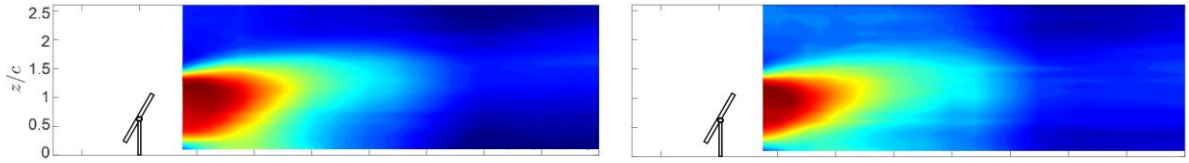

(c) I_u =13%, α =60°

(d) I_u =15%, α =60°

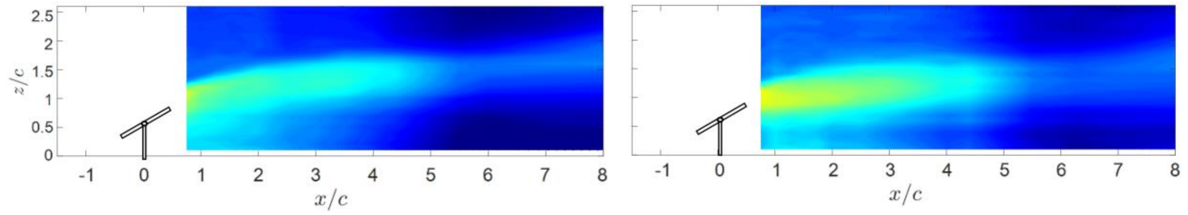

(e) I_u =13%, α =30°

(f) I_u =15%, α =30°

Figure 5.4. Streamwise velocity deficit, $U_{in} - U$, normalised with freestream velocity, U_∞, in the wake in the xz-plane for the two inflow boundary layers (left: Boundary Layer A, right: Boundary Layer B): (a–b) α =90°, (c–d) α =60°, (e–f) α =30°.

Vertical profiles of the mean streamwise and vertical velocity at different streamwise distances are compared for the three elevation angles in Figure 5.5, where the streamwise velocity deficit and the wake-induced vertical velocity are clearly seen. In the near wake region, Figure 5.5(a), the variations of the streamwise and vertical velocity occur at different extents based on the elevation angle of the plate, for example at x/c=2 the reduction of streamwise velocity is the largest for α =90°. The increased gap between the bottom edge of the plate and the ground at α =60° and α =30° creates a jet flow in this region which is more significant at α =30° resulting in a larger streamwise velocity compared to the other two angles and a positive vertical velocity. In the far wake, Figure 5.5(d), the differences diminish by x/c=8, and the profiles closely match one other, while still differ from the inflow profile in Figure 5.2(a).

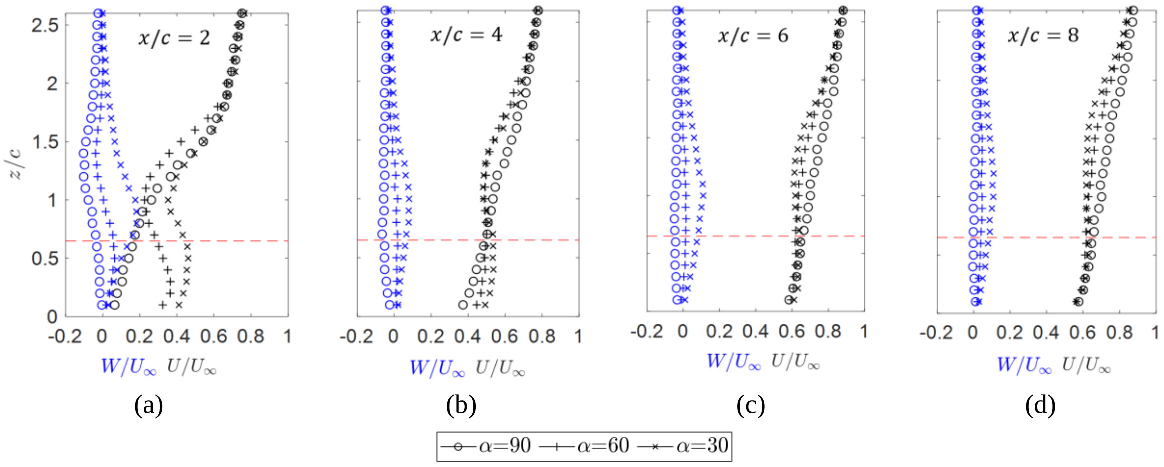

Figure 5.5. Vertical profiles of mean streamwise, U, and vertical velocity, W, at different streamwise locations in the wake in Boundary Layer B at I_u =15% for α =90°, 60°, 30°: (a) x/c =2, (b) x/c =4, (c) x/c =6, (d) x/c =8. The black and blue colours represent the streamwise and vertical velocity, respectively. The horizontal dashed lines show the heliostat model hinge height.

5.2.3.2 Wake Turbulence

Figure 5.6 shows the normalised turbulence kinetic energy calculated from the variance of all three velocity components in the wake at different elevation angles and inflow conditions. As shown in Figure 5.6, there is a significant increase in turbulence kinetic energy in the near wake region, x/c <4, which is caused by the separation of the flow at the edge of the plate. The increased turbulence kinetic energy region is mainly concentrated at the top edge of the plate and much less effect is seen at the bottom edge of the plate. This asymmetry is due to velocity gradient of the incoming boundary layer flow and the ground proximity where shear is smaller at lower heights.

Comparison of the turbulence kinetic energy for the plates at the three elevation angles shows that the increase in turbulence energy is larger for the plate at α =90° compared to α =60° and 30°. Furthermore, the regions of increased turbulence kinetic energy are extended further downstream for lower elevation angles which is due to the increased gap between the plate and the ground, forming a stronger wall jet in the gap region as discussed in (Krampa-Morlu and Balachandar, 2007; Shinneeb and Balachandar, 2016a).

The inflow condition has a slight impact on the turbulence kinetic energy distributions as shown in Figure 5.6. For instance, comparison of the turbulence kinetic energy at α =90° for the two inflow conditions, Figure 5.6(a) and Figure 5.6(b), shows a slightly larger peak of turbulence kinetic energy in the wake of the plate in boundary layer A. This can be attributed to the inflow conditions. The difference between the inflow turbulence intensities is not significant, (I_u =13% and 15% in A and B, respectively). Hence, the larger shear, τ_H, in boundary layer A, which is twice that in boundary layer B, may be the source of the larger peak turbulence kinetic energy in the wake.

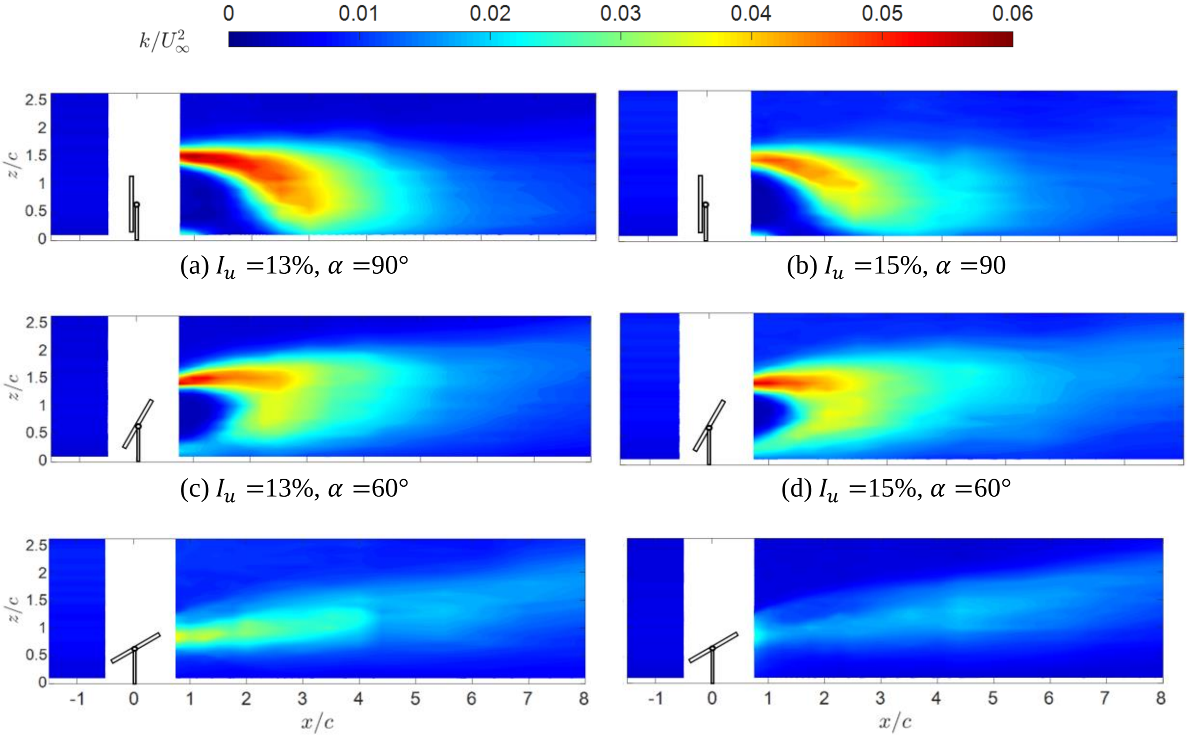

(a) I_u =13%, α =90°

(b) I_u =15%, α =90

(c) I_u =13%, α =60°

(d) I_u =15%, α =60°

(e) I_u =13%, α =30°

(f) I_u =15%, α =30°

Figure 5.6. Normalised turbulence kinetic energy in the wake in the xz-plane for the two inflow boundary layers (left: Boundary Layer A, right: Boundary Layer B): (a–b) α =90°, (c–d) α =60°, (e–f) α =30°.

Figure 5.7 shows normalised Reynolds shear stress representing the vertical momentum flux for the different cases. Turbulent momentum fluxes indicate flow entrainment into the wake which significantly affects wake recovery. As shown in Figure 5.7, two regions of positive and negative Reynolds stress are seen for all cases. Large positive Reynolds stresses indicating downward momentum fluxes exist in the near wake at the top edge of the plate for α =90° and 60° (Figure 5.7(a–d), and upward momentum fluxes which are much smaller in magnitude are located at the bottom edge of the plate. Existence of the peak magnitudes at the top edge of the plate is due to the larger velocity gradient and shear at the top edge. At α =30°, Figure 5.7(e–f), due to the increased gap flow, the upward momentum fluxes are extended further downstream diminishing the extent and magnitude of the positive Reynolds stresses.

Furthermore, the streamwise extent of the regions of positive and negative Reynolds stresses is larger for lower elevation angles, similar to the turbulence kinetic energy distributions.

Comparison of the shear stress distributions for the two inflow conditions shows that the regions of large Reynolds stress extend further downstream in boundary layer A. A similar effect is observed for the turbulence kinetic energy in Figure 5.6. The increased spatial extent of regions of large turbulence kinetic energy and Reynolds stress in boundary layer A is due to the larger mean shear and the lower turbulence intensity in boundary layer A (Table 5.1).

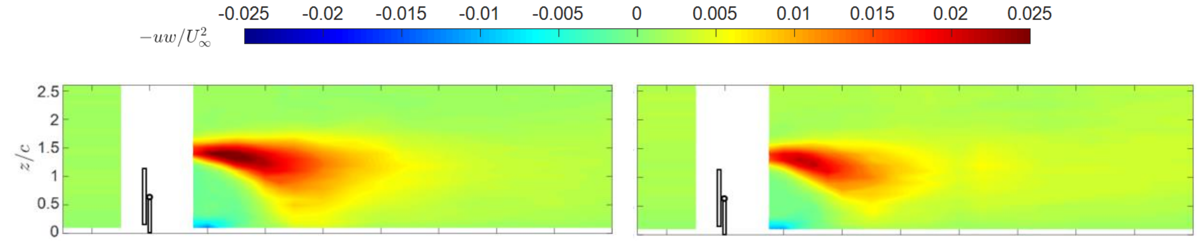

(a) I_u =13%, α =90° (b) I_u =15%, α =90

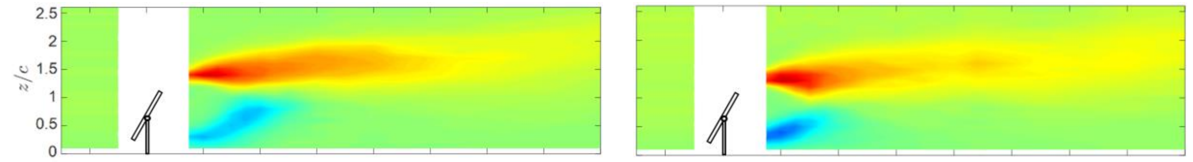

(c) I_u =13%, α =60° (d) I_u =15%, α =60°

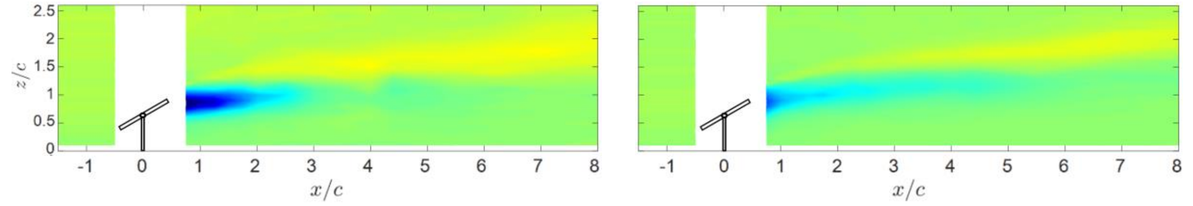

(e) I_u =13%, α =30° (f) I_u =15%, α =30°

Figure 5.7. Normalised mean Reynolds shear stress in the wake in the xz-plane for the two inflow boundary layers (left: Boundary Layer A, right: Boundary Layer B): (a–b) α =90°, (c–d) α =60°, (e–f) α =30°.

5.2.3.3 Spectral Characteristics of Velocity Fluctuations

The power spectral density of the streamwise velocity fluctuations in the wake of the plate at α =90° is shown in Figure 5.8. The power spectral density pre-multiplied by frequency and normalised with the velocity variance, fS_{uu}/σ_u^2, is presented. This non-dimensional form is chosen as it displays the frequencies which are the major carriers of energy in the flow. As similar trends were found for the streamwise and vertical velocity spectra, only the results for the streamwise velocity are presented here. Figure 5.8(a) shows the normalised spectra in the near wake region, x/c=1, at different vertical heights inside and outside the wake flow. A clear distinction between the spectral distributions in the wake, z/c=0.5–1, and outside the wake, z/c=2–2.5, is found. Outside the wake flow, at z/c=2–2.5, the peak of the spectrum is at fc/U_∞ =0.03, which is the dominant peak of the turbulent boundary layer flow corresponding to the integral length scale. There is an increase in the energy of non-dimensional frequencies fc/U_∞ >0.1 at z/c=1.5, which is the location of increased turbulent kinetic energy (Figure 5.6(a)). When descending further into the wake flow, z/c=0.5–1, the spectral distribution changes drastically showing transfer of energy to high frequencies such that the inflow peak diminishes. The transfer of energy from the large-scale turbulence structures to the small scales shows the breakdown of large inflow turbulence structures by the plate. Figure 5.8(b) shows the power spectral density in the wake of the plate at α =90° and the plate hinge height, z/c=0.65, at several downstream distances. The turbulence spectrum of the incoming boundary layer is also shown. At x/c=1, the higher frequencies have the highest energy which shows the existence of smaller turbulence scales and breakdown of the larger inflow turbulence structures. At x/c=2, an increased energy level at the higher end of the spectrum is seen showing the remainder of the wake-induced small vortices. Further downstream, in the far wake region, x/c=4 to 8, the spectral distribution is more similar to the inflow although containing higher energy at the mid- to high frequencies, fc/U_∞ >0.1, compared to the inflow. Furthermore, comparison of the spectrum at x/c=8 with the inflow spectrum shows that the wake flow has not fully recovered up to x/c=8 (as also shown in mean velocity contours in Figure 5.4).

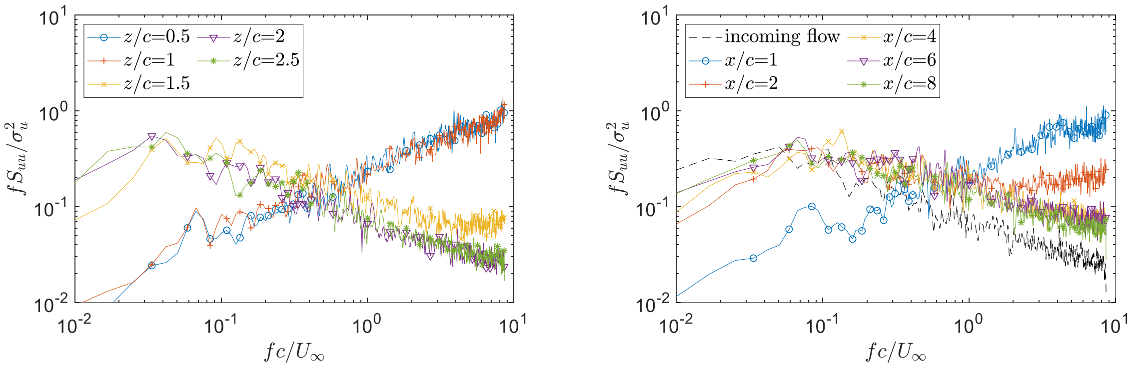

(a) (b)

Figure 5.8. Normalised power spectral density of streamwise velocity fluctuations, fS_{uu}/σ_u^2, in the wake for α=90°: (a) at several vertical positions at x/c=1, (b) at several downstream positions at z/c=0.65.

The results in Figure 5.8 show no dominant shedding peak in the turbulence spectrum making it difficult to determine a unique Strouhal number for vortex shedding. Instead, an increase in the energy of a range of turbulence scales is identified. Lack of a distinguished shedding frequency in the wake was also found by Hearst *et al.* (2016) in the wake of a cube exposed to free-stream turbulence, where an increase in the energy over a range of frequencies was observed instead of a prominent shedding frequency. Rind and Castro (2012) also found that inflow turbulence damped vortex shedding and reduced its energy, such that at high inflow turbulence intensities the trace of vortex shedding in the turbulence spectrum was hardly visible.

Figure 5.9 shows the normalised spectral density of streamwise velocity fluctuations at z/c=0.65 at several downstream distances for the plate at α =60° and α =30°. For both elevation angles, increase of higher-frequency turbulent scales is evident in both the near and far wake regions showing that the plate at both elevation angles breaks down the large inflow turbulence structures. To identify the effect of the elevation angle, the near wake spectra at the hinge height for the three elevation angles are compared in Figure 5.9(c–d), which show the energy transfer is more significant at α =90°.

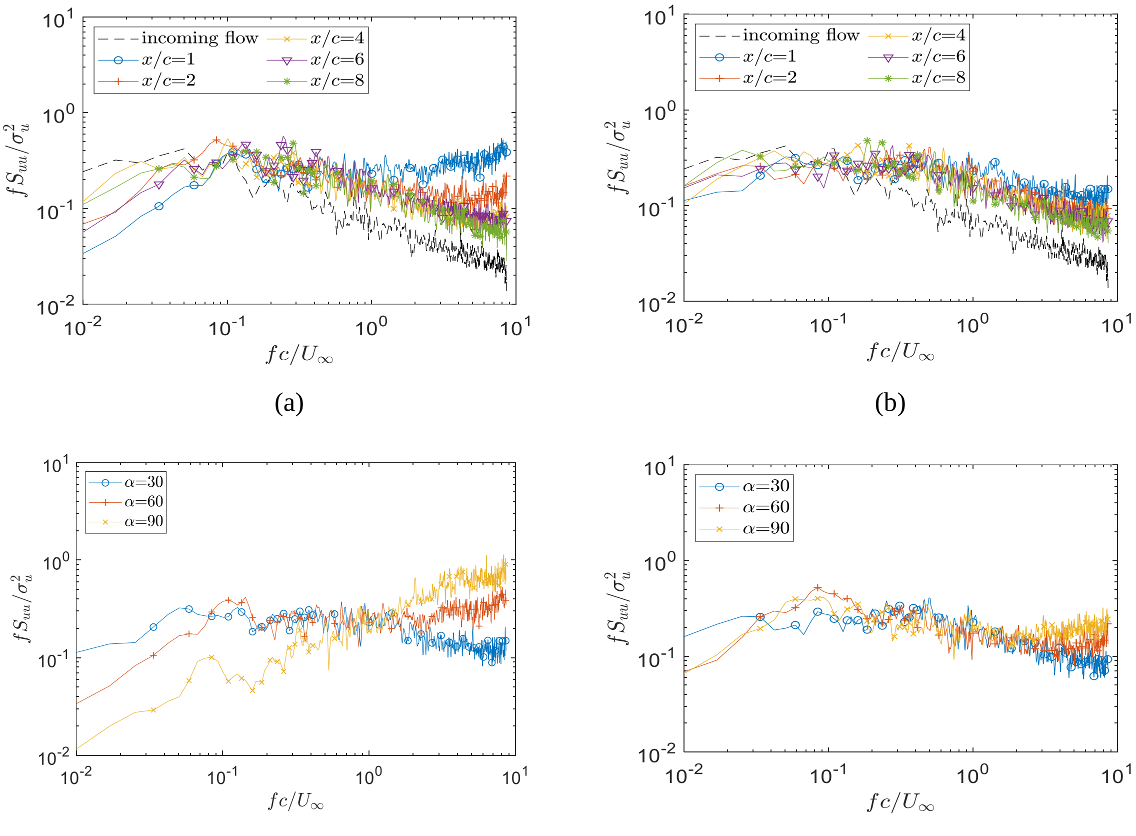

(a) (b)

(c) (d)

Figure 5.9. Normalised power spectral density of streamwise velocity fluctuations, fS_{uu}/σ_u^2, in the wake at z/c=0.65: (a–b) at several downstream locations for α=60° and α=30°, (c–d) comparison of the spectra for the three elevation angles at x/c=1 and x/c=2, respectively.

5.2.3.4 Orthogonal Wavelet Decomposition of Velocity Fluctuations

To determine the most energetic scales in the wake flow, the orthogonal wavelet method is employed in this study to decompose velocity according to the scales of turbulence structures. Using the wavelet multi-resolution technique, the velocity signal is broken down into frequency bands which directly represent the scales of turbulent structures (Razali *et al.*, 2010). The decomposed velocity signals corresponding to each level can then be analysed individually in time or frequency domain providing detailed information about each specific turbulence scale. Using this method, a better understanding of the various scales in the wake flow can be achieved. This method has been used in the literature for analysis of turbulent structures in wake flows (Rinoshika and Zhou, 2005; Zhou *et al.*, 2006; Rinoshika and Zhou, 2007; Razali *et al.*, 2010; Rinoshika and Omori, 2011; Ali *et al.*, 2016). Further details of the orthogonal wavelet method are given in (Rinoshika and Zhou, 2005; Razali *et al.*, 2010).

The wavelet basis function used in this study is the Daubechies wavelet with an order of 20, as according to Rinoshika and Zhou (2007) the Daubechies is a suitable filter for turbulence analysis due to its smoothness and frequency localisation. Using the orthogonal discrete wavelet transform, the streamwise and vertical velocity signals are decomposed into 10 levels. The wavelet component of the velocity signal in each level provides information about the turbulent structures in its corresponding frequency band regardless of the number of wavelet levels. The frequency bands corresponding to each wavelet level are shown on the spectra of longitudinal and vertical velocity fluctuations in Figure 5.10. The higher wavelet levels correspond to lower frequencies and larger turbulence structures. The longitudinal and vertical integral length scales of turbulence are also shown in Figure 5.10. As shown in Figure 5.10, Levels 8–10 and Levels 7–10 represent the turbulent structures larger than the streamwise, L_u^x, and vertical, L_w^x, integral length scales.

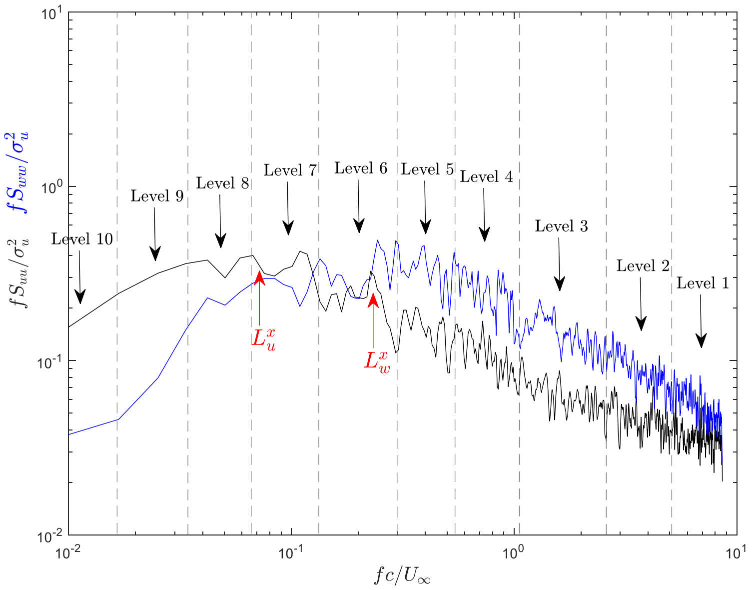

Figure 5.10. The normalised frequency bandwidth of the wavelet levels shown on the spectra of streamwise and vertical velocity fluctuations, the black and blue lines, respectively, in Boundary Layer B.

After decomposing the velocity signal into different scales, the variance of each scale is calculated. By comparison of the variance of each wavelet level to the variance of the original velocity signal, the contributions to velocity variance from different scales are found. Figures 5.11(a) and 5.11(c) show the normalised variance of streamwise and vertical velocity in the wake of the plate at α=90° at z/c=0.65 from x/c=0.75 to x/c=8. The streamwise and vertical velocity variances in the wake increase to reach a peak at x/c=2.5 and 3, respectively, which is then followed by a decrease in the variance (the same trend as turbulent kinetic energy in Figure 5.6). The normalised variance of the wavelet levels of the streamwise and vertical velocity components in the wake is shown in Figure 5.11(b) and 5.11(d), respectively. According to Figure 5.11(b), the variances of wavelet Levels 1–3, which represent the small turbulence structures, remain almost constant along the streamwise direction. In contrast, the variances of large scales, wavelet Levels 8–10, increase significantly reaching a peak at x/c=2.5. According to Figure 5.11(b) and Figure 5.11(d), in the near wake region at x/c=1, the variances of all 10 levels are almost in the same order due to the breakdown of large scales to smaller scales which leads to reduction of energy of large scales, which agrees with the spectral analysis in Figure 5.8. Further downstream as the large scales grow, their energy increases and the variances of Levels 8–10 increase by four to five times between x/c=2 and x/c=8. A similar trend is observed in Figure 5.11(d) for the variances of the wavelet components of vertical velocity showing that the large turbulence structures are the major contributors to the peak of the vertical velocity variance, which occurs at x/c=3, and further downstream, while at x/c=1 the breakdown of large scales to smaller scales results in a significant reduction in the variance of large scales. These results along with the spectral analysis show that the dominant mechanism in close proximity of the plate in the near wake is breakdown of large-scale turbulence structures of the inflow boundary layer and transfer of energy to small scales. When moving further downstream, the flow starts to recover, and turbulence scales develop towards the inflow distribution. Evolution of turbulence structures towards the external turbulence was also found in the in the far wake of a sphere exposed to inflow turbulence by Rind and Castro (2012).

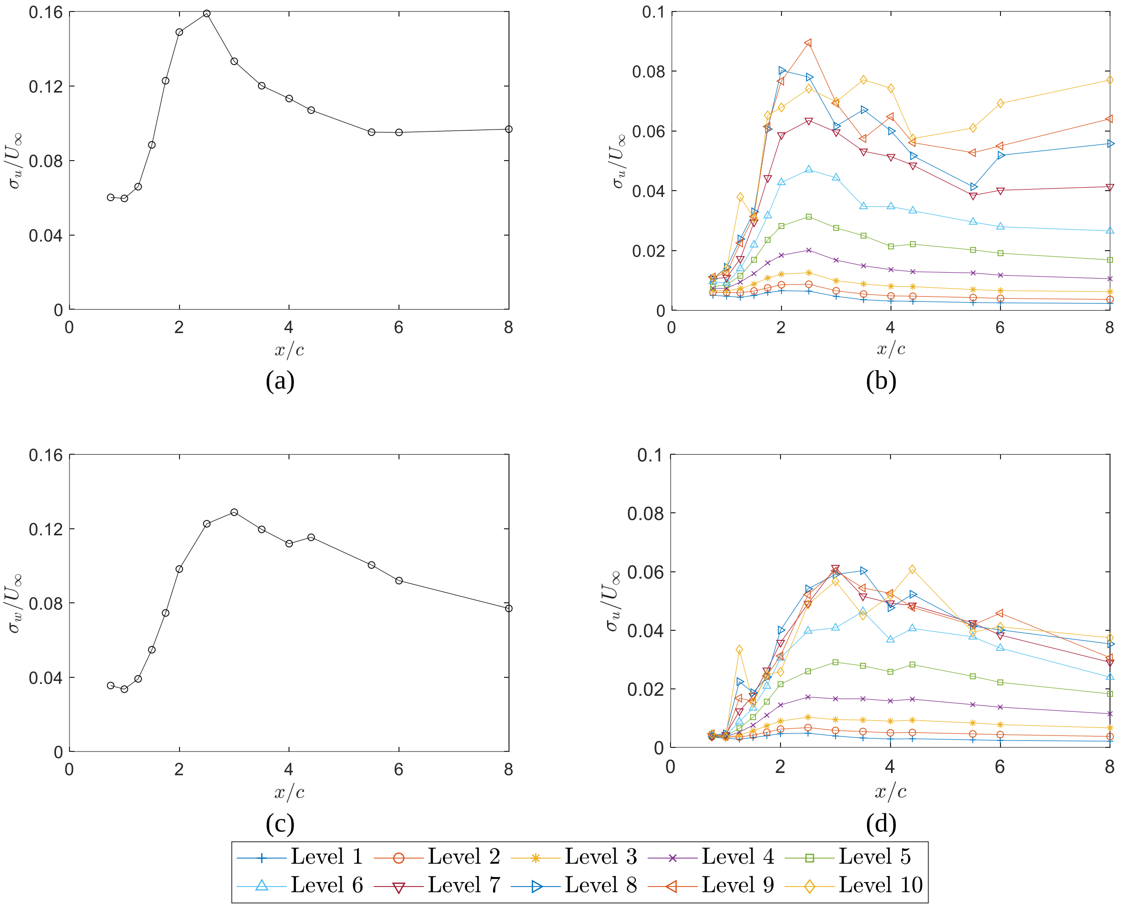

Figure 5.11. Normalised velocity variance in the wake in streamwise direction for α=90° at z/c= 0.65: (a–b) variance of streamwise velocity and its wavelet levels, (c–d) variance of vertical velocity and its wavelet levels.

Figure 5.12 shows the normalised variance of the wavelet levels of the streamwise velocity component in the wake at z/c=0.65 for α =60° and α =30°. The streamwise distribution of the different wavelet levels in Figure 5.12(a) for α =60° is similar to that in Figure 5.11(b) for α =90° with a slightly larger magnitude of the variance of the large scales in the proximity of the plate. For α =30°, Figure 5.12(b), no significant change in the streamwise distribution of the variances of the different levels is observed indicating that there is much less breakdown of large scales by the plate compared to the other two elevation angles. This agrees with the results found from the spectral distributions in Figure 5.9(b).

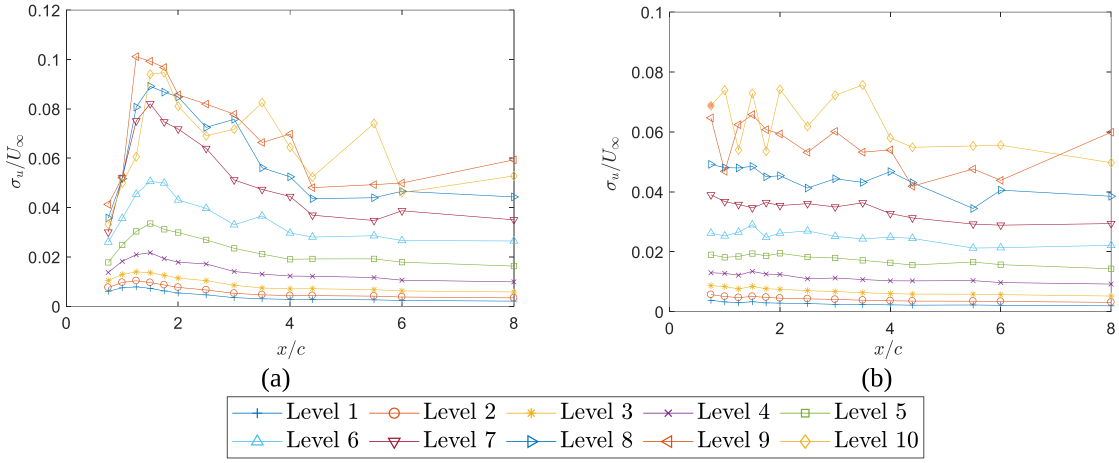

Figure 5.12. Normalised variance of the wavelet levels of streamwise velocity component in streamwise direction at z/c= 0.65 in the wake for: (a) α=60°, (b) α=30°.

The wavelet analysis results show a transfer of energy to smaller turbulence scales in the immediate downstream of the heliostat, while at x/c >2, the large turbulence scales in the order of the integral length scale of the inflow boundary layer have larger turbulence intensities. Since the length scales of turbulence and their corresponding intensity can directly impact the wind loads on structures placed in the wake flow, these results can have important implications for the dynamic wind loads in an array of heliostats, which are discussed in Section 4.

5.2.4 Wake-induced wind loads in a heliostat field

The results in Section 3 provide an insight into the velocity and turbulence characteristics in the wake of a model heliostat in a simulated atmospheric boundary layer flow. In a heliostat field, the heliostats which are placed inside the field are exposed to the wake flow of the upstream heliostats. Although the presence of the other heliostats in the wake affects the flow, the wake characteristics can be used as a basis for prediction of the flow characteristics in the field. As the flow turbulence characteristics are directly related to the wind loads on heliostats, the findings in Section 3 can have several implications for the design of heliostat fields which are discussed in this section.

A summary of changes in mean velocity and velocity variances in the wake flow compared to the inflow boundary layer is presented in Figure 5.13. To highlight how the flow in the wake changes from the inflow atmospheric boundary layer, the mean velocity, streamwise and vertical velocity variances, and the streamwise and vertical turbulence intensities in the wake are normalised with their inflow values and are given for the plates at the three elevation angles. According to Figure 5.13, despite the decrease in mean wake velocity, the velocity variance is larger than the inflow condition. Except at x/c <1.5 for α=90°, both the streamwise and vertical velocity variances are larger in the wake for all other cases. The increase of velocity variance accompanied with reduction of mean velocity leads to an increased turbulence intensity, such that both the streamwise and vertical turbulence intensities are larger than the inflow at x/c <5 for all the three elevation angles. The maximum velocity variances in the wake flow for all three elevation angles occur at approximately x/c =2, where the velocity variance is more than double the inflow value. The maximum turbulence intensity at the heliostat hinge height occurs at x/c =1.5 with more than 12-times increase in turbulence intensity for α=90° and 60°, Figure 5.12(a–b).

5.2.4.1 Operating wind loads

Figure 5.13 shows that velocity variance and turbulence intensity in the wake are in general larger than the inflow boundary layer. Hence, the heliostats positioned inside the field are exposed to an increased turbulence intensity compared to the heliostats in the first row which is in agreement with the field measurements by Sment and Ho (2014). Since the increased turbulence intensity is directly correlated with an increase in unsteady forces (Bearman, 1971; Peterka *et al.*, 1989; Jafari *et al.*, 2018; Pfahl, 2018), the unsteady wind loads on the in-field heliostats are expected to be larger than the wind loads on the heliostats in the first row. For instance, according to Figure 5.13(a), I_u in the wake of a heliostat at α=90° at x/c =2 increases to a value 7-times larger than the inflow turbulence intensity. If a second heliostat is placed at this location, it will be exposed to $I_u = 7.6\, I_{u,in}$. Such increase in turbulence intensity will lead to more than 80% increase in the unsteady drag force coefficient on the second heliostat according to the relationship given in Jafari *et al.* (2018). Hence, a significant increase in the unsteady loads on the downstream heliostats in a field is expected due to the increase of turbulence intensity.

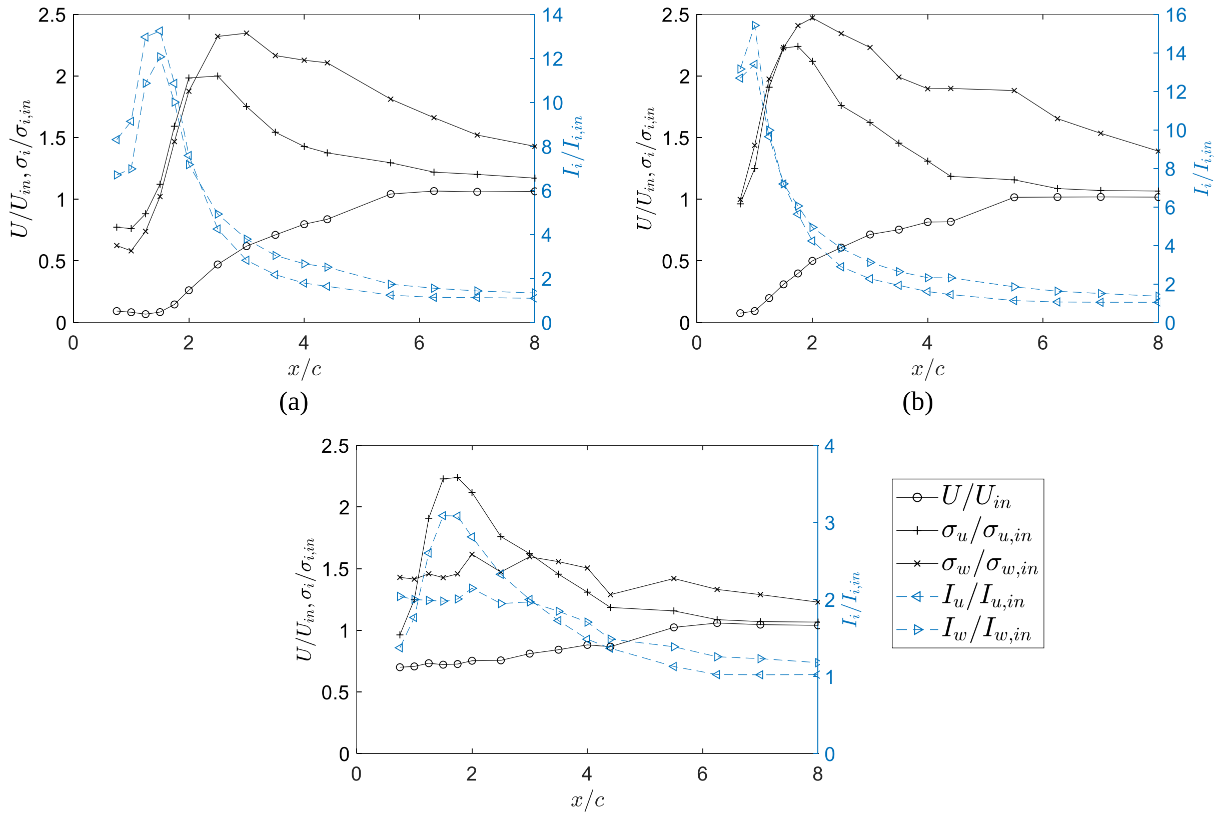

(a)

(b)

(c)

Figure 5.13. The changes in velocity and turbulence in the wake compared to their inflow values, represented by the subscript *'in'*, at the plate hinge height, z/c=0.65, for (a) α=90°, (b) α=60°, and (c) α=30°. In each figure, the black solid lines show magnitude of normalised mean velocity, streamwise and vertical velocity variances on the left axis and the blue dashed lines show the normalised streamwise and vertical turbulence intensities on the right axis.

The changes in wind loads predicted from the wake turbulence is confirmed by experimental measurements of wind loads on tandem heliostats. Measurements of pressure distribution on two heliostat models placed in tandem show that the pressure distribution on the heliostat panel varies significantly as the gap between the two heliostats changes leading to variations in the position of the centre of pressure (Jafari *et al.*, 2019a), which can be attributed to the turbulence in the wake of the upstream heliostat. The standard deviation of the position of centre of pressure, representing the unsteady variations of the pressure distribution on the downstream heliostat panel, was found to be larger than the single heliostat when the gap between the two heliostats, x/c, varied between 1 and 7 reaching a peak at x/c=2 (Jafari *et al.*, 2019a). Furthermore, the standard deviation of the position of centre of pressure was the largest when both plates were elevated at 90° which shows the effect of the dramatically increased turbulence intensity in the wake of the heliostat at α=90°.

As the magnitude of the forces on the panel and the position of the centre of pressure vary, the induced moments at the heliostat hinge and pylon base change, which is important for the design of elevation drives and foundation. Figure 5.14 shows the hinge moment coefficient, C_{MHy}, on the second tandem heliostat compared to the single heliostat based on the experimental measurements by (Jafari *et al.*, 2019a). The mean and peak coefficients and the root mean square (RMS) of the fluctuating coefficient normalised with those on a single heliostat are shown. It is observed that the peak and RMS coefficients are larger than those for the single heliostat for all the gap ratios for α=90° and 60°, and at $x/c \geq 2$ for α=30°. The increase in the peak and RMS coefficients is larger for α=90° and 60° compared to α=30° which shows the effect of the larger increase in turbulence intensity in the wake of the heliostat at the two larger elevation angles. Moreover, the results of Figure 5.14 show an increase in the mean hinge moment coefficient at $x/c \geq 2$ for α=30° and 60° and x/c=3–4 for α=90°. The increase of mean hinge moment is despite the reduction of mean lift and drag force coefficients reported by Peterka *et al.* (1987a) for the heliostats in five downstream rows, which is due to the reduction of mean velocity in the wake of the upstream heliostat. Larger mean hinge moment coefficient, in spite of lower mean lift and drag force coefficients, is attributed to the unsteady variations of the position of the centre of pressure as reported by Jafari *et al.* (2019a), and is a consequence of the increase of turbulence intensity and variation of the length scales of turbulence in the wake of the upstream heliostat. Hence, the increase in turbulence intensity in the wake of a heliostat not only leads to an increase in the fluctuating lift and drag forces on the downstream heliostat, but may also lead to an increase of the mean hinge moment coefficient. This highlights the importance of modification of heliostat design for the heliostats positioned inside the field compared to those at the front rows.

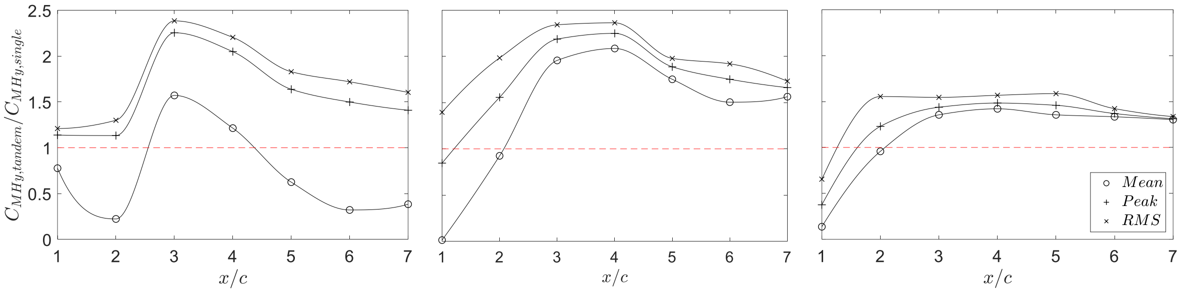

(a) (b) (c)

Figure 5.14. The mean, peak and RMS hinge moment coefficient, C_{MHy}, on a second tandem heliostat normalised against the moment coefficients on a single heliostat for (a) α=90°, (b) α=60°, and (c) α=30°. Reproduced from Jafari *et al.* (2019a).

5.2.4.2 Effect of field density on operating wind loads

Since the wake flow characteristics are found to vary at different streamwise distances, the distance between the rows in a heliostat field, which is indicated by field density, is an important parameter affecting the flow and the wind loads. According to Figure 5.13, the maximum turbulence intensity in the wake flow for all three elevation angles occurs at approximately $x/c =$1.5, and both streamwise and vertical turbulence intensities are significantly larger at $x/c \leq$3 being more than 4-times larger than the inflow for α=90° and 60° and double the inflow for α=30° (Figure 5.13). Hence, in high-density areas of a heliostat field, where the gap between the heliostat rows is between 1–3 times the characteristic length, the unsteady wind loads are expected to be larger than other regions of the field indicating a critical design case. The increase in the unsteady wind loads on the inner field heliostats is expected to be less in regions of the field with a very low density, $x/c >$6, as the increase in the turbulence intensity is less than 20%, where the 20% increase is for α=90°. Hence, the wind loads on heliostats in the low-density regions near the perimeter of the field are likely to show a smaller variation with distance into the field than those in high-density regions close to the tower. The predicted effects are in agreement with the pressure measurements on tandem heliostats which show the largest variations of the position of the centre of pressure at $x/c =$1–3 (Jafari *et al.*, 2019a) and the maximum hinge moment coefficients at $x/c =$3 for α=90° and 60° (Figure 5.14).

Field density can also affect the dominant frequencies and scales of turbulence in the flow. Based on the spectral analysis of wake turbulence, it was found that the spectral distribution of turbulence in the immediate wake at $x/c =$1 differs significantly from the atmospheric boundary layer spectrum showing an increase of small scale turbulence structures and breakdown of the larger inflow turbulence structures (Figure 85.). The wavelet analysis also showed that the different frequency bands of turbulence spectrum have a similar variance, without a prominent peak at the heliostat hinge height at $x/c =$1 (Figure 5.11). In contrast for $x/c > 2$, the frequencies with the peak variance and energy are the same as the peak frequencies of the inflow boundary layer. The peak frequencies in the wake flow at $x/c > 2$ are therefore dominated by the incoming flow. As the minimum gap ratio in a heliostat field is typically larger than $x/c = 1$ (Hui, 2011), for gaps between the rows in a dense region of a field where $x/c \leq 2$, the spectral content of the flow will differ significantly from the inflow boundary layer. In contrast, peak frequencies of the velocity fluctuations in the field in regions where $x/c > 2$ will be similar to the atmospheric boundary layer flow. As the unsteady wind loads and the length scales of turbulence in the flow are strongly correlated (Jafari *et al.*, 2019c), these changes will affect the unsteady wind loads on heliostats in very dense regions. Furthermore, Emes *et al.* (2018) found that the frequency of peak pressure fluctuations at the leading edge of a heliostat at α=0° matches the frequency corresponding to the integral length scale of the flow. Hence, the variation of the spectral distribution of turbulence in the wake may change the dominant frequency of the fluctuating forces on downstream heliostats in high-density regions. This indicates the necessity for further investigation of dynamic wind loads for the heliostat field in future due to the possible implications it may have such as dynamic coupling of the unsteady forces and the natural frequency of the heliostat structure.

5.2.4.3 Stow wind loads

During periods of high wind speeds, heliostats are usually stowed by aligning the mirror panel horizontally to reduce the mean wind loads. The unsteady forces on the stowed heliostats in the turbulent atmospheric flow however can be large due to the large vertical velocity variance which is correlated with the unsteady lift force on stowed heliostats (Jafari *et al.*, 2019b). The peak turbulence-induced forces are critical for survivability of the heliostat structure since heliostats need to withstand the largest wind speeds at stow position. Partial stowing of a heliostat field has been suggested to increase the field operation hours over a larger range of wind speeds such that heliostats in regions of predicted larger wind load coefficients are stowed at lower mean wind speeds, with other regions of the field still in operation (Pfahl *et al.*, 2017). Such stowing strategies require a reliable estimation of the wind loads in different regions of the field in order to determine the regions which need to go to stow. Based on the wind direction, the stowed heliostats may be positioned in the wake of the heliostats which are still in operation. As according to Figure 5.13, the vertical velocity variance and turbulence intensity in the wake of the operating heliostats for all three elevation angles are always larger than the inflow, the stowed heliostats will be exposed to increased vertical turbulence intensity. For instance, vertical turbulence intensity in the wake of a heliostat at α =30° at x/c =2 is approximately double its inflow level according to Figure 5.13(c). If a stowed heliostat is placed in the wake of the mentioned heliostat at x/c =2, the doubled vertical velocity will subject it to 40% increase in the peak lift force coefficient according to Jafari *et al.* (2019b). Hence, the results of this study show that in addition to mean wind speed as the criteria for partial stowing, vertical turbulence intensity in the field must also be considered.

5.2.5 Conclusions

The mean and spectral turbulence characteristics in the wake of a flat plate placed in turbulent atmospheric boundary layers were investigated. The results showed a significant increase in turbulence kinetic energy in the near wake region, x/c <4 at the top edge of the plate. The increase in turbulence kinetic energy was the largest for α =90° and the lowest for α =30°. Spectral analysis of velocity fluctuations in the wake showed two distinct regions. There was an increase in high frequencies and smaller scales of turbulence structures at $x/c \leq$ 2, while in the far wake region, x/c=4–8, the spectral distribution was a closer match to the incoming turbulent boundary layer. Furthermore, the variances of the streamwise and vertical velocity components were compared to the variances of their wavelet levels. It was found that in the immediate wake region, x/c=1, breakdown of large inflow turbulence structures to smaller scales was the dominant effect. When moving further downstream turbulence within the wake evolved towards the external turbulence structure.

The results of this study were applied to predict the wake-induced turbulence in a heliostat field. It is acknowledged that the presence of the downstream heliostats in the wake affects the flow pattern and the flow around multiple heliostats is more complex compared to a single heliostat. The results of the wake of a single heliostat could however be used as a basis for estimation of the turbulence changes in a heliostat field and consequently the wind loads. Based on this analysis, it was proposed that due to the increased turbulence intensity in the wake flow, the unsteady wind loads on the in-field heliostats increased compared to the front row, with a peak at high-density areas of a field where the gap between the heliostat rows is between one to three times the characteristic length of the heliostat panel. Depending on the wind direction, the high-density regions of a field, which are typically positioned close to the tower, may be positioned in the wake of their upstream heliostats. Although the mean wind speed is lower in the wake, they are subjected to higher turbulence intensities in the wake of the upstream heliostats, which highlights the importance of dynamic wind loading for design of heliostats in regions of high density. Further studies in future are required to investigate the dynamic wind loading in different regions of a field, and to determine the effect of the field layout and wind direction on the wake flow.

Acknowledgements

Financial support for the project has been provided by the Australian Government Research Training Program, the University of Adelaide Scholarship and the Australian

Renewable Energy Agency (ARENA) through Australian Solar Thermal Research Initiative (ASTRI). The authors would like to acknowledge the School of Mechanical Engineering and the workshops at the University of Adelaide.

5.2.6 References

Ali, N., Kadum, H. F., and Cal, R. B. 2016. Focused-based multifractal analysis of the wake in a wind turbine array utilizing proper orthogonal decomposition, *Journal of Renewable and Sustainable Energy*, 8: 063306.

Aliferis, A. D., Jessen, M. S., Bracchi, T., and Hearst, R. J. 2019. Performance and wake of a Savonius vertical-axis wind turbine under different incoming conditions, *Wind Energy*: 1-14.

Amoura, Z., Roig, V., Risso, F., and Billet, A.-M. 2010. Attenuation of the wake of a sphere in an intense incident turbulence with large length scales, *Physics of Fluids*, 22: 055105.

Barlow, J. B., Rae, W. H., and Pope, A. 1999. *Low-Speed Wind Tunnel Testing*, Wiley.

Bearman, P. W. 1971. An investigation of the forces on flat plates normal to a turbulent flow, *Journal of Fluid Mechanics*, 46: 177-98.

Bearman, P. W., and Zdravkovich, M. M. 1978. Flow around a circular cylinder near a plane boundary, *Journal of Fluid Mechanics*, 89: 33-47.

Bell, J. R., Burton, D., Thompson, M., Herbst, A., and Sheridan, J. 2014. Wind tunnel analysis of the slipstream and wake of a high-speed train, *Journal of Wind Engineering and Industrial Aerodynamics*, 134: 122-38.

Boddupalli, N., Yadav, N. K., and Chandra, L. 2018. The unsteady flow features behind a heliostat in a narrow channel at a high Reynolds number: Experiment and Large Eddy Simulation, *International Journal of Mechanical Sciences*, 136: 424-38.

Bosch, G., Kappler, M., and Rodi, W. 1996. Experiments on the flow past a square cylinder placed near a wall, *Experimental Thermal and Fluid Science*, 13: 292-305.

Draskovic, N. 2017. *Measurement methods in turbulent flows*, Master of Engineering Thesis, Norwegian University of Science and Technology.

Emes, M. J., Ghanadi, F., Arjomandi, M., and Kelso, R. M. 2018. Investigation of peak wind loads on tandem heliostats in stow position, *Renewable Energy*, 121: 548-58.

Gilhome, B. 2017. *Unsteady and time-averaged near-wake flow over the rear of sedan automobiles*, Doctorate, Doctoral Thesis, Monash University.

Hearst, R. J., Gomit, G., and Ganapathisubramani, B. 2016. Effect of turbulence on the wake of a wall-mounted cube, *Journal of Fluid Mechanics*, 804: 513-30.

Hui, T. M. 2011. *Design and optimization of heliostatt field using spinning-elevation sun tracking method based on computational analysis*, Master of Engineering Thesis, Universiti Tunku Abdul Rahman.

Humphries, W., and Vincent, J. H. 1976. Experiments to investigate transport processes in the near wakes of disks in turbulent air flow, *Journal of Fluid Mechanics*, 75: 737-49.

Jafari, A., Emes, M. J., Cazzolato, B. S., Ghanadi, F., and Arjomandi, M. 2019a. An Experimental investigation of unsteady pressure distribution on tandem heliostats. In *SolarPaces*. Daegu, AIP Conference Proceedings.

Jafari, A., Ghanadi, F., Arjomandi, M., Emes, M. J., and Cazzolato, B. S. 2019b. Correlating turbulence intensity and length scale with the unsteady lift force on flat plates in an atmospheric boundary layer flow, *Journal of Wind Engineering and Industrial Aerodynamics*, 189: 218-30.

Jafari, A., Ghanadi, F., Emes, M. J., Arjomandi, M., and Cazzolato, B. S. 2018. Effect of free-stream turbulence on the drag force on a flat plate. In *21st Australasian Fluid Mechanics Conference*. Adelaide, Australia.

Jafari, A., Ghanadi, F., Emes, M. J., Arjomandi, M., and Cazzolato, B. S. 2019c. Measurement of unsteady wind loads in a wind tunnel: Scaling of turbulence spectra, *Journal of Wind Engineering and Industrial Aerodynamics*, 193: 103955.

Kolb, G. J., Ho, C.K., Mancini, T.R., and Gary, J.A. 2011. Power tower technology roadmap and cost reduction plan, *SAND2011-2419, Sandia National Laboratories*.

Krampa-Morlu, F. N., and Balachandar, R. 2007. Flow recovery in the wake of a suspended flat plate, *Journal of Hydraulic Research*, 45: 270-78.

Lam, H. F., and Peng, H. Y. 2017. Measurements of the wake characteristics of co- and counter-rotating twin H-rotor vertical axis wind turbines, *Energy*, 131: 13-26.

Lam, K. M., and Leung, M. Y. H. 2005. Asymmetric vortex shedding flow past an inclined flat plate at high incidence, *European Journal of Mechanics - B/Fluids*, 24: 33-48.

Legendre, D., Merle, A., and Magnaudet, J. 2006. Wake of a spherical bubble or a solid sphere set fixed in a turbulent environment, *Physics of Fluids*, 18: 048102.

Nedić, J., Ganapathisubramani, B., and Vassilicos, J. C. 2013. Drag and near wake characteristics of flat plates normal to the flow with fractal edge geometries, *Fluid Dynamics Research*, 45: 061406.

Peng, H. Y., Lam, H. F., and Lee, C. F. 2016. Investigation into the wake aerodynamics of a five-straight-bladed vertical axis wind turbine by wind tunnel tests, *Journal of Wind Engineering and Industrial Aerodynamics*, 155: 23-35.

Peterka, J. A., Bienkiewicz, B., Hosoya, N., and Cermak, J. E. 1987a. Heliostat mean wind load reduction, *Energy*, 12: 261-67.

Peterka, J. A., Tan, L., Bienkiewcz, B., and Cermak, J. E. 1987b. Mean and peak wind load reduction on heliostats, *Technical Report for Colorado State University*.

Peterka, J. A., Tan, Z., Cermak, J. E., and Bienkiewicz, B. 1989. Mean and peak wind loads on heliostats, *Journal of Solar Energy Engineering*, 111: 158-64.

Pfahl, A. 2018. *Wind loads on heliostats and photovoltaic trackers*, Doctoral Thesis, Technische Universiteit Eindhoven.

Pfahl, A., Coventry, J., Röger, M., Wolfertstetter, F., Vásquez-Arango, J. F., Gross, F., Arjomandi, M., Schwarzbözl, P., Geiger, M., and Liedke, P. 2017. Progress in heliostat development, *Solar Energy*, 152: 3-37.

Razali, S. F. M., Zhou, T., Rinoshika, A., and Cheng, L. 2010. Wavelet analysis of the turbulent wake generated by an inclined circular cylinder, *Journal of Turbulence*, 11: N15.

Richards, P. J., Hoxey, R. P., Connell, B. D., and Lander, D. P. 2007. Wind-tunnel modelling of the Silsoe Cube, *Journal of Wind Engineering and Industrial Aerodynamics*, 95: 1384-99.

Rind, E., and Castro, I. P. 2012. On the effects of free-stream turbulence on axisymmetric disc wakes, *Experiments in Fluids*, 53: 301-18.

Rinoshika, A., and Omori, H. 2011. Orthogonal wavelet analysis of turbulent wakes behind various bluff bodies, *Experimental Thermal and Fluid Science*, 35: 1231-38.

Rinoshika, A., and Zhou, Y. 2007. Effects of initial conditions on wavelet-decomposed structures in a turbulent far-wake, *International Journal of Heat and Fluid Flow*, 28: 948-62.

Rinoshika, A., and Zhou, Y. U. 2005. Orthogonal wavelet multi-resolution analysis of a turbulent cylinder wake, *Journal of Fluid Mechanics*, 524: 229-48.

Shinneeb, A. M., and Balachandar, R. 2016a. Effect of gap flow on the shallow wake of a sharp-edged bluff body – mean velocity fields, *Journal of Turbulence*, 17: 94-121.

Shinneeb, A. M., and Balachandar, R. 2016b. Effect of gap flow on the shallow wake of a sharp-edged bluff body – turbulence parameters, *Journal of Turbulence*, 17: 122-55.

Sment, J., and Ho, C. K. 2014. Wind patterns over a heliostat field, *Energy Procedia*, 49: 229-38.

Tieleman, H. W. 2003. Wind tunnel simulation of wind loading on low-rise structures: A review, *Journal of Wind Engineering and Industrial Aerodynamics*, 91: 1627-49.

Vino, G., Watkins, S., and Mousley, P. 2003. The passenger vehicle wake under the influence of upstream turbulence. In., SAE Technical Paper 2003-01-0650.

Yang, D., Pettersen, B., Andersson, H. I., and Narasimhamurthy, V. D. 2012. Vortex shedding in flow past an inclined flat plate at high incidence, *Physics of Fluids*, 24: 084103.

Zhou, T., Rinoshika, A., Hao, Z., Zhou, Y., and Chua, L. P. 2006. Wavelet multiresolution analysis of the three vorticity components in a turbulent far wake, *Physical Review E*, 73: 036307.

5.3 Wind loads on tandem heliostats

This section consists of the following conference paper:

Jafari, A., Emes, M. J., Cazzolato, B. S., Ghanadi, F., and Arjomandi, M. 2019. An experimental investigation of unsteady pressure distribution on tandem heliostats. *SolarPACES2019*. Daegu, South Korea.

The article is identical to its published format with the following exceptions:

- The numbering of figures, tables and equations have been altered to include the chapter number.
- The position of some figures and tables have been changed to improve legibility.

Statement of Authorship

Title of Paper	An experimental investigation of unsteady pressure distribution on tandem heliostats.
Publication Status	☐ Published ■ Accepted for Publication ☐ Submitted for Publication ☐ Unpublished and Unsubmitted work written in manuscript style
Publication Details	Jafari, A., Emes, M. J., Cazzolato, B. S., Ghanadi, F., and Arjomandi, M. 2019. Experimental investigation of unsteady pressure distribution on tandem heliostats. *SolarPACES2019*. Daegu, South Korea.

Principal Author

Name of Principal Author (Candidate)	Azadeh Jafari		
Contribution to the paper	Developed ideas, conducted experiments, performed data analysis and interpreted results, wrote manuscript, and acted as corresponding author.		
Overall percentage (%)	75		
Certification	This paper reports on original research I conducted during the period of my Higher Degree by Research candidature and is not subject to any obligations or contractual agreements with a third party that would constrain its inclusion in this thesis. I am the primary author of this paper.		
Signature		Date	25/05/2020

Co-Author Contributions

By signing the Statement of Authorship, each author certifies that:

i. the candidate's stated contribution to the publications is accurate (as detailed above);

ii. permission is granted for the candidate in include the publication in the thesis; and

iii. the sum of all co-author contributions is equal to 100% less the candidate's stated contribution.

Name of Co-Author	Matthew Emes		
Contribution to the paper	Helped in the development of the research, contributed in academic discussion and manuscript review.		
Signature		Date	26/05/2020

Name of Co-Author	Benjamin Cazzolato		
Contribution to the paper	Supervised the development of the research, helped in developing ideas, contributed in academic discussion and manuscript review.		
Signature		Date	26/5/2020

Name of Co-Author	Farzin Ghanadi		
Contribution to the paper	Supervised the development of the research, helped in developing ideas, contributed in academic discussion and manuscript review.		
Signature		Date	26/05/2020

Name of Co-Author	Maziar Arjomandi		
Contribution to the paper	Supervised the development of the research, participated in developing ideas and concepts, helped in interpretation of results, provided critical revision of manuscript.		
Signature		Date	25/05/2020

An experimental investigation of unsteady pressure distribution on tandem heliostats

Azadeh Jafari, Matthew Emes, Benjamin Cazzolato, Farzin Ghanadi, Maziar Arjomandi

Abstract

The unsteady surface pressure distribution on heliostats in a tandem arrangement is investigated in this experimental study. The differential pressure on the panel of a heliostat model is measured for a range of gaps between the two tandem heliostats, varying from 1 to 7 times the chord length dimension of the panel. The heliostat models are placed in a simulated turbulent atmospheric boundary layer in the University of Adelaide wind tunnel. The measured surface pressures are analysed and compared with those of a single heliostat, at three elevation angles of 30°, 60° and 90°. The results showed that the peak pressure distribution on the tandem heliostat differs significantly from the single heliostat. Regions of large-magnitude pressure occur near the edges of the panel at smaller gap ratios. Large unsteady variations of the position of the centre of pressure are found for the tandem heliostat at gap ratios equal to and less than 5, which lead to an increase of the hinge moment relative to the single heliostat. The peak hinge moment coefficient on a tandem heliostat is found to be 40% and 70% larger than the coefficient on the single heliostat at elevation angles of 30° and 60°, respectively. The results therefore indicate the importance of the unsteady wind loads in different rows of a field for the design of heliostats as they vary significantly from the loads on a single heliostat dependent on the field arrangement.

5.3.1 Introduction

The turbulence within the atmospheric boundary layer induces unsteady aerodynamic loads on heliostats. Mean and peak wind loads on isolated heliostat models at different operating conditions have been studied by wind tunnel experiements (Peterka *et al.*, 1989; Emes *et al.*, 2017; Pfahl, 2018; Jafari *et al.*, 2019a). Wind loads in a heliostat field are however different from an isolated heliostat. Heliostats act as bluff bodies within the flow and due to the interference of their wakes with each other, the aerodynamics of multiple bluff bodies differ from a single bluff body and depend on the arrangement of the bodies and the spacing between them. The vortices shed by an upstream body can impose vibrations and fluctuating loads on the downstream structures, especially if situated in their intermediate wake areas. Hence, the arrangement of heliostats in a field and the spacing between them is an important parameter that affects the wind loads on heliostats in different rows of the field. The gap between subsequent rows of a heliostat field typically varies from a value equal to the chord length of the mirror panel to about 8-times the chord length as the heliostats are installed further away from the central tower (Hui, 2011). Wind tunnel experiments on heliostats in an array arrangement show that decreasing the spacing between heliostats reduces loads on the heliostats in inner rows due to the blockage effect of upstream heliostats (Peterka *et al.*, 1986). Peterka *et al.* (Peterka *et al.*, 1987) measured the drag and hinge moment coefficients on a heliostat in the fourth row of a four-row arrangement with low and high densities. They reported that the mean drag force and hinge moment coefficients are about 10% to 50% less than the loads on a heliostat in the first row (Peterka *et al.*, 1987). In contrast, the peak drag force on the heliostat in the fourth row was found to be 40% larger than that on a heliostat in the first row (Peterka *et al.*, 1987). Emes et al. (Emes *et al.*, 2018) reported that for two sequential heliostats in stow position the peak lift force on the second tandem heliostat is 47% less than the isolated stowed heliostat. Yu et al. (Yu *et al.*, 2019) found that the peak drag coefficient on an operating heliostat in tandem configuration is up to 50% less than the isolated heliostat when the gap betwen the two heliostat pylons is between 2 to 3 times the chord length dimension of the mirror panel.

More important than the lift and drag forces is the distribution of pressure loads on the mirror panel, which is decisive for the design of the heliostat structure. The unsteady pressure distributions on the mirror panel impose unsteady moments at the heliostat hinge and base, which can lead to critical load conditions for the heliostat drives, pedestal and foundation. It is therefore necessary to gain an understanding of the variations of the unsteady moments for the design of heliostats. Moreover, the pressure distributions on in-field heliostats are influenced by the wake and shielding effect of the upstream operating heliostats. However, the unsteady pressure distributions on heliostats in a field have not been studied in the literature. Hence, in this study, the pressure distribution on a heliostat in tandem arrangement at different operating conditions is investigated, and the effect of the gap spacing between the two tandem heliostats is studied. The surface pressure distributions are analysed and compared to the single heliostat. Furthermore, the effect of the unsteady pressure distributions on the hinge moment of the tandem heliostat is investigated. The variations of the hinge moment are crucial for determination of the critical load conditions of the elevation drive, and hence provide an insight into design of heliostats for a field arrangement.

5.3.2 Methodology

Experiments were conducted in a large-scale wind tunnel at the University of Adelaide. The test section of the boundary layer wind tunnel has a cross-sectional area of 3 m × 3 m and a development length of 17 m. Atmospheric boundary layer models were generated using spires and roughness elements. Five spires with a height of 1.3 m were placed at the centre-line distance of 0.5 m in the lateral direction. The spires were followed by a 7.2 m fetch of wooden roughness elements of 90 mm × 90 mm cross section and 45 mm height. The roughness elements covered approximately 24% of the floor area over the fetch length. The heliostat model was placed 8.8 m downstream of the spires, which was determined to be sufficient for flow development through measurement of velocity at several streamwise locations. Figure 5.15 shows a schematic of the setup in the wind tunnel.

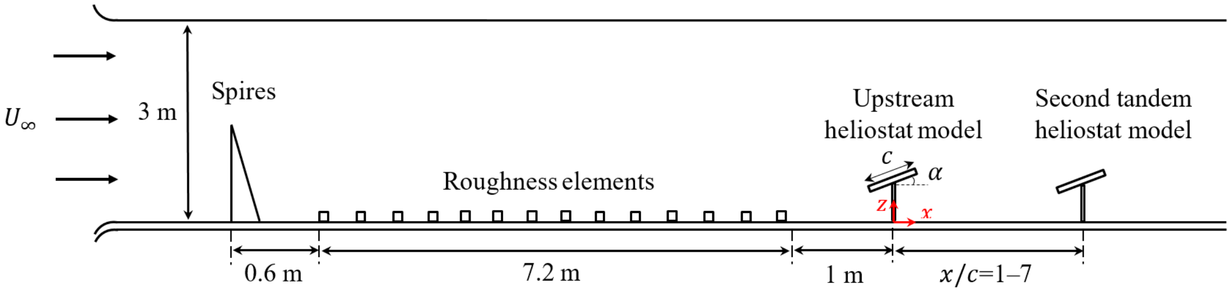

Figure 5.15. Schematic of the experimental setup at the university of Adelaide wind tunnel showing spires and roughness elements and the heliostat models. The gap between the two heliostat models, x/c, varies between 1 and 7 in the experiments.

A Turbulent Flow Instrumentation (TFI) multi-hole pressure probe was used to measure the three components of velocity (in x, y, z directions) at a sampling frequency of 1kHz, and the mean and turbulence characteristics of the simulated boundary layer were determined from the measured velocity. Figure 5.16(a–c) show the vertical profiles of mean velocity, turbulence intensity and integral length scales at the position of the upstream heliostat and in the absence of the heliostat models. The thickness of the generated boundary layer is determined to be 1 m, and the mean velocity in the boundary layer is found to match a logarithmic profile with an aerodynamic surface roughness value of 0.002 m. The longitudinal and vertical turbulence intensity at the heliostat hinge height, H, shown by the horizontal dashed lines, are approximately 9% and 6%, respectively. For the purpose of this study, similarity of mean velocity and turbulence intensity were only considered. A detailed discussion of the similarities and differences of the turbulence spectra and integral length scales in the wind tunnel and atmospheric boundary layer, and the effect of scaling of turbulence in the wind tunnel is provided in Jafari *et al.* (Jafari *et al.*, 2019b).

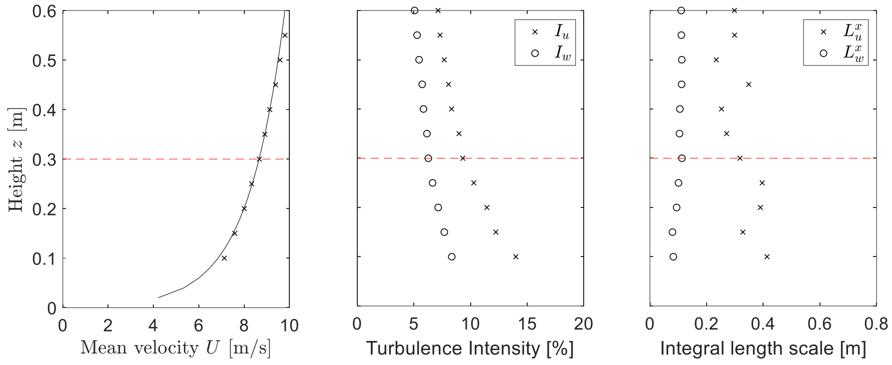

(a) (b) (c)

Figure 5.16. Mean velocity and turbulence characteristics in the simulated boundary layer: (a) Mean velocity in the boundary layer compared to the logarithmic profile (the solid line), (b) longitudinal I_u and vertical I_w turbulence intensities, (c) longitudinal L_u^x and vertical L_w^x integral length scales. The horizontal dashed line shows the heliostat hinge height, H.

Two heliostat models were placed in the wind tunnel in tandem arrangement at different elevation angles, α, of 30°, 60° and 90°. In all configurations, both heliostats were elevated at the same angle. Furthermore, the gap between the heliostats was varied between 1 to 7 times the chord length of the mirror panel, c, by moving the second heliostat downstream while keeping the upstream heliostat at a constant position. Figure 5.17(a–b) show the heliostat model. The heliostat models were made of a square panel with a chord length of c=0.4 m mounted on a pylon of 0.3 m height. A hinge joint was used, which allows setting the elevation angle of the panel between 0° and 90°. One of the models was equipped with pressure transducers inside the heliostat panel cavity (with a thickness of 22 mm) to measure the differential pressure between the taps on the upper and lower surfaces of the panel, as shown in Figure 3.17(c). 30 pressure taps were used on each the upper and lower surfaces of the heliostat panel. *Honeywell TruStability* board- mount pressure sensors with a differential measurement range of ±250 Pa were used. Two *National Instruments* NI-9220 data acquisition modules and the LabVIEW control software were used to collect and convert the measured voltages to the pressure values. The pressure measurements on the second tandem heliostat were conducted for a duration of 180 s at each location at a sampling rate of 1 kHz. The pressure on the upstream heliostat in the absence of the second tandem heliostat, herefater refered to as the single heliostat,was also measured for comparison with the tandem configuration.

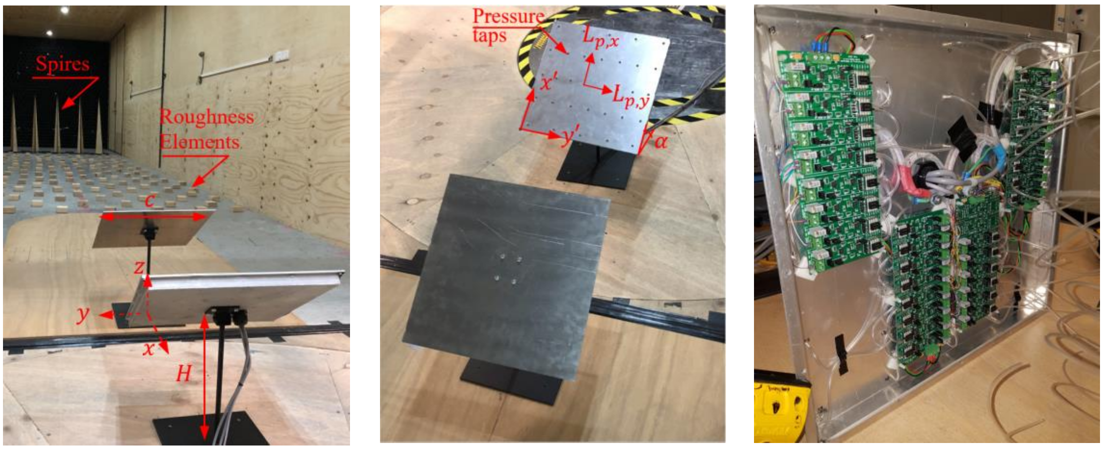

(a) (b) (c)

Figure 5.17. (a) The heliostat models and the boundary layer generation setup at the University of Adelaide wind tunnel, (b) the coordinate axes (x', y') for surface pressure measurements, (c) the custom-made pressure transducer boards inside the panel cavity.

The pressure coefficients were calculated from:

$$C_{P_i} = \frac{P_i^f - P_i^b}{1/2 \rho U_H{}^2} \tag{5.1}$$

where the numerator shows the instantaneous differential pressure between the upper and lower surfaces of the panel at each location. ρ is the air density, and U_H is the mean velocity at the heliostat elevation axis height. In order to compare the pressure coefficients for different tandem configurations, U_H, the mean velocity measured at the location of the upstream heliostat in Figure 5.17, is used for all single and tandem cases.

5.3.3 Results and Discussion

5.3.3.1 Unsteady Surface Pressure Distributions

Figure 5.18 shows the time-averaged distributions of pressure coefficient on the second tandem heliostat in comparison with the single heliostat. The mean surface pressure distributions for the single heliostat configurations show a similar pattern to those presented by Gong *et al.* (Gong *et al.*, 2013), which demonstrates the validity of the currrent measurements. The pressure coefficients are maximum in the centre of the panel for α =90°. As the elevation angle decreases to α =60° and α =30°, the location of maximum pressure coefficients moves closer to the leading edge of the panel.

The mean pressure coefficients of the second heliostat are in general smaller than the single heliostat for x/c between 1 and 3 as the second tandem heliostat is shielded by the upstream heliostat. The mean velocity in the wake of the upstream heliostat is lower than the mean velocity in the boundary layer, and thereby the second tandem heliostat is exposed to a lower mean velocity. This blockage effect is more significant for $\alpha = 90°$ where the mean pressure coefficients on the tandem heliostat are about one third of those on the single heliostat. At $x/c = 1$, when the tandem heliostat is placed in the near wake of the upstream heliostat, negative pressure coefficients are observed indicating larger pressure at the back of the heliostat panel. The region of negative pressure is mainly concentrated near the leading edge at $\alpha = 30°$, whereas at $\alpha = 90°$, almost the entire panel is exposed to negative pressure. The observed phenomena can be related to the existence of an extended-body flow regime in which the free shear layers from the upstream heliostat overshoot the tandem heliostat resulting in a very low pressure region between the two heliostats. The extended-body flow regime was also observed by Auteri *et al.* (Auteri *et al.*, 2009) to occur for gap ratios up to 1 for two tandem plates at $\alpha = 90°$ exposed to a uniform flow and Reynolds numbers of up to 78500.

Regions of high-magnitude pressure similar to the single-heliostat reappear at $x/c = 4$. As the gap ratio increases to x/c between 5 and 7, and the wake starts to recover, the distribution of the mean pressure coefficients on the heliostat panel becomes similar to that on the single heliostat. The magnitude of the pressure coefficients however remains slightly less than the single heliostat as the tandem heliostat is still exposed to lower mean velocity in the recovering wake flow. The results in Figure 5.18 show that the time-averaged distribution of pressure on the tandem heliostat does not differ significantly from the distribution on a single heliostat when the gap ratio between the two heliostats is 4 and above.

Figure 5.19 compares the distribution of peak pressure coefficients on the second tandem heliostat at different gap ratios with the single heliostat. The peak pressure coefficients are calculated as the sum of the mean pressure coefficients and 3-times the standard deviation (Simiu and Scanlan, 1996). The distributions of peak pressure for the single heliostat show a similar pattern to those found by Gong *et al.* (Gong *et al.*, 2013), in which a region of high-magnitude pressure exists at the leading edge for $\alpha = 30°$, and in the centre for $\alpha = 90°$.

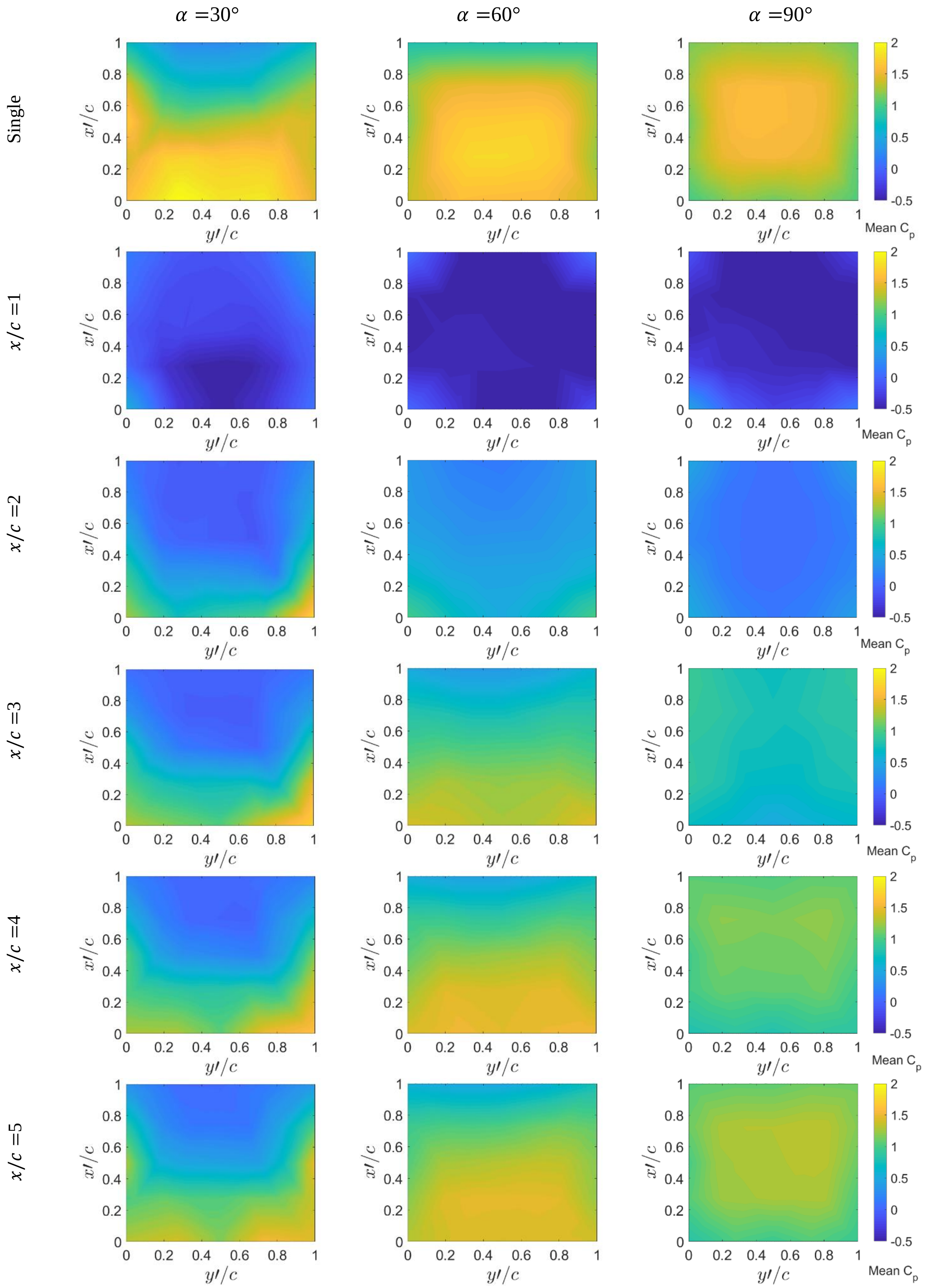
α =30°
α =60°
α =90°
Single
x/c =1
x/c =2
x/c =3
x/c =4
x/c =5
x′/c
y′/c
0
0.2
0.4
0.6
0.8
1
Mean C_p
2
1.5
1
0.5
0
-0.5

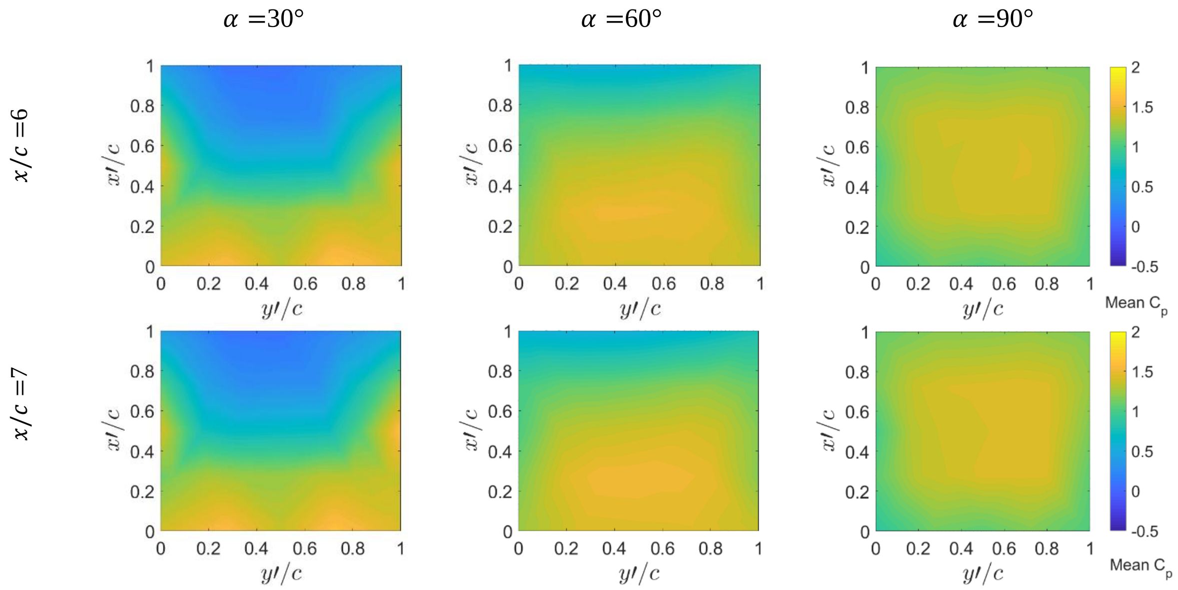

Figure 5.18. Contours of surface distribution of the mean pressure coefficients on the heliostat panel for a single heliostat and the second tandem heliostat at gap ratios, x/c =1–7, and different elevation angles α =30°, 60°, 90°.

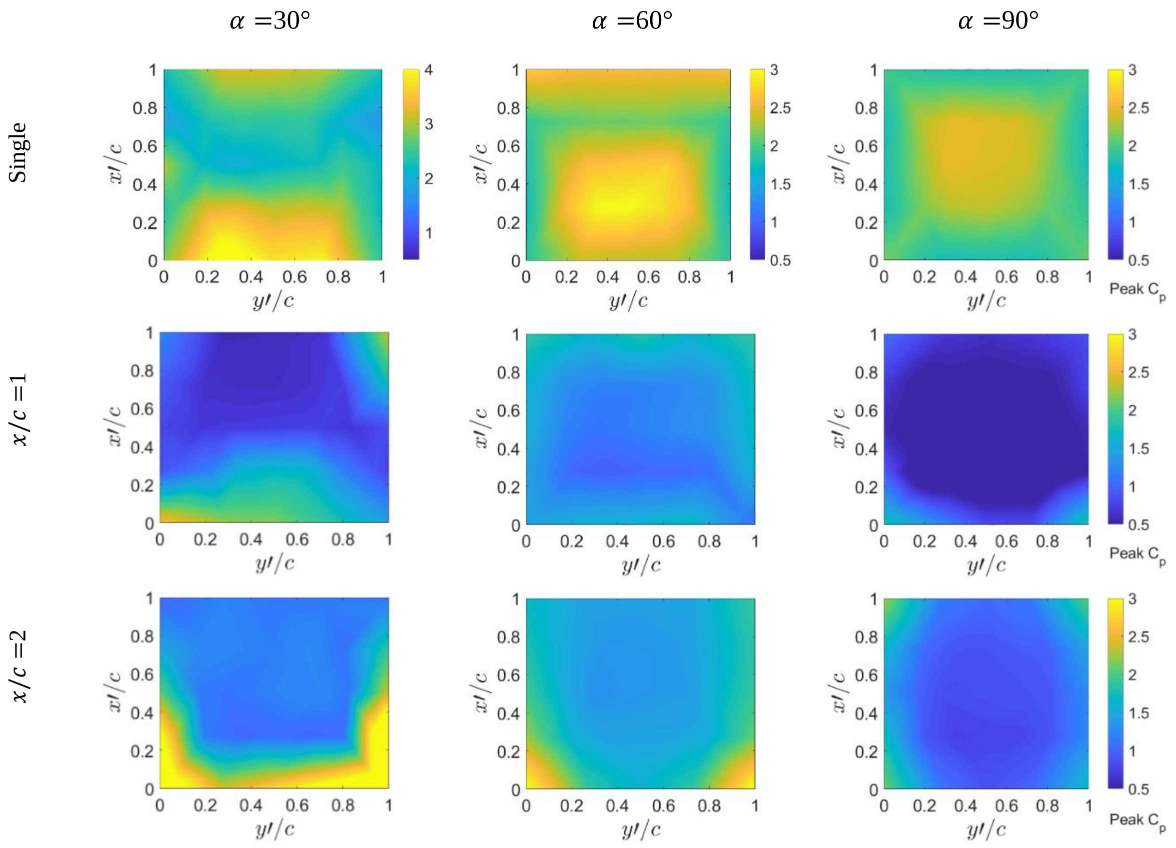

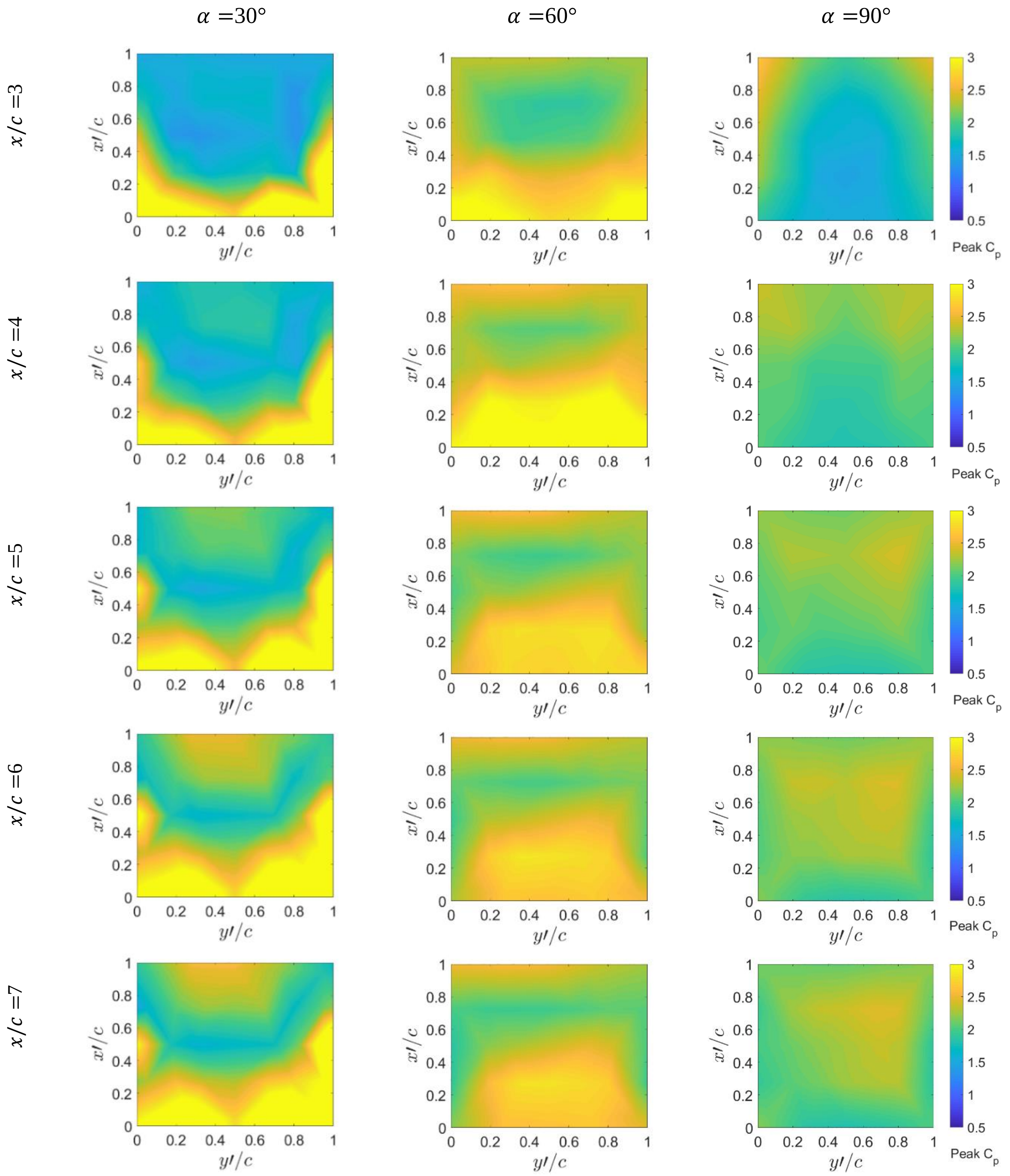

Figure 5.19. Contours of surface distribution of the peak pressure coefficients on the heliostat panel for a single heliostat and the second tandem heliostat at gap ratios, x/c =1–7, and different elevation angles α =30°, 60°, 90°.

The distribution of peak pressure on the second tandem heliostat at smaller gap ratios differs noticeably from the distribution on a single heliostat, while similar to the trends observed for the mean pressure distribution, the distribution of the peak pressure coefficients are a closer match to the single configuration at larger gap ratios (x/c =6–7). For the tandem heliostat at smaller gap ratios (x/c =1–4), the largest peak pressure coefficients are found near the edges of the heliostat panel. These high-magnitude regions are exposed to the shear layers separating from the edges of the upstream heliostat imposing a large-magnitude unsteady pressure on them. The high-magnitude peak pressure coefficients are mainly concentrated at the leading edges of the panel at elevation angles of 30° and 60°. The largest magnitude of the peak pressure coefficient at the high magnitude regions occurs at x/c =3 for all elevation angles of the heliostat panel. This determines x/c =3 as a critical gap ratio for the design of heliostats in the second row of a field exposed to the oncoming wind direction.

5.3.3.2 Centre of Pressure on the Heliostat Panel

As shown in the mean and peak pressure distributions in Figure 5.18 and Figure 5.19, the non-uniform pressure distribution on the heliostat panel varies when the gap ratio between the two tandem heliostats changes. The centre of pressure represents the position where the net normal pressure force acts on the heliostat panel. The distance of the centre of pressure from the centre of the heliostat panel ($x^{'} = \frac{c}{2}$, $y^{'} = \frac{c}{2}$) is found from the following (Emes *et al.*, 2019):

$$L_{px} = \frac{\int_0^c x' p(x',y')\, dx'}{\int_0^c p(x',y')\, dx'} - \frac{c}{2} \tag{5.2}$$

$$L_{py} = \frac{\int_0^c y' p(x',y')\, dy'}{\int_0^c p(x',y')\, dy'} - \frac{c}{2} \tag{5.3}$$

The calculated centre of pressure of the second tandem heliostat for different heliostat gap ratios and elevation angles are displayed in Figure 5.20. The centre of pressure of the single heliostat is also shown at x/c =0. The points in the figure show the time-averaged position of the centre of pressure and the error bars represent the standard deviation of the centre of pressure for each configuration. Figure 5.20(a) displays L_{px}/c for different gap ratios between the tandem heliostats. It is found that the changes in the position of the centre of pressure from the single heliostat configuration are more significant for α =30°, in which L_{px}/c varies from -0.06 for the single heliostat to approximately -0.22 for the second tandem heliostat at gap ratios between 2 and 3. At α =60°, L_{px}/c varies between -0.03 and -0.1 for the range of investigated gap ratios, while the mean L_{px}/c remains near zero for α =90°. As the gap ratio between the tandem heliostats increases, the centre of pressure moves closer to its position for the single heliostat which is consistent with the trend observed for pressure distributions in Figure 5.18. The increased distance between the centre of pressure and the centre of the heliostat panel is likely to impose larger hinge and base over-turning moments on the heliostat. Moreover, the standard deviation of the centre of pressure, which represents the fluctuations of the centre of pressure, is much larger at smaller gap ratios, i.e. x/c <5, indicating the significant effect of turbulence in the near wake of the upstream heliostat. Furthermore, the standard deviation of the centre of pressure decreases with an increase of the gap ratio.

Figure 5.20(b) shows L_{py}/c for different gap ratios between the tandem heliostats. The changes in the mean L_{py}/c are less than 0.05, being largest at α =30°, and it generally remains near zero. The standard deviation of L_{py} is however noticeable at smaller gap ratios with a magnitude of 0.06 at x/c =2. Hence, it can be concluded from the results in Figure 5.20(a) and Figure 5.20(b) that the unsteady variation of the centre of pressure is a dominant effect at x/c <5. Furthermore, the results show that at α =30° the wake of the upstream heliostat does not recover over the measured gap ratios as both L_{px} and L_{py} differ from their values for the single heliostat even at x/c =7.

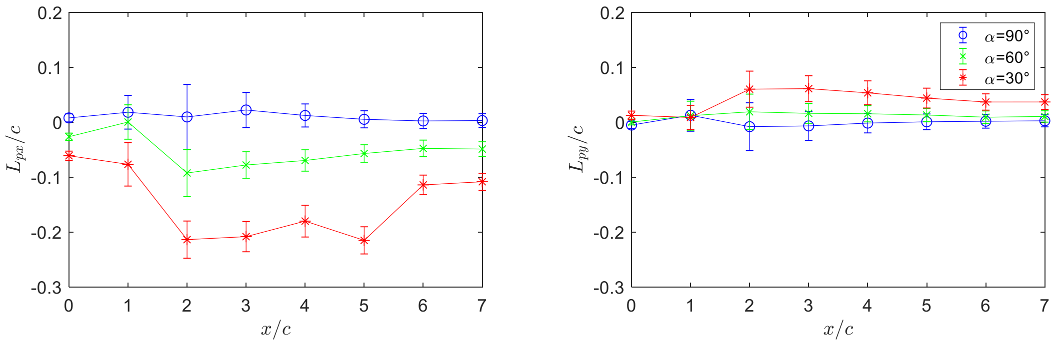

(a) (b)

Figure 5.20. Time-averaged position of the centre of pressure for different gap ratios, x/c =0–7, where x/c =0 represents the single heliostat configuration; (a) L_{px}/c, the centre of pressure in x' direction, and (b) L_{py}/c, the centre of pressure in y' direction, measured from the centre of the heliostat panel ($x' = \frac{c}{2}$ and $y' = \frac{c}{2}$) as defined in Figure 5.17(b). The error bars show the standard deviation of the centre of pressure from the mean values.

5.3.3.3 Unsteady Hinge Moment Coefficient

The unsteady variations of the pressure distribution on the tandem heliostat impose unsteady moments at the heliostat hinge and foundation which affect the design of heliostat components. Hence, in this section, the hinge moment, which is critical for the design of the elevation drive, is calculated for the different cases. The unsteady hinge moment coefficient is found as $C_{MHy} = C_{F_N}\left(L_{px}/c\right)$, where $C_{F_N} = \oint C_{P_i}\, dA$ is the area-average of pressure coefficients (Emes *et al.*, 2019). The mean and peak of the hinge moment coefficient are then determined from the unsteady coefficients. Figure 5.21(a–b) show the time-averaged and peak hinge moment coefficients on the tandem heliostats and the single heliostat (x/c =0). According to Figure 5.21(a), when x/c ≥3, the mean hinge moment coefficient is larger than that of the single heliostat for α =30° and α =60°. The larger hinge moment coefficient is due to the increased distance between the centre of pressure and the panel centre (Figure 5.20(a)). On the other hand, at x/c =1, due to the very small pressure force, the mean hinge moment coefficient on the tandem heliostat is near zero.

The peak hinge moment coefficients show a significant increase at gap ratios equal to and larger than 3 for all elevation angles (Figure 5.21(b)) during operation of a heliostat field. This indicates the significant effect of the pressure fluctuations, in terms of both magnitude and distribution, on the tandem heliostat. According to Figure 5.21 (b), the peak hinge moment coefficient is approximately 40% and 70% larger than the single heliostat at x/c =4 for α =30° and α =60°, respectively. Furthermore, at α =90°, despite the near zero mean hinge moment coefficient, the peak hinge moment coefficient varies between 0.16 and 0.1 for x/c =3 to 7. Furthermore, similar to the mean hinge moment, there is a decrease in the peak hinge moment coefficient at x/c =1 compared to the single heliostat such that the peak hinge moment coefficient at α =30° is 60% less than the single heliostat. Hence, the results show that the unsteady moment at the hinge induced by the surface pressure fluctuations varies significantly depending on the gap between the two heliostats. Therefore, heliostats must be designed according to the variations of wind loads in high-density and low-density areas of a field.

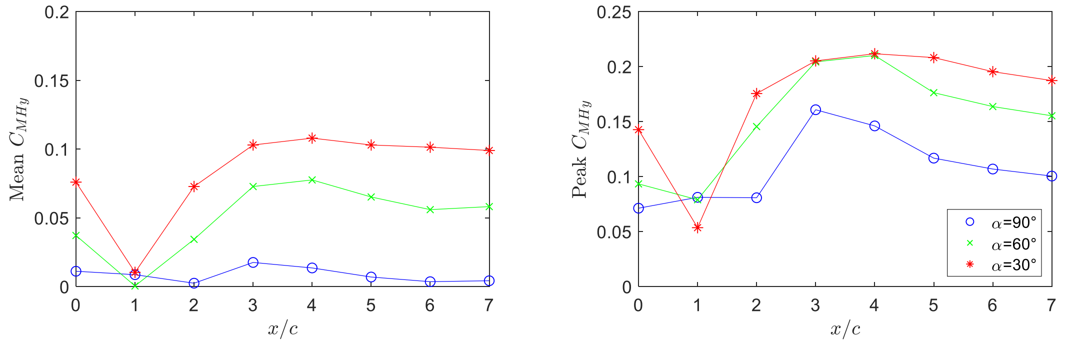

(a) (b)

Figure 5.21. (a) The time-averaged, and (b) the peak hinge moment coefficients for α =30°, 60° and 90°, and for different gap ratios, x/c =0–7, where x/c =0 represents the single heliostat configuration.

5.3.4 Conclusions

The unsteady surface pressure distribution on heliostats in tandem arrangement was investigated in this study. The differential pressure between the upper and lower surfaces of the heliostat panel was measured through wind tunnel experiments for different gap ratios between the tandem heliostats and at different elevation angles of operating heliostats. The results were compared to the surface pressure distributions on a single heliostat. It was found that while the mean pressure coefficients on the second tandem heliostat are in general smaller than the single heliostat for gap ratios between 1 and 3, concentrated regions of large-magnitude peak pressure exist near the edges of the panel. The magnitude of the peak pressure coefficient at the panel edges of the tandem heliostat was the largest at a gap equal to 3-times the panel chord length for all of the investigated elevation angles. The time-averaged position of the centre of pressure was found to differ significantly from the single heliostat at elevation angles of 30° and 60°. Moreover, the results showed that the position of the centre of pressure fluctuates noticeably about its time-averaged position at smaller gap ratios. Hence, in dense areas of a heliostat field, the unsteady variations of the pressure on the heliostats have a dominant effect on the maximum hinge moments, which must be considered for the design of the heliostat elevation drive. Furthermore, the results indicate that the changes in the unsteady pressure distribution on a heliostat in tandem arrangement significantly affect the peak and unsteady wind loads, such that at $x/c \geq 3$, the peak hinge moment coefficient on a tandem heliostat can increase by 40% and 70% from that of the single heliostat at $\alpha = 30°$ and $\alpha = 60°$, respectively. Hence, design of heliostats in a field arrangement requires understanding the unsteady wind loads within the field which dependent on the field arrangement can differ significantly from a single heliostat. Moreover, the results suggest the possibility to reduce the cost of heliostats by optimization of the layout of the heliostat field with respect to the wind loads. It is recommended to develop the arrangement of heliostats in a field according to the site terrain type such that the unsteady wind loads on the in-field heliostats will be reduced and therefore by reduction of design wind loads cheaper heliostats can be produced.

Acknowledgments

Financial support for the project has been provided by the Australian Government Research Training Program, the University of Adelaide Scholarship and the Australian Solar Thermal Research Initiative (ASTRI). The authors would like to acknowledge the School of Mechanical Engineering and the workshops at the University of Adelaide.

5.3.5 References

Auteri, F., Belan, M., Cassinelli, C., and Gibertini, G. 2009. Interacting wakes of two normal flat plates an investigation based on phase averaging of LDA signals, *Journal of Visualization*, 12: 307-21.

Emes, M. J., Arjomandi, M., Ghanadi, F., and Kelso, R. M. 2017. Effect of turbulence characteristics in the atmospheric surface layer on the peak wind loads on heliostats in stow position, *Solar Energy*, 157: 284-97.

Emes, M. J., Ghanadi, F., Arjomandi, M., and Kelso, R. M. 2018. Investigation of peak wind loads on tandem heliostats in stow position, *Renewable Energy*, 121: 548-58.

Emes, M. J., Jafari, A., Ghanadi, F., and Arjomandi, M. 2019. A method for the calculation of the design wind loads on heliostats, *AIP Conference Proceedings*, 2126: 030020.

Gong, B., Wang, Z., Li, Z., Zang, C., and Wu, Z. 2013. Fluctuating wind pressure characteristics of heliostats, *Renewable Energy*, 50: 307-16.

Hui, T. M. 2011. *Design and optimization of heliostatt field using spinning-elevation sun tracking method based on computational analysis*, Master of Engineering Thesis, Universiti Tunku Abdul Rahman.

Jafari, A., Ghanadi, F., Arjomandi, M., Emes, M. J., and Cazzolato, B. S. 2019a. Correlating turbulence intensity and length scale with the unsteady lift force on flat plates in an atmospheric boundary layer flow, *Journal of Wind Engineering and Industrial Aerodynamics*, 189: 218-30.

Jafari, A., Ghanadi, F., Emes, M. J., Arjomandi, M., and Cazzolato, B. S. 2019b. Measurement of unsteady wind loads in a wind tunnel: Scaling of turbulence spectra, *Journal of Wind Engineering and Industrial Aerodynamics*, 193: 103955.

Peterka, J. A., Hosoya, N., Bienkiewicz, B., and Cermak, J. E. 1986. Wind load reduction for heliostats, *Technical Report for Colorado State University*.

Peterka, J. A., Tan, L., Bienkiewcz, B., and Cermak, J. E. 1987. Mean and peak wind load reduction on heliostats, *Technical Report for Colorado State University*.

Peterka, J. A., Tan, Z., Cermak, J. E., and Bienkiewicz, B. 1989. Mean and peak wind loads on heliostats, *Journal of Solar Energy Engineering*, 111: 158-64.

Pfahl, A. 2018. *Wind loads on heliostats and photovoltaic trackers*, Doctoral Thesis, Technische Universiteit Eindhoven.

Simiu, E., and Scanlan, R. H. 1996. *Wind Effects on Structures*, John Wiley & Sons.

Yu, J. S., Emes, M. J., Ghanadi, F., Arjomandi, M., and Kelso, R. 2019. Experimental investigation of peak wind loads on tandem operating heliostats within an atmospheric boundary layer, *Solar Energy*, 183: 248-59.

Chapter 6

Reduction of turbulence

6.1 Chapter overview

This chapter explores the feasibility of the application of mesh fences as a flow control method for reducing unsteady wind loads on heliostats. Based on the developed knowledge in the previous chapters, the unsteady and peak wind loads on heliostats are directly correlated with the turbulence properties of the approaching wind. Therefore, alteration of flow properties will impact the wind loads. Hence, the flow control method investigated in this chapter targets reduction of intensity and integral length scale of turbulence as the two key parameters that significantly affect the unsteady wind loads. Mesh fences can be utilised to achieve this goal due to their potential for turbulence manipulation as discussed in Section 2.5. Furthermore, this control method can be adopted in heliostat fields since perimeter fences are commonly used around fields of heliostats and photovoltaic solar panels to prevent unauthorised access to the field, avoid damage to the panels, and also protect trespassers and animals from an exposed danger. Hence, there is a potential to reduce the unsteady wind loads on heliostats by modification of the design of perimeter fences with the aim of reduction of turbulence. This however requires an in-depth understanding of variations of turbulence properties behind a mesh fence.

In this chapter, the turbulence reduction performance of woven wire mesh fences within an atmospheric boundary layer flow is studied. Turbulence properties downstream of mesh fences of various mesh opening widths and porosities are determined from experimental measurements in a wind tunnel. Correlations describing the variations of turbulence intensity and integral length scale with the downstream distance are developed, which show that these variations scale with the mesh opening width. The decay of turbulence behind the fences is however found to be dependent on mesh porosity. The results show that among the investigated mesh porosities between 0.46 and 0.75, a larger reduction in turbulence intensity and integral length scale can be achieved using fences with medium porosities. It is found that the porosity of the woven wire meshes is the key parameter that impacts the reduction of turbulence as fences with different mesh opening widths, but similar porosities have a similar turbulence reduction performance.

The findings show that based on the achieved reduction of turbulence intensity and integral length scale, the peak drag force on a vertical heliostat can be reduced between 48% and 19% using a wire mesh fence with a porosity between 0.46 and 0.75, respectively. Furthermore, with application of wire mesh fences, the peak lift force on a heliostat at stow position can be reduced between 53% and 15% for a porosity of between 0.46 and 0.75, respectively. These estimations are however based on the placement of heliostats within a downstream distance of up to 70-times the mesh opening width, and the wind load reductions may vary based on the distance of heliostats from the fence and the fence height. Therefore, the results show a potential to reduce the peak lift and drag forces on heliostats. However, future investigations are needed to further investigate the practicability of application of fences for reduction of wind loads in a heliostat field.

This chapter consists of the following journal article submitted for publication:

Jafari, A., Emes, M. J., Cazzolato, B. S., Ghanadi, F., and Arjomandi, M. 2020. Reduction of turbulence in an atmospheric boundary layer flow by wire mesh fences. Submitted to *Experiments in Fluids*.

The article is identical to the submitted manuscript with the following exceptions:

- The numbering of figures, tables and equations have been altered to include the chapter number.
- The position of some figures and tables have been changed to improve legibility.

Statement of Authorship

Title of Paper	Reduction of turbulence in an atmospheric boundary layer flow by wire mesh fences.	
Publication Status	☐ Published ■ Submitted for Publication	☐ Accepted for Publication ☐ Unpublished and Unsubmitted work written in manuscript style
Publication Details	Jafari, A., Emes, M. J., Cazzolato, B. S., Ghanadi, F., and Arjomandi, M. 2020. Reduction of turbulence in an atmospheric boundary layer flow by wire mesh fences. Submitted to *Experiments in Fluids*.	

Principal Author

Name of Principal Author (Candidate)	Azadeh Jafari		
Contribution to the paper	Developed ideas, conducted experiments, performed data analysis and interpreted results, wrote manuscript, and acted as corresponding author.		
Overall percentage (%)	75		
Certification	This paper reports on original research I conducted during the period of my Higher Degree by Research candidature and is not subject to any obligations or contractual agreements with a third party that would constrain its inclusion in this thesis. I am the primary author of this paper.		
Signature		Date	25/05/2020

Co-Author Contributions

By signing the Statement of Authorship, each author certifies that:

i. the candidate’s stated contribution to the publications is accurate (as detailed above);

ii. permission is granted for the candidate in include the publication in the thesis; and

iii. the sum of all co-author contributions is equal to 100% less the candidate’s stated contribution.

Name of Co-Author	Matthew Emes		
Contribution to the paper	Helped in the development of the research, contributed in academic discussion and manuscript review.		
Signature		Date	26/05/2020

Name of Co-Author	Benjamin Cazzolato		
Contribution to the paper	Supervised the development of the research, helped in developing ideas, contributed in academic discussion and manuscript review.		
Signature		Date	26/5/2020

Name of Co-Author	Farzin Ghanadi		
Contribution to the paper	Supervised the development of the research, helped in developing ideas, contributed in academic discussion and manuscript review.		
Signature		Date	26/05/2020

Name of Co-Author	Maziar Arjomandi		
Contribution to the paper	Supervised the development of the research, participated in developing ideas and concepts, helped in interpretation of results, provided critical revision of manuscript.		
Signature		Date	25/05/2020

Reduction of turbulence in an atmospheric boundary layer flow by wire mesh fences

Azadeh Jafari, Farzin Ghanadi, Maziar Arjomandi, Matthew J. Emes, Benjamin S. Cazzolato

Abstract

Reduction of turbulence within an atmospheric boundary layer flow by application of woven wire mesh fences is investigated. Turbulence properties behind fences of different porosities and mesh opening widths were determined from velocity measurements in a wind tunnel. It is found that with the application of a fence with a porosity of 0.46, the streamwise turbulence intensity can be reduced from the inflow level of 12.5% to 8.8% and the integral length scale can be reduced from 380 mm to 270 mm. The results show that behind the mesh fences turbulence kinetic energy decays as a power law function of the downstream distance for all wire mesh fences tested in the wind tunnel. The decay rate of turbulence kinetic energy is faster, and a larger reduction in the integral length scale is achieved for fences with porosities between 0.46 and 0.64 compared to higher porosities of between 0.73 and 0.75. Porosity of the woven wire meshes is found to be the key parameter which influences their turbulence reduction performance. In the end, application of the wire mesh fences for reduction of wind loads on solar panels and heliostats is discussed. Evaluation of wind loads based on the reduction of turbulence intensity and integral length scale show that up to 48% and 53% reduction in peak drag and lift forces on a heliostat, respectively, can be achieved with application of mesh fences.

Nomenclature

A	panel area (m^2)
C_D, C_L	drag and lift force coefficients
d	wire diameter (mm)
f	frequency (Hz)
F_D, F_L	drag and lift forces (N)
H	height of fence (m)
I_u, I_v, I_w	streamwise, lateral and vertical turbulence intensities (%)
k	turbulent kinetic energy (J/kg)

L_u^x, L_w^x	longitudinal and vertical integral length scales (m)
M	mesh opening width (mm)
Re_d	Reynolds number based on wire diameter
S_{uu}, S_{ww}	power spectral density of the streamwise and vertical velocity fluctuations (m^2/s)
u, v, w	absolute velocity components in the $x-, y-, z-$ flow directions, respectively (m/s)
U	time averaged mean streamwise velocity (m/s)
U_∞	free-stream velocity (m/s)
x, y, z	distance in the streamwise, lateral and vertical directions (m)
Symbols	
α, β	power law exponents of turbulence decay rate
δ	boundary layer thickness (m)
ρ	density (kg/m^3)
σ_u, σ_u, σ_w	standard deviation of streamwise, lateral and vertical velocity components (m/s)
ϕ	fence porosity

6.2 Introduction

The control of turbulence is a fundamental problem of interest in experimental fluid mechanics and engineering applications. One common method for flow control is application of screens including honeycombs, perforated plates, grids and wire meshes. Screens can be used to either create or diminish time-mean velocity distributions, a change in flow direction, and to decrease or increase turbulence (Laws and Livesey, 1978). Porous fences, which are made of wire mesh screens, perforated plates and vertical or horizontal slats, are also commonly used as a flow control method to reduce wind speed. Common examples of fences as wind barriers are for sand erosion control in deserts and coastal areas (Li and Sherman, 2015), and protection against snow drifting (Dong *et al.*, 2007). In addition to their common application for reduction of wind speed, fences can be manipulated to reduce atmospheric turbulence. Particular applications of turbulence reduction by fences include reduction of wind loads on structures such as photovoltaic solar panels and heliostats. This study focuses on turbulence reduction by utilising porous fences in the atmospheric boundary layer.

Heliostats and solar panels are subjected to the turbulence within the atmospheric boundary layer, which creates highly unsteady lift and drag forces on these structures. Therefore, wind loading is a key parameter in the design of their support structures and drives, as they must be designed to survive large fluctuating and dynamic wind loads during extreme conditions. For instance, up to 80% of the capital cost of a heliostat are related to the wind loads (Kolb, 2011), and the structural cost of ground-mounted photovoltaic panels contribute to 20% of their installation cost (Mayer and Gróf, 2020). Hence, by reduction of wind loads the structural stiffness can be decreased and hence mass, leading to a reduction of the capital cost of the solar plant, and thereafter a reduction of the levelised cost of electricity (Emes *et al.*, 2015). The unsteady wind loads on solar panels and heliostats are directly correlated with the turbulence properties of the approaching wind (Peterka and Derickson, 1992; Sun *et al.*, 2014; Pfahl, 2018). Two key parameters that significantly affect the unsteady wind loads on these structures are intensity and integral length scale of the turbulence within the atmospheric boundary layer (Peterka *et al.*, 1989; Emes *et al.*, 2017; Jafari *et al.*, 2018; Emes *et al.*, 2019; Jafari *et al.*, 2019). For example, as streamwise turbulence intensity decreases from 18% to 14%, the peak drag force on heliostats and parabolic dish collectors decreases by 25% (Peterka and Derickson, 1992). Reducing the ratio of longitudinal integral length scale to the chord length dimension of a heliostat from 2.3 to 0.97 can also lead to a reduction of the unsteady drag force coefficient by 41% (Jafari *et al.*, 2018). Therefore, the unsteady wind loads on heliostats and solar panels can be reduced by application of a flow control method to reduce the intensity and integral length scale of turbulence of the approaching wind.

Mesh fences are a promising candidate for reducing the wind loads on solar panels and heliostats due to their potential for altering flow properties and their ease of application in a solar field. Perimeter fences are commonly used around fields of heliostat mirrors and photovoltaic solar panels for dust control and for preventing unauthorised access to the field and protecting trespassers and animals from an exposed danger. Therefore, with a modification in their design, it is possible to utilise them as a load reduction method in addition to their other protective roles. There have been a few experimental studies on application of fences for wind load reduction in the literature. For instance, García *et al.* (2014) measured the lift and drag forces on parabolic trough collectors placed behind a fence with a porosity of 0.5, which is defined as the ratio of the open area to the total area of the fence, and found that up to 60% reduction in mean and peak wind loads could be achieved. However, for some configurations with varying the height of the porous fence and addition of a variable height solid fence, and varying the distance from the solar collectors, the peak loads were found to be larger than an isolated solar collector. Peterka *et al.* (1989) measured the wind loads on an array of heliostats with and without mesh fences, which were placed both upstream of the front row and in between the rows. While it was reported that the peak drag and lift force coefficients on a heliostat placed within the array were generally reduced compared to a single heliostat, for some cases the wind loads were larger than an isolated heliostat. Unfortunately, in their results the effect of the porous fence was not distinguished from the blockage created by the upstream heliostats, and therefore, the effectiveness of the fences in wind load reduction is not clear. As the wind loads and approaching flow properties are directly correlated, understanding how turbulence properties change behind a porous fence can help to provide an evaluation of the effect of the fence on the wind loads. More importantly, this knowledge can be employed to modify the design of fences such that a desirable reduction in wind loads can be achieved.

Flow behind a porous fence is influenced by blockage, flow separation, and the flow passing through the mesh openings, known as the bleed flow. The interaction of the displaced flow and the bleed flow is determined by the level of permeability of a fence given by its porosity, ϕ. Porosity of a fence is an important parameter which affects the flow properties downstream of it. By decreasing porosity, the bleed flow decreases, and the pressure drop across the fence increases. The increased blockage leads to formation of reverse flow and a recirculation zone in the wake of the fence for $\phi <0.3$ (Lee and Kim, 1999; Dong *et al.*, 2010). With increasing the porosity of the fence from $\phi =0$ to $\phi =0.3$, the mean drag force coefficient on the fence decreases and the recirculation zone becomes smaller in both height and length (Basnet and Constantinescu, 2017). No recirculation zone is formed for porosities larger than 0.3 (Dong *et al.*, 2010; Tsukahara *et al.*, 2012).

A key parameter for designing a fence for the reduction of wind loads is to decrease the intensity of turbulence in the approaching flow. While a less porous fence creates a larger mean velocity deficit, turbulence intensity behind it is also larger (Lee and Kim, 1999), which could therefore make it less effective in reduction of wind loads. Three distinct regions exist behind a porous fence, as shown schematically in Figure 6.1. : a wall layer close to the ground, a shear layer resulting from separation of flow at the top edge of the fence, and the wake of the fence. Turbulent velocity fluctuations are larger in the wall layer and the shear layer due to the large mean shear in these two layers (Rodríguez-López *et al.*, 2017). The separated shear layers create a region of increased turbulence intensity at the top of the fence, which becomes weaker with increasing the porosity of the fence. The region of increased streamwise turbulence intensity, I_u, behind a porous fence placed in a wind tunnel boundary layer with an inflow streamwise turbulence intensity of 10%, is found to be concentrated at z/H between 1 and 1.5 (Dong *et al.*, 2010), where H and z are the fence height and the wall-normal distance, respectively. This region is found to extend in the streamwise direction, x, up to $x/H =10$ for

ϕ ≤0.2, while for ϕ ≥0.3 the increase in the magnitude of turbulence intensity is significantly lower and only occurs up to x/H =1.5. A similar trend is found for the vertical turbulence intensity, I_w, showing an increase compared to the inflow level at a region above the fence, z/H >1, for ϕ ≤0.2 (Dong *et al.*, 2010). An increase in streamwise turbulence intensity is also found in the wall layer close to the ground, which is of a smaller magnitude compared to that in the shear layer at the top edge (Lee and Kim, 1999). Concentration of maximum turbulence intensities at the top of the fence implies that for the purpose of reduction of wind loads, heliostats and solar panels should not be subjected to the shear layer and the wall layer. Therefore, the fence height should be larger than the solar panel height to avoid their exposure to increased turbulence intensity.

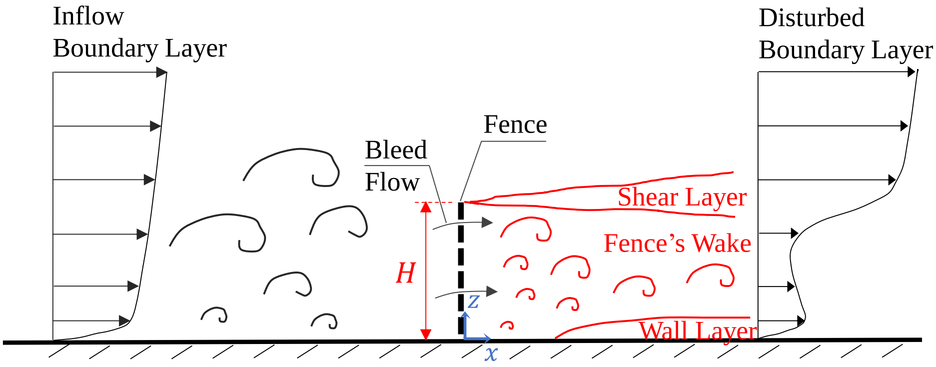

Figure 6.1. A schematic of the flow behind a porous fence within the atmospheric boundary layer, in which the fence porosity is above 0.3 and no reverse flow exists.

Turbulence properties in the wake of the fence outside the shear layer and the wall layer are determined by the interaction of two effects: alteration of inflow turbulence as the flow passes through the fence and the fence generated turbulence. For a wire mesh screen, when the Reynolds number based on the wire diameter, $Re_d = Ud/\nu$, is above 40, the mesh wires generate turbulence due to separation of flow and vortex shedding (Loehrke and Nagib, 1972). However, the decay of mesh-generated turbulence is found to be faster than the decay of turbulence in the shear layer and the wall layer (Rodríguez-López *et al.*, 2017). Tan-Atichat *et al.* (1982) investigated the interaction between inflow turbulence and mesh-generated turbulence by studying the flow downstream of wire mesh screens and perforated plates. The screens were placed in a wind tunnel covering the entire cross-section of the tunnel and were subjected to uniform grid-generated turbulent flows. Turbulence intensity was found to increase immediately downstream of the screens in the near wake, becoming larger than the inflow level, I_u =0.007, due to the mesh-generated turbulence. With increase of the downstream distance, turbulence intensity decreased and reduced to below its inflow level. It was found that turbulence decay rate downstream of the screen was significantly dependent on the scale and intensity of freestream turbulence. When the freestream turbulence was of low turbulence intensity, I_u =0.7%, and contained no large scales compared to the mesh width, turbulence decay rate was higher in comparison with the inflow cases with large turbulence scales and intensity of turbulence, I_u =8%. As the effectiveness of a fence in reduction of wind loads depends on the level of reduction of turbulence intensity, the decay of turbulence behind a fence within the atmospheric boundary layer is an important design parameter for the placement of fences with respect to the exposed outer row of a heliostat field. However, this knowledge is lacking in the literature and the decay rate of turbulence behind a porous fence when placed within the turbulent atmospheric boundary layer is not known.

For the purpose of reducing the unsteady wind loads on heliostats and solar panels, in addition to reducing turbulence intensity, reducing the integral length scale of turbulence and suppression of prominent eddies within the atmospheric surface layer is also necessary. Through analysis of the power spectral density of pressure measured downstream of a full-scale fence, 50 m long and 2 m high and ϕ =0.5, Richardson (1989) found that low frequencies were significantly attenuated downstream of the fence, at x/H =5 and x/H =10. The flow in the immediate downstream of a screen placed in a wind tunnel, over a downstream distance of up to 15–25 mesh widths, was also found to be dominated by mesh-generated turbulence with the peak frequency of the turbulence spectrum at length scales in the order of a few mesh widths (Groth and Johansson, 1988). Prominence of turbulence structures of smaller scales was also indicated from a shift of power spectral density of the streamwise velocity fluctuations to higher frequencies, compared to the atmospheric boundary layer inflow, downstream of porous fences with ϕ =0.2 and ϕ =0.5 at z/H =0.6 and x/H =2 (Raine and Stevenson, 1977). At x/H =15, the spectrum recovered to the inflow shape while the peak of the spectrum had a shift to frequencies 2 to 3 times higher than the inflow. Shiau (1998) also reported gradual recovery of the flow with increasing the downstream distance, such that the peak of the turbulence spectrum was found to shift to lower frequencies with an increase of the downstream distance from x/H =10 to x/H =20 behind a porous fence with ϕ =0.5 at z/H =0.4 (Shiau, 1998). A screen is suggested to be more effective if the mesh-generated turbulence is of smaller scales than the inflow turbulence such that the generated turbulence enhances energy transfer from large scales to the smaller ones (Tan-Atichat *et al.*, 1982). The geometric properties of the screen are therefore important design parameters due to the dependence of the mesh-generated turbulence on its geometric parameters. For example, a fractal grid is found to create a larger turbulence dissipation compared to a non-fractal simple grid (Keylock *et al.*, 2012). A remaining gap however is the key geometric parameter, which impacts the variations of length scales of turbulence behind a simple mesh fence where the openings are of the same shape. Whether the mesh opening width has a stronger effect or the porosity of the fence is not well known. An understanding of the effects of geometric parameters of the fence is therefore required for design of fences for the aim of wind load reduction.

Design of porous fences for reduction of wind loads requires an in-depth understanding of the effects of fence geometric parameters and inflow conditions. Furthermore, an understanding of how the intensity and length scales of turbulence change behind the fence is required. The studies in the literature on fences within the atmospheric boundary layer have mainly focused on mean velocity deficit for general windbreak applications or flow properties very close to the ground that are important for sand erosion control. However, for reduction of wind loads on heliostats and solar panels, the turbulence properties at their corresponding heights are important. On the other hand, the studies on screens used in wind tunnels provide an insight into the performance of wire meshes for turbulence reduction. However, their findings are not completely applicable for fences within the atmospheric boundary layer due to their different conditions. For the problem of screens in wind tunnels, the screens cover the whole cross-section of the test section and therefore pressure drop contributes to turbulence attenuation. Furthermore, the inflow turbulence is typically not of high intensities. In contrast, turbulence within the atmospheric boundary layer consists of large-scale turbulence structures and is highly anisotropic. Heliostats and solar panels are subjected to streamwise turbulence intensities between 10% to 25% depending on their surrounding terrain (ESDU85020, 2010). Therefore, due to the different inflow conditions in the atmospheric boundary layer, it is necessary to characterise the turbulence reduction performance of a porous fence when subjected to these conditions. Hence, this study aims to characterise the decay of turbulence intensity and length scales behind a wire mesh fence in an atmospheric boundary layer inflow with respect to the geometric properties of the mesh.

6.3 Experimental methodology

6.3.1 Generation of an atmospheric boundary layer flow

Experiments were conducted in the University of Adelaide large-scale wind tunnel which has a test section of 3 m × 3 m × 17 m, and a turbulence intensity between 1% and 3% in the empty tunnel. An atmospheric boundary layer flow was generated using spires and floor roughness elements. Five identical spires were placed at the inlet of the test section separated by a centre-line distance of 0.5 m in the spanwise direction. The spires had a height of 1.3 m and width of the front panel at the bottom was 155 mm. The spires were followed by a 7.2 m streamwise fetch of wooden roughness elements, of 90 mm × 90 mm cross section and 45 mm height, which covered approximately 24% of the floor area over the fetch length. The test setup is shown in Figure 6.2.

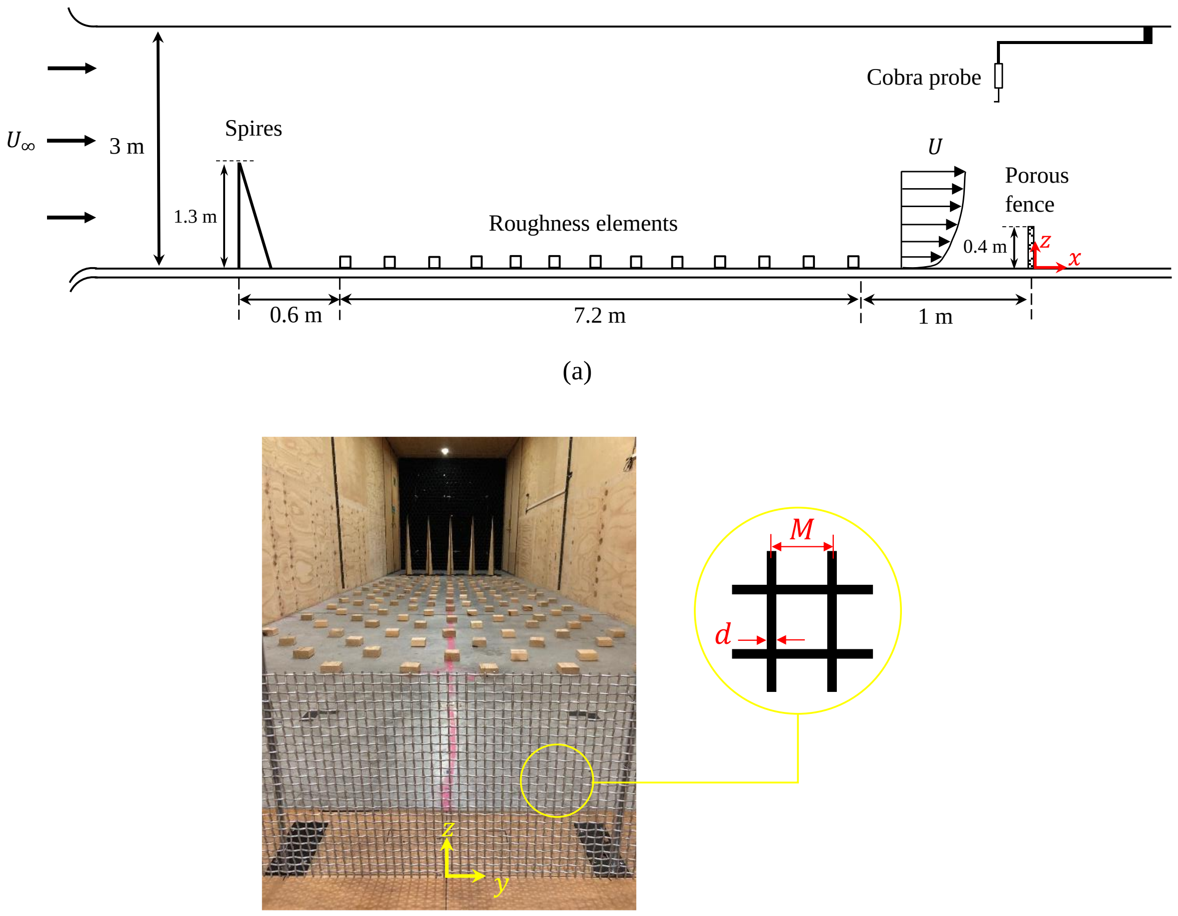

(a)

(b)

Figure 6.2. The experimental setup in the University of Adelaide wind tunnel showing the spires, roughness elements and the wire mesh fence: (a) Schematic of the setup, (b) photograph of the setup looking upstream.

To characterise the generated boundary layer, the velocity was measured over an area of 1 m^2 in lateral-wall normal planes at different streamwise locations starting from 1 m downstream of the roughness fetch. Using the described setup, a boundary layer with a thickness of $\delta = $0.98 m, determined as $\delta_{0.99}$ from the mean velocity profile, was generated. Vertical profiles of mean streamwise velocity, U, normalised with the free-stream velocity, U_∞, streamwise and vertical turbulence intensities, $I_u = \sigma_u/U$, and $I_w = \sigma_w/U$, and integral length scales of turbulence, L_u^x and L_w^x, measured at the location of the fence and in its absence, are given in Figure 6.3. The mean velocity profile in Figure 6.3(a) represents a logarithmic profile with an aerodynamic surface roughness value of 0.002 m. As shown in Figure 6.3(b), at the heights where the fence is placed, $z = $0–400 mm, I_u is between 10% and 13.5%, and I_w is between 6.7% and 8.7%. The integral length scales in the wind tunnel, as shown in Figure 6.3(c), increase with increasing height from the ground initially, but remain almost constant as the height from the ground further increases above 0.2–0.3 m. It is also reported in the literature that the integral length scales do not increase with height in a similar trend to that observed in the atmospheric boundary layer since the development of turbulent structures in a wind tunnel are constrained due to its limited cross-sectional dimensions (De Paepe *et al.*, 2016; Iyengar and Farell, 2001; Kozmar, 2011). A detailed discussion of the similarities and differences between the wind tunnel boundary layer and the atmospheric boundary layer in terms of profiles of turbulence intensity, integral length scale, and spectral characteristics is given in Jafari *et al.* (2019). Furthermore, the variations of turbulence properties in the streamwise direction within the boundary layer and in the absence of the fences were investigated through velocity measurements taken from $x = $0 mm, i.e., from the location of the fence, to $x = $1500 mm. Over this distance, I_u was found to decrease from 12.5% to 11%, and I_w decreased from 7.8% to 7.1%. Furthermore, L_u^x was found to increase from 380 mm at $x = $0 mm to $L_u^x = $444 mm at $x = $1500 mm.

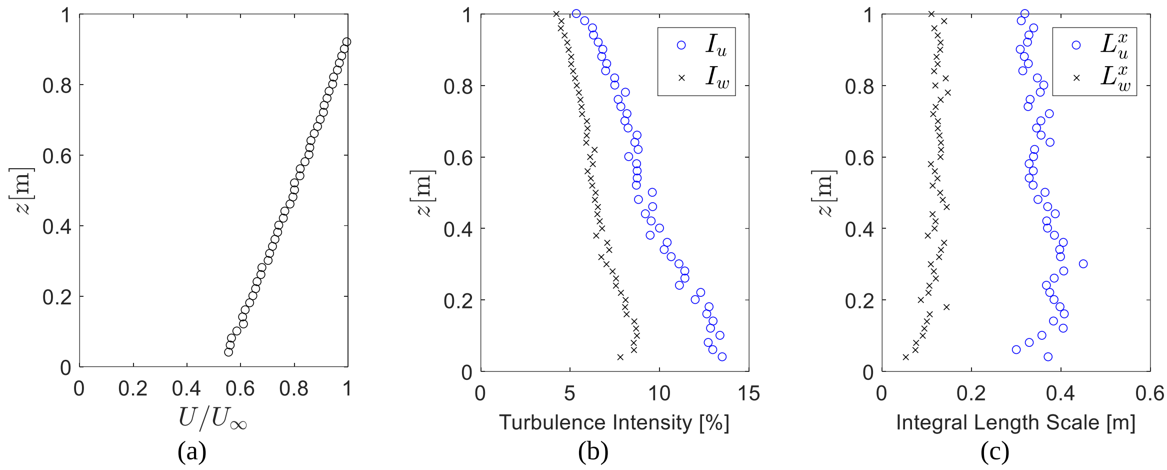

(a) (b) (c)

Figure 6.3. Profiles of the inflow boundary layer: (a) Mean streamwise velocity normalised with free stream velocity, U_∞ =11.1 m/s, (b) streamwise turbulence intensity, I_u, and vertical turbulence intensity, I_w, and (c) integral length scale of streamwise, L_u^x, and vertical velocity components, L_w^x.

6.3.2 Specifications of porous fences

Fences made from woven wire meshes were placed downstream of the roughness elements as shown in Figure 6.2. The geometric properties of the woven wire meshes are given in Table 6.1.. The meshes were made of a range of wire diameters, d, and mesh opening widths, M, which are illustrated in Figure 6.2(b), with porosities varying between ϕ =0.46 and ϕ =0.75, where $\phi = (1 - d/M)^2$. This range of porosities were selected, as for fences with porosities below 0.3, the increased blockage and separation lead to formation of a recirculation zone and increase of turbulence intensity (Lee and Kim, 1999; Tsukahara *et al.*, 2012). Since the present study focuses on turbulence reduction, fences with porosities below 0.3 were not used. Furthermore, the distribution of the wires and the shape of the mesh openings were kept similar to remove their effects on turbulence properties in the near wake of the fence as evidenced in the literature (Kim and Lee, 2001; Keylock *et al.*, 2012). All the fences had a height of H =400 mm and spanned the test section in the lateral direction, y. This resulted in a blockage ratio below 10% for all the different meshes, where the blockage ratio is defined as the ratio of the solid area covered by the fence to the tunnel cross-sectional area. A maximum of 10% blockage was applied to ensure that blockage does not affect the measurements. Furthermore, it must be noted that it is not possible to achieve a ratio of fence height to boundary layer depth, H/δ, in a wind tunnel experiment that would be identical to the H/δ in the atmospheric boundary layer for a full-scale fence. However, for the purpose of this study, the results are interpreted with respect to the inflow conditions and the scaling does not affect the results.

Table 6.1. The geometric properties of woven wire mesh fences. M and d denote the mesh opening width and wire diameter, as shown in Figure 6.2(b). $\phi = (1 - d/M)^2$ is the porosity of the fence, and $Re_d = Ud/\nu$ is the Reynolds number based on wire diameter and mean streamwise velocity at the mid-height of the fence, i.e., U =7.2 m/s. Also given in the table are the symbols used to refer to each mesh in the results section.

Symbols	M (mm)	d (mm)	ϕ	Re_d
○	5	1.6	0.46	737
+	6	1.2	0.64	553
▽	11.2	1.6	0.73	737
▷	12.5	3.15	0.56	1452
◁	19	2.5	0.75	1152
×	22.4	3.15	0.74	1452

6.3.3 Velocity measurements

Velocity measurements at each point were obtained for a duration of 60 seconds at a sampling frequency of 2 kHz using a Turbulent Flow Instrumentation (TFI) multi-hole pressure probe (Cobra probe). The accuracy of the measured velocity by the Cobra probe, according to the manufacturer datasheet, is within ±0.5 m/s and ±1° in pitch and yaw angles for turbulence intensities of up to 30%, which is well above the turbulence intensities in this study. Furthermore, a low-pass filter was applied to all the velocity signals filtering them at 900 Hz to avoid aliasing. The adopted frequency response is deemed sufficient for the measurements as it allows resolving the entire energy containing frequencies. Furthermore, the spatial resolution of the measurements based on this frequency response is approximately 1.26 mm, which is estimated based on Taylor's frozen turbulence theory at a mean velocity of 7.2 m/s. This spatial resolution is two orders of magnitude smaller than the integral length scale of turbulence within the boundary layer (380 mm), and three orders of magnitude smaller than the depth of the boundary layer (980 mm). Hence, the measurements provide an acceptable accuracy at this frequency response.

Figure 6.4 shows the velocity measurement grid in the $x - y$ plane downstream of the fences. Velocity was measured at different streamwise positions ranging from x=25 mm up to x=1500 mm, with Δx =5M for distances up to x=30M, and Δx =10M further downstream. At each streamwise distance, the measurements were acquired at five lateral positions, $y =$

±50 mm, $y = \pm 20$ mm, and $y = 0$ mm, and the average of the five lateral measurements is reported in order to reduce the possible errors associated with the position of the wires and mesh openings for different fences. The largest standard deviation of the five lateral measurements for the different fences was found to be 1.18% for mean velocity and 2.55% for turbulence intensities. The standard deviations of the five lateral measurements were larger for the integral length scales and are shown by error bars on the corresponding figures. Furthermore, the results in the next section are presented for $z = 200$ mm, which is the mid-height of the fence, $z/H = 0.5$. Due to the similarity of the variations of turbulence properties at $z/H = 0.5$ with the trends for other heights within the wake of the mesh, the results are only presented at this height.

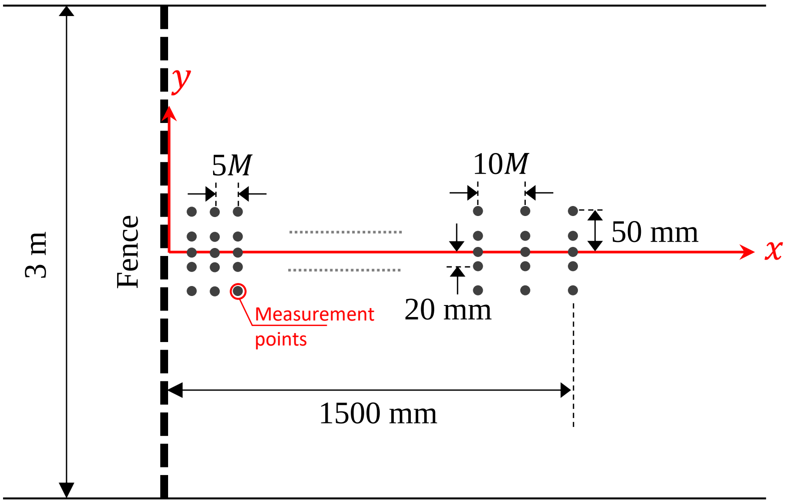

Figure 6.4. A schematic showing the locations of velocity measurements behind the fence in the $x - y$ plane. The dimensions are not to scale.

The obtained velocity measurements are used to determine the variations of the turbulence parameters, including turbulence intensity, integral length scale and power spectral density, downstream of the fences. The integral length scale of turbulence is calculated from the time scale of turbulence determined from the integration of the autocorrelation function of fluctuating velocity component. Furthermore, the power spectral density of velocity fluctuations is determined using the *pwelch* function in MATLAB using the Hann window with 50% overlap between the segments.

6.4 Results

The power spectral density of the streamwise velocity fluctuations, S_{uu}, at different downstream positions behind the fence with M =5 mm and ϕ =0.46 is presented in Figure 6.5(a). The turbulence spectrum of the inflow boundary layer in also given to provide a comparison. As shown in Figure 6.5(a), there is an increase in dissipation of turbulence energy specifically in the immediate downstream of the fence, x/M =5–10. The increased energy at high frequencies is caused by shear layers separating from the mesh wires. This mesh-generated turbulence creates a transfer of energy from low frequencies to high frequencies resulting in a suppression of larger inflow turbulence structures. With increasing the downstream distance, the flow gradually recovers and at x/M =70 the spectrum has a similar shape to the inflow boundary layer but contains lower energy over all the frequencies. A similar behaviour is found in the power spectral density of the vertical velocity fluctuations, S_{ww}, shown in Figure 6.5(b), demonstrating the dissipation of turbulence energy induced by the fence. The overall decrease of turbulence energy in the vertical component over the measured distance is however smaller than that found in the streamwise direction.

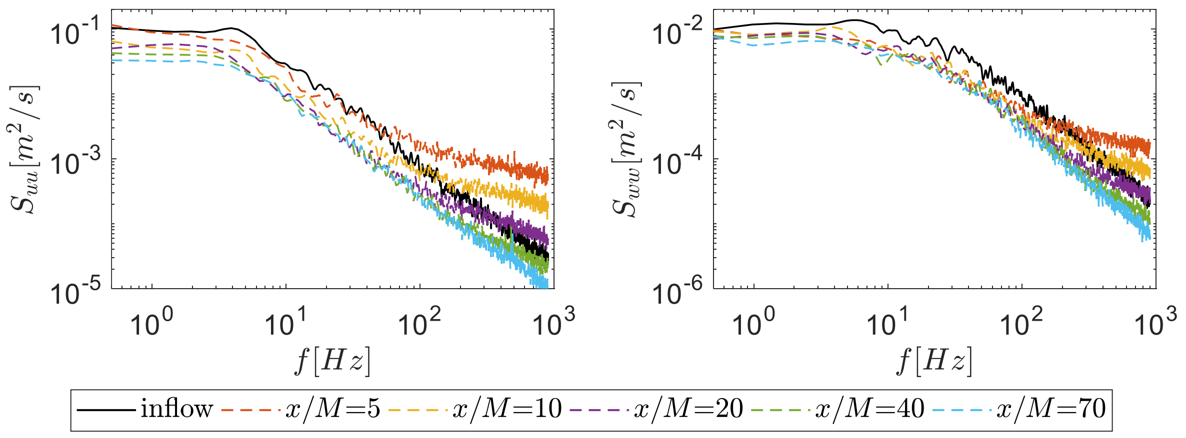

(a) (b)

Figure 6.5. Power spectral density of (a) streamwise velocity fluctuations, S_{uu}, and (b) vertical velocity fluctuations, S_{ww}, at different downstream position, x/M, for the fence with M =5 mm and ϕ =0.46. The solid black line shows the power spectral density of inflow velocity fluctuations.

The effect of fence porosity and mesh dimensions on the turbulence spectrum is demonstrated in Figure 6.6, which compares the power spectral density of streamwise velocity fluctuations behind the different fences at two downstream positions, the immediate downstream, x/M =5, and the furthest location at x/M =70. As shown in Figure 6.6(a), turbulence dissipation increases behind all the fences. However, the increased dissipation is more significant behind the fences with ϕ =0.46–0.56 compared to ϕ =0.73–0.75. Hence, the amongst the tested fences in the wind tunnel, the medium porosity fences create a larger dissipation of turbulence energy. The turbulence spectrum at x/M =70 in Figure 6.6(b) shows that the turbulence spectrum recovers to its inflow shape for all the fences. However, the turbulence energy is further reduced for fences with ϕ =0.46–0.56.

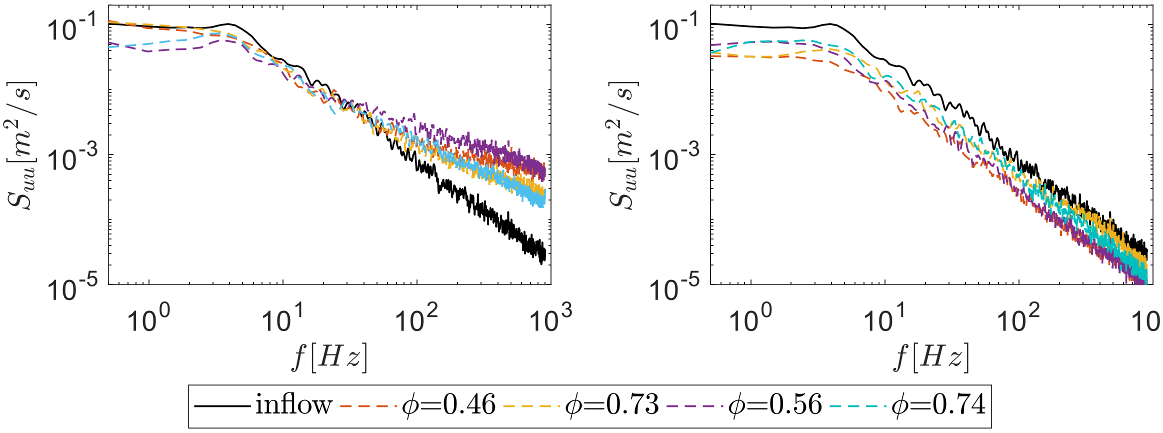

(a) (b)

Figure 6.6. Power spectral density of streamwise velocity fluctuations, S_{uu}, for different meshes at (a) x/M =5, and (b) x/M =70. The solid black line shows the power spectral density of inflow velocity fluctuations.

The effect of the mesh dimensions on turbulence dissipation is suggested to be correlated with the scale of the mesh-generated turbulence. According to Tan-Atichat *et al.* (1982), for the mesh-generated turbulence to enhance the transfer of energy from large scales to small scale, it should be of smaller scales than the energy containing scales of the inflow turbulence, but it should not be as small as the eddies within the dissipation range of the spectrum. The scale of the turbulence generated by a mesh grid is reported to be dependent on the mesh opening width by Watanabe and Nagata (2018) who found the peak of turbulence energy spectrum at a wave number of $k = 2\pi/M$. On the other hand, Lavoie *et al.* (2005) found that the spectral peaks in the turbulence generated by round rod grids scaled with the wire diameter such that the spectral peak was located at a Strouhal number of $St = kd/2\pi$ =0.035. Furthermore, Irps and Kanjirakkad (2016) found that for a constant mesh opening width, the length scale of turbulence generated by a mesh grid increased with increasing its porosity. The results of the present study show no significant effect of either d or M on the turbulence spectrum. Instead, the results suggest that the porosity which is a function of d/M is the effective parameter. This can be demonstrated through a comparison of the turbulence spectrum in Figure 6.6(a–b) for the fences with different mesh dimensions and similar porosities, which show a similar behaviour indicating that porosity is the key parameter that influences the turbulence reduction by the woven wire fence.

Figure 6.7(a–b) show the variations of streamwise turbulence intensity, I_u, behind the fences. The variations of turbulence intensity in Figure 6.7(a) are plotted against the downstream distance normalised by mesh height, H, which is equal to 400 mm for all the fences. In Figure 6.7(b), the streamwise turbulence intensity is plotted as a function of the downstream distance normalised by mesh opening width, M. Comparison of the two sub-figures demonstrates that the downstream variations of I_u scale with M, which is similar to the turbulence behind a mesh grid with a uniform inflow. While it is common practice in the literature to characterise the flow properties downstream of the fences in the atmospheric boundary layer with the fence height, the results show that the mesh opening width is a more suitable length scale for variations of turbulence intensity compared to H. As shown in Figure 6.7(b), the turbulence intensities plotted against x/M for the fences with different geometric specifications collapse into a single trend, with a maximum of 2% difference between the turbulence intensities for the different fences at $x/M >$10. A similar trend is found for other turbulence properties, and therefore the rest of the results in this section are presented as functions of x/M. As shown in Figure 6.7(b), there is an increase in streamwise turbulence intensity immediately downstream of the fences up to $x/M =$10. The increase of I_u compared to the inflow is due to the mesh-generated turbulence resulting from the shear layers separating from the wires, as also evidenced in the literature (Tan-Atichat *et al.*, 1982; Tsukahara *et al.*, 2012), which were observed in Figure 6.5(a) in the form of increase of high-frequency turbulence. The mesh generated turbulence decays quickly and after this initial region, I_u decreases to below its inflow level, $I_u =$12.5%, which is shown by the red dashed line, for all of the fences. Over the measured downstream distance, streamwise turbulence intensity decreases from the inflow level of 12.5% to $I_u =$8.8%–9.9%.

Figure 6.8(a–b) show the variations of lateral and vertical turbulence intensities, I_v and I_w, behind the fences. The level of inflow turbulence intensities is also shown in the figures. Similar to the variations of streamwise turbulence intensity, immediately downstream of the fences up to $x/M =$15, I_v and I_w increase to values larger than their inflow levels due to the mesh-generated turbulence. With further distance downstream, both lateral and vertical turbulence intensities decrease to below their inflow levels. Lateral and vertical turbulence intensities reduce by 1.45% and 1.40% on average from their inflow levels over the measured distance. Comparison of the results with I_u shows that a larger reduction of turbulence intensity is achieved in the streamwise component compared to lateral and vertical components. The larger reduction of turbulence intensity in the streamwise direction is in agreement with the findings of Groth and Johansson (1988) for the turbulence reduction behind a mesh grid covering the cross section of a wind tunnel which was subjected to a uniform and homogenous inflow turbulence.

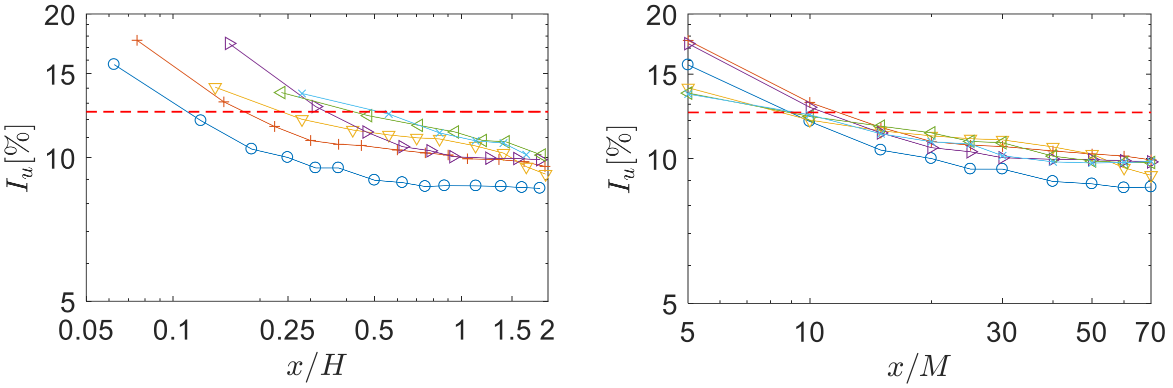

(a) (b)

Figure 6.7. Variations of streamwise turbulence intensity, I_u, behind the fence as a function of: (a) downstream distance normalised with mesh height, x/H, (b) downstream distance normalised with mesh size, x/M. The red dashed line shows the inflow level, I_u =12.5%. The symbols are as given in Table 6.1.

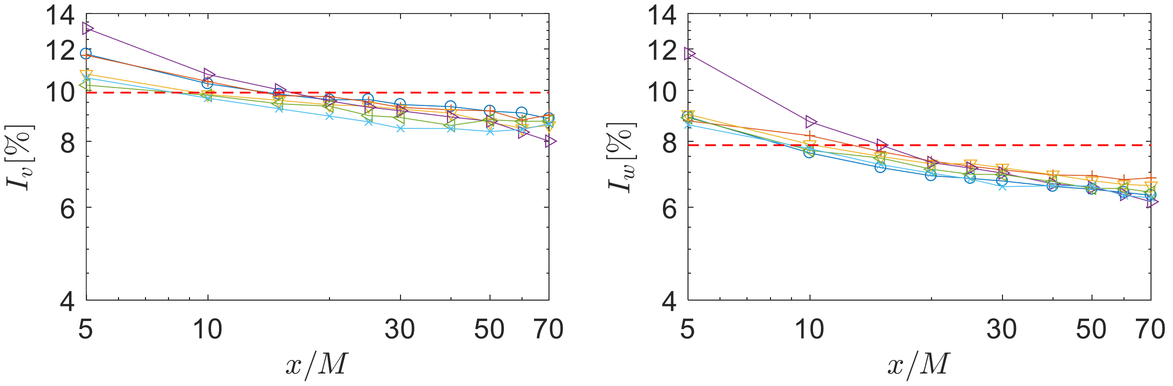

(a) (b)

Figure 6.8. Variations of (a) lateral, I_v, and (b) vertical turbulence intensity, I_w, behind the fence as a function of downstream distance normalised with mesh size, x/M. The red dashed line shows the inflow levels, I_v =9.9% and I_w =7.87%. The symbols are as given in Table 6.1.

In order to compare the effectiveness of the fences with different porosities and mesh dimensions in turbulence reduction, the decay rate of turbulence behind the different fences is determined. Figure 6.9(a) shows the variations of streamwise velocity variance normalised with the free-stream velocity, $(\sigma_u/U_\infty)^2$, with the downstream distance. As shown in Figure 6.9(a), for all of the fences, the decay of streamwise velocity fluctuations can be described by a power law function of the downstream distance, i.e., $(\sigma_u/U_\infty)^2 \propto (x/M)^\alpha$. The exponent of the power law curve fit, $\alpha(\phi)$, is found to be dependent on the porosity of the fences. For meshes with porosities of 0.46, 0.56 and 0.64, the power law exponent of the best fit is between –1.2 and –1.37, while for the meshes with porosities of $\phi =$0.73–0.75, the power law fit is given by $\alpha(\phi) =$–0.27. Hence, the streamwise turbulence decays with a faster rate for the meshes with porosities between 0.46 and 0.64. The trends for decay of streamwise velocity fluctuations within the atmospheric boundary layer inflow found in this study are similar to that reported for turbulence behind mesh grids with porosities of 0.64–0.68, which were placed in a wind tunnel subjected to uniform and homogenous inflow turbulence, where $(\sigma_u/U_\infty)^2$ was proportional to $(x/M)^{-1}$ (Tan-Atichat *et al.*, 1982). Furthermore, the decay rate of turbulence behind the fences is similar to that of the turbulence behind a mesh grid placed within a uniform flow, which is known to decay as a power law function of x/M, where α is dependent on the Reynolds number and varies between –1.2 and –1.6 for $Re_M = UM/\nu$ between 10^3 and 10^5 (Lavoie *et al.*, 2005; Kurian and Fransson, 2009; Watanabe and Nagata, 2018). The similarity of decay of turbulence behind the fences placed within an atmospheric boundary layer flow to grid turbulence behind a mesh grid with a uniform flow shows that the mesh-generated turbulence dominates the flow behaviour. The interaction of the mesh-generated turbulence with the inflow turbulence however leads to a different decay rate in the present study. Furthermore, unlike the turbulence generated behind a mesh grid in a uniform flow, which is approximately isotropic at $x/M >$40 (Laws and Livesey, 1978), and the decay rate of turbulence in all three directions is approximately the same (Kurian and Fransson, 2009), the results show that for the fences placed within the atmospheric boundary layer, the decay of turbulence is the largest for the streamwise component (see Figure 6.7 and Figure 6.8).

A similar trend is found for turbulence kinetic energy, $k = \frac{1}{2}(\sigma_u^2 + \sigma_v^2 + \sigma_w^2)$, as shown in Figure 6.9(b), such that for meshes with porosities of 0.46, 0.56 and 0.64, $\alpha(\phi)$ is between –1 and –1.2, while for the meshes with porosities of 0.73–0.75, $\alpha(\phi)$ is equal to –0.2. Therefore, the results show that the turbulence kinetic energy and turbulence intensity behind the fences, while scaling with mesh opening width, are dependent on fence porosity which is proportional to d/M. Furthermore, comparison of the trends in Figure 6.9 shows that porosity has a more significant effect on the decay rate as meshes with similar porosities but different mesh sizes (i.e., ϕ =0.73–0.75 and M =11.2 mm, 12.5 mm and 22.4 mm) have an identical decay rate. For a clear demonstration of the effect of porosity, the variations of streamwise velocity variance and turbulence kinetic energy as a function of porosity are plotted in Figure 6.10(a–b) at different downstream distances. As shown in Figure 6.10(a–b), at x/M ≥15, streamwise velocity variance and turbulence kinetic energy behind the fences increase with increase of porosity, and the largest reduction in σ_u^2 and k is achieved behind the mesh with ϕ =0.46. A different trend is only observed in the immediate downstream of the fences, x/M =5, which is where the flow is dominated by the mesh-generated turbulence, and an increase in turbulent velocity fluctuations is found. Hence, the results of this study show that the decay of turbulence is approximately identical behind meshes with different mesh opening widths with an identical porosity, and M and d do not significantly impact turbulence reduction, instead the ratio of d/M, which defines the porosity of the wire mesh, is the key parameter.

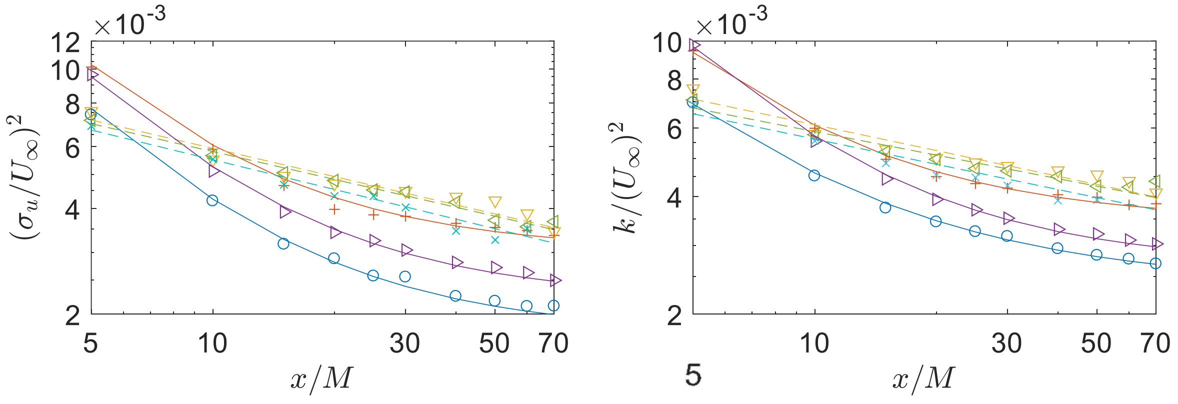

(a) (b)

Figure 6.9. Decay of turbulence with downstream distance behind the fence. (a) Decay of streamwise velocity variance, σ_u^2, (b) Decay of turbulence kinetic energy, $k = \frac{1}{2}(\sigma_u^2 + \sigma_v^2 + \sigma_w^2)$. The solid and dashed lines show power law curves fitted to the data. The symbols are as given in Table 6.1.

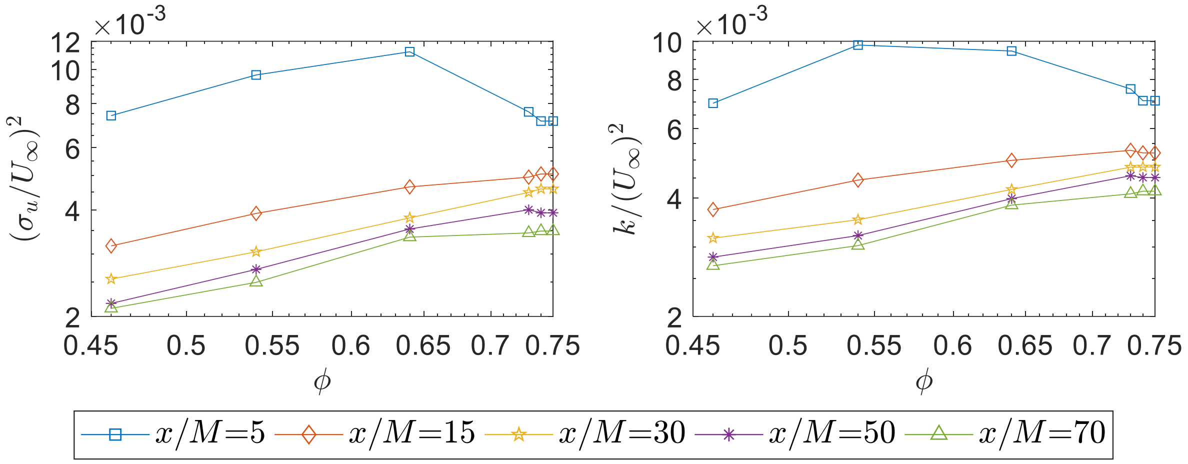

(a) (b)

Figure 6.10. Variations of (a) streamwise velocity variance, σ_u^2, and (b) turbulence kinetic energy, k, behind the fences as a function of fence porosity, ϕ, at different downstream positions, x/M.

Figure 6.11(a–b) present a measure of turbulence anisotropy showing the ratio of streamwise velocity variance, σ_u, to lateral and vertical velocity variances, σ_v and σ_w, downstream of the fences. The corresponding values in the inflow boundary layer, σ_u/σ_v =1.26 and σ_u/σ_w =1.62, are also shown by the horizontal dashed lines, which are representative of the anisotropic turbulence within the atmospheric surface layer, where σ_u/σ_v =1.28 and σ_u/σ_w =1.85 (ESDU85020, 2010). It must be noted that σ_u/σ_w in the wind tunnel boundary layer is not identical to the atmospheric boundary layer, due to limitations in the wind tunnel experiments, in which the development of turbulence structures is restricted by the tunnel cross-sectional dimensions (Iyengar and Farell, 2001; De Paepe *et al.*, 2016).

The results in Figure 6.11(a–b) show that the level of turbulence anisotropy in general reduces behind the mesh fences. Furthermore, the reduction in the anisotropy measure, in both lateral and vertical directions, is the largest for fences with medium porosities. The lowest values of σ_u/σ_v and σ_u/σ_w are reached for ϕ =0.46, followed by ϕ =0.56, and the anisotropy levels for the three fences with similar porosities, ϕ =0.73–0.75, despite their different mesh width dimensions, are very similar. According to Figure 6.11(a), in the immediate downstream region, x/M =5, σ_u/σ_v is larger than its inflow level. The relative increase in streamwise turbulence component can be associated with the mesh generated turbulence. After this immediate downstream region, the level of anisotropy behind the fences reduces and σ_u/σ_v decreases to below its inflow level due to the larger decay of turbulence in the streamwise direction. As shown in Figure 6.11(a), isotropic conditions are reached in the lateral direction for x/M ≥30, where σ_u/σ_v =1, for the fence with the lowest porosity and the smallest mesh dimensions, i.e., ϕ =0.46 and M =5 mm. The ratio of streamwise to vertical velocity variance also reduces to below its inflow level behind the fence for x/M ≥10, as shown in Figure 6.11(b). Turbulence anisotropy persists in the vertical direction for all the fences, and the largest reduction in σ_u/σ_w is achieved for the fence with ϕ =0.46 and M =5 mm, where σ_u/σ_w reaches 1.36.

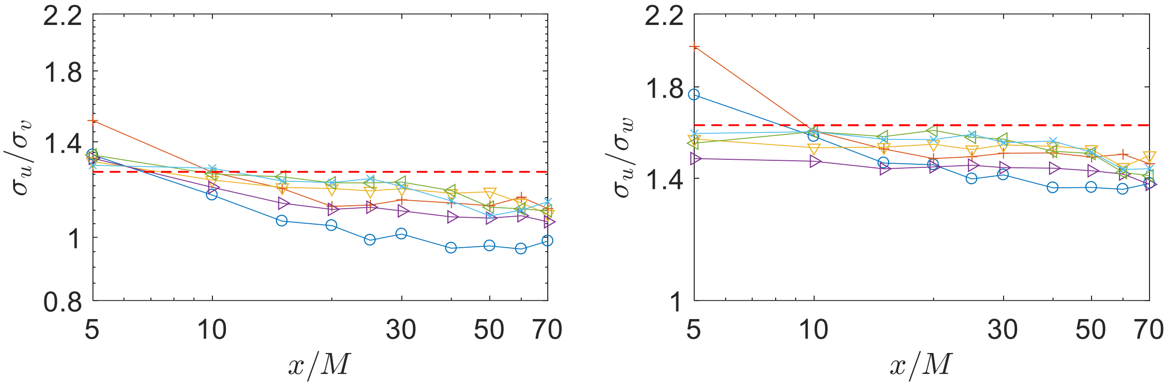

(a) (b)

Figure 6.11. Anisotropy measure behind the fence as a function of downstream distance normalised with mesh size, x/M. (a) The ratio of streamwise to lateral velocity variance, σ_u/σ_v, (b) The ratio of streamwise to vertical velocity variance, σ_u/σ_w. The red dashed line shows the inflow levels, σ_u/σ_v =1.26 and σ_u/σ_w =1.62. The symbols are as given in Table 6.1.

Figure 6.12(a) shows the variations of longitudinal integral length scale, L_u^x, behind the fences as a function of x/M, which is calculated from the autocorrelation of fluctuating streamwise velocity component. According to Figure 6.12(a), the longitudinal integral length scale is significantly smaller than its inflow level immediately behind the fences, such that at x/M =5, L_u^x reduces to values between 0.105 m and 0.235 m for the different fences, which is due to the inflow turbulence structures being broken down into smaller scales and the prominence of mesh-generated turbulence. As the downstream distance increases, with the increased dissipation (see Figure 6.5), the integral length scale becomes larger. The results in Figure 6.12(a) show that the reduction of L_u^x depends on the porosity of the fences as the values of L_u^x behind the fences are very similar for the three fences with similar porosities, ϕ =0.73–0.75. Furthermore, the fences with medium porosities create a larger reduction in the integral length scale compared to the fences with larger porosities. For fences with porosities between 0.46 and 0.64, L_u^x remains below the inflow level over the measured distance such that at x/M =70, L_u^x is between 270 mm and 330 mm.

The variations of the longitudinal integral length scale with the downstream distance behind the fence in Figure 6.12(a) can be divided into two regions: an initial region behind the fence, $x/M \leq 25$, where turbulence is highly inhomogeneous and L_u^x increases logarithmically, and a further downstream region, $x/M > 25$, where due to the decay of turbulence kinetic energy L_u^x remains approximately constant. Figure 6.12(b) shows the variations of the longitudinal integral length scale in the initial downstream region behind the fence normalised with the mesh opening width. As shown in Figure 6.12(b), L_u^x/M in this region increases as a power law function of x/M, i.e., $L_u^x/M \propto (x/M)^{\beta}$, where the power law exponent, $\beta(\phi)$, is dependent on fence porosity. $\beta(\phi)$ is found to be between 0.42 and 0.65 for the fences with ϕ =0.46–0.64 and is approximately 0.3 for ϕ =0.73–0.75. Therefore, the variations of L_u^x/M in the initial downstream region, similar to the turbulence decay rate, vary based on the fence porosity. The growth of L_u^x/M is faster for medium porosities, ϕ =0.46 and 0.64. However, as shown in Figure 6.12(a), L_u^x behind these fences does not reach the inflow level and remains smaller. Moreover, the trends demonstrated in Figure 6.12(b), resemble the variations of the longitudinal integral length scale behind a mesh grid subjected to a uniform inflow, where according to Laws and Livesey (1978), $L_u^x/M \propto (x/M)^{0.5}$ if $M/d{\sim}5$. In the present study, M/d ranges between 3.125 and 5 for the fences with ϕ =0.46–0.64 for which β is between 0.42 and 0.65. The similarity of the variations of the integral length scales in the present study to those for grid turbulence indicates that the mesh-generated turbulence dominates the flow properties in the initial downstream region.

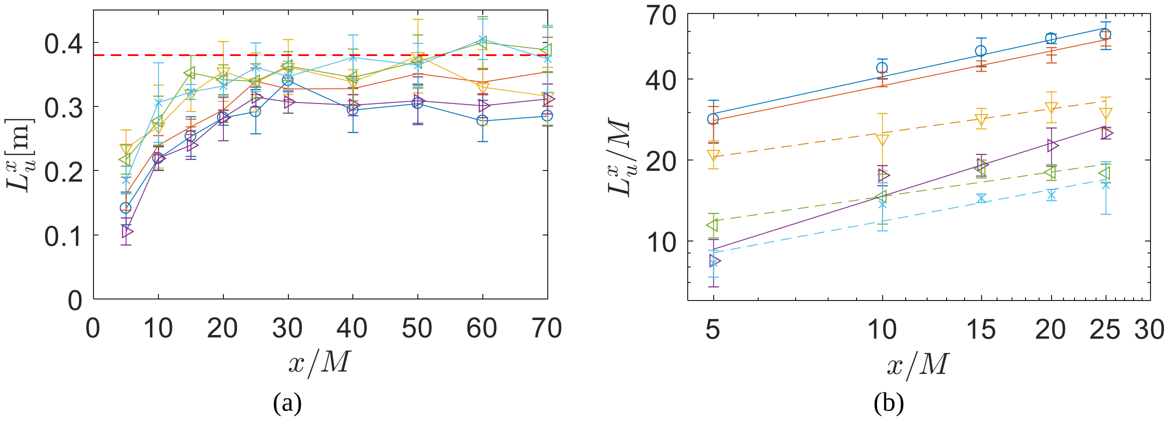

(a) (b)

Figure 6.12. (a) Variations of longitudinal integral length scale, L_u^x, behind the fence as a function of downstream distance normalised with mesh size, x/M. The red dashed line shows the inflow level, L_u^x =380 mm. (b) Longitudinal integral length scale normalised with mesh size, L_u^x/M, as a power law function of downstream distance normalised with mesh size, x/M, in the initial downstream region behind the fence. The solid and dashed lines show power law curve fits. The symbols are as given in Table 6.1. The error bars show the standard deviation of measurements of five lateral positions.

6.5 Discussion

The results in the previous section show that both turbulence intensity and integral length scale within an atmospheric boundary layer flow can be reduced by application of wire mesh fences. As discussed in the introduction section, by reducing turbulence, unsteady wind loads on structures such as solar panels and heliostats can be reduced. Figure 6.13(a–b) show predictions of the achievable wind load reduction on a heliostat with application of mesh fences. The estimations are based on the measured reduction of turbulence intensity and integral length scale behind the fence, according to the results presented in Figure 6.7 to Figure 6.12 for a downstream distance of x/M=70. The wind load reductions are predicted using the relationships given in (Jafari *et al.*, 2018; Jafari *et al.*, 2019) that correlate the wind loads with turbulence properties. As the flow has recovered at x/M=70 and the turbulence spectrum has a similar shape to the inflow atmospheric boundary layer (Figure 6.5), the relationships in (Jafari *et al.*, 2018; Jafari *et al.*, 2019) can be used for this purpose. Furthermore, the wind load reduction predictions are presented at the non-dimensional distance of x/M=70 for all the different meshes, to enable implementation of the results for full-scale industrial heliostats by scaling up the distance from the mesh opening dimension.

Figure 6.13(a) presents the peak drag force on a heliostat at vertical position, which corresponds to the largest peak drag force during its operation. The peak drag force coefficient is directly correlated with streamwise turbulence intensity and longitudinal integral length scale (Jafari *et al.*, 2018). Based on the findings of the present study, the peak drag force coefficient, C_D, on a heliostat can be reduced between 8% and 30% with application of mesh fences with porosities between 0.46 and 0.75, Figure 6.13(a). The reduction in the peak drag force, $F_D = 0.5C_D\rho U^2A$, is larger as the mean velocity is also reduced behind the fence. As shown in Figure 6.13(a), the peak drag force per area of the panel can be reduced between 19% and 48%. Similarly, the peak lift force on a stowed heliostat, where the mirror panel is aligned horizontally, can be reduced with application of fences, as shown in Figure 6.13(b). The reduction of peak lift force on a stowed heliostat is correlated with the reduction of vertical turbulence intensity and integral length scale (Jafari *et al.*, 2019). According to Figure 6.13(b), between 4% and 37% reduction in the peak lift force coefficient, C_L, on a stowed heliostat can be achieved. Furthermore, peak lift force per area of the panel, $F_L/A = 0.5C_L\rho U^2$, can be reduced between 15% and 53% using wire mesh fences with porosities between 0.46 and 0.75. As shown in Figure 6.13(a–b), with increasing the fence porosity from 0.46 to 0.75, a smaller reduction in peak wind loads can be achieved. This is due to the lower reduction in turbulence intensity and integral length scale with increase of porosity as was discussed in the previous section. Based on the achievable reductions in wind loads shown in Figure 6.13, application of the wire mesh fences with a porosity of between 0.46 and 0.75 can lead to a reduction of between 35% and 25% in the foundation cost and between 29% and 14% in the cost of drives of a heliostat based on the cost model given in Emes *et al.* (2020).

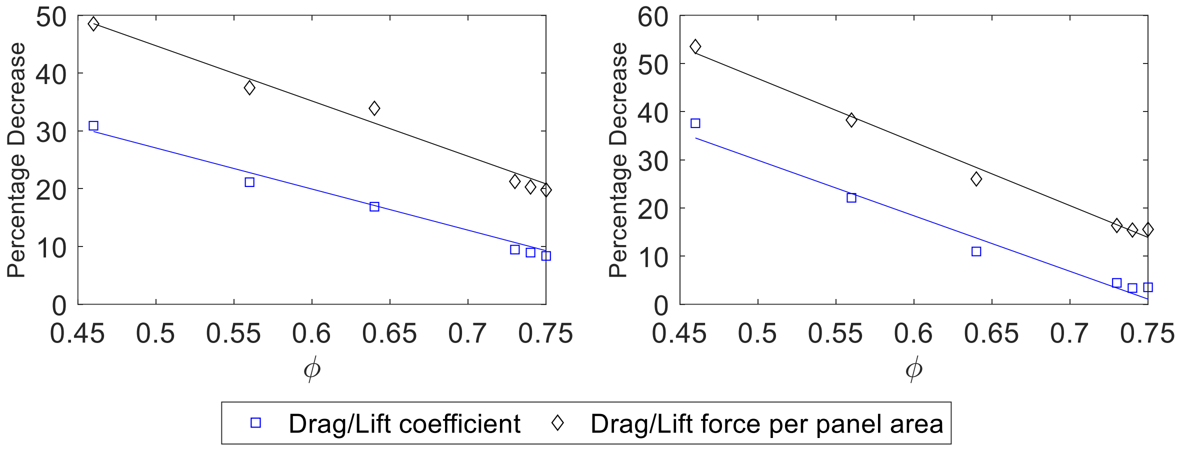

(a) (b)

Figure 6.13. The percentage reduction in peak wind loads on a heliostat with application of wire mesh fences as a function of mesh porosity: (a) the peak drag force on a vertical heliostat, (b) the peak lift force on a stowed heliostat.

The estimated wind load reductions show a high potential for utilisation of mesh fences in a heliostat field. These estimations however may vary based on the distance of heliostats from the fence and the fence height. As the dimensions of heliostats used in concentrating solar plants vary in a wide range, with heliostat panels as small as 2 m^2 up to large-scale heliostats of 150 m^2 (Pfahl *et al.*, 2017), future research is required to determinate the suitable arrangement of a fence in a solar field for the optimum wind load reduction. Application of fences for reducing the wind loads may be more suitable for heliostats of smaller dimensions as for large-scale heliostats due to the large field area, a larger fence may be required. However, for smaller heliostats, with a modification in the design of perimeter fences that are already used for protection purposes, it is possible to achieve a reduction in wind loads. Fences can be used either in the form of perimeter fences or in the form of in-field fences placed within the rows, as recommended by Peterka *et al.* (1987b), to increase their effectiveness for heliostats within the field. Furthermore, application of fences can be effective for fields of photovoltaic solar panels as they are usually within a height of up to 2 m. Therefore, porous fences can be easily used around the field to reduce the wind loads on the first rows of a field, which are exposed to the largest wind loads (Tadie *et al.*, 2019). Ground-mounted solar panels placed in the third row and further within the field benefit from the sheltering effect of the upstream rows formed by the dense packing of the field and are subjected to smaller wind loads (Peterka *et al.*, 1987a). The structural supports of the photovoltaic solar panels are however usually designed for the largest wind loads on the first two rows (Bogdan and Cretu, 2019). Therefore, there is a potential to reduce the wind loads on the first rows by application of fences and thereby reduce the total structural cost of the panels.

6.6 Conclusions

The reduction of turbulence by a woven wire mesh fence within a simulated atmospheric boundary layer flow was investigated in this study. The results showed that streamwise velocity fluctuations and turbulence kinetic energy behind the fence decreased as power law functions of the downstream distance normalised with mesh opening width. The exponent of the power law was found to depend on the porosity of the fences such that the decay rate of turbulence was faster for meshes with porosities between 0.46–0.64 compared to ϕ =0.73–0.75. With the application of the fences, the streamwise turbulence intensity was reduced from an inflow level of 12.5% to between 8.8% and 9.9% behind the fences. The level of turbulence anisotropy was found to reduce behind the fences and a larger reduction of turbulence intensity was achieved in the streamwise component compared to lateral and vertical components. The integral length scale of turbulence was found to be significantly reduced in the immediate downstream of the fences, which afterwards grew as a power law function of downstream distance over the distances between x/M =5 and x/M =25, where M is the mesh opening width. The longitudinal integral length scale for fences with porosities between 0.46 and 0.64 reduced from 380 mm in the inflow to between 270 mm and 330 mm at x/M =70.

The results of the present study show that porosity of the woven wire meshes is the key parameter which dominates their turbulence reduction performance. The findings of this study can be applied to the design of fences for reduction of wind loads on structures within the atmospheric boundary layer, such as solar panels and heliostats. It is predicted that through reduction of intensity and integral length scale of turbulence, the peak drag force on a heliostat placed behind wire mesh fences with porosities between 0.46 and 0.75 may be reduced between 48% and 19%, respectively. Furthermore, the peak lift force on a stowed heliostat can be reduced by up to 53% with application of a wire mesh fence.

Acknowledgements

Financial support for the project has been provided by the Australian Government Research Training Program, the University of Adelaide Scholarship and the Australian Renewable Energy Agency (ARENA) through Australian Solar Thermal Research Initiative (ASTRI). The authors would like to acknowledge the School of Mechanical Engineering and the workshops at the University of Adelaide.

6.7 References

Basnet, K., and Constantinescu, G. 2017. The structure of turbulent flow around vertical plates containing holes and attached to a channel bed, *Physics of Fluids*, 29: 115101.

Bogdan, O., and Cretu, D. 2019. Wind load design of photovoltaic power plants by comparison of design codes and wind tunnel tests, *Mathematical Modelling in Civil Engineering*, 15: 13-27.

De Paepe, W., Pindado, S., Bram, S., and Contino, F. 2016. Simplified elements for wind-tunnel measurements with type-iii-terrain atmospheric boundary layer, *Measurement*, 91: 590-600.

Dong, Z., Luo, W., Qian, G., Lu, P., and Wang, H. 2010. A wind tunnel simulation of the turbulence fields behind upright porous wind fences, *Journal of Arid Environments*, 74: 193-207.

Dong, Z., Luo, W., Qian, G., and Wang, H. 2007. A wind tunnel simulation of the mean velocity fields behind upright porous fences, *Agricultural and Forest Meteorology*, 146: 82-93.

Emes, M. J., A., J., Coventry, J., and Arjomandi, M. 2020. The influence of atmospheric boundary layer turbulence on the design wind loads and cost of heliostats, *Solar Energy (Under Review)*.

Emes, M. J., Arjomandi, M., Ghanadi, F., and Kelso, R. M. 2017. Effect of turbulence characteristics in the atmospheric surface layer on the peak wind loads on heliostats in stow position, *Solar Energy*, 157: 284-97.

Emes, M. J., Arjomandi, M., and Nathan, G. J. 2015. Effect of heliostat design wind speed on the levelised cost of electricity from concentrating solar thermal power tower plants, *Solar Energy*, 115: 441-51.

Emes, M. J., Jafari, A., Ghanadi, F., and Arjomandi, M. 2019. Hinge and overturning moments due to unsteady heliostat pressure distributions in a turbulent atmospheric boundary layer, *Solar Energy*, 193: 604-17.

ESDU85020. 2010. Characteristics of atmospheric turbulence near the ground - part ii: Single point data for strong winds (neutral atmosphere), *Engineering Sciences Data Unit*.

García, E. T., Ogueta-Gutiérrez, M., Ávila, S., Franchini, S., Herrera, E., and Meseguer, J. 2014. On the effects of windbreaks on the aerodynamic loads over parabolic solar troughs, *Applied Energy*, 115: 293-300.

Groth, J., and Johansson, A. V. 1988. Turbulence reduction by screens, *Journal of Fluid Mechanics*, 197: 139-55.

Irps, T., and Kanjirakkad, V. 2016. On the interaction between turbulence grids and boundary layers, *EPJ Web of Conferences*, 114: 02048.

Iyengar, A. K. S., and Farell, C. 2001. Experimental issues in atmospheric boundary layer simulations: Roughness length and integral length scale determination, *Journal of Wind Engineering and Industrial Aerodynamics*, 89: 1059-80.

Jafari, A., Ghanadi, F., Arjomandi, M., Emes, M. J., and Cazzolato, B. S. 2019. Correlating turbulence intensity and length scale with the unsteady lift force on flat plates in an atmospheric boundary layer flow, *Journal of Wind Engineering and Industrial Aerodynamics*, 189: 218-30.

Jafari, A., Ghanadi, F., Emes, M. J., Arjomandi, M., and Cazzolato, B. S. 2018. Effect of free-stream turbulence on the drag force on a flat plate. In *21st Australasian Fluid Mechanics Conference*. Adelaide, Australia.

Keylock, C. J., Nishimura, K., Nemoto, M., and Ito, Y. 2012. The flow structure in the wake of a fractal fence and the absence of an "inertial regime", *Environmental Fluid Mechanics*, 12: 227-50.

Kim, H.-B., and Lee, S.-J. 2001. Hole diameter effect on flow characteristics of wake behind porous fences having the same porosity, *Fluid Dynamics Research*, 28: 449-64.

Kolb, G. J., Ho, C.K., Mancini, T.R., and Gary, J.A. 2011. Power tower technology roadmap and cost reduction plan, *SAND2011-2419, Sandia National Laboratories*.

Kurian, T., and Fransson, J. H. M. 2009. Grid-generated turbulence revisited, *Fluid Dynamics Research*, 41: 021403.

Lavoie, P., Burattini, P., Djenidi, L., and Antonia, R. A. 2005. Effect of initial conditions on decaying grid turbulence at low rλ, *Experiments in Fluids*, 39: 865-74.

Laws, E., and Livesey, J. 1978. Flow through screens, *Annual Review of Fluid Mechanics*, 10: 247-66.

Lee, S.-J., and Kim, H.-B. 1999. Laboratory measurements of velocity and turbulence field behind porous fences, *Journal of Wind Engineering and Industrial Aerodynamics*, 80: 311-26.

Li, B., and Sherman, D. J. 2015. Aerodynamics and morphodynamics of sand fences: A review, *Aeolian Research*, 17: 33-48.

Loehrke, R. I., and Nagib, H. M. 1972. Experiments on management of free-stream turbulence, *Technical Report AGARD Report No. 598*.

Mayer, M. J., and Gróf, G. 2020. Techno-economic optimization of grid-connected, ground-mounted photovoltaic power plants by genetic algorithm based on a comprehensive mathematical model, *Solar Energy*, 202: 210-26.

Peterka, J. A., Bienkiewicz, B., Hosoya, N., and Cermak, J. E. 1987a. Heliostat mean wind load reduction, *Energy*, 12: 261-67.

Peterka, J. A., and Derickson, R. G. 1992. Wind load design methods for ground-based heliostats and parabolic dish collectors, *Technical Report for Sandia Laboratories*.

Peterka, J. A., Tan, L., Bienkiewcz, B., and Cermak, J. E. 1987b. Mean and peak wind load reduction on heliostats, *Technical Report for Colorado State University*.

Peterka, J. A., Tan, Z., Cermak, J. E., and Bienkiewicz, B. 1989. Mean and peak wind loads on heliostats, *Journal of Solar Energy Engineering*, 111: 158-64.

Pfahl, A. 2018. *Wind loads on heliostats and photovoltaic trackers*, Technische Universiteit Eindhoven.

Pfahl, A., Coventry, J., Röger, M., Wolfertstetter, F., Vásquez-Arango, J. F., Gross, F., Arjomandi, M., Schwarzbözl, P., Geiger, M., and Liedke, P. 2017. Progress in heliostat development, *Solar Energy*, 152: 3-37.

Raine, J. K., and Stevenson, D. C. 1977. Wind protection by model fences in a simulated atmospheric boundary layer, *Journal of Wind Engineering and Industrial Aerodynamics*, 2: 159-80.

Richardson, G. M. 1989. A permeable windbreak: Its effect on the structure of the natural wind, *Journal of Wind Engineering and Industrial Aerodynamics*, 32: 101-10.

Rodríguez-López, E., Bruce, P. J. K., and Buxton, O. R. H. 2017. Flow characteristics and scaling past highly porous wall-mounted fences, *Physics of Fluids*, 29: 075106.

Shiau, B.-S. 1998. Measurement of turbulence characteristics for flow past porous windscreen, *Journal of Wind Engineering and Industrial Aerodynamics*, 74-76: 521-30.

Sun, H., Gong, B., and Yao, Q. 2014. A review of wind loads on heliostats and trough collectors, *Renewable and Sustainable Energy Reviews*, 32: 206-21.

Tadie, M., Hemmati, A., Lange, C., and Fleck, B. 2019. Performance of turbulence models in simulating wind loads on photovoltaics modules, *Energies*, 12: 3290.

Tan-Atichat, J., Nagib, H. M., and Loehrke, R. I. 1982. Interaction of free-stream turbulence with screens and grids: A balance between turbulence scales, *Journal of Fluid Mechanics*, 114: 501-28.

Tsukahara, T., Sakamoto, Y., Aoshima, D., Yamamoto, M., and Kawaguchi, Y. 2012. Visualization and laser measurements on the flow field and sand movement on sand dunes with porous fences, *Experiments in Fluids*, 52: 877-90.

Watanabe, T., and Nagata, K. 2018. Integral invariants and decay of temporally developing grid turbulence, *Physics of Fluids*, 30: 105111.

Chapter 7

Conclusions and future work

The effect of turbulence within the atmospheric boundary layer on the unsteady wind loads experienced by heliostats was investigated in this thesis. Comprehensive experimental investigations were conducted for characterisation of the turbulence in a wind tunnel boundary layer and measurement of forces on heliostat models. The foremost contribution of the conducted research is establishment of a correlation between flow turbulence and the unsteady lift and drag forces applied on a stowed heliostat and an operating heliostat at vertical position, respectively. Furthermore, with the aim of developing an understanding of wind loads in a heliostat field, turbulence in the wake of a heliostat model in a wind tunnel was analysed. The turbulence properties in the wake of a heliostat were correlated with the forces on a downstream heliostat. Based on the findings, a discussion of the variations of turbulence properties of the flow within a heliostat field and their effects on the wind loads on the heliostats placed within a field was provided. Ultimately, the effect of the fences that are used around a heliostat field on the turbulence within the atmospheric boundary layer was investigated, and the feasibility of reduction of the wind loads on heliostats using the fences was analysed. In the following sections, the main outcomes and achievements of the presented research with respect to the defined objectives presented in Chapter 1 are outlined. The chapter concludes with a discussion of recommendations for future work.

7.1 Establishment of similarity criteria for measurement of wind loads in a wind tunnel experiment

Accurate measurement of wind loads in scale-model testing of heliostats in wind tunnels requires similarity of the appropriate turbulence parameters in a wind tunnel to the atmospheric boundary layer. However, the small dimensions of full-scale heliostats compared to the depth of the atmospheric boundary layer result in an inevitable mismatch of the geometric scaling ratios of the heliostat and the boundary layer in wind tunnels. This leads to a mismatch of turbulence spectra in a wind tunnel with the atmospheric boundary layer. The effect of this mismatch on the wind loads measured on scale-model heliostats in a wind tunnel experiment was investigated in Chapter 3.

Atmospheric boundary layer flows with different levels of turbulence intensity and length scale were generated in a large wind tunnel. An analysis of the turbulence properties of the simulated boundary layers was conducted to characterise the turbulence and establish its similarities and differences from an atmospheric boundary layer. Differences in the turbulence spectrum arising from non-identical scaling ratios of the boundary layer and the heliostat structure were determined. It was demonstrated that the turbulence spectrum shifted to higher frequencies in the wind tunnel compared to the corresponding height of the full-scale heliostat within the atmospheric boundary layer. Furthermore, the lift and drag forces on models with different scaling ratios were analysed to determine the effect of the geometric scaling ratio of heliostats on the measured wind loads. A direct impact of the turbulence spectrum on the forces was demonstrated through spectral analysis of the measured forces and turbulence. It was found that turbulent eddies within a range of reduced frequencies between approximately 0.01 and 1 directly affected the unsteady wind loads. It was demonstrated that similarity of this range of reduced frequencies of the turbulence spectrum in a wind tunnel experiment is required for accurate prediction of wind loads on the full-scale structure. It was found that for measurement of the unsteady drag force on a vertical heliostat, similarity of the streamwise velocity spectrum is required which permits a model with larger dimensions to be used. In contrast, accurate measurement of the unsteady lift force on a stowed heliostat requires similarity of the vertical turbulence spectrum, which can only be achieved for a model with smaller dimensions. It was shown that for a heliostat with a panel area of 144 m^2 in an open-country terrain, for the measurement of the drag force at vertical position in a wind tunnel, geometric scaling ratios of 1:24 and 1:17 could be used, while for the measurement of the lift force at stow position, a geometric scaling ratio of 1:60 provided a better match of the vertical turbulence spectrum. Hence, the suitable geometric scaling ratio of a heliostat model should be determined according to the turbulence spectrum for the corresponding full-scale structure, considering the effects of both terrain and height, and the spectrum of the simulated boundary layer in a wind tunnel.

7.2 Development of a correlation between turbulence characteristics of the flow and the unsteady wind loads

A correlation between the turbulence properties of the flow, namely, turbulence intensity and integral length scale, was investigated in Chapter 4. This correlation enables evaluation of the wind loads on heliostats with respect to the turbulence properties in their surrounding terrain. As the intensity and integral length scale of the turbulence in the neutral atmospheric boundary layer vary with the surface roughness of the terrain and the height from the ground, heliostats are subjected to different turbulence conditions based on their surrounding terrain and dimensions. Therefore, a correlation between the turbulence properties and the lift and drag forces is important for the determination of the design wind loads on heliostats. Furthermore, it can provide a link between the measurements on scale-model heliostats in a wind tunnel and the wind loads on full-scale heliostats.

Comprehensive experimental measurements were conducted to determine the lift and drag forces on heliostat models subjected to different levels of turbulence intensity and length scale within two atmospheric boundary layer flows. Through analysis of the forces, a correlation between intensity and integral length scale of the turbulence and the peak wind loads was developed considering the mutual effect of both parameters. It was demonstrated that the peak lift force on a stowed heliostat was more strongly correlated with vertical turbulence than the streamwise turbulence. It was shown that the peak lift force coefficient on a stowed heliostat was a function of a turbulence parameter defined by the vertical turbulence intensity and vertical integral length scale, as $C_{L,p} = 0.267\ln(\eta) + 1.566$, where $\eta = I_w(\frac{L_w^x}{c})^{2.4}$. Furthermore, the peak drag force on a heliostat when the mirror panel was vertical, was found to be correlated with the streamwise turbulence components. A correlation between the peak drag force on a vertical heliostat and the streamwise intensity and longitudinal integral length scale of turbulence was developed, such that the peak drag force coefficient was found to be a logarithmic function of these parameters, as $C_{D,p} = 1.046\ln(\eta) + 4$, where $\eta = I_u(\frac{L_u^x}{c})^{0.48}$.

The developed correlations are of significance for the design wind loads since they provide an estimation of the wind loads on full-scale heliostats with respect to the specific terrain type and heliostat height. While there are limitations in reproducing the turbulence conditions within the atmospheric surface layer in a wind tunnel and similarity of the turbulence spectrum cannot be achieved for scale models, using the developed correlations between the turbulence properties of the approaching flow and the wind loads a reliable method for evaluation of the wind loads on full-scale industrial heliostats can be achieved. These correlations incorporate the effect of the integral length scale of turbulence within the atmospheric surface layer and thus provide a significant improvement in the estimation of the wind loads compared to the common design methods in which only the effect of turbulence intensity is considered. Furthermore, as the intensity and integral length scale of the turbulence are dependent on the terrain type and the height from the ground, the developed method can be easily utilised for determination of the design wind loads requiring only the terrain roughness and the height of the heliostats. Application of the developed correlations was demonstrated through the evaluation of the turbulence parameter and the peak lift force on stowed heliostats of different dimensions for a range of terrain roughness values. It was demonstrated that, due to the correlation of turbulence intensity and integral length scale with the height from the ground in a specific terrain, the peak stow lift force could be expressed as a linear function of the ratio of the pylon height to chord length dimension of the mirror panel of a heliostat. Furthermore, it was found that by reducing the height to chord length ratio from 0.5 to 0.2 at stow position, the peak lift force could be reduced by 80% independent of the terrain type. As heliostats are subjected to the largest wind loads at stow position, by reduction of the peak stow lift force, it is possible to reduce the mass and strength of the heliostat support structure and foundation depth, and therefore the cost of heliostats. Hence, the results show a potential for reducing the cost of heliostats by reducing the pylon height at stow position, which can be achieved by design of telescopic pylons with adjustable heights.

7.3 Analysis of the effect of wake-induced turbulence on wind loads

The wind loads on the heliostats positioned within a field may vary significantly from the loads on a single heliostat due to their exposure to the turbulence in the wake of their upstream heliostats. The variations of the wind loads on the heliostats positioned in different regions of a field are however not well established due to the challenges of modelling an entire field in a wind tunnel. However, the wind loads on the heliostats within the field can be estimated from the mean and turbulence properties of the flow in a heliostat field due to the direct impact of the flow properties on the wind loads. As a first step towards understanding the flow properties in a heliostat field, the flow in the wake of a heliostat was investigated in Chapter 5.

The turbulence in the wake of a heliostat model placed in simulated atmospheric boundary layers in the wind tunnel was characterised through extensive velocity measurements. It was found that in the wake of a heliostat, the turbulence properties were significantly different from the inflow atmospheric boundary layer. The results showed a velocity deficit in the wake which did not recover over the measured downstream distance equal to 8 times the chord length of the heliostat panel, x/c =8. A significant increase in turbulence intensity in the wake up to a downstream distance equal to 4 times the chord length was found, with a peak at approximately x/c =1.5, where the streamwise and vertical turbulence intensities increased by more than 12-times at elevation angles of 60° and 90°. Furthermore, it was found that in the wake immediately downstream of the heliostat, the length scales of turbulence were significantly smaller as the large inflow turbulence length scales were broken into smaller scales.

The experimental characterisation of wake was accompanied by the measurement of wind loads on tandem heliostats. The differential pressure distribution on a second tandem heliostat at different gaps between the two heliostats was compared with the pressure distribution on a single heliostat. Significant differences were found, as such despite the lower mean pressure coefficient on the second tandem heliostat, regions of large-magnitude peak pressure existed at the leading edge of the panel. Furthermore, analysis of the unsteady pressure distributions showed increased unsteady variations in the position of the centre of pressure on the second tandem heliostat, specifically at elevation angles of 30° and 60°. The unsteady variations of the position of the centre of pressure as a result of the increased turbulence intensity in the wake were found to lead to an increase of the mean and peak hinge moment coefficients on the second heliostat. The large increase of the hinge moment coefficient can outweigh the reduced wind speed in the wake dependent on the gap between the heliostats and the elevation angle of the heliostat panel, and can lead to an increase of the hinge moment which is important for design of heliostat drives and torque tube. For example, at an elevation angle of 30°, and a gap between 4 to 8 times the chord length dimension of the heliostat panel, the mean wind speed reduced by less than 10%, while the hinge moment coefficient was 50% larger than the single heliostat, leading to an increase of between 20% and 50% in the peak hinge moment. Hence, the results highlight a possible need for modification of the heliostat design for the heliostats positioned inside the field compared to those at the front rows dependent on the gap between the heliostats.

A number of findings regarding the heliostat field design were made from the results of turbulence characterisation in the wake and wind load measurements on tandem heliostats. Field density was identified as a key parameter which affects the wind loads in a field. It was estimated that in high-density regions of a heliostat field, with a gap between the heliostat rows of $x/c=$1–3, the unsteady wind loads are larger than other regions due to the increased turbulence intensity in the wake, which highlights the importance of dynamic wind loads for design of heliostats as they are likely to influence the dominant frequencies of the fluctuating forces on heliostats in high-density regions of a field. Furthermore, despite the reduced mean wind speed within the field, static wind loads such as the hinge moment can increase within the field dependent on the field density and the elevation angle of heliostats during operation. The results of this research provide an improved understanding of the variations of the wind loads within a heliostat field compared to the heliostat in the first row of the field. This knowledge can be used to improve the field design with respect to the wind loads. For instance, with determination of the regions of a field with increased turbulence intensity, the structural design of the heliostats placed in these regions can be improved to account for the increased wind load fluctuations and dynamic loads that they need to withstand by increasing the mechanical impedance of the support structure. Furthermore, in low-density regions of a field where the wind load fluctuations decrease, the structural stiffness and foundation depth of heliostats can be decreased.

7.4 Investigation of a flow control method for reduction of turbulence

The effectiveness of wire mesh fences in reducing the turbulence within the atmospheric boundary layer was investigated. Fences were chosen as they are commonly used around a solar field to prevent unauthorised access to the field and to protect trespassers and animals from a possible danger. Therefore, a potential exists to utilise them as a turbulence reduction method in addition to their other protective roles with a modification in their design. Hence, the effect of wire mesh fences on the turbulence within the atmospheric boundary layer was investigated to evaluate the possibility of reducing the wind loads on heliostats using wire mesh fences.

Variations of intensity and integral length scale of turbulence with respect to fence geometric parameters were characterised through extensive velocity measurements behind various wire mesh fences placed in an atmospheric boundary layer flow in a wind tunnel. The results showed that with application of fences with porosities between 0.46 and 0.75, an inflow streamwise turbulence intensity of 12.5% could be reduced to between 8.8% and 9.9%. The decay of streamwise velocity fluctuations and turbulence kinetic energy behind the fences were found to be a power law function of the downstream distance normalised with the mesh opening width. The exponent of the power law was dependent on the porosity of the fences, such that the decay rate of turbulence was faster for meshes with porosities between 0.46 and 0.64 compared to porosities of 0.73–0.75. Furthermore, the integral length scale of turbulence was found to be significantly reduced immediately downstream of the fences and grew afterwards with increasing the downstream distance, remaining below the inflow level for the fences with porosities between 0.46 and 0.64. Through comparison of the turbulence reduction behind wire mesh fences with different porosities and mesh opening widths, it was found that porosity was the key parameter which determined the reduction in turbulence intensity and length scales.

The effectiveness of wire mesh fences for reducing the wind loads on heliostats was discussed based on the variations of turbulence intensity and integral length scale behind the fences. It was estimated that through reduction of mean velocity, streamwise turbulence intensity and integral length scale, the peak drag force on a heliostat at the vertical position could be reduced by 48% with utilisation of a wire mesh fence with a porosity of 0.46. Furthermore, the peak lift force on a stowed heliostat could be reduced by 53% behind a wire mesh fence with a porosity of 0.46. With increasing the porosity of the wire mesh fence to 0.75, the reduction in peak drag and lift forces reached 19% and 15%, respectively. The estimated wind load reductions are based on the assumption that the height of the fence is larger than the heliostats and heliostats are placed at a downstream distance of 70-times the mesh opening width. Therefore, these estimations may vary with increasing the distance of heliostats from the fence and changing the fence height. As the dimensions of heliostats used in concentrating solar plants vary in a wide range, future research is required to determine the effectiveness of perimeter fences in wind load reduction based on the arrangement of the field. Application of fences for reducing the wind loads may be more suitable for heliostats of smaller dimensions as for large-scale heliostats, due to the large field area, very large fences may be required. However, for smaller heliostats, with a modification in the design of perimeter fences that are already used for protection purposes, it may be possible to reduce the wind loads. Furthermore, additional fences within the field of heliostats can also be utilised to reduce the wind loads on the heliostats positioned in the inner rows. Hence, the results of this research indicate a potential to reduce the peak lift and drag forces on heliostats, especially for heliostats of smaller dimensions, that can lead to reductions in the costs of support structures and drives. Future investigations are however required to further investigate the practicability of application of fences for reduction of wind loads in a heliostat field.

7.5 Recommendations for future work

The findings of the research presented in this thesis, have shown that the unsteady wind loads on heliostats are directly correlated with the incoming turbulence, and progress has been taken towards understanding turbulence in a heliostat field. However, the complexity of the flow in a heliostat field warrants further investigation in the future. While this study focused on development of a more in-depth knowledge of the effect of atmospheric turbulence on wind loads, further complementary work is required to implement this knowledge for design of heliostat fields. Some recommendations for future investigations are discussed in the following.

7.5.1 Measurement of wind loads on full-scale heliostats in the atmospheric surface layer

Using the developed correlation between turbulence and wind loads in this thesis, wind loads on full-scale heliostats at different terrains were predicted in Chapter 4. Future research can focus on the measurement of wind loads on full-scale heliostats to support the accuracy of these predictions. The lift and drag forces on a single full-scale heliostat placed within the atmospheric surface layer could be measured over different time periods, from which time-averaged mean and peak force coefficients could be determined. The measurement of forces should be accompanied with simultaneous measurements of three components of wind speed and temperature. Wind speed measurements are necessary to characterise the approaching flow in terms of mean wind speed, turbulence intensity and power spectral density of wind velocity fluctuations. Furthermore, the temperature measurements could help to determine time periods of neutral stability within the atmospheric boundary layer, which is required to allow comparison of the measurements with the wind tunnel data. Analysis of wind loads on full-scale structures with respect to the incoming wind turbulence can help build upon the wind tunnel experiments to provide a more reliable estimation of wind loads in the field.

7.5.2 Theoretical analysis of the effect of turbulence on wind loads on heliostats

The effect of atmospheric boundary layer turbulence on the heliostat wind loads was investigated in this thesis through wind tunnel measurement of forces at different inflow turbulence conditions. The relationship between turbulence spectrum and the lift and drag forces on heliostats was studied through analysis of the aerodynamic admittance, and correlations between intensity and integral length scale of the flow and the lift and drag force coefficients on a stowed and a vertical heliostat were developed. In order to better understand how turbulence interacts with the heliostat structure at different elevation angles of the mirror panel, future studies can focus on theoretical analysis of this interaction. Theoretical models including thin airfoil theory and rapid distortion theory based on the models in the literature (Jackson et al., 1973; McKeough and Graham, 1980) can be developed and improved to incorporate the properties of the anisotropic turbulence within the atmospheric boundary layer. These models can be used to analyse the unsteady lift and drag forces on a flat plate within the atmospheric boundary layer turbulence at different elevation angles. The theoretical analysis when validated and accompanied with wind tunnel experimentations can be used to develop models for prediction of the unsteady forces on heliostats at different elevation angles.

7.5.3 Characterisation of turbulence and wind loads in an array of heliostats

The wakes of multiple heliostats placed side-by-side in a row and in subsequent rows interact with each other. This interaction affects the flow and aerodynamics of multiple heliostats. While in this study turbulence in the wake of a single heliostat was characterised, future research is required for a better understanding of flow around multiple heliostats. Due to the size restrictions in a wind tunnel, it is not possible to model an entire heliostat field. However, experiments could be conducted to study the flow around an array of a limited number of heliostats and to investigate the interaction of their wakes. This investigation could provide an improved understanding of the effects of wind direction, field arrangement and the spacing between the heliostats on the flow properties and consequently the wind loads on the heliostats in an array. Wind tunnel experimentations including flow visualisation and measurement of forces in an array of heliostats will help to provide a better understanding of complex variations of the wind loads in a heliostat field.

7.5.4 Optimisation of field layout with respect to wind loads

The arrangement of heliostats in a field is typically determined based on optimisation of the optical performance of the field through reduction of the blocking and shading effects. However, as the field arrangement affects the flow within the field and consequently the wind loads on heliostats, there is an opportunity to improve the field design with consideration of the variations of wind loads in addition to the optical effects. Future research could investigate field design strategies for reducing the wind loads. Methods such as channelling the flow by allowing a gap in the field in an appropriate direction could be studied. Furthermore, the effect of arrangement of heliostats in staggered and tandem layouts on the wind loads could be compared. Wind tunnel experiments including flow visualisation and velocity measurements within a scaled array of heliostat models could be conducted to characterise the effect of these layout arrangements on the flow properties. The knowledge of the flow and turbulence properties from the wind tunnel experiments could be used to estimate the variations of wind loads on heliostats, which could help to develop methods for improvement of the design of the field layout.

7.5.5 Development of an improved stowing strategy

The commonly used criterion for stowing heliostats is the increase of wind speed above a certain threshold, which is typically measured at one or two locations in the field. However, based on the layout and spacing of the heliostats in a field, the wind loads are different in different regions of a field. It may not be necessary for the heliostats in some regions to be stowed as they may experience lower loads due to the sheltering effect of their upstream heliostats. In contrast, the increased turbulence in dense regions of a field leads to an increase of the peak wind loads in these regions, which may necessitate stowing them at lower wind speeds than the pre-determined velocity threshold. Therefore, with the knowledge of the wind loads in different regions of a field, it is possible to develop smarter stowing strategies that allow partial stowing of the field. This requires an in-depth understanding of the effects of field layout and wind direction on the flow and turbulence properties in the field and the wind loads. This is potentially an area for future research which can lead to improvements in the field operation and power output.

7.5.6 Investigation of perimeter and in-field fence configurations for reducing wind loads in a heliostat field

Mesh fences as a method for manipulating turbulence were investigated in Chapter 6, and the effectiveness of the wire mesh fences in reducing turbulence was demonstrated. For this method to be employed in a heliostat field, future research is required to determine the optimum arrangement of the fence, in form of perimeter or in-field fences, and to investigate how the fence affects the wind loads in a heliostat field. Whether the wind load reduction influence of a perimeter fence is limited to the first row of heliostats or it affects the wind loads on the next rows needs to be investigated. Heliostats in the second row of a field are mainly influenced by the flow properties in the wake of the heliostats in the first row. However, through altering the approaching flow, the presence of the fence affects the wake of the heliostats in the first row, and thereby the fence can affect the wind loads on the heliostats in the second row. Wind tunnel experiments could be carried out to investigate the effect of the fence on the wind loads on tandem heliostats. Mean and peak lift and drag forces on a second heliostat model placed in tandem of an upstream one could be measured with and without the presence of a wire mesh fence in the upstream of the first heliostat. The distances between the two tandem heliostats and between the fence and the first heliostat could be varied to determine the configurations in which the fence could effectively reduce the wind loads on the second heliostat. The wind load measurements could be accompanied with characterisation of the flow properties in the wakes of the fence and the first heliostat.

Another area of future research could focus on application of in-field fences for reducing the wind loads on the heliostats placed within the field. Experimental measurements could be conducted to determine the lift and drag forces on the second tandem heliostat when a wire mesh fence is placed within the two tandem heliostats. Furthermore, velocity measurements should be obtained behind the fence and in the wake of the first heliostat in the absence of the fence, to determine the effect of the fence on the intensity and length scales of turbulence in the wake of the heliostat in the first row. Characterisation of turbulence properties and the wind load measurements on the tandem heliostat will help to determine the effectiveness of application of in-field fences within rows of a heliostat field.

7.5.7 Investigation of wind loads during non-neutral atmospheric conditions

Wind loads are commonly investigated in a neutrally stratified boundary layer. The diurnal cycle, induced by heating and cooling of the Earth’s surface during day and night, however, affects the turbulence within the atmospheric boundary layer. During the daytime, the upward heat flux from the Earth’s surface increases the turbulence production and the wind speed increases rapidly with height deviating from the logarithmic mean wind speed profile of the neutral conditions. Thermal instability in the atmosphere affects turbulence intensity and integral length scale within the surface layer. As thermal buoyancy effects and diurnal variations are less significant during extreme weather conditions with clouds and high wind speeds, they do not affect the survival wind loads. However, wind loads in a heliostat field during its operation in sunny weather conditions may be influenced by the buoyancy in the atmosphere. This is potentially an area for future research to determine the effect of thermal stability in the atmospheric boundary layer on wind loads on operating heliostats.

7.5.8 Investigation of dynamic response of heliostats under wind loading

Future studies are required to investigate the dynamic response of a heliostat to unsteady wind loads. The coupling between the temporal and spectral variations of wind loads with the dynamic properties of a heliostat structure creates vibrations within the heliostat panel, which are important for the tracking accuracy of a field. Large vibrations of the mirror panels decrease the tracking accuracy and the overall optical performance of the field leading to a reduction of the power output. A comprehensive study of the dynamic response of the heliostat structure, considering different structural designs of heliostats, is therefore necessary in the future. Experimental measurements of the displacements of the panel of a heliostat model and measurements of differential pressure distributions on the panel when subjected to a turbulent atmospheric flow can be obtained in a wind tunnel. The displacement measurements should be obtained for various panel sizes, heights, and thicknesses of the pylon. Analysis of the displacements along with surface pressure distributions with respect to the turbulence within the flow will provide an understanding of the dynamic response of a heliostat structure to turbulence within the atmospheric surface layer. The structural analysis could be further expanded by development of a numerical model of a heliostat under unsteady wind loading. The high cost and time required for such numerical analysis, however, may require simplifications of the turbulent fluid flow.

7.6 References

Jackson, R., Graham, J. M. R., and Maull, D. J. 1973. The lift on a wing in a turbulent flow, *Aeronautical Quarterly*, 24: 155-66.

McKeough, P. J., and Graham, J. M. R. 1980. The effect of mean loading on the fluctuating loads induced on aerofoils by a turbulent stream, *Aeronautical Quarterly*, 31: 56-69.